Backgrounds in XENON1T

Breur, Sander

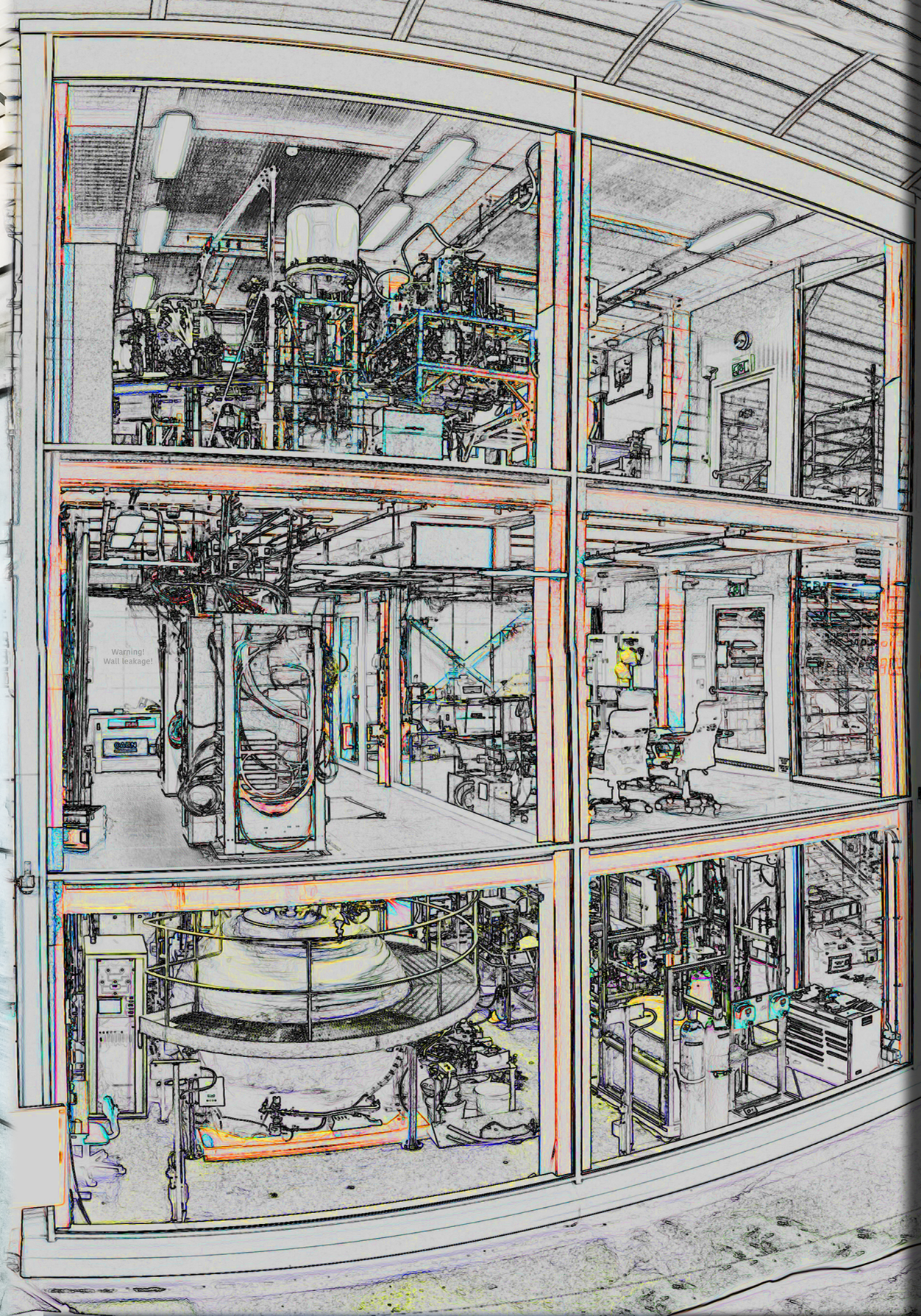

BACKGROUNDS IN XENON1T

P.A. (Sander) Breur

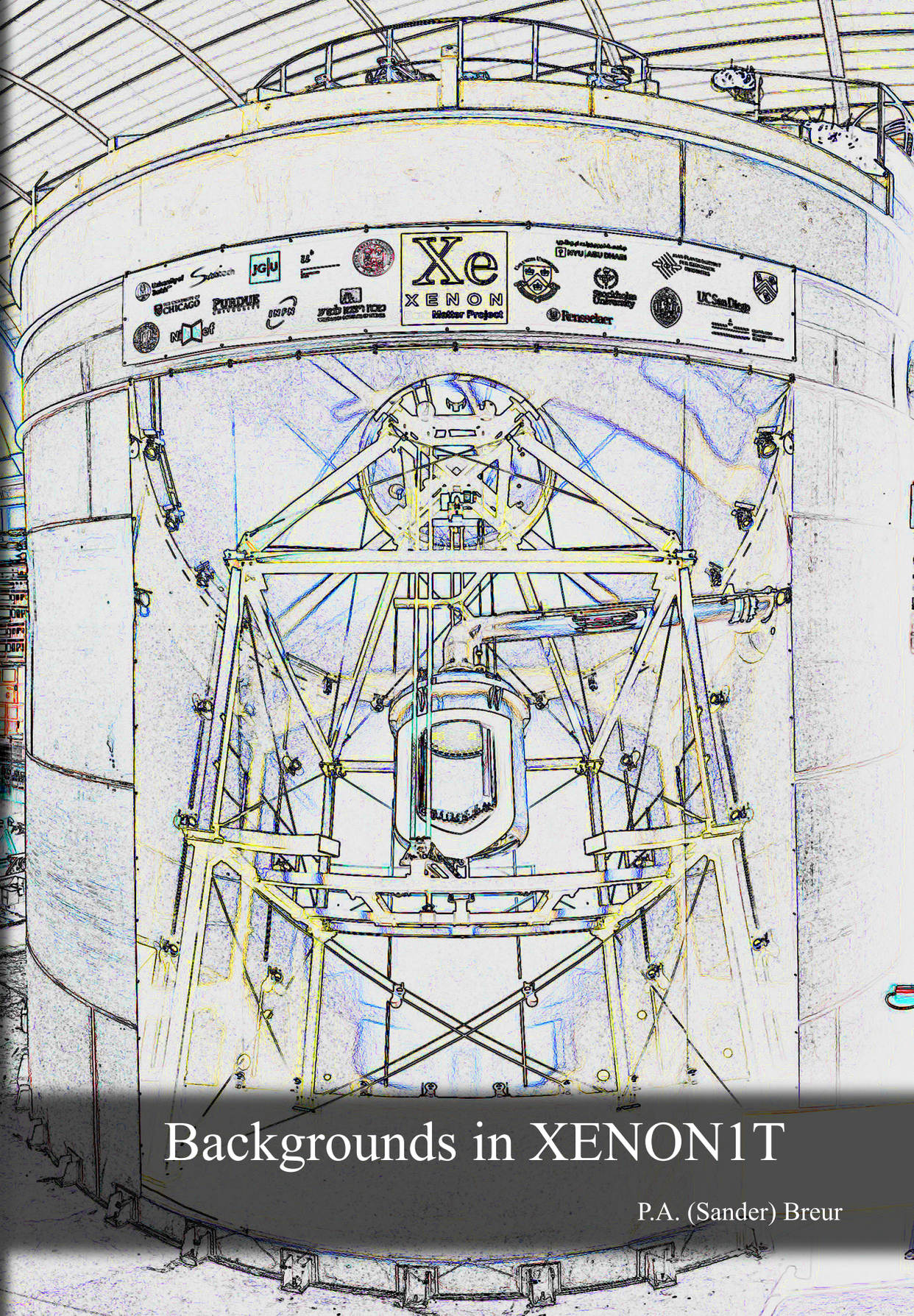

Backgrounds in XENON1T

P.A. (Sander) Breur

Backgrounds in XENON1T

P.A. (Sander) Breur

This work is part of the research programme of the Foundation for Fundamental Research on Matter (FOM), which is part of the Netherlands Organisation for Scientific Research (NWO). The work is carried out at the National Institute for Subatomic Physics (Nikhef) in Amsterdam, The Netherlands.

ISBN 978-94-6323-475-7

Cover design by Jasper Nobelen. Based on a photo of the XENON1T experiment by R. Corrieri and P. de Perio.

Printed by Gildeprint

Backgrounds in XENON1T

Academisch Proefschrift

ter verkrijging van de graad van doctor
aan de Universiteit van Amsterdam
op gezag van de Rector Magnificus
prof. dr. ir. K.I.J. Maex
ten overstaan van een door het College voor Promoties ingestelde
commissie, in het openbaar te verdedigen in de Aula der Universiteit
op vrijdag 11 januari 2019, te 11:00 uur

door

Pieter Alexander Breur

geboren te Amsterdam.

Promotiecommissie:

Promotores:	Prof. dr. M.P. Decowski	Universiteit van Amsterdam
	Prof. dr. F.L. Linde	Universiteit van Amsterdam
Overige Leden:	dr. G. Bertone	Universiteit van Amsterdam
	Prof. dr. A.P. Colijn	Universiteit Utrecht / Universiteit van Amsterdam
	Prof. dr. ir. P.J. de Jong	Universiteit van Amsterdam
	dr. R.F. Lang	Purdue University, Indiana, USA
	Prof. dr. H.G. Raven	Vrije Universiteit Amsterdam
	Prof. dr. M. Schumann	Universität Freiburg, Germany
	dr. M. Vreeswijk	Universiteit van Amsterdam

Faculteit der Natuurwetenschappen, Wiskunde en Informatica

Dedicated to my father, Evert Maarschall.

The best way to teach, is to lead by example.

Contents

Summary: The hunt for dark matter with XENON1T

We are missing 85% of the matter in our Universe. This simple statement motivates thousands of physicists around the world to search for and explain dark matter. The first observations suggesting the existence of more non-luminous (e.g., dark matter and neutrinos) than luminous matter (e.g., stars, planets and gas) are now about 100 years old. However, only in the last decade has the field of experimental dark matter physics really taken flight. The reason for this is that more and more ground, sky and space telescopes have measured very precisely how much mass we are really 'missing'. Figure 1 depicts this best: only 1% of the mass of the Universe can be explained by stars (and planets), and only 14% by (diffuse) gas. Without the missing 85% of the mass we cannot explain the beginning of our Universe, the structure formation we see today or even the fact that we have planets and stars. No manuscript can be comprehensive enough to explain all the theoretical and experimental work going on in this field. This summary simply attempts to answer the five main questions that led to the five chapters in this PhD thesis. After the summary, the author gives a personal recommendation of work to further improve the understanding of XENON1T and future upgrades.

Chapter 1: Why do we believe there is dark matter? The first observations of missing matter (non-luminous) were made in the 1920's. Since then, almost all new observations have painted a more precise picture of how much matter we need in order to explain our Universe. Astrophysical measurements include: the Cosmic Microwave Background, colliding galaxy clusters, gravitational lensing, large-scale structure formation and rotational velocity curves of galaxies. The improved sensitivity of these measurements over the last decade constrain the total matter and energy

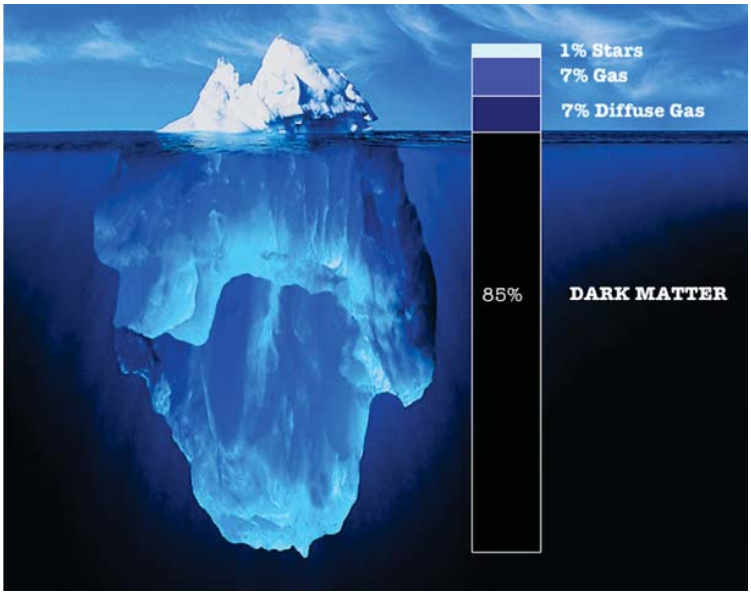

Figure 1: A beautiful iceberg illustrating the extent of our knowledge about the matter content of the Universe. We currently have only observed about 15% of all matter in the Universe (including stars, planets, gas, etc.,). The main part of the iceberg, still being obscured from our vision, corresponds to the missing 85% dark matter. Original image from [1], credits: Ralph Clevenger.

density in our Universe with high precision ($\Omega_m = 0.308 \pm 0.0012$, $\Omega_\Lambda = 0.692 \pm 0.0012$). Of the approximately 30% of matter in our Universe, about 85% is something we call dark matter, and what this consists of is yet to be determined.

Several particle candidates have been proposed to answer this dark matter mystery. These are for example: sterile neutrinos, axions and WIMPs. For WIMPs the relic dark matter density we see today can be explained under the assumption of an interaction cross section on the order of the weak scale. This, together with the fact that WIMP particles fit extensions of the Standard Model of particle physics, makes the WIMP an excellent candidate to search for.

Chapter 2: How do we use the XENON1T detector to find dark matter? The XENON1T experiment (see cover) is located at the underground Laboratori Nazionali del Gran Sasso in Italy. It uses 3.2 t of xenon as target material, which is purified and cooled continuously during operation. 248 light detectors (PMTs) are used to measure every particle interaction. To determine if dark matter interactions are found we com-

pare the number of light flashes seen with the number we expect from Monte Carlo simulations. The detector operates as a dual-phase liquid xenon Time Projection Chamber (TPC), which is explained in figure 2.

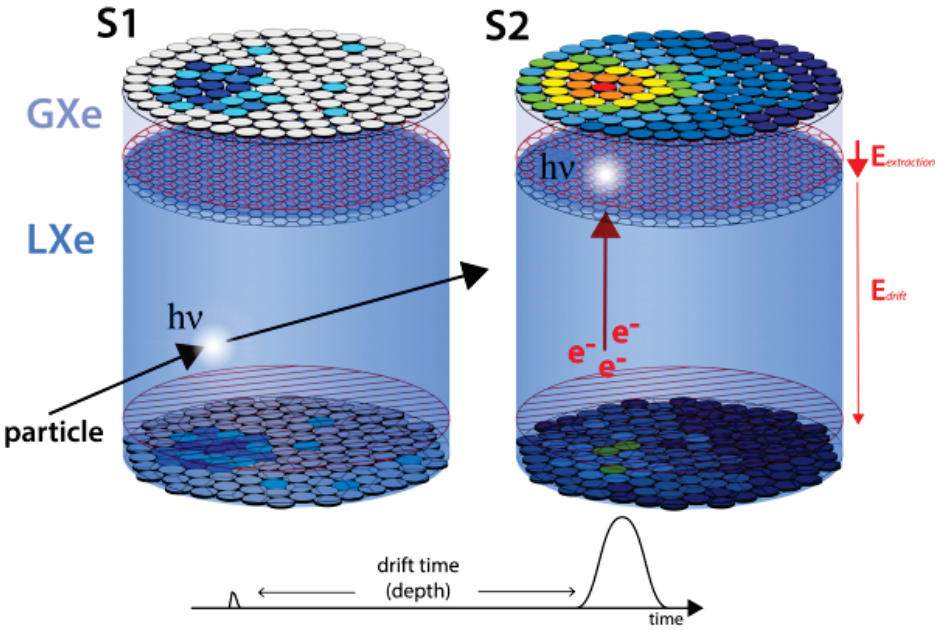

Figure 2: Detection principle of XENON1T, which uses a dual-phase liquid xenon Time Projection Chamber (TPC). Particles interact in liquid xenon (LXe) and produce a direct light signal (S1), and gaseous xenon (GXe) to convert the freed electrons into a delayed light signal (S2). The time and interaction position (x,y,z) is reconstructedvent. From [2].

Figure 2 shows a particle interacting in the liquid xenon and producing a light (left) and charge (right) signal. The primary scintillation light signal (S1) is observed by several of the 248 light detectors (PMTs), placed at the top and bottom of the TPC. For the charge signal, the freed electrons first drift upwards to the liquid-gas interface where they create a secondary scintillation light signal (S2). The ratio of the S1 and S2 signals will determine if we measured a background-like (electronic recoils) or signal-like (nuclear recoils) particle. The pattern of the S2 signal is used for the (x,y) position reconstruction, while the time between the S1 and S2 is used to determine the depth (z).

If a WIMP collides with ordinary matter we expect low energy depositions of about $\mathcal{O}(10)$ keV. As the (spin independent) WIMP-nucleon cross section scales with the atomic number squared (A^2), xenon has a higher detection potential than most other stable elements. At a temperature of

about -100 °C and pressure of about 2 bar, xenon is a transparent liquid in which emitted photons can travel freely. The XENON1T experiment measures both the light (photons) and charge (electrons) resulting from any particle interacting in the detector (e.g., alpha, beta, gamma, neutrons and hopefully WIMPs).

Chapter 3: How does XENON1T discriminate between signal and background events? To reconstruct the deposited energy of particles that interact in the liquid xenon we need to correct the S1 and S2 signals for any time- and spatial-dependent signal losses. The S1 (light signal) is corrected for an (x,y,z)-dependent light collection efficiency in the TPC. The S2 (charge signal) is corrected for a time- and depth-dependent electron-lifetime. This is because electrons can be lost if they attach to impurities in the liquid xenon while drifting. The S2 is also corrected for (x,y)-dependent amplification variations due to dead PMTs and warping of the meshes. Krypton calibration data, with its mono-energetic low-energy decay, is used to build the relevant correction maps.

An electric field distortion due to the low electric field configuration, was not expected, but a dedicated correction was found and applied. After a total of 16 data quality and selection cuts, over 80% of events in our low energy region remain. The energy calibration shows a very high total photon detection efficiency of about 14%, which is in accordance with the designed high reflectivity of the TPC walls, high transparency of the meshes and high quantum efficiency of the photo multiplier tubes. The shape and position of the final electronic recoil (background-like) and nuclear recoil (signal like) bands are shown in figure 3.

Electronic recoils produce much larger S2 signals than nuclear recoils (at the same S1 signal). Any event below the mean of the nuclear recoil band (red solid line) is most likely a signal event, and this is where XENON1T is most sensitive to WIMP interactions (nuclear recoils). At a 50% nuclear recoil acceptance XENON1T can detect WIMP-like events in the detector, while at the same time rejecting $(99.82 \pm 0.05)\%$ of all electronic recoil background events.

Chapter 4: Where do the background signals in XENON1T come from? To have a chance of measuring WIMPs scattering off xenon nuclei, XENON1T was designed and built as an ultra-low background experiment. Even with the discrimination power of about 99.8% between nuclear and electronic recoils, the total electronic recoil background should not exceed $\mathcal{O}(1000)$ events. From Monte Carlo simulations we know the main background component in the low energy region (1-12 keV) is from

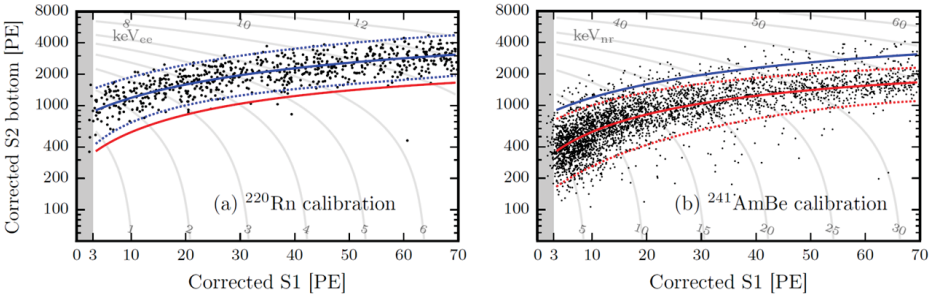

Figure 3: Observed event distribution in cS2$_b$ vs. cS1 for (a) ^{220}Rn electronic recoil (ER) calibration and (b) ^{241}AmBe nuclear recoil (NR) calibration data. The mean (solid) and $\pm 2\sigma$ quantiles (dashed) are shown for both the ER band (blue) and NR band (red). The shift in median cS2 value for the same cS1 value is used to distinguish between signal-like (NR) and background-like (ER) events. From [3].

(naturally occurring) radon (^{222}Rn), or more specifically, from the decay of one of its daughter ^{214}Pb.

To constrain estimates of the concentration of ^{214}Pb, the concentration of its mother isotope ^{218}Po and daughter isotope ^{214}Po are determined by means of an S1-only alpha analysis. Seven alpha lines are identified in figure 4, all originating from the radon and thoron (^{220}Rn, ^{216}Po and ^{212}Po) decay chains. The found concentrations of ^{218}Po $(13.7 \pm 1.1)\,\mu$Bq/kg and ^{214}Po $(4.4 \pm 0.2)\,\mu$Bq/kg give an upper and lower limit on the concentration of ^{214}Pb, respectively. Both isotopes show stable decay rates over time and a homogeneous distribution throughout the TPC. From the alpha spectrum it is clear that the thoron decay chain will not contribute more than $\mathcal{O}(1\%)$ to the total ER background.

The one isotope found in the alpha spectrum that does not originate from within the liquid xenon is ^{210}Po. This isotope is found to originate mostly from the PTFE (Teflon) walls, where it was deposited during construction.

To get a better estimate of the precise ^{214}Pb concentration, its spectrum was determined and compared to the full ER background spectrum. A ^{214}Pb concentration of $(8.4 \pm 1.2)\ \mu$Bq/kg is found, about 16% lower than the Monte Carlo expectations of $10\,\mu$Bq/kg. By fitting all the individual ER background components together, the total ER background rate was found to be $(1.90 \pm 0.24) \times 10^{-4}\ (\mathrm{kg \cdot day \cdot keV})^{-1}$, which is in agreement with the expected $(1.80 \pm 0.15) \times 10^{-4}\ (\mathrm{kg \cdot day \cdot keV})^{-1}$ from simulation. This does not only show that XENON1T has achieved its

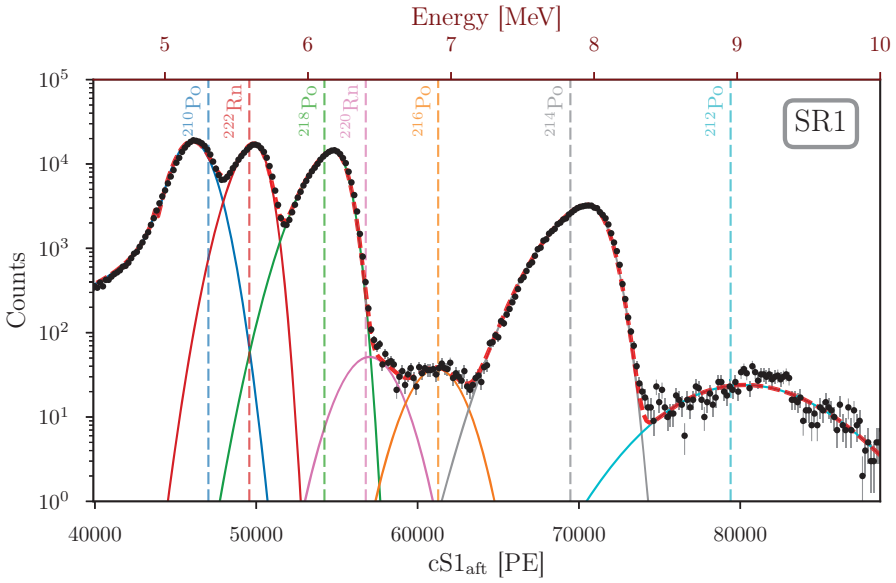

Figure 4: Alpha spectrum of ^{210}Po (blue), ^{222}Rn (red), ^{218}Po (green), ^{220}Rn (pink), ^{216}Po (orange), ^{214}Po (grey) and ^{212}Po (light blue) in Science Run 1. The top axis shows scaling cS1$_{\mathrm{aft}}$ to energy, assuming a linear scaling relationship and using the ^{222}Rn peak as anchor. The dashed lines indicate the respective alpha energies.

ultra-low background goals, but also that XENON1T has the lowest low-energy ER background rate of all dark matter experiments.

Chapter 5: Did we find dark matter with XENON1T? No, unfortunately, we did not. But I can proudly say that we are world leading in finding nothing.

For a WIMP search analysis, the fiducial volume needs to be determined. This is the liquid xenon volume within the TPC that maximizes the sensitivity for detecting WIMPs. The sensitivity is influenced by both the total exposure (ton $\times$ year) and the ratio of expected signal over background events. Under the assumption of a flat signal acceptance within the whole TPC, the goal is thus to find the largest liquid xenon volume in which the background is only dominated by the internal (i.e., radon) and not the external (i.e. material) backgrounds.

For Science Run 0 a cylindrical fiducial volume of (1042 ± 12) kg was designed to specifically exclude backgrounds from gas events and wall leakage. The wall leakage was an unexpected background of events originating from the PTFE wall, which is mis-reconstructed with an inward

radial bias. This is caused by a lower field configuration, together with the charge build up over time on the PTFE wall, resulting in a ϕ-dependent radial bias of the reconstructed positions. The expected rate of wall events leaking into the Science Run 0 fiducial volume is 0.5 ± 0.3.

The total background expectation of Science Run 0 includes six backgrounds: electronic recoils, nuclear recoils from radiogenic neutrons and from coherent elastic neutrino-nucleus scattering (CEvNS), accidental coincidences from random pairing of uncorrelated lone S1 and S2 peaks, wall leakage and an anomalous background observed in ER calibration data. Both the spectral shape and the rates of each background were fixed before unblinding. The total background expectation in the cS1 $\in [3, 70]$ PE, cS2$_b \in [50, 8000]$ PE search region was (63 ± 8) events. From the about 16 M events digitized during SR0, only 63 survived the selection criteria after unblinding. Only one of these events was found below the NR median. The data of SR0 is consistent with a background-only hypothesis, which lead to a comparable exclusion limit on the wimp-nucleon cross section to other experiments when published.

For the analysis of Science run 0 and 1 together, resulting in a 1 tonne-year exposure, the spatial reconstruction was improved by including a 3D field distortion correction. The fiducial volume was increased to (1.30 ± 0.01) t and the spatial distribution of the background models were included into the likelihood analysis. XENON1T reached an ER background level of $(2.2^{+0.1}_{-0.1}(\text{syst}) \pm 0.1(\text{stat}))$ $(\text{kg} \cdot \text{day} \cdot \text{keV})^{-1}$. Again, the data was consistent with the background-only hypothesis. This (final) result of XENON1T, shown in figure 5, on the spin-independent WIMP-nucleon cross section is the most stringent (as of the time of this writing). It is now up to the next generation of detectors to discover a dark matter particle, and to hopefully explain an observation that is now almost a century old.

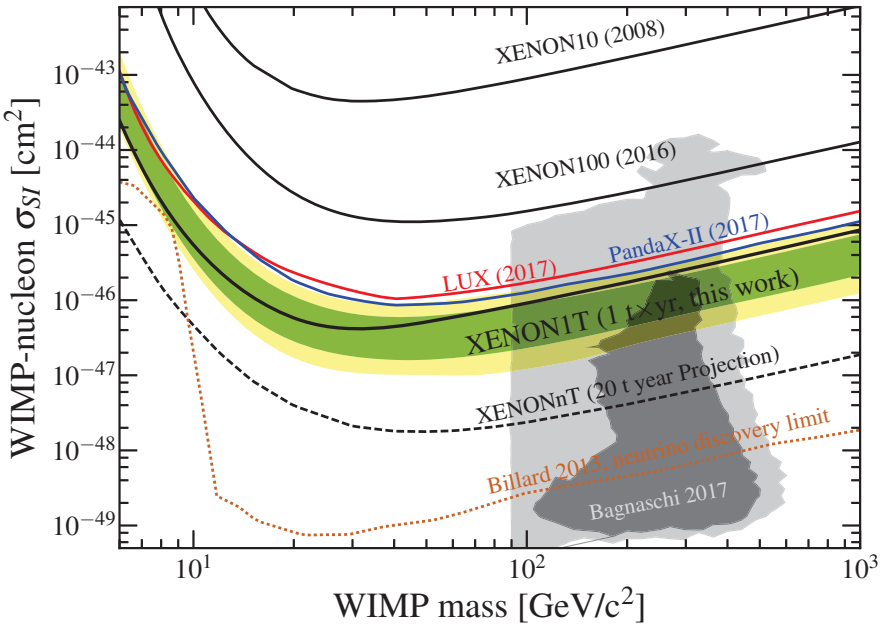

Figure 5: Limit on the spin-independent WIMP-nucleon cross section versus WIMP mass for SR0 + SR1 at 90% confidence (black line). The 1- and 2 σ sensitivity band are given by the green and yellow bands, respectively. For comparison, previous results are shown from XENON10 [4], XENON100 [5], LUX [6] and PandaX-II [7]. The projected sensitivity of XENONnT [8], the upgrade of XENON1T, shows the next step from the XENON collaboration in the search for WIMPs. Not all current theoretical WIMP space [8] can be probed before experiments start measuring more nuclear recoils from CEvNS (orange dotted) [9] than from WIMPs.

0.2 Recommendations

No scientific work can ever be completely finished, and this one is no exception. Here I will give some recommendations, in my opinion, to improve our understanding of the XENON1T detector and improve the construction of future dual-phase liquid xenon TPCs.

To higher drift fields XENON1T did not reach its design goal of −100 kV on the cathode, but reached only −12 kV and −8 kV for SR0 and SR1, respectively. As a consequence we experienced:

- drift field inhomogeneities (reflected in the systematic uncertainty on $g1$ and $g2$ (section 3.5.1) and the need of applying a field distortion correction (sections 3.2.2 and 5.5.1));
- decreased ability to reject multiple scatters (seen in the ^{214}Pb spectral shape difference between MC and measurement (section 4.5.1)); and
- an increased radial bias in the mis-reconstruction of events from the TPC wall (a cause of the wall leakage background (section 5.2)).

Luckily, the ER discrimination in XENON1T is actually better than the Monte Carlo expectation (section 3.6). Still, the following task remain open:

- Investigate the underlying cause for the light- and charge-emission problems on the cathode in XENON1T. It is planned to visually inspect the cathode wires after opening XENON1T. But this can also be done by opening and inspecting the cathode of XENON100 as it experienced similar problems. For future large-scale XENON detectors there are two options: either do full-scale test measurements of the cathode, or lower the expected design voltage on the cathode and construct a low-field TPC accordingly.

Lowering the wall leakage The unexpected background in XENON1T was the wall leakage (section 5.2). For SR0, this decreased the maximum fiducial volume to 1 t (section 5.1.2). In SR1, the fiducial volume could be increased to 1.3 t by incorporating this background into a spatial likelihood (section 5.5.2). Still, we need to better understand and mitigate of this background. For this, the following actions are proposed:

- Investigate the physics behind the accumulation of charge (over time) on the PTFE walls. Krypton calibration data shows that

the build-up of charge accumulation has a similar symmetry as that of the construction of the PTFE wall panels. But it remains unclear why some panels charge up more/faster than others.

- Reduce the accumulation of the radon progeny on the PTFE during construction. Recent measurements have shown that the radon daughter plate-out on PTFE can be orders of magnitude larger than that for other materials [10]. The PTFE panels for the TPC walls should be constructed (and transported) in a radon free environment.

Radon as a tool Radon, as a topic, is mostly discussed with the goal of mitigating or determining its concentration as a background source. We have shown that radon decays can be successfully used to get a better understanding of the TPC. Alpha decays from radon are now used to monitor the electron lifetime, monitor the charge and light yield stability, and determine the reconstructed position of the PTFE wall. But there are still more avenues to work on such as:

- Determine the spatial distributions of the isotopes from the thoron chain (section 4.1.3). This could tell us how much of it comes from the TPC materials, and how much comes from the purification inlet.
- Use alpha decays from surfaces, such as ^{210}Po, to build a system that daily monitors the afterpulse rates of the PMTs (section 4.4.5).
- Investigate how the cathode cleaning effect (section 4.2.4) is dependent on applied cathode voltage, LXe flow, and cathode and TPC design. This will improve the MC expectation of the ^{214}Pb concentration for future experiments.
- Check if the observed depth-dependence of the ^{210}Po concentration (section 4.4.4) is perhaps caused by a depth-dependent efficiency loss. If the actual ^{210}Po concentration is flat, we are underestimating the concentration of this isotope by as much as a factor of 5. Following the work of [11] and [12] this could give an extra (unaccounted) neutron background of about 0.5 events/year, caused by (alpha,n) reactions from ^{210}Po on the carbon and fluorine in PTFE.

Chapter 1

The Dark Matter hypothesis

For the moment we might very well call them DUNNOS (Dark Unknown Nonreflective Nondetectable Objects Somewhere)
— Bill Bryson, *A Short History of Nearly Everything*

Introduction Why has the scientific community embraced the idea that we are missing the bulk of matter in our Universe? Answering that question is the main goal of this chapter. Over the past century dark matter research went from first astrophysical observations of possible missing matter to a fast-paced experimental field with large-scale ground and sky-based experiments searching for dark matter signals or candidates. This chapter will give a brief history of the problem of missing non-luminous matter. In the first section we will start with the mathematical model of our Universe and how it describes its time evolution. After that, several different astrophysical observations will be discussed to explain how they determine the densities of matter and energy in the Universe, with a focus on the Cosmic Microwave Background (CMB) measurements. Once the problem of the missing matter is clear, a number of dark matter candidates will be described together with their motivation and characteristics. Special attention is given to the Weakly Interactive Massive Particle (WIMP), as this is the candidate that XENON1T searches for. The next two chapters will explain how to look for WIMPs with the XENON1T experiment and how XENON1T actually performs, while this chapter focusses first on the theoretical foundation of dark matter.

1.1 Evidence for the existence of dark matter

Contrary to popular belief it was not F. Zwicky, but H. Poincaré who in 1906 first coined the name *Dark Matter* [13]. Then in 1922, it was the Dutch astronomer J.C. Kapteyn who was among the first to work on a quantitative model for the shape and size of the Galaxy with his paper *First attempt at a general theory of the distribution of masses, forces and velocities in the stellar system* [14]. His abstract reads: *"It is incidentally suggested that when the theory is perfected it may be possible to determine the amount of dark matter from its gravitational effect."* Even though his thought process was correct, it was only in 1933 that dark matter became the problem we know today, owing to the work of Swiss physicist F. Zwicky [15]. He was the first to state that the amount of non-luminous matter in the Universe must be greater than that of luminous matter [16]. Zwicky took the virial theorem from thermodynamics and applied it to astrophysics. He thus could relate the gravitational potential energy of an astrophysical system to its kinetic energy. This made it possible to estimate the total mass of a cluster of galaxies, namely the Coma Cluster. Subsequently, he calculated its average kinetic energy and velocity distribution, which differed from the observed velocity distribution by more than an order of magnitude. He thus concluded: *"If this would be confirmed, we would get the surprising result that dark matter is present in much greater amount than luminous matter."* Over the last century more and more astrophysical observations confirming the existence of dark matter have emerged and several will be described in this work. To interpret them, we first need to understand our model of the Universe.

1.1.1 Our model of the Universe - ΛCDM

The Λ Cold Dark Matter(ΛCDM) model [17] [18] is a (physics) model to describe the development of the Universe since its beginning about 13.7 billion years ago. It is the simplest (least number of free parameters) parametrization of Big Bang Cosmology and is called the *standard model* of cosmology. ΛCDM can account for observational evidence such as the accelerating expansion of the Universe, the anisotropies in the Cosmic Microwave Background and the age of the Universe. The derived parameters, which are constrained by observational evidence (as will be described in the next sections), describe among other things the rate of expansion of space itself (H_0) and the densities of baryonic matter (Ω_b), dark matter (Ω_c) and dark energy (Ω_Λ). These densities will tell us what the Universe is composed of and thus which parts we have yet to detect.

Mathematical groundwork To build the model, one starts with Einstein's gravitational field equations in the presence of matter, published in 1916 [19]. These equations describe how the geometry of the Universe is determined by its energy content [20]:

$$R_{\mu\nu} - \frac{1}{2} g_{\mu\nu} R = \frac{8\pi G_N}{c^4} T_{\mu\nu} - \Lambda g_{\mu\nu}, \tag{1.1}$$

where $R_{\mu\nu}$ and R are the Ricci tensor and scalar, respectively. $g_{\mu\nu}$ is the metric tensor, G_N is Newton's constant, $T_{\mu\nu}$ is the energy-momentum tensor and Λ the cosmological constant. The Ricci tensor and scalar on the left-hand side together describe the curvature of space-time. On the right-hand side the energy-momentum tensor describes the density and flux of momentum and energy in the Universe. Finally, the Λ term, which characterizes the innate energy of empty space, was added in 1917 by Einstein to counteract the net force of gravity on cosmological scales to obtain a static Universe [21]. At that time, Λ was believed to be zero and thus the Universe to be flat. The Einstein's gravitational field equations tell us -read from left to right- that momentum (of moving mass) causes curvature and a change in how distance is measured.

In 1922, Friedman [22] started with the simplifying assumption that the Universe is spatially homogeneous and isotropic, which can be observed on scales of about 100 Mpc, leading to a new specific form of the metric. Using this metric for Einstein's field equation gave him one component of the solution called the Friedman equation:

$$\left(\frac{\dot{a}}{a}\right)^2 + \frac{kc^2}{a^2} = \frac{8\pi G_N}{3} \rho_{\text{tot}}, \tag{1.2}$$

where a is a dimensionless *scale factor* at certain time that relates to the redshift (the shift in wavelength of the light due to the expansion of the Universe), k is a constant describing the spatial curvature and can take the values $k = -1, 0, +1$ and ρ_{tot} is the total average energy density of the Universe. Using the Hubble parameter $H^2(t) = \left(\frac{\dot{a}}{a}\right)^2$ and the circumstance that for a critical density ρ_c the Universe is flat ($k = 0$) one now writes:

$$\rho_c = \frac{3H^2}{8\pi G_N}. \tag{1.3}$$

To find the abundance of a component in the Universe in units of ρ_c, one defines the quantity Ω_i for the species i and density ρ_i as follows:

$$\Omega_i \equiv \frac{\rho_i}{\rho_c}, \tag{1.4}$$

which in terms of the Friedmann equation (1.2) can be written as:

$$\Omega - 1 = \frac{kc^2}{H^2 a^2}, \tag{1.5}$$

where $\Omega = \sum_i \Omega_i$, the ratio of total energy density to P_c, is used. Ω takes values greater, equal or less than 1, corresponding by definition to a closed, flat or open universe. The densities are constructed such that

$$\Omega_m + \Omega_\Lambda = \Omega \tag{1.6}$$

where $\Omega_m = \Omega_b + \Omega_c$ is the total matter energy density[1]. The focus now will be on the constraints on the value of Ω_c as that answers the following question: *How much non-luminous matter are we actually missing?*

The six parameters The ΛCDM model can be described by a minimum of six parameters: the physical baryon density ($\Omega_b h^2$), the physical dark matter density ($\Omega_c h^2$), the scalar spectral power-law index (n_s), the primordial curvature perturbation amplitude (A_s), the measure of the sound horizon at last scattering (Θ_{MC}) and the reionization optical depth (τ). One uses here $h = H_0/(100\text{kms}^{-1}\text{Mpc}^{-1})$, the reduced Hubble constant. The scalar spectral power-law index describes the smoothness of the mass-energy density over all distance scales in the early universe. The curvature fluctuations are caused by the amplification of quantum fluctuations during inflation, it leads both to cosmological structure formation and anisotropies in the Cosmic Microwave Background (CMB). The measure of the sound horizon at last scattering is the angular size of the sound horizon. It is determined by the division of the distance that sound waves could have travelled before recombination over the distance to the surface of last scattering. The reionization optical depth refers to how far photons could travel before Thompson scattering due to free electrons during and after the reionization of the Universe by the light of the first stars.

A lot of cosmological-scale measurements such as those of the anisotropies of the CMB, supernovae surveys and cosmological large scale structures are used to validate this model. These will be described here to show how they constrain the densities described in equation 1.6.

Inflation and recombination To understand the link between the parameters of the ΛCDM model and the observable Universe today a short introduction to the history of the Universe is needed (see figure 1.1).

[1] We leave the radiation part Ω_R out due to its low value of about 10^{-4} at present time.

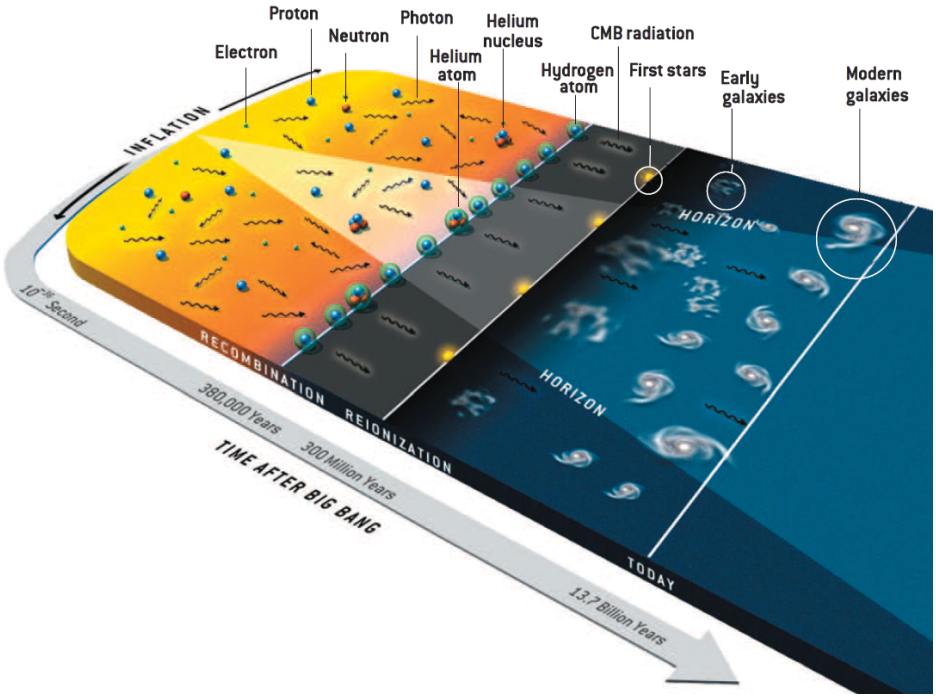

Figure 1.1: Artist impression of the time line of the Universe with inflation and recombination. Before recombination, photons kept being absorbed and re-emitted by free charged particles, this ended when the temperature dropped low enough (recombination) to form stable neutral atoms and the Universe thus became transparent. When the first stars formed, their light re-ionized the gas and thus influenced the free travelling photon's energy distribution. The photons from the recombination are still seen today as the CMB and give clues about how the early Universe must have formed. Adapted from [23].

After the Big Bang and before t of about 10^{-32} s the Universe underwent an accelerated expansion which we call the period of inflation (yellow in figure 1.1). During this period quantum fluctuations, magnified by rapid expansion, formed fluctuation in energy densities. These initial disturbances on all scales, influenced the energy and direction of photons travelling in and out of denser regions. When the Universe cooled down to temperatures[2] of $1-0.1$ MeV, protons and neutrons formed the lightest elements (D, ^{3}He, ^{4}He, Li), which is described by Big Bang Nucleosynthesis (BBN) [24]. Recombination finally started when the temperature dropped below about 0.4 eV and nuclei and electrons formed neutral particles. From that moment on, photons could travel freely in our now trans-

[2]For an ideal gass the temperature T and kinetic energy E_k are related by $E_K \propto k_b \times T$, with k_b the Boltzmann constant.

parent Universe as they were no longer absorbed and re-emitted all the time. ΛCDM parameters describing the smoothness of the mass-energy density and the size of the curvature fluctuation are used to explain how the Universe formed the structures we observe today.

1.1.2 The Cosmic Microwave Background

The Cosmic Microwave Background (CMB) is the oldest light that we can see in our Universe today and it is measured by ground, sky and space telescopes alike. The CMB photons were only decoupled from the photon-baryon-electron plasma once the Universe cooled down enough to suppress the photo-dissociation of the lightest elements. In the hot plasma, hydrogen formed by the process $p^+ + e^- \rightarrow H + \gamma$, but broke up immediately by $H + \gamma \rightarrow p^+ + e^-$ due to the excess of high energy photons. When due to adiabatic expansion the Universe's temperature became low enough for hydrogen to finally stabilize, the mean free path of the photons became roughly the size of the Universe. The moment this happens we call the 'time of last scattering', it happened at around 380 thousand years (redshift z of about 1100) after the Big Bang [25]. These photons still carry with them the information about the density distributions they were formed in and thus give a picture of the early Universe.

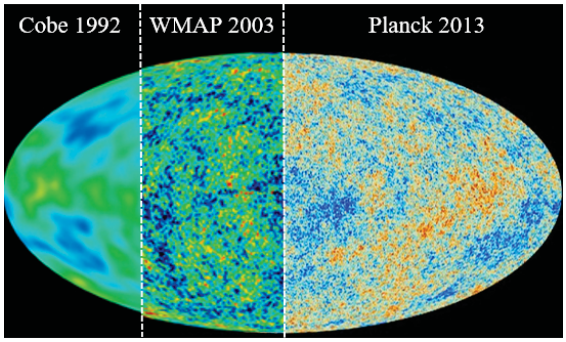

Figure 1.2: Maps of the temperature anisotropies of the Cosmic Microwave Background for three different space telescope measurements. Fluctatuons are shown compared to the average CMB temperature of about 2.7 K. Temperature scales range from $\pm 100\,\mu$K, $\pm 200\,\mu$K and $\pm 300\,\mu$K for the Cobe, WMAP and Planck results, respectively. Great improvement in the granularity has been made in the last two decades, going from about 7 degrees by COBE to 1/12th of a degree by Planck. Data from [26], [27] and [28].

The results from the Planck satellite [28] show the finest granularity to date in the temperature anisotropies of the CMB as seen in figure 1.2. Even though the entire Universe is filled with (2.722 ± 0.027) K black-

body radiation in all directions, tiny temperature fluctuations of about $\pm$ 250 μK [25] are observed, which we call the CMB anisotropy. Their original wavelength was reduced to the low energy microwave radiation one measures today due to the expansion of the Universe. The large (30°) and small scale ($\frac{1}{10}^{\circ}$) fluctuations are caused by different processes and thus give us different clues about how the density of the early Universe was distributed during the time of inflation. The increased map resolution from COBE (1992) [26], to WMAP (2003) [27] and then to Planck (2013) [28] also shows the improved accuracy with which we constrain the parameters of the ΛCDM model.

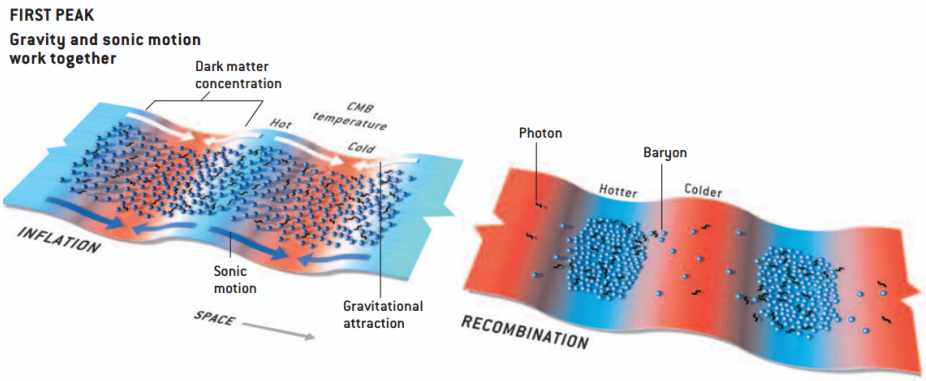

Figure 1.3: Artist impression of how during inflation (*left*) and recombination (*right*) dark matter density distributions can amplify temperature anisotropies. During inflation baryons (blue dots) and photons (black wiggles) start uniformly distributed, but the baryons get pulled together due to gravitational attraction. If dark matter density concentrations were of the same scale as the first fundamental wave during inflation, they could enhance each other to get the scale of the anisotropies we see today after recombination [29]. Red and blue illustrate the respectively red- and blueshift from the electromagnetic radiation moving out of the gravitational fields. From [23].

Figure 1.3 shows an artist impression of the process of how such an anisotropy can form for the fundamental wave. The fundamental sound wave (further described in the next paragraph) is the one that fitted precisely within the distance of the time frame between the moment that inflation started and that recombination ended. Apart from the fundamental wave the full CMB anisotropies have several overtones with shorter wavelengths. During inflation baryons (blue dots) are gravitationally attracted to higher densities of dark matter. The fundamental wave, which is here represented by the grooves in this potential energy diagram, is influenced by dark matter density concentrations of the same scale as the wavelength. Depending on how the dark matter density was distributed

throughout space during inflation, these large scale fluctuations will thus modulate the final amplitude of such an anisotropy. After recombination, about 380 ky later, the energy of the photons that leave the time of last scattering, still hold the information about the region where they were emitted. From the amplitude and scale of the CMB anisotropies it is thus possible to deduce what the density of the cold dark matter component must have been.

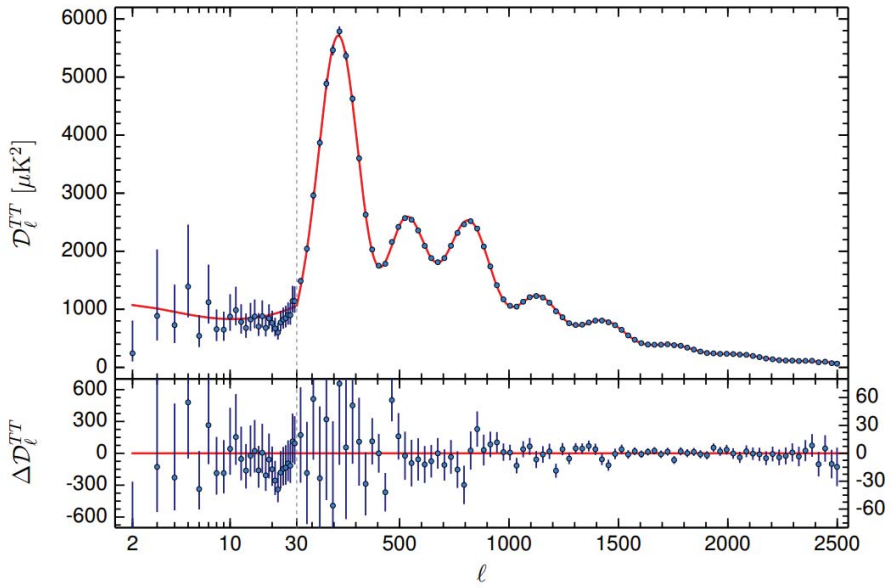

Figure 1.4: Power spectrum (top panel) of the CMB temperature anisotropies with residuals (bottom panel) of the best ΛCDM fit to data, obtained using multipolar analysis of the Planck CMB map from figure 1.2. Around l is 250 the first acoustic peak is seen, the peaks of the overtones are seen at higher l. The measurements of the position, height and width of the distinct peaks constrain the ΛCDM model matter and energy densities, and other parameters with high precision. From [30].

The *Planck 2015* angular power spectrum [30] of the temperature anisotropy (figure 1.4) combines the data from all multipole moments l to the best fit of the ΛCDM model. The features of this power spectrum arise from the acoustic oscillations of the matter densities in the plasma during inflation and before the time of last scattering. One separates the angular scales by means of a multipole analysis using a spherical harmonic

expansion such as:

$$T(\theta,\phi) = \sum_{l=0}^{\infty} \sum_{m=-l}^{l} a_{lm} Y_{lm}(\theta,\phi), \tag{1.7}$$

where $T(\theta,\phi)$ is the CMB temperature, l is the multipole number and m is the multipole projection number. The first monopole ($l = 0$) is the mean CMB temperature, while the next multipoles represent the finer scaled anisotropies. This decomposition in spherical harmonics shows a spatial dependence in the form of peaks in the power spectrum. The first peak, the fundamental wave, corresponds to the interaction between gravitational contraction and radiation pressure, as described by figure 1.3. From its shape the size of the gravitational wells, where radiation accumulated before it finally decoupled from baryonic matter, is determined. The position of the first peak is also strongly correlated with the age of the Universe. The second and third peak, caused by how radiation waves in the plasma travelled into and out of it, describe the matter and energy densities of our universe. The best fit size, position and width of the peak determine the ΛCDM parameters with high precision.

Parameter	**Value 68% limits**
$\Omega_b h^2$	0.02226 ± 0.00023
$\Omega_c h^2$	0.1186 ± 0.0020
$100\Theta_{MC}$	1.04103 ± 0.00046
$ln(10^{10} A_s)$	3.062 ± 0.029
n_s	0.9677 ± 0.0060
τ	0.066 ± 0.016
t_0	13.799 ± 0.038 Gy
Ω_m	0.308 ± 0.012
Ω_Λ	0.692 ± 0.012
H_0	67.81 ± 0.92 km s^{-1} Mpc^{-1}
N_{eff}	3.13 ± 0.62
$\sum m_\nu$	< 0.23 eV

Table 1.1: Selection of *Planck* 2015 Cosmology results [31]. Parameters for the base ΛCDM model computed from the Planck CMB power spectra in combination with lensing reconstruction and external data. The values above the line are the base parameters used for fitting, while those below the line are derived values. Values from [25].

Table 1.1 lists several of the cosmology results for the 6-paramater ΛCDM model from the analysis of the Planck CMB power spectra. These

determine not only the Hubble constant and age of the Universe, but also the total energy and matter densities (Ω_m, Ω_Λ). $\Omega_m + \Omega_\Lambda = 1$ shows that the Universe is fully composed of matter ($\sim 30\%$) and dark energy ($\sim 70\%$). Of the total matter density in the Universe only about 15% of it consists of luminous baryonic matter (i.e.; gas, stars and planets), while about 85% consists of cold dark matter. From this model other parameters such as the Hubble constant (H_0), the effective number of relativistic degrees of freedom (N_{eff}) and an upper limit on the sum of the neutrino mass ($\sum m_\nu$) can be derived. The effective number of relativistic degrees of freedom prescribe the number of neutrino species during inflation, which, e.g., influenced the rate of temperature decrease in the early Universe [32].

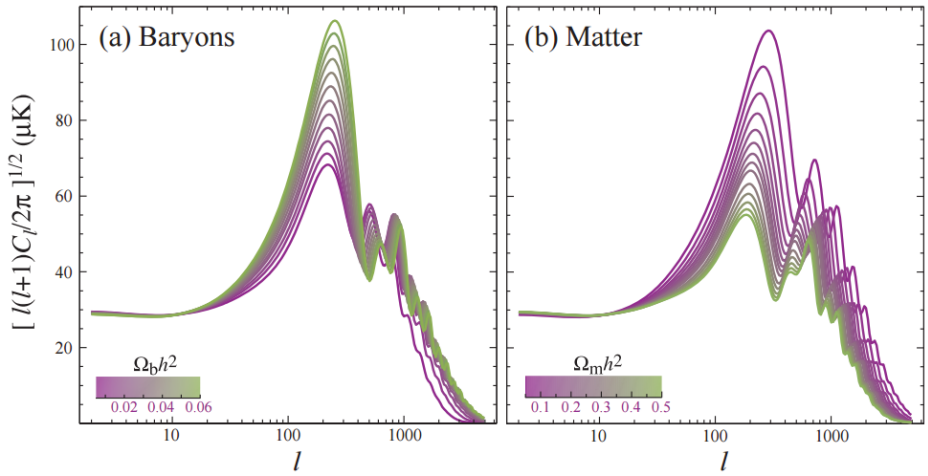

Figure 1.5: CMB power spectrum changed due to test variations of the baryon and matter density components. Deviation of these densities changes the amplitude, width and position of the first and subsequent peaks in the CMB. From [33].

The high precision of these measurements can be better understood by seeing how a small deviation in a single ΛCDM model parameter changes the resulting power spectrum as shown in figures 1.5. The baryon density ($\Omega_b h^2$) is increased from its reported value of about 0.02 to 0.06 (left panel) and the matter density ($\Omega_m h^2$) varies from its reported value (~ 0.3) to between 0.05 and 0.5 (right panel). One can now visually compare these spectrum deviations to the discovered agreement between data and the best fit of ΛCDM in figure 1.4 to understand the incredible precision that is obtained from the CMB measurements.

1.1.3 More evidence from astrophysical observations

From the CMB measurements we now know that we live in a flat ($|\Omega_k| < 0.005$) universe[3], filled with mostly energy and some matter, ($\Omega_m, \Omega_\Lambda \sim 0.3, 0.7$). Of all matter only about 15% of it consists of luminous baryonic matter while the other 85% consists of cold dark matter. Over the past century a lot more astrophysical observations have been brought forth which all point towards the same direction: if we assume our laws of gravity to hold over cosmological distances, the amount of matter we detect (including stars, gas, planets, etc.) is not enough to explain our observations. Here, a short overview of this evidence is given, for a more complete overview see [1], [34] and [35].

Rotational velocity curves of galaxies In the 1970's, Vera Rubin [36] studied the rotational movement of objects in spiral galaxies versus their radius to the center. The velocity of any stellar object at a distance r from the center is described by:

$$v(r) = \sqrt{\frac{GM(r)}{r}}, \tag{1.8}$$

where $v(r)$ is the velocity of a stellar object at radius r, G is Newton's constant and $M(r)$ the mass within a radius r. Outside of the visible disk, where $M(r)$ stays constant, r increases, so one would expect $v(r)$ to also decrease. The expectation is that for objects outside of the central mass region (up to about 5 kpc) of a spiral galaxy the velocity should thus decrease with the distance from the center.

The measurements of Rubin showed, however, that those rotational velocities remain constant over distances up to about 80 kpc as illustrated by figure 1.6. This shows the galactic rotational curve for such a spiral galaxy (here NGC 6503) with its expected velocity distribution contribution from the stellar objects and gas parts. Those two contributions together should lead to a decreasing velocity distribution outside of the radius of the visible disk itself. The data does not agree with the expectation, but shows a nearly constant velocity versus radius relation. This can be explained by the hypothesis of a dark matter halo with a mass distribution of $M(r > R) \propto r$. This in turn leads to a dark matter density that should be distributed as $\rho(r) \propto 1/r^2$. With these measurements Rubin strengthened for the first time on a larger scale the dark matter hypothesis that Zwicky proposed in 1933. Even though these measurements do not constrain Ω_c for the whole Universe, they do illuminate how dark matter

[3] Ω_k is the spatial curvature density, with k from equation 1.2.

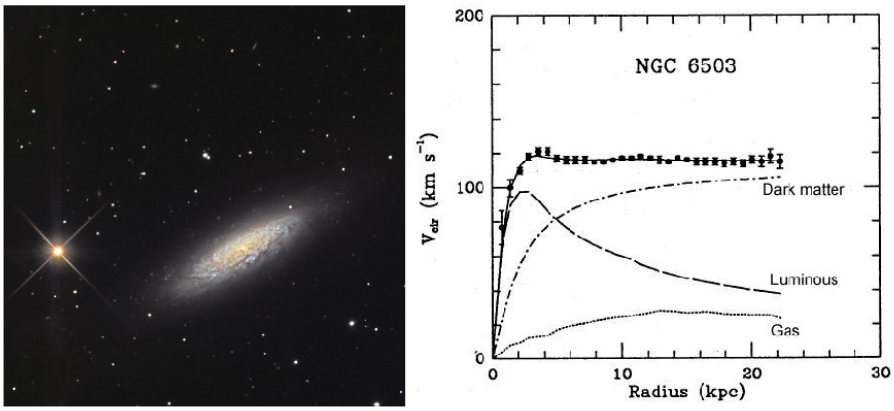

Figure 1.6: Galactic Rotational curve. *Left:* Image of the NGC6503 spiral galaxy seen in visible light (Image courtesy of NASA). *Right:* Measurements of the rotational velocity distribution of NGC6503. The constant velocity for $r > 5\,\text{kpc}$ cannot be understood from the combination of luminous matter and gas together but needs a dark matter component with a density distribution of $\rho(r) \propto 1/r^2$. From [37].

is distributed throughout a galaxy, which will be used later on when we focus on our own Milky Way.

The accelerating Universe from supernovae Figure 1.7 shows a combination of supernovae, galaxy clusters and CMB measurements that constrain Ω_m and Ω_Λ, made by the Supernovae Cosmology Project.

These older CMB measurements (prior to 2011) are already superseded by the 2015 Planck CMB results, but still illustrate how the constraints on these densities influence the fate of the Universe. Depending on the values of Ω_m and Ω_Λ the Universe expands forever or recollapses eventually. The curvature of space-time (Ω_k) tells us if the Universe is closed, flat or open. The latest CMB measurements ($\Omega_m, \Omega_\Lambda \approx 0.3, 0.7$) [25], which are in agreements with the supernovae observations ($\Omega_m, \Omega_\Lambda = 0.28^{+0.09}_{-0.08}, 0.76 \pm 0.05$) [39], point towards our Universe expanding forever and being flat.

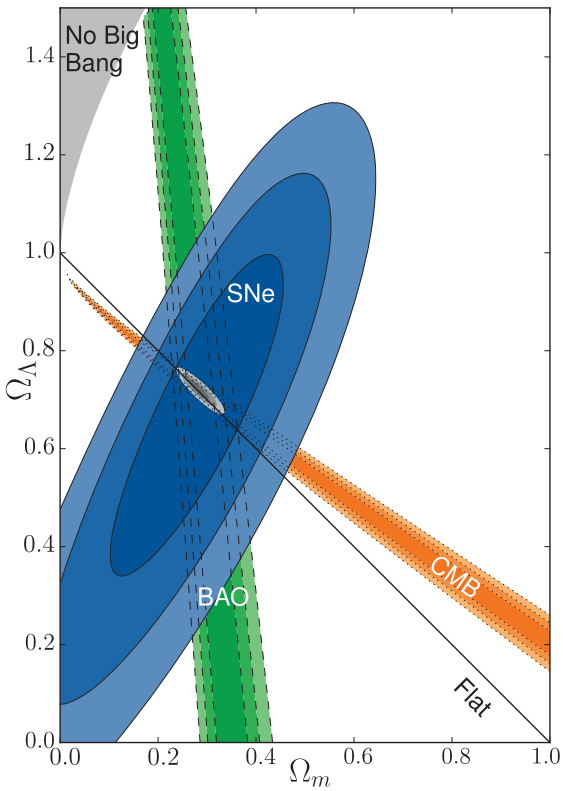

Figure 1.7: Energy matter density constraints with 68.3%, 95.4%, and 99.7% confidence regions from Supernovae (SNe), Baryonic Acoustic Oscillations (BAO) and WMAP CMB measurements. The new 2015 CMB measurements point towards our Universe expanding forever ($\Omega_m, \Omega_\Lambda \sim 0.3, 0.7$) and being flat ($|\Omega_K| < 0.005$). From [38].

1.1.4 Mass distributions in colliding galaxy clusters

Another piece of evidence comes from the merger of colliding galaxy clusters. Figure 1.8 shows measurements of the Bullet Cluster, which is a merger of two galaxy clusters. Galaxy clusters are groups of up to a thousand of individual galaxies that are gravitationally bound together. They spread typically out from 2 to 10 Mpc and consist of a total mass between 10^{14} to 10^{15} solar masses. Most of this mass is highly ionized gas distributed between the galaxies (5 - 15%) compared to the visible stellar component (1 - 2%, i.e., stars, planets)[40] [41]. Sometimes whole galaxy clusters collide with each other and their signature gives us clues about how their mass distributions interact.

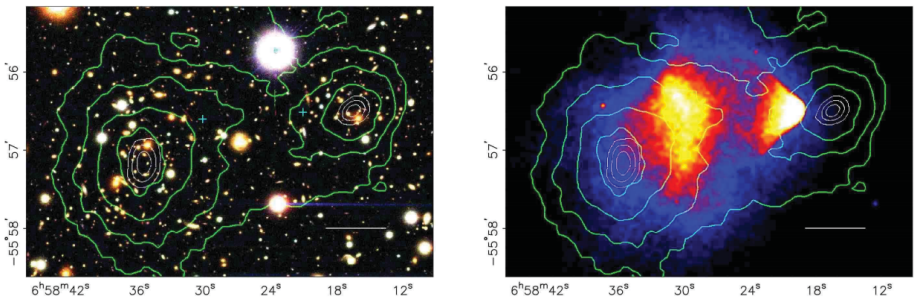

Figure 1.8: *left*: Image of two merging galaxy clusters (1E0657-558, Bullet Cluster), the grey bar indicates a distance scale of 200kpc. Green contours give the mass density inferred from the mass reconstruction from gravitational lensing. The blue '+' markers indicate the locations of the centres used to measure the masses of the plasma distribution. *right*: The $5 \cdot 10^5$ s Chandra exposure X-ray image of the same colliding galaxy clusters, with the false color indicating the plasma distribution and again the green mass contours. The discrepancy between the position of the hot ionized gas and that of the main mass contribution indicates the presence of a large frictionless dark matter component. From [42].

The stellar part is expected to behave as collision-less particles during merger, while this cannot be said for the plasma component. When the gas of one galaxy cluster moves through the gas of the other it experiences a ram pressure of: $P_r \approx \rho_e v^2$, where ρ_e is the gas density and v is the relative speed of the gas. As the colliding gas will experience collisional forces it heats up and emits X-rays which can be observed. The drag that the gas experiences decouples the stellar component of colliding galaxy clusters from the gas component. Using measurements of the hot plasma distribution, by means of X-rays, and the total mass distribution,

by means of gravitational lensing[4], one can distinguish the different mass components.

Both images show in green the mass reconstruction from gravitational lensing. In the right image the plasma distribution is shown. The difference between the positions of these distributions show that the main matter component is not the gas, in contradiction to what was expected, but behaves like a collision-less and non-luminous component. When galaxy clusters collide, the dark matter component moves through each other at a higher velocity than the plasma, which is slowed down due to the drag of ram pressure. Further studies using the Chandra and Hubble space telescopes on 72 such colliding galaxy clusters all show similar behaviour from which they confirm the existence of a dark matter component at a $7.6\,\sigma$ significance [43].

1.1.5 Conclusion on Dark Matter evidence

The 2015 Planck CMB measurements give the following interpretation of the energy matter density in the ΛCDM model:

1. our Universe consists of about 70% dark energy and about 30% matter;
2. only about 15% of the total matter density consists of luminous baryonic matter (i.e., gas, stars, planets);
3. the other 85% consists of non-luminous (dark) matter.

1.2 Dark matter candidates

Now that we have established that most of the matter in the Universe is non-luminous, the next question arises: *what kind of matter is dark matter?* From cosmological observations a dark matter particle candidate is favoured if its characteristics are compatible with the following qualities:

1. Electrically and color neutral[5];
2. Cold (non relativistic particles)[6];

[4] Gravitational lensing is a technique which uses the curvature of light around massive object to estimate the mass of the object.

[5] Strong Self-Interacting Dark Matter (SIDM) were postulated in 2000 [44] to explain the smoothness of the dark matter halo, but their possible parameter space seems to be excluded by CMB and indirect dark matter measurements [45].

[6] DM particles should be relatively slow-moving as dark matter shows structure formation. If they are relativistic particles, like neutrinos, these structures would wash out.

3. Very low self interaction cross section (collisionless);
4. Created in the early Universe (long lived);
5. Massive (gravitational attraction).

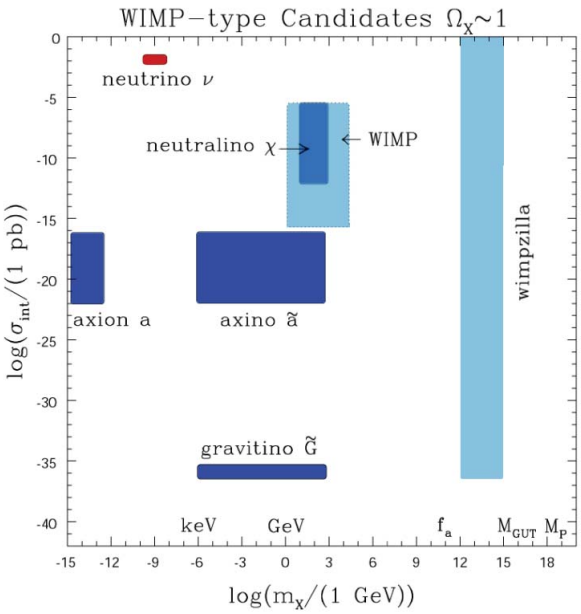

Figure 1.9: Schematic representation of possible dark matter candidates. The shown bands are the regions in mass and cross section for which these theoretical particles could exist. Blue and red represent cold and hot dark matter, respectively. The WIMP region itself contains several different possible candidates (1 pb = 10^{-36} cm^2). From [46].

The unsolved question of the nature of dark matter has led to no shortage of candidates. Figure 1.9 shows for several candidates the possible interaction cross section with baryonic matter (σ_{int}) versus the mass of the dark matter candidate (m_X). One problem for the field of dark matter search experiments is that these candidates span around 40 orders of magnitude in cross section and around 30 orders of magnitude in mass. As different experimental set-ups can only probe specific cross sections and masses, a very wide field of detection strategies is needed, which is represented by the wide range of experiments searching for dark matter candidates. In the following section a selection of candidates will be discussed: Sterile neutrinos, axions and WIMPs. We will focus mostly on the WIMP, which the XENON1T experiment searches for. For a thorough review of more possible dark matter candidates see, e.g.: [20], [1], [47] and [48].

1.2.1 Neutrinos and axions

Standard Model and sterile neutrinos The Standard Model (SM) neutrino was an obvious candidate for dark matter as it certainly exists and is non-luminous. The total neutrino matter density can be derived from cosmological observations (in a model-dependent way). The total SM neutrino density is restricted to $\Omega_\nu \lesssim 0.001$ (assuming $\Omega_\nu h^2 = \frac{\sum m_\nu}{93\text{eV}}$ and $\sum m_\nu < 0.234$ eV from table 1.1) [49]. At less than about 1% of the total mass density of the Universe, SM neutrinos cannot account for the full missing dark matter density. This still leaves the possibility of the existence of a sterile neutrino which is heavily sought after [49]. In 1993 these where proposed by Dodelson and Widrow [50]. Sterile neutrinos have no ordinary charged or neutral current weak interactions, but can only interact through neutrino mixing. If in the early Universe their production rate was lower than the expansion rate they never reached thermal equilibrium, but can still make up a considerable amount of the missing mass.

Axions The axion was originally not hypothesised as a solution for the dark matter problem, but as a solution to the problem of quantum chromodynamics (QCD) not breaking CP-symmetry in 1977 [51] [52]. In principle QCD permits violation of the combined charge conjugation (C) and parity (P) symmetries. Large CP-violating interactions would introduce an observable large electric dipole moment of the neutron which has not been observed. A solution to why the CP-violation would be so small can be found by introducing a new field and adding a new global symmetry that becomes spontaneously broken. Thus axions arise as pseudo-Goldstone bosons by the introduction of a new spontaneously broken global symmetry. The allowable mass of the axion as a cold dark matter candidate is approximately restricted to be between μeV and meV [53] [54].

1.2.2 Weakly Interactive Massive Particles

The Weakly Interactive Massive Particle (WIMP) is a well motivated dark matter candidate. If produced in the early Universe, its mass and annihilation cross section can be estimated from its relic density. WIMPs can arise from theoretical extensions to the SM and have a chance to be detected in the near future by current experiments.

Relic abundance After being formed in the Big Bang, WIMPs would be in thermal equilibrium in the early Universe. SM particles would produce WIMPs at the same rate that WIMPs would annihilate into SM

particles. Once the temperature has dropped below the WIMP mass (due to expansion), the WIMP density would decrease faster than the SM particle density as the production rate of WIMPs would decrease. The lowered WIMP density would eventually lead to these particles not being able to self annihilate any more and the WIMP density would freeze-out. From that point on the WIMP density only decreases due to the expansion of the Universe itself. This relic density, that can be measured today, thus depends on the WIMP mass and its annihilation cross section.

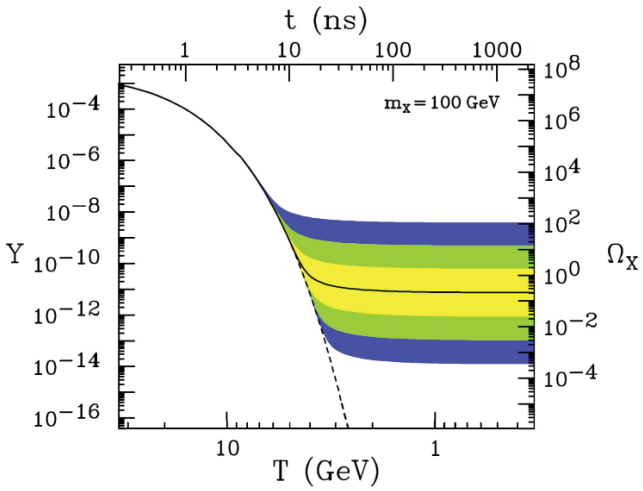

Figure 1.10: WIMP *freeze-out* of the comoving number density Y as a function of the temperature of the early Universe for a 100 GeV WIMP. On the right axis the resulting thermal relic density Ω_X is shown. The density follows the drop off curve until the expansion rate of the Universe equals the annihilation rate at a temperature $T \sim M_X$. This freeze out to the relic density is shown as the solid contour. The coloured bands represent the range of resulting densities for cross sections of 10 (yellow), 100 (green) and 1000 (blue) times higher (and lower) than the present relic density. From [46].

Figure 1.10 shows this evolution of the WIMP's density number. Here a WIMP with a mass (m_X) of 100 GeV is chosen as an example[7]. On the left vertical axis the comoving density number (Y) is shown, this is a measure of the number of WIMP particles, per solid angle and per redshift interval, which corrects for the fact that the Universe is expanding. At temperatures (T) higher than about 30 GeV, these WIMPs are in thermal equilibrium and Y remains constant. The number density (n_X) of a gas

[7]We will omit any '/c^2' in this work for convienence.

of WIMPs in thermal equilibrium follow Boltzman statistics [55]:

$$n_X = \left(\frac{m_X T}{2\pi}\right)^{3/2} e^{-m_X/T}. \tag{1.9}$$

When the temperature drops below about 30 GeV WIMPs become Boltzmann suppressed and are expected to drop exponentially to zero through collisional annihilation (as indicated by the solid to dashed black line). This behaviour changes when the Universe further expands to the point where the time to travel across the Universe surpasses the time for a WIMP to annihilate with a partner. The resulting relic density Ω_X (right vertical axis) depends on the thermal average of the WIMP annihilation cross section $\langle\sigma_{ann}v\rangle$ and can be calculated. An order of magnitude estimation of the relic density is:

$$\Omega_X h^2 \sim \frac{3\times10^{-27}\ \mathrm{cm}^3\ \mathrm{s}^{-1}}{\langle\sigma_{ann}v\rangle}, \tag{1.10}$$

which leads for thermally-averaged annihilation cross sections $\langle\sigma_{ann}v\rangle$ of order 10^{-25} cm^3 s^{-1} (the scale of the weak interaction) to a relic abundance of $\Omega_X \sim 0.1$. The fact that the WIMP relic density combined with weak scale cross sections leads to a relic dark matter abundance similar to one found by the previously discussed CMB measurements is called the 'WIMP miracle'.

WIMPs from supersymmetry Supersymmetry (SUSY) [56] is a theoretical extension of the Standard Model in which all known particles have a supersymmetric partner. SM fermions would have supersymmetric boson partners while SM bosons would have supersymmetric fermion partners. These have not (yet) been observed in nature, but the stable Lightest Supersymmetric Particle (LSP) serves as a WIMP candidate [57]. The Minimal Supersymmetric Standard Model (MSSM) [58], a minimal SUSY extension of the SM, does not conserve baryon or lepton numbers. This would lead to very fast proton decay which disagrees with observations. A solution for this is found by introducing a new symmetry [59] in the form of:

$$P_R = (-1)^{3(B-L)+2S}, \tag{1.11}$$

with B, L and S the baryon number, lepton number and spin respectively. The MSSM introduces this R-parity to explain the stability of the proton. It grants all supersymmetric particles R = −1, while giving all standard model particles R = +1. The MSSM gives rise to not one, but 4 *higgsinos*. The gauge bosons flavour eigenstates, $W^{\pm}$, W^0 and B also get their supersymmetric *gaugino* spartners called *winos* and *bino*. These higgsinos and

gauginos mix with each other giving a set of eight new particles with four of them being charged ($\tilde{\chi}_i^{\pm}, i = 1, 2$) and four neutral ($\tilde{\chi}_i^0, i = 1, 2, 3, 4$). The lightest *neutralino* ($\tilde{\chi}_1^0$), would be stable thanks to R-parity, as it cannot decay into SM particles. This ensures that its abundance after freeze-out would have remained constant and makes it a prime WIMP candidate. For a good review on the state of SUSY parameter space and the current and projected sensitivities for direct and indirect detection experiments see [60].

1.3 Summary and outlook

Starting from the first observations of missing non-luminous matter in the 1920's, all observations have led us to believe that about 85% of the matter in the Universe has not been detected so far. Astrophysical observations such as the Cosmic Microwave Background constrain the matter and energy density ($\Omega_m = 0.308 \pm 0.0012$, $\Omega_\Lambda = 0.692 \pm 0.0012$) in our flat Universe ($|\Omega_k| < 0.005$). The base (and derived) parameters of the ΛCDM model build a consistent understanding of the evolution of our Universe. Understandably, this dark matter problem has sparked a wide field of hypothetical particles which are sought after such as: sterile neutrinos, axions and WIMPs. For WIMPs, the combination of the WIMP's relic density together with the fact that WIMP particles fit extensions of the Standard Model, makes this an excellent candidate to search for ('WIMP miracle').

The next chapter will present how to detect WIMPs using a dual-phase xenon time projection chamber. In the third chapter we will see how the XENON1T detector performs and follow the path from light and charge deposition to being able to discriminate between background and signal events. The fourth chapter will present the electronic recoil background, with a heavy focus on measuring the dominating background from radon. Finally, in the last chapter we will present the latest XENON1T results.

Chapter 2

Using XENON1T to detect dark matter

It is a mistake to think you can solve any major problems just with potatoes.

— Douglas Adams, *The Hitchhiker's Guide to the Galaxy*

In the previous chapter, evidence for the existence of dark matter was presented together with several of the possible dark matter candidates. This chapter explains how we search for WIMP particles by using xenon in our direct detection experiment, XENON1T. We start, in the first section, with calculating the expected rate and energy deposition for WIMP particles scattering off different detection materials. The second section then focusses on how we measure the energy deposition of WIMPs in liquid xenon. That leads to the concept of the dual-phase liquid xenon Time Projection Chamber, used in XENON1T. The third section gives a brief overview of the major components of the XENON1T experiment. In the last section we focus on the work that was done to reduce backgrounds in XENON1T. After discussing the design principles of XENON1T in this chapter, we will compare this with its performance in the next chapter.

2.1 Expected WIMP recoil spectrum

2.1.1 WIMP scattering rate and velocity distribution

A direct detection dark matter experiment, like XENON1T, measures the differential rate $\frac{dR}{dE_R}$, as a function of deposited recoil energy E_R. The differential recoil rate from WIMP interactions with matter can be written

as [61]:

$$\frac{dR}{dE_R} = \frac{\rho_0}{m_\chi}\frac{1}{m_A}\int d^3\mathbf{v}\ F(\mathbf{v})\ |\mathbf{v}|\ \frac{d\sigma}{dE}(\mathbf{v}), \tag{2.1}$$

with ρ_0 the local WIMP density, m_χ the mass of the WIMP particle, m_A the mass of the target nucleus, $F(\mathbf{v})$ the WIMP velocity distribution in the detector's frame, and $\frac{d\sigma}{dE}(\mathbf{v})$ the differential WIMP-nucleus cross section. The WIMP velocity profile is assumed to be an isotropic Maxwell-Boltzmann distribution [62]:

$$F_g(\mathbf{v_g}) = k\left(\frac{1}{\sqrt{\pi}v_0}\right)^3 \exp\left(-\frac{v_g^2}{v_0^2}\right), \tag{2.2}$$

where v_0 is the modal WIMP velocity in the galactic frame, v_g is the WIMP velocity in the galactic frame and k a normalization constant. The WIMP's velocity distribution is truncated ($F_g(\mathbf{v_g}) = 0$) at the escape velocity $v_g \geq v_{esc}$ [63]. WIMPs with a higher velocity are not gravitationally bound by the gravitational potential of our galaxy. The modal WIMP velocity is given by $v_0 = \sqrt{2k_BT/m_\chi}$, with k_B the Boltzmann constant. The normalization constant k is defined as

$$k = \text{erf}\left(\frac{v_{esc}}{v_0}\right) - \frac{2}{\sqrt{\pi}}\frac{v_{esc}}{v_0}\exp\left(-\frac{v_g^2}{v_0^2}\right), \tag{2.3}$$

with erf the error function. The rotation of the Earth around the Sun gives a slight (few %) change in the expected WIMP rate, but as XENON1T is not a directional sensitive detector, we will ignore this annual modulation here. The Earth moves with an average velocity (v_E) of about 232 km/s with respect to the galactic frame. The modal WIMP velocity is thus $\sqrt{v_0^2 + v_E^2}$ in the local detector frame, with a maximum observable WIMP velocity of $v_{esc} + v_E$. Figure 2.1 shows the galactic and local WIMP speed distributions.

2.1.2 The Standard Halo Model

XENON1T aims to measures a differential WIMP rate within a certain exposure (mass × measurement time). If no WIMP collisions are measured this sets for every detectable WIMP mass a limit on the WIMP-nucleon cross section. This is always done for a specific set of astrophysical parameters, for which we use the Standard Halo Model (SHM). This model assumes an isotropic and isothermal dark matter sphere with a density profile of $\rho \propto 1/r^2$. The SHM parameters are $\rho_0 = 0.3\,\text{GeV/cm}^3$, $v_0 = 220\,\text{km/s}$ and $v_{esc} = 533\,\text{km/s}$ [65] [66] [63]. Though these values are model dependent [67], the SHM is commonly used to compare the results between different direct detection dark matter experiments.

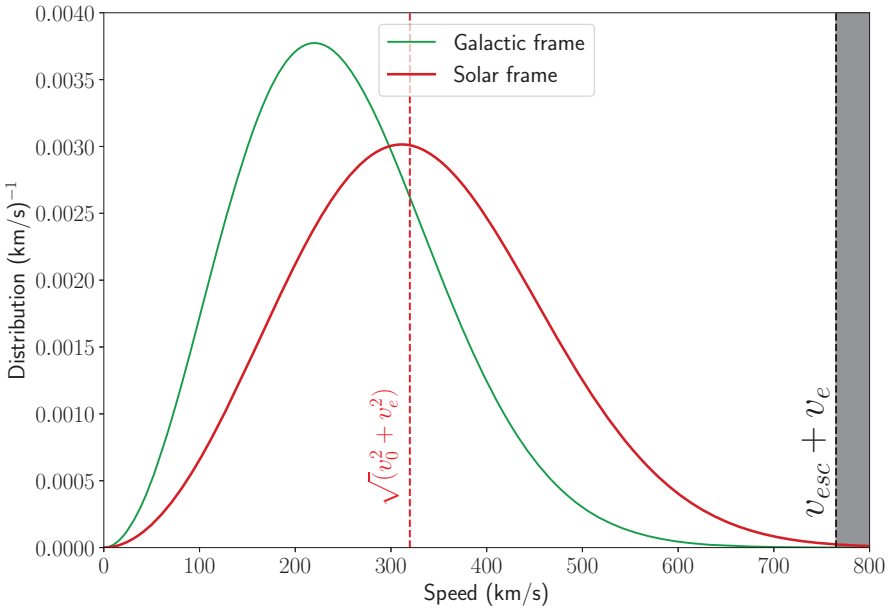

Figure 2.1: Expected WIMP speed distribution in the galactic (green) and solar (red) frame according to the Standard Halo Model. The galactic WIMP velocity distribution is described by an Maxwell-Boltzmann distribution with a modal velocity of v_0, cut off at the escape velocity v_{esc}. In our local frame the modal WIMP velocity is $\sqrt{v_0^2 + v_E^2}$ (dashed red line), with a maximum observable WIMP velocity of $v_{esc} + v_E$ (grey dashed line). Code from [64].

2.1.3 Cross section and form factor

The differential cross section, for zero momentum transfer, can be written as:

$$\frac{d\sigma}{dE}(E, v) = \frac{m_A}{2\mu^2 v^2}(\sigma_0^{\text{SI}} F_{\text{SI}}^2(q) + \sigma_0^{\text{SD}} F_{\text{SD}}^2(q)), \tag{2.4}$$

where $\mu = m_\chi m_A/(m_\chi + m_A)$ is the reduced WIMP-nucleus mass, $F_{\text{SI}}(q)$ and $F_{\text{SD}}(q)$ are the spin-independent (SI) and spin-dependent (SD) form factors, respectively [68]. For spin-independent interactions the Helm form factor is convenient, as it is an analytic function:

$$F(q) = \frac{3j_1(qr_n)}{qr_n} e^{-(qs)^2/2}, \tag{2.5}$$

where $q = \sqrt{2m_A E_r}$ is the momentum transfer, $j_1(qr_n)$ is the spherical Bessel function of the first kind, s ($\sim$ 0.9 fm) is a measure of the skin

thickness and r_n ($\approx 1.14\,A^{1/3}$ fm) is the radius of the nucleus[1]. The Helm form factor contains all the dependencies on the transferred momentum, while the cross section contains all the dependencies of the interaction. The Helm form factor assumes a uniform charge density of the core of the nucleus with a Gaussian surface smearing density. Figure 2.2 shows the Helm form factor for two commonly used detector materials; xenon and argon. Once the transferred momentum (q) increases beyond the point where the de Broglie wavelength ($\lambda = h/q$) is no longer large in comparison to the nuclear radius, the effective cross section begins to decrease. For xenon, $F(E)$ drops to zero around 90 keV nuclear recoil energy and is too small to be detectable after about 100 keV [69].

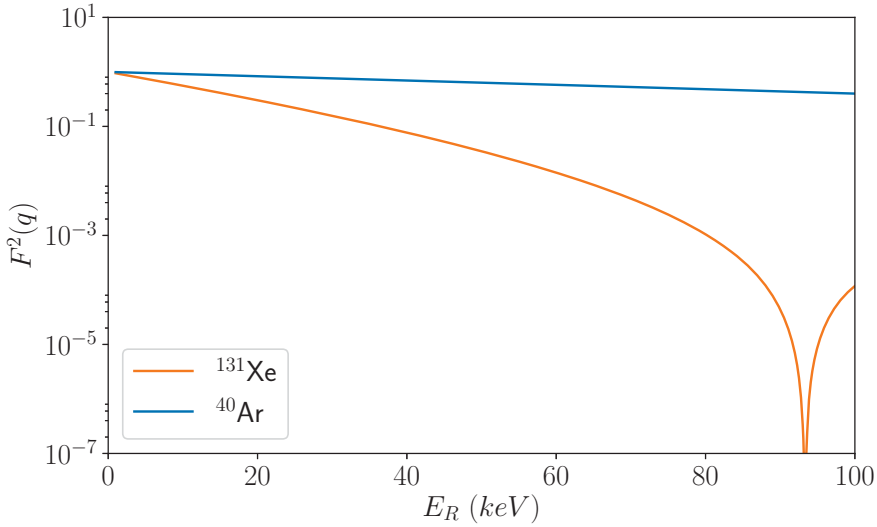

Figure 2.2: Helm form factor for xenon (orange) and argon (blue) from equation 2.5. When the energy transfer increases, the corresponding wavelength becomes $\leq$ the size of the nucleus and the case of coherent scattering is lost. The location of the first minimum is set by the nuclear radius. Code from [64].

The spin-independent WIMP-nucleus cross section, which we focus on, can be expressed at zero momentum transfer as

$$\sigma_0^{\mathrm{SI}} = \sigma_p \frac{\mu_A^2}{\mu_p^2} f_p [Z + f_n (A - Z)]^2, \tag{2.6}$$

where μ_p is the reduced WIMP-nucleon mass, μ_A is the reduced WIMP-nucleus mass, f_p and f_n are the WIMP couplings to protons and neutrons

[1]This allows for a convenient separation of variables.

respectively, Z is the atomic number and A the total nucleon number. Under the assumption that the contribution of protons and neutrons to the total coupling strength is equal ($f_p \approx f_n$), this reduces to $\sigma_0^{\mathrm{SI}} \propto A^2$. For the simplest case of SI interactions with sufficiently low momentum transfer ($qr_n \ll 1$, with r_n the radius of the nucleus) the scattering amplitude of a single nucleon thus adds in phase to give a cross section $\propto A^2$. This shows how important the atomic mass of the chosen target material is for the discovery potential. The SD part [70] [71] will not be discussed here, but it is important to mention that SD searches can only be done with nuclei with a non-vanishing total nuclear spin. When limits are presented for direct search experiments they will be separated for SI and SD, but always in the cross section versus WIMP mass space and normalized to the WIMP-nucleon cross section. Also, we assume that for SI or SD WIMP-nucleus scattering all of the nuclear recoil energy is either attributed to the one or the other.

2.1.4 The WIMP recoil spectrum

We can now calculate the expected SI scattering rates as a function of recoil energy for a given cross section, WIMP mass and target material. This is shown in figure 2.3 (left). Materials with a higher A have a higher WIMP discovery potential per unit mass at low recoil energies. Depending on the size of the nucleus, the Helm form factor has a local minimum in the rate for a specific recoil energy. The WIMP search region energy range is chosen to maximise the possible observed rate. The left edge ($\sim 5\,\mathrm{keV}$) is given by the detector threshold, while the right edge is set where the expected rate has dropped by about an order of magnitude.

Figure 2.3 (right) shows how the sensitivity of a direct detection dark matter experiment changes depending on detector parameters. The black oval is a signal contour of a WIMP with specific mass and cross section. If no signal is found a reference limit is reported. For a smaller target nucleus the experiment becomes more sensitive to lower WIMP masses. For increased exposure (mass $\times$ time) the whole limit shifts downwards, while a detector with a lower threshold is more sensitive to all WIMP masses. The XENON1T limit will be presented in section 5.5.3.

2.2 Scintillation and ionization principle

Over the last couple of decades the scintillation and ionization processes of liquid noble gasses, such as argon and xenon, have been extensively studied [73] [74] [75]. Still, a complete picture of the working principle of the energy transfer mechanism and how the energy is divided between the

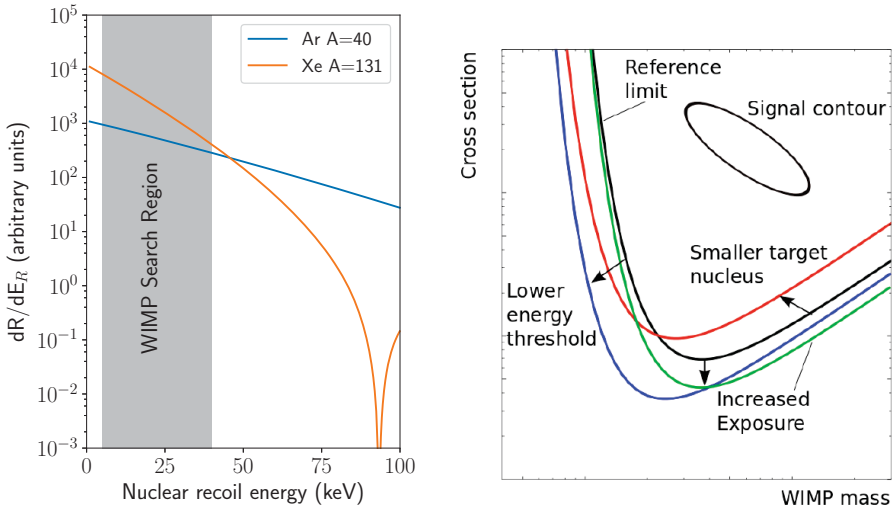

Figure 2.3: *Left*: Differential event rate (in arbitrary units) for a 100 GeV WIMP in xenon (orange) and argon (blue). The wimp search energy region of XENON1T is about 5-40 keV nuclear recoil energy (grey band). Code from [64]. *Right*. Change in sensitivity for a direct dark matter detection experiment (black) for a smaller target nucleus (red), a lower energy treshold (blue) and an increased exposure (green). From [72].

different channels for all energies is missing. Here a short introduction is given to the scintillation and ionization principles in xenon.

2.2.1 Energy deposition in liquid xenon

The transfer of deposited energy (E_{dep}) into ionization, excitation and sub-excitation electrons can be expressed via Platzman's equation [76], as:

$$E_{dep} = N_i\, E_i + N_{ex}\, E_{ex} + N_i\, E_e, \tag{2.7}$$

where N_i is the number of electron-ion pairs, N_{ex} is the number of excited atoms, E_i and E_{ex} are the average energies needed to create an electron-ion pair or excited atom, respectively, and E_e is the average kinetic energy of sub-excitation electrons. The sub-excitation electrons do not generate any further excitations and their energy is lost as heat, therefore we will not discuss them further. Figure 2.4 shows the transfer of deposited energy into the different channels schematically.

The initial number of quanta produced is dependent on the type of the interacting particle. Equation 2.7 is true for incoming electrons and

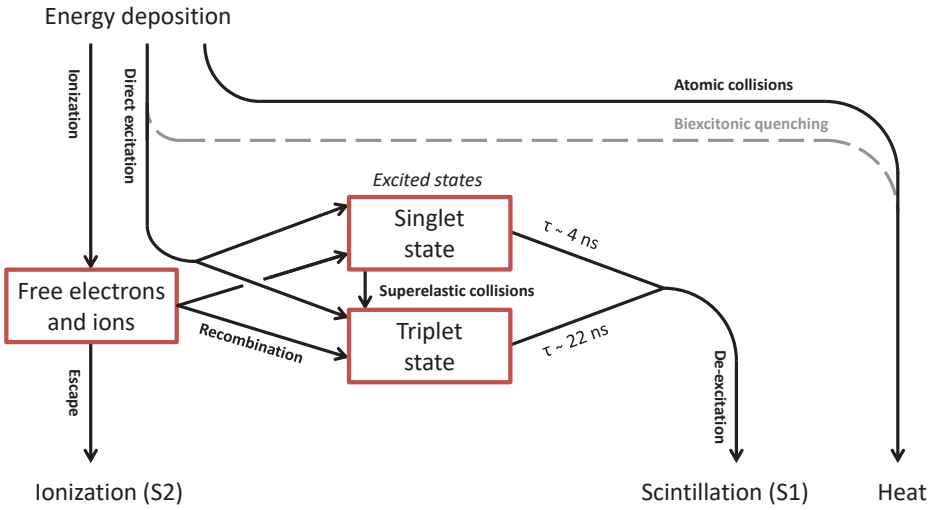

Figure 2.4: Schematic representation of the transfer of deposited energy in liquid xenon into ionization, excitation and heat. In XENON1T the ionization (S2) and scintillation (S1) signals are measured. Recombination of electrons with ions decreases the number of free electrons that escape (and form the ionization signal) and increases the number excited states that lead to the scintillation signal. Biexcitonic and Penning quenching (grey dashed lines) are most relevant in high density tracks. The S2/S1 and singlet/triplet ratios are different for electronic recoils, nuclear recoils and alphas. From [77].

γ-rays, which induce electronic recoils, but for neutrons (and WIMPs), which induce nuclear recoils, a quenching factor L is introduced to account for the energy loss due to atomic motion and heat. This quenching factor L, from Lindhard's theory [78], describes the fraction of nuclear recoil energy transferred to electrons:

$$L = \frac{k\, g(\epsilon)}{1 + k\, g(\epsilon)}, \tag{2.8}$$

with k a proportionality constant related to the electronic stopping power and the velocity of the recoiling nucleus. The quantity $g(\epsilon)$ is proportional to the ratio of electronic to nuclear stopping power and is energy dependent [75] (ϵ is a dimensionless measure of energy).

By introducing the W-value, defined as the average energy needed to produce one electron-ion pair, and assuming $E_{ex} \approx E_i + E_e$ with E_e very small, equation 2.7 can be rewritten to account for nuclear recoils as:

$$E_{dep} = \frac{(N_{ex} + N_i)\, W}{L}. \tag{2.9}$$

For electronic recoils, nuclear quenching does not play a role and equation 2.9 is reduced to $E_{\text{dep}} = (N_{ex} + N_i)\,W$. The W-value of $(13.7 \pm 0.2)\,\text{eV/quanta}$ is from a fit of a semi-empirical physical model of the generation of photons and electrons in liquid xenon to experimental data [75]. Without taking the nuclear quenching into account this means that for any energy deposition we expect $N_{quanta} = E_{dep}/13.7\,\text{eV}$ of ion-electron pairs or excited atoms deposited in the detector.

Apart from Lindhard quenching, Penning quenching (also called biexcitonic quenching) reduces the measurable amount of quanta in liquid xenon. In Penning quenching two excitons interact to form one electron-ion pair and one ground state [79]. When the electron-ion pair recombines, it will just release one photon instead of the expected two photons if both excitons would have formed excimers[2]. For tracks with a higher ionization density, such as nuclear recoils, the probability of ionization density dependent quenching increases.

2.2.2 Scintillation mechanism and decay times

Primary scintillation light is generated through the creation of diatomic excited-xenon molecules. These can be produced either by direct excitation or by recombination after ionization (as shown in figure 2.4). The excitation process of xenon atoms by β-radiation can be described by the following four steps:

$$
\begin{aligned}
e^- + Xe &\rightarrow Xe^* + e^- && \textit{impact excitation}\\
Xe^* + Xe &\rightarrow Xe_2^{*,v} && \textit{excimer formation}\\
Xe_2^{*,v} + Xe &\rightarrow Xe_2^* + Xe && \textit{relaxation}\\
Xe_2^* &\rightarrow Xe + Xe + h\nu && \textit{VUV emission}
\end{aligned}
$$

Here $*$ and v are used to distinguish between purely excited states $(*)$ and states with vibrational excitation (v). The excited diatomic molecules (excimers) in the last step can be in one of two electronic excited states: a singlet state $({}^1\sum_u^+)$ or a triplet state $({}^3\sum_u^+)$. Due to the triplet state having a forbidden transition to the ground state $({}^1\sum_g^+)$, in liquid xenon the decay times of the singlet and triplet state are $(4.3 \pm 0.6)\,\text{ns}$ and $(22.0 \pm 1.5)\,\text{ns}$, respectively [80] [81]. For α-, β- and neutron-interactions, due to a different track profile, the ratio between singlet and triplet states are different, which result in different scintillation pulse shapes [77].

[2] See the next section for exciton and excimer production.

The recombination process, after ionization, can be described by the following six step process:

$$
\begin{aligned}
&e^- + Xe \rightarrow Xe^+ + 2e^- && \textit{ionization} \\
&Xe^+ + Xe + Xe \rightarrow Xe_2^+ + Xe && \\
&e^- + Xe_2^+ \rightarrow Xe^{**} + Xe && \textit{recombination} \\
&Xe^{**} + Xe \rightarrow Xe^* + Xe + \text{heat} && \\
&Xe^* + Xe + Xe \rightarrow Xe_2^* + Xe + \text{heat} && \\
&Xe_2^* \rightarrow Xe + Xe + h\nu && \textit{VUV emission}
\end{aligned}
$$

Depending on the electric field strength and the ionization density, a certain part of the electrons escape, while the rest recombine into excimers. Even though the final stage of this process is similar to the direct scintillation process, the singlet to triplet ratio differs in liquid xenon. A third component to the time profile thus comes from recombination, where time constants of 34 to 45 ns have been reported [80] [82].

Electrons, neutrons and alpha particles all have a different energy density deposition profile [75], as this influences the singlet to triplet ratio, the pulse width of the light can be used to distinguish between these particles. The heavier the recoiling particle, the denser the track profile. In section 3.6.2 a comparison will be presented between XENON1T data and simulation for the light and charge yield of electronic recoils (from electrons and γ-rays).

Light and charge signals The ionization signal, in number of electrons measured in the detector, is the number of deposited electrons that reach the amplification region at the gas-liquid interface. For a single electron reaching the amplification region, between 21 and 22 photoelectrons [PE] are detected[83].

The number of excited atoms (N_{ex}) is increased by recombination, but decreased by Penning effects. As the recombination probability is track-profile dependent, a denser track has a higher recombination probability due to a lower average interaction distance between the electron and ion. Penning quenching increases with increased energy for nuclear recoils, due to a higher ionization density along the track of the recoiling Xe atom. The resulting number of excited states (N_{ex}) eventually de-excite and produce vacuum ultraviolet (VUV) photons at 178 nm, for which liquid xenon is transparent[3].

[3] 'Vacuum' refers to the fact that at 178 nm the light is normally absorbed by atmospheric oxygen.

2.2.3 Dual-phase TPC working principle

The XENON1T experiment is a *dual-phase liquid xenon TPC*. The working principle is shown in figure 2.5.

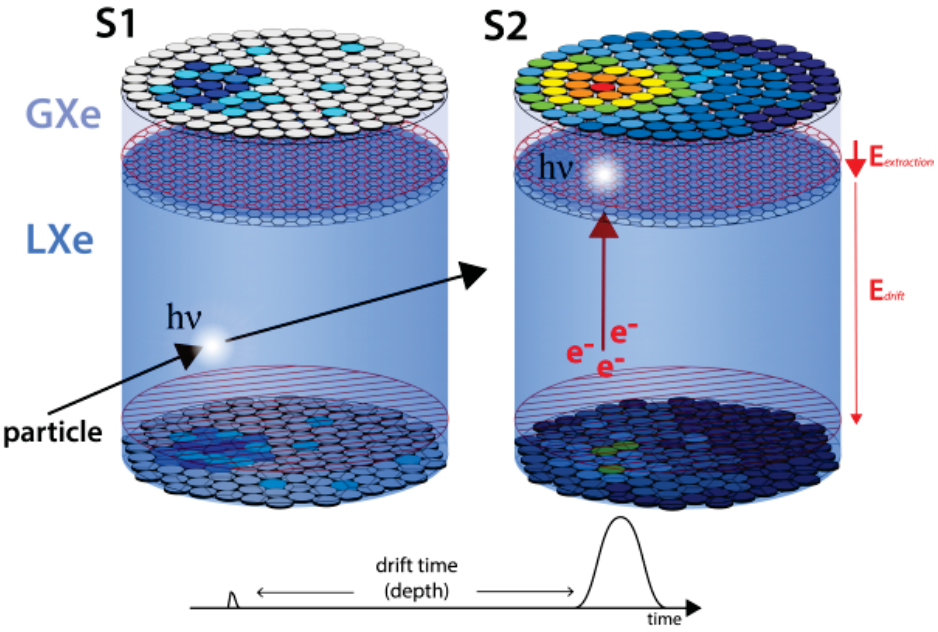

Figure 2.5: Working principle of the dual phase liquid xenon (LXe) Time Projection Chamber (TPC). An incoming particle will produce primary scintillation light (S1) and secondary scintillation light (S2). The light is measured by light detectors at the top and bottom (colour scale represents signal size measured in PE) of the TPC. To collect the electrons at the gas-liquid interface, an electric field is set over the drift region (E_{drift}). The drift region is defined between the cathode wires at the bottom (red wires) and the gate mesh at the top (black mesh) of the liquid. To convert the electrons into a light signal a much stronger extraction field ($E_{\text{extraction}}$) is set over the gass-liquid interface. The extraction region is defined by the gate and the anode mesh (red mesh). The distance between gate and anode is 5 mm, with the liquid-gas interface 2.5 mm above the gate. The time difference, as shown in the waveform (bottom), between the S1 (left peak) and S2 (right peak) signal gives a measure of the depth of the interaction. From [2].

Particles passing through liquid xenon have a high probability of losing energy by scattering. Due to the high density, most low energy particles are fully stopped in the large LXe TPC of XENON1T. The amount of deposited energy and the type of interaction depends on the energy and type of the incoming particle. Neutrons (and WIMPs) produce nuclear

recoils (NR) where the xenon nucleus leaves a dense track of ionization and excitation in the liquid. NR have a reduced deposited energy due to quenching. β- and γ-radiation create electronic recoils with less dense tracks.

To be able to discriminate between particle type, the produced photons and electrons are measured independently, as their ratio will provide the needed information. The photons, travelling in all directions, are directly measured by photo multiplier tubes (PMT) at the top and bottom of the TPC. This signal is thus called the primary scintillation signal or the S1 signal. The freed electrons are not measured directly, but need to be converted into photons. By applying a drift field ($\sim 100\,\mathrm{V/cm}$) over the drift region, the electrons drift upwards until they reach the amplification region. Here a strong amplification field ($\sim \mathrm{kV/cm}$) is set over the liquid-gas interface. The electrons accelerate and excite molecules in the gaseous xenon (GXe) to produce a secondary light signal. This signal is called the secondary (or proportional) scintillation signal or S2 signal. As the drift velocity of electrons is known for a given drift field and xenon density, the time difference between the S1 and S2 signals gives a measure of the depth of the interaction. The PMT hit-pattern, as shown in the top of figure 2.5, provides the (x,y) position of the interaction.

2.3 The XENON1T experiment

The XENON1T experiment, which utilizes this dual-phase liquid xenon TPC technique, is located at the Laboratori Nazionali del Gran Sasso (LNGS), Italy, which is the largest underground laboratory in the world. The experiment itself sits in one of the three main halls of the laboratory. Thanks to the entrance of LNGS being situated next to a public car tunnel, it is easily accessible day and night for both regular maintenance and for emergencies. The mountain range, with Gran Sasso as its highest mountain, gives the laboratory an average depth of 3600 m water equivalent to shields against cosmic rays.

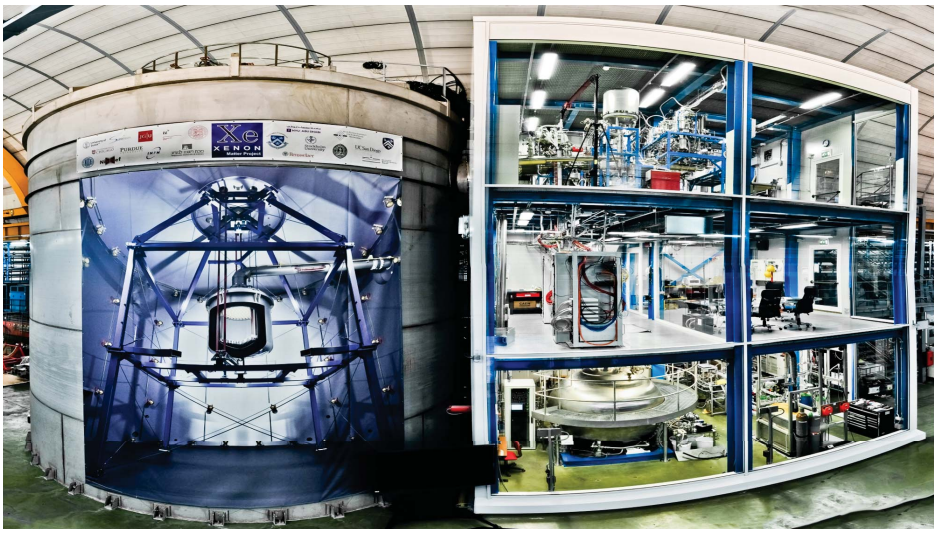

Figure 2.6: Photo of the XENON1T experiment located underground at LNGS. The 10 by 10 m muon veto water tank is shown on the left with a schematic drawing of the TPC and support structure on it. The maintenance building is shown on the right with the cryogenics and purification systems on the top floor, the electronics and data acquisition on the middle floor, and the storage and further distillation systems on the bottom floor. Credits: R. Corrieri and P. de Perio.

Figure 2.6 shows a side view of the experiments with on the left side the water tank and on the right side the XENON1T maintenance building. The front of the water tank depicts a schematic representation of the actual detector, the support structure and the light detectors of the muon veto. These all reside within the water tank. On the right, the maintenance building (with glass walls) holds from top to bottom: the purification and distillation systems, the electronics and data acquisition,

and the storage and further distillation systems. Their functions will be discussed in the following sections.

2.3.1 Time Projection Chamber

The center of the experiment is a cryogenic vessel filled with liquid xenon, acting as a TPC. Here background (and possibly dark matter) particles interact with the liquid xenon producing light and charge signals that are recorded. For every particle interaction, a total of 248 PMTs, divided into a top and bottom array, record the photons from the primary (S1) and secondary (S2) scintillation signals. From the the S1 and S2 signals we infer both the interaction position (x,y,z) and the deposited energy. The following paragraphs describe the working of the XENON1T TPC in more detail.

TPC design The cylindrical TPC encloses 2 t of liquid xenon and has a height of 97 cm and a diameter of 96 cm. Figure 2.7 shows a schematic of the TPC and the TPC parameters are shown in table 2.1. The walls are made from highly reflective PTFE (polytetrafluoroethylene, Teflon) panels, which are interlocked to create a light tight container. Behind the PTFE, 74 copper field-shaping electrodes reside, connected by two parallel redundant resistor chains consisting of 74 individual 5 GΩ resistors each, to ensure a homogeneous drift field. The drift field is confined between the cathode, set at negative high voltage, and the gate, set at ground. The design voltage for the cathode is −100 kV, leading to a design drift field of about 1 kV/cm.

The amplification field is defined by the gate and the anode (set at positive high voltage), which are 5 mm apart from each other. These are labelled as *Top TPC electrodes* in figure 2.7, but are better shown in figure 2.5. The top part of the TPC is built as a diving bell, so that the xenon gas pressure sets the liquid level with sub mm precision in the middle in between the gate and the anode. This result in an amplification field of >10 kV/cm in the gas phase, which is needed to produce secondary scintillation. The liquid level is read out continuously by long and short (capacitance) level meters. To achieve maximal light collection efficiency, the cathode, gate and anode have transparencies between about 90% and 97%.

Outside of the sensitive volume, another 1.2 t of LXe sits acting as self shielding. Several PMTs are placed within this region for diagnostic purposes. The whole LXe volume is confined by an inner stainless steel vessel, which is within an outer stainless steel vessel with vacuum insulation in

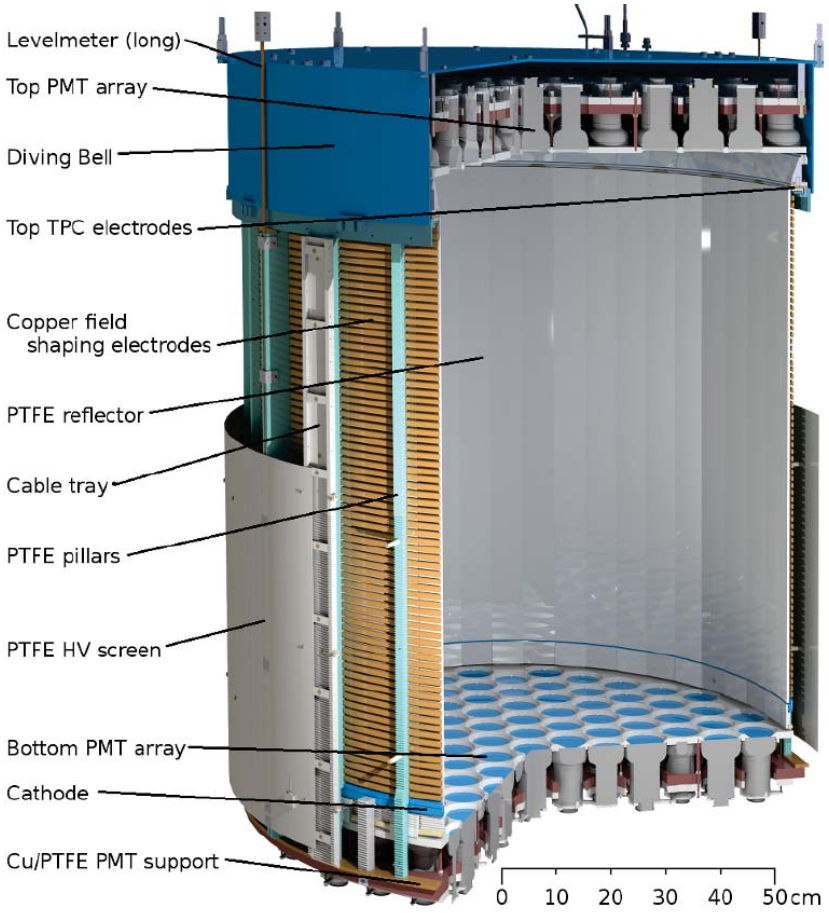

Figure 2.7: Illustration of the XENON1T TPC. The materials were selected for low radioactivity, while the insides of the TPC has been constructed to maximize reflectivity for VUV light. The active volume of the TPC is defined between the cathode and gate (*Top TPC electrodes*) and encloses 2 t of liquid xenon. For a closer look at the amplification region (gate and anode) see figure 2.5. From [84].

between. All PMT signal and voltage cables follow the cable trays to exit the TPC at the top towards the maintenance building.

Photomultiplier tube arrays

A total of 248 3" photomultiplier tubes (PMTs), Hamamatsu model R11410-21, are used to detect the photon signals in the TPC. The top array (figure

Parameter	Value	Units
LXe temperature	-96.07 ± 0.04	°C
LXe pressure	1.93 ± 0.001	bar
LXe density	2.862 ± 0.004	g/cm^3
LXe within TPC	2003.8 ± 5.2	kg
TPC radius	478 ± 0.5	mm
Maximum drift length	969 ± 2	mm
Xe recirculation flow	51.85 ± 0.62	slpm

Table 2.1: Overview of TPC parameters for SR0. (slpm stands for standard litres per minute)

2.8, left panel) consist of 127 PMTs arranged in a radial structure to maximize the position reconstruction accuracy. The secondary scintillation signal is created at the liquid-gass interface and is thus mostly observed by the top array. The bottom array (figure 2.8, right panel) consists of 121 PMT's tightly packed to maximize the light collection efficiency. The light from the direct scintillation signals (S1) is mostly observed by the bottom array as the light is reflected at the liquid-gas interface. The PMTs are designed and tested to operate at a cryogenic temperature of -96°C, with an average gain of 5.3×10^6 [85]. They have an average quantum efficiency (QE) of 34.5% at 178 nm (measured at room temperature) and a photoelectric collection efficiency (CE) of 90%. To improve the total average light collection efficiency for S1 signals, PMTs with the highest quantum efficiency and collection efficiency are placed at the center of the bottom array.

Figure 2.8: The top (left) and bottom (right) PMT arrays equipped with 127 and 121 PMTs respectively. The 3" PMTs are from Hamamatsu, model R11410-21, with an average quantum efficiency of 34.5% at 178 nm, gain of 5.3×10^6 and photoelectric collection efficiency of 90%. From [84].

As our detector aims to measure energy depositions from keV (dark matter) to MeV (calibration), each PMT should idealy have a linear response from a single photon to tens of thousands of photons. The PMT is linear if the output current of the PMT is equal to the number of created photoelectrons by a constant factor. Each PMT has a base that divides the high voltage (HV) over the different dynode stages and connects the signal and ground to the readout electronics. Specific for XENON1T, the PMT bases were designed to enable high linearity by adding several capacitors to the last few dynode stages. Dedicated measurements show that the PMT with base has a linear output up to 14,000 photoelectrons (PE) at a max rate of 100 Hz [86].

2.3.2 Liquid xenon plant

The xenon is purified continuously to increase the signal yields, and cooled to keep the temperature stable. The LXe system is shown in figure 2.9. LXe is siphoned from the bottom of the TPC and evaporated in a heat exchanger. The gas then flows trough the purification system consisting of gas transfer pumps (CHART QDrive), mass flow controllers (MKS 1579A) and high-temperature high-rate gas purifiers (getter, SEAS PS4-MT50-R). The getter removes electronegative impurities, such as water and oxygen, by forming very stable chemical bonds with the getter material, namely zirconium. Without purification, these impurities (which are constantly out-gassing into the liquid xenon by all the detector components) would lower the signal yields by absorbing scintillation light and capturing drifting electrons.

To keep the liquid xenon at a temperature of -96°C in the TPC, two redundant pulse-tube refrigerators (PTRs) are used in the cryogenic system to liquefy the xenon gas back into the TPC. To keep the liquid level stable, the xenon pressure inside the TPC is kept constant by controlling the temperature of the PTR using resistive heaters. This is done 24/7 at a constant flow of around 50 slpm. The other two systems in figure 2.9 are the cryogenic distillation column and the storage and recovery vessel (ReStoX). The working principle of the distillation column, used to remove ^{85}Kr from the xenon, will be explained in more detail in section 2.4.2. The ReStoX storage vessel facility was built to recover the xenon in case of an emergency. It can hold up to 7.6 t of liquid or gaseous xenon and withstands pressures upto 73 bar.

2.3.3 Calibration system and sources

By exposing the TPC to particles of a known origin (type and energy) we measure the performance of the detector and calibrate the expected signals

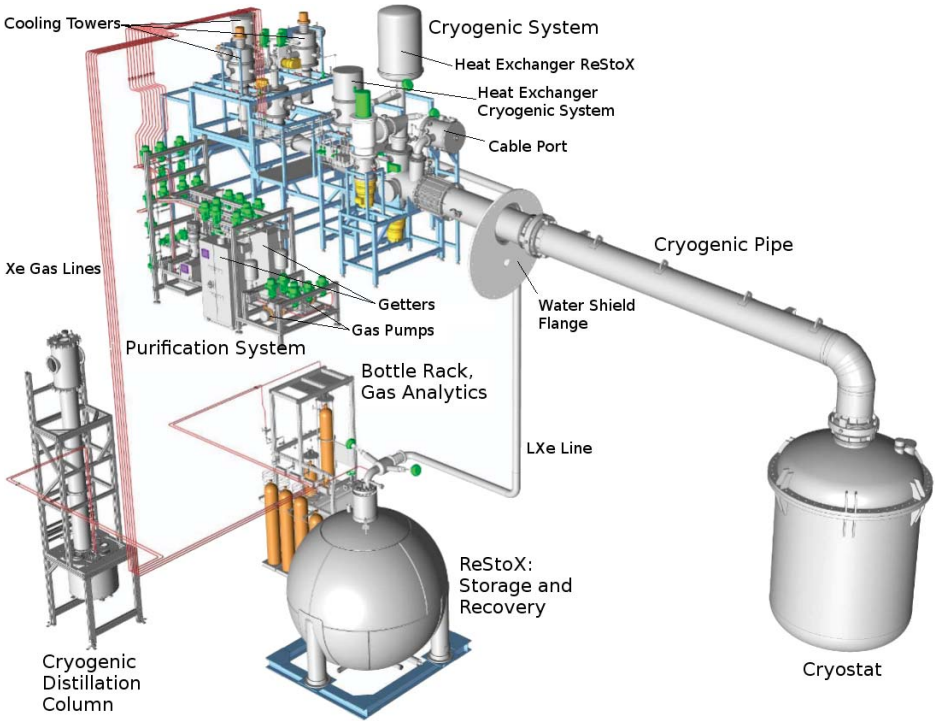

Figure 2.9: The main parts of the xenon circulation system consisting of cryogenics (for cooling), purification (removal of electro-negative impurities), distillation (^{85}Kr removal) and ReStoX (storage and recovery). The cryostat and TPC are located within the water tank, while the other systems are located in the maintenance building. The cryogenic pipe contains all the GXe, LXe and electrical connections between the TPC and the rest of the systems. A continuous flow of 50 slpm is kept between the TPC, purification and cryogenic to reduce impurities in the LXe. The LXe within the TPC is kept at a constant temperature of -96°C at a pressure of 1.9 bar. From [84].

from background and WIMP particles. For such calibrations, radioactive sources are used that emit α-, β-, γ- or neutron radiation. To deploy a radioactive source in XENON1T we either place the source next to the cryostat in the water tank (by either a belt system or a rope) or dissolve it directly into the LXe. To calibrate the gain of the PMTs, dedicated fibres transfer low-level light pulses from a blue LED into the TPC at various heights and angles. Table 2.2 shows the different calibration sources used in XENON1T.

Figure 2.10 shows the XENON1T calibration system outside the cryostat in the water tank. It consists of three belt systems, designed to hold gamma sources. Due to the size of the TPC and the effective self shielding

Source	Goal	Source location
^{231}AmBe	Nuclear Recoil response	U-Belt
Neutron generator	Nuclear Recoil response	Next to Cryostat
^{220}Rn	Electronic Recoil response	Dissolved in LXe
^{83m}Kr	S1 and S2 signal corrections	Dissolved in LXe
LED	PMT gain determination	Fibres in TPC

Table 2.2: Overview of calibration sources used in XENON1T. The neutron generator is an improvement over the ^{231}AmBe due to it's higher neutron rate. The source locations next to the TPC are shown in figure 2.10.

external gammas do not reach the center of the TPC to yield sufficient statistics. The electronic recoil calibration is thus done by dissolving ^{220}Rn into the LXe flowing into the TPC. The two I-belts can move vertically, while the U-belt can also move horizontally below the cryostat. By placing a lead slug into the U-belt the ^{231}AmBe could be used in the U-belt for neutron calibration[4]. The deuterium-deuterium plasma fusion neutron generator is placed next to the cryostat.

Here, we give a short description of the ^{231}AmBe, ^{220}Rn and ^{83m}Kr calibration sources. The NR and ER calibration are described in more detail in section 3.6, while the krypton calibration is presented in section 3.3.

- **NR calibration with ^{231}AmBe**. The combination of an alpha source (americium oxide) with a low-atomic-weight isotope (beryllium metal) leads to an effective neutron source with energies up to 10 MeV [88]. The ^{231}AmBe source has an activity of 3.7 MBq ($T_{1/2}$ of ^{241}Am = 432 y), which leads to a total emission of about 220 n/s produced at the source. This source is placed within a lead box (to shield gamma-rays) on the U-belt system for nuclear recoil (WIMP-like) calibration data.

- **ER calibration with ^{220}Rn**. This isotope of radon is gaseous and has a relatively short half life ($T_{1/2}$ = 3.8 d). ^{228}Th is deposited on a stainless steel disk, which is placed in the gas system to emanate ^{220}Rn [89] into the LXe. The decay daughters produce α-, β- and γ-radiation, which makes this source useful for a wide range of studies. For the low energy electronic recoil calibration, βs of the radon daughter ^{212}Pb ($T_{1/2}$ = 10.66 hours, Q-value of 569.8 keV) are selected [90]. Because the radon mixes homogeneously with the

[4]The lead reduces the amount of emitted high-energy gammas entering the TPC.

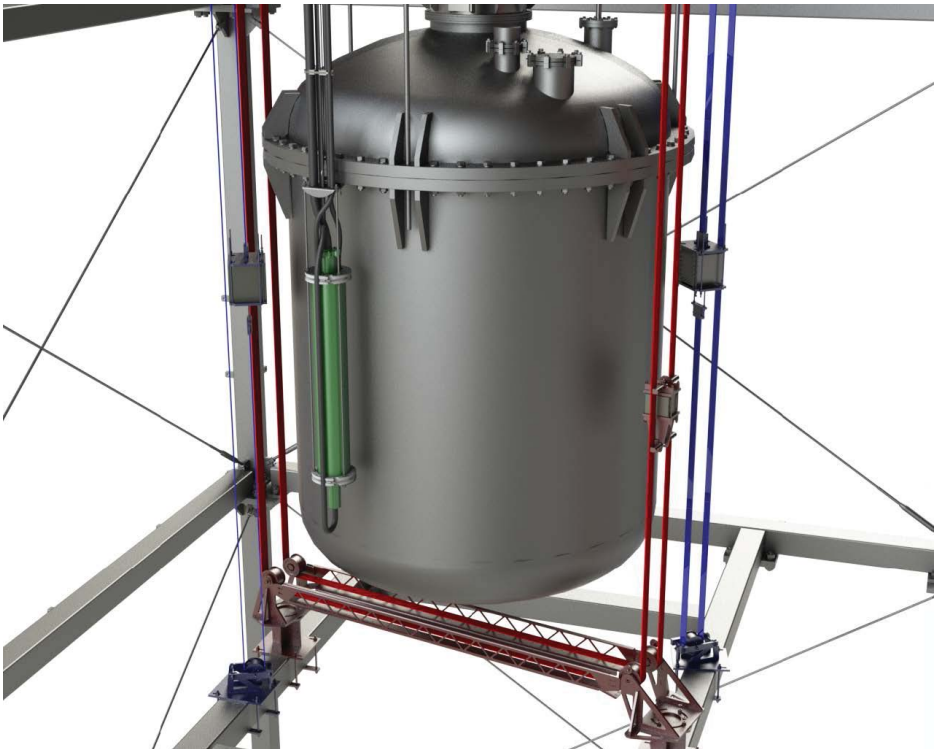

Figure 2.10: Schematic representation of the calibration system of XENON1T placed next to the cryostat in the water tank. Sources can be placed in the two I-belts (blue) that move vertically, or in the U-belt (red) that can also move horizontally below the cryostat. The neutron generator (green) can also be placed in two other locations. From [87].

LXe, this low energy (background-like) calibration can be done in all regions of the TPC at the same time.

- β **calibration with** ^{83m}**Kr**. The metastable ^{83m}Kr, which is generated from ^{83}Rb ($T_{1/2}$ = 86.2 d), is also solvable in LXe [91]. It has a short half life of 1.83 h and most importantly emits two low energy conversion electrons (9.4 and 32.1 keV) shortly after each other ($T_{1/2}$ = 154.4 ns). This makes this event topology easily distinguishable against any background signals. Because there are no other decay products in the chain, this calibration source is used to map out the whole TPC with very high statistics.

Neutron calibrations take up to a week or two of data taking and are normally taken at the beginning and end of a science run. After a neutron

calibration many gamma lines are observed due to neutron activated isotopes, these are used for calibrating the energy response. Radon calibrations are taken monthly, and take up several days. Krypton calibrations are taken bi-weekly to monitor for any time dependent effects in the TPC and only take a day or two. LED calibrations are done weekly to monitor any gain changes. In the next chapter the data from the calibration sources will be presented to determine the performance of the XENON1T experiment.

2.3.4 Data Acquisition and electronics

Figure 2.11 shows the Data Acquisition (DAQ) system of XENON1T. The signals from the 248 PMTs are first individually amplified ($\times 10$). Then they are digitized (*V1724 ADC*) and saved by reader PCs in a buffer database (*MongoDB*). A software trigger determines which periods of time are stored as events by looking at the coincidence of light pulses from the PMTs. During search data taking this results in a rate of 5 Hz, with event windows being in the order of milliseconds. During calibration the data rate rises to max 50 or 140 Hz for krypton and radon calibration, respectively. After the trigger decides what events to save the event builder writes them to disk.

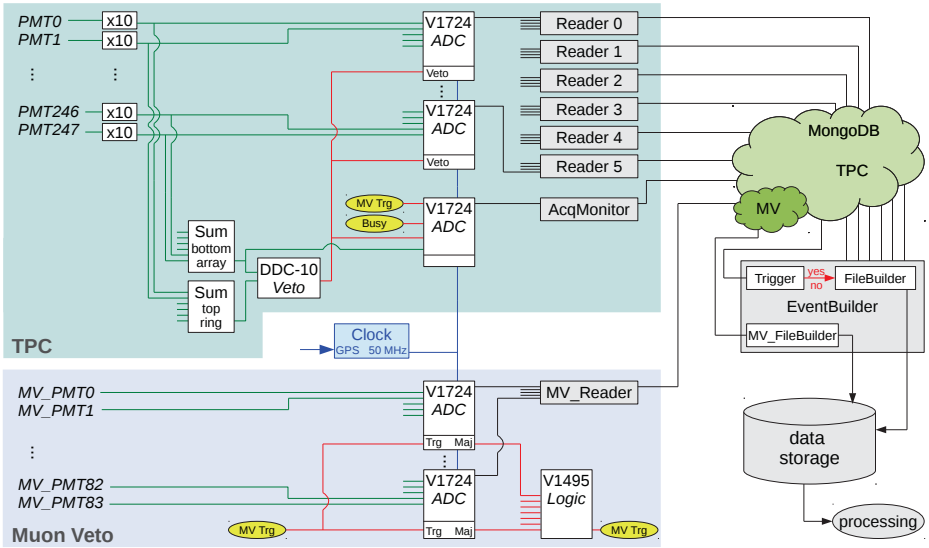

Figure 2.11: Overview of the XENON1T DAQ system with 248 PMTs from the TPC (top part) and 84 PMTs of the muon veto (bottom part). Events from both systems are synchronised and saved in the same data format. From [84].

During calibration data taking, a High Energy Veto (HEV) (*DDC-10 Veto*) is used to decide if an event should be excluded by looking at the sum of all bottom PMTs. This is to reduce data storage for calibrations that aim to only map the low-energy response of the detector. If any of the digitizers experiences a too high data rate, a *busy* signal is sent to temporary stop the flow of incoming data. Both the HEV and the busy will be used in section 3.4 to correct the life-time. The data from

[4]The maximum drift time between a correlated S1 and S2 signal is about 700 μs for a drift field of about 120 V/cm.

the 84 PMTs of the Muon Veto (MV) is digitized and saved by a similar system. All ADCs share a common clock to synchronise both systems. An acquisition monitor digitizes the busy, veto, raw sum waveform and MV trigger for diagnostic purposes.

The amplification of the PMT signals is done with Phillips 776 X10 amplifiers. These low noise, direct-coupled amplifiers were tested for linearity. For rates between 50 and 2000 Hz, pulse widths of 1 μs and up to total signals of 14,000 PE, no non-linear variations above the 1% level were observed [86]. Signals from the amplifiers are connected to the Analog-to-Digital Converters (ADC). XENON1T uses the CAEN V1724 100 MHz ADC, which has an input range of 2.25 V, 14 bit resolution and 10 nanoseconds sampling. Every signal PMT signal is converted from measured ADC counts (per 10 ns bin) to number of photoelectrons (PE) measured by the PMT. The current for one ADC count per bin is

$$I = \frac{U}{R} = \frac{2.25\ [V]\ /\ 2^{14}\ [\text{ADC counts}]}{50\ [\Omega]} = \frac{0.137\ [mV]}{50\ [\Omega]} = 2.7 \times 10^{-6} A. \tag{2.10}$$

One photoelectron is thus equal to:

$$1\ [PE] = \frac{e^{-}[C] \cdot G_{\text{PMT}} \cdot G_{\text{Amp}}}{I[A] \cdot t_{\text{bin}}[s]} = \frac{1.6 \times 10^{-19}\ [C] \cdot 2.4 \times 10^{6} \cdot 10}{2.7 \times 10^{-6}\ [A] \cdot 10 \times 10^{-9}[s]}, \tag{2.11}$$

with e^{-} the charge of one electron, G_{PMT} the average gain of the PMTs in XNEON1T, G_{Amp} the amplification of the amplifier, I the current per bin from equation 2.10 and t_{bin} the time of one sample. This simplifies to:

$$1\ [PE] = 142\ [\text{ADC counts}]. \tag{2.12}$$

Any signal above the digitizer self-trigger threshold of 15 ADC counts per bin is digitized. As the height of an signal is about 40% of its integral, every signal above 0.5 PE will be recorded. Very high signals with an amplified pulse height over 2.25 V will be capped by the ADCs. This is reached by a single PMT when it records a signal of about 14,000 PE at a width of 1 μs (assuming a single PMT gain of 10^6). The width of 1 μs is chosen here to resemble a real S2-pulse width in XENON1T. We will see in section 4.2 what the effects are of saturated signals.

2.4 Background suppression

The goal of XENON1T is achieving the world's best sensitivity for the direct detection of WIMPs. For this it is designed with:

- a huge fiducial mass (1 t LXe fiducial); and

- an ultra low electronic background (~ 0.2 events t^{-1} keV^{-1} d^{-1}).

To decrease the total background rate the following measures were taken:

- The detector is shielded by a mountain (against cosmic rays) and a water tank (against γ-rays and neutrons).
- All TPC materials were screened and only those with the lowest radioactivity were selected [92].
- The LXe was distilled to remove trace amounts of krypton.

During the design phase of XENON1T, dedicated Monte Carlo (MC) studies were performed to determine the expected background [93]. Here we will describe the shielding and distillation. The MC expectation values of the background levels will be presented in section 4.1.1.

2.4.1 The water tank and muon veto

As described in the beginning of this section, the cryostat of the TPC is enclosed by water in a 10 m high by 10 m diameter tank. This stops all low energy and most of the high energy γ-rays originating from outside of the water tank. In water a 3 MeV γ-ray has a mean free path of less than half a meter. The total event rate in the TPC before and after water filling dropped from 1 kHz to below 10 Hz. Figure 2.12 shows the energy spectrum measured in the TPC before the water tank filling, revealing the backgrounds that are present in Hall B of the Gran Sasso laboratory.

This data was taken at zero drift field, and thus only the scintillation light (S1) signal is used as an energy estimator. Seven hours of data is used without any cuts or selection criteria, after that a data-driven light collection efficiency versus depth correction was applied[5]. The spectrum is shown for an approximate depth of -70 cm $< z < -20$ cm. The depth is estimated by using the fraction of the S1 area observed in the top array[6].

The spectrum (black solid line) shows several peaks from known origin such as ^{40}K, ^{214}Bi (from the uranium chain) and ^{208}Tl (from the thorium chain). These are primordial radioactive isotopes, which can be found in any (natural) material on Earth. To convert from the deposited energy to the number of deposited photons in LXe, the light yields from NEST (< 50 keV), Yamashita and Ni (> 50keV) were used[7] [94]. The Noble Element Simulation Technique (NEST) package is used to simulate the

[5] This method will be presented in section 4.2.2.

[6] This method will be presented in section 4.2.2.

[7] NEST is optimized for low energy, Yamashita and Ni showed better agreement at higher energies.

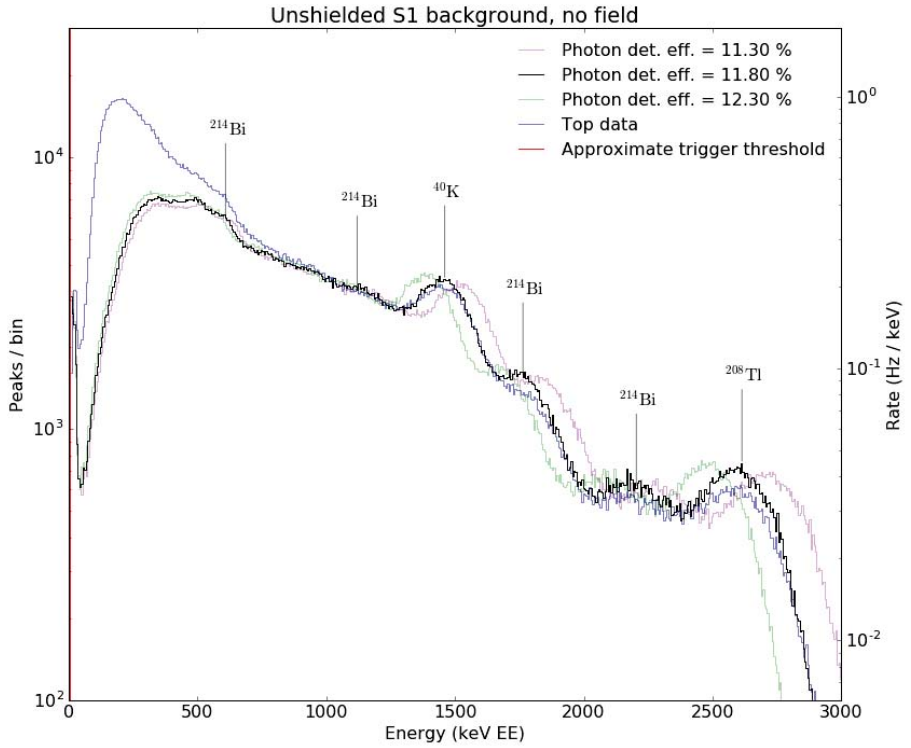

Figure 2.12: The unshielded spectrum of γ-radiation, originating from outside the cryostat. The spectrum (black line) is shown with the best fit photo-detection efficiency, the green and purple lines show the effect of a small offset to the photon detection efficiency.

excitation, ionization, and corresponding scintillation processes in liquid noble elements such as xenon [94] [95] [96]. To convert from the number of measured photons to the number of deposited photons one needs to know the photon detection efficiency. We fixed the photon detection efficiency by matching the peaks to their known energy. The best fit gives a detection efficiency of 11.8% [8].

For comparison, the spectra for two other detection efficiencies (11.3% and 12.3%) are shown. The drop in the spectrum below a few hundred keV, is caused by the outer layer of LXe shielding the low energy radiation. We also show the spectrum for only the top part (approximately z > −20 cm) of the detector (as a sanity check). This shows, as expected,

[8] A more precise measurement of the photon detection efficiency will be presented in section 3.5.1.

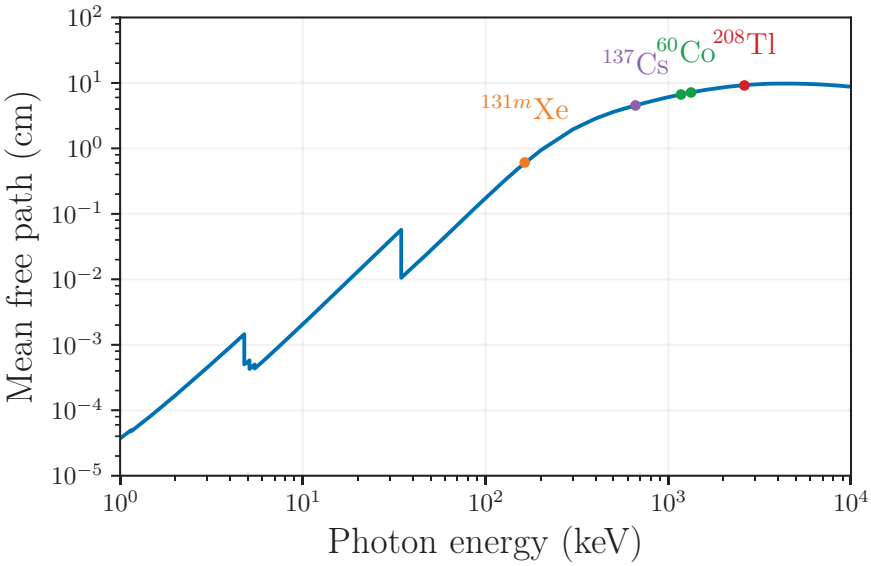

Figure 2.13: Gamma-ray interaction mean free path in liquid xenon ($\rho_{\mathrm{LXe}} = 2.86\,\mathrm{g/cm^3}$). For an internal source such as $^{131\mathrm{m}}$Xe (orange) the mean free path is less than one cm, while external sources such as ^{137}Cs (blue), ^{60}Co (green) and ^{208}Tl (red) have a mean free path of less than 10 cm. This shows the excellent self shielding properties of LXe. Data from [97].

more low-energy events appear due to less LXe for self shielding, but still gives the same shape at higher energies. This can be understood by looking at the mean free path of gamma-ray interactions. Figure 2.13 shows the mean free path for gamma-ray interactions in liquid xenon. For several gamma-ray sources in XENON1T we show the specific energy and mean free path. For an internal source such as $^{131\mathrm{m}}$Xe interactions happen within $\mathcal{O}(1)\,\mathrm{cm}$, while for external sources such as ^{137}Cs, ^{60}Co and ^{208}Tl interact within $\mathcal{O}(10)\,\mathrm{cm}$ (see section 4.5.2 for a description of these background sources). For this reason XENON1T utilizes an inner LXe volume for any dark matter search analysis to shield against external backgrounds.

2.4.2 Distillation

Xenon bought from commercial partners will always contain a certain concentration of krypton. This isotope ^{85}Kr, ($T_{1/2} = 10.76$ y), is a β-emitter with an endpoint energy of 687 keV. It therefore is a background

in our low energy search region and thus it has to be removed before data taking. This is achieved using a novel cryogenic distillation technique with the distillation column shown in figure 2.14.

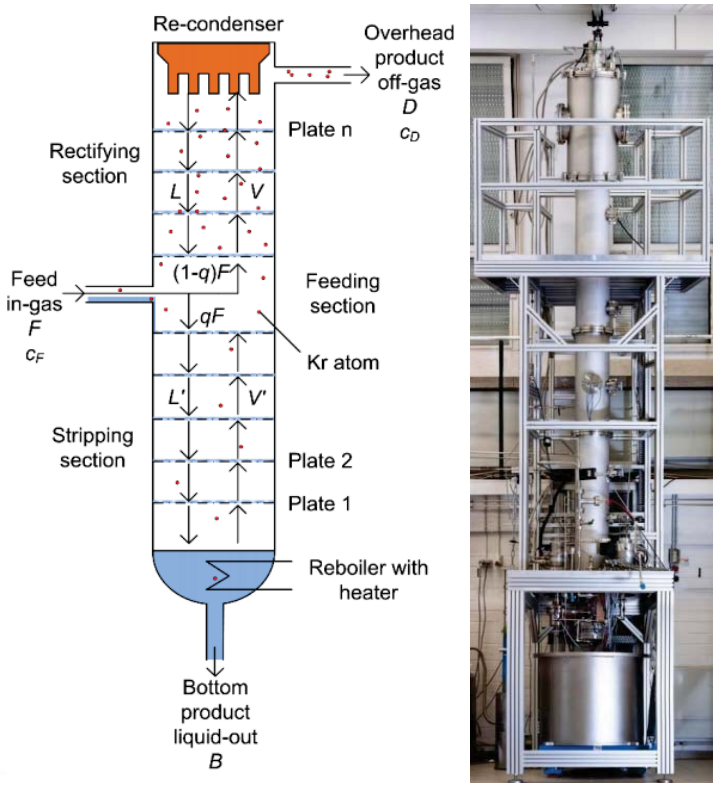

Figure 2.14: Schematic representation (left) and photo (right) of the XENON1T distillation column. Xenon gas from the TPC is fed into the column (F), which works thanks to the difference in vapour pressure of xenon and krypton. Krypton is trapped in the gas flow going upwards, while xenon liquefies and flows down. At the top, krypton-enriched gas is extracted (D) and stored, while the rest of the gas is liquefied to enter the distillation stages again. The clean xenon at the bottom is extracted (B) and fed back into the TPC. This leads to a total reduction factor of about 10^5. From [98].

The column's distillation process is based on the difference in vapour pressure between krypton and xenon. The whole system consists of three parts: the stripping section, the feeding section and rectifying section. Gas from the TPC is fed into the column at the feeding section where it enters one of the distillation stages. Due to the difference in vapour pressure, at every stage, most of the xenon liquefies and flows downward (L) while the krypton evaporates and flows upwards (V). The addition of ex-

tra distillation stages increases the total reduction factor, for XENON1T seven stages are used. At the top, krypton enriched gas is taken out (D), while the rest of the gas is liquefied again[9]. At the bottom, purified liquid xenon is extracted and siphoned back to the TPC (B). A novel functionality is that this system can run in parallel with normal data taking of XENON1T. This has reduced the total commissioning time by at least several weeks, as normally distillation is done before turning the detector on. Dedicated tests showed that the column has a krypton reduction factor of 6.4×10^5 with thermodynamic stability at process speeds above 3 kg/h. This results in a ^{nat}Kr/Xe concentration below 26 ppq (parts per quadrillion), far below the required value of below 200 ppq for XENON1T [98].

[9]The enriched gas is siphened off and stored in bottles, for XENON1T about 35 kg of enriched xenon was set aside in this way.

2.5 Summary and outlook

For WIMP interactions with ordinary matter, low energy depositions of $\mathcal{O}(10)$ keV are expected. As the spin independent WIMP-nucleon cross section scales with A^2, xenon has a higher detection potential than most other elements. By choosing xenon as the detection medium, the XENON1T experiment measures two out of the three possible excitation channels: light and charge. The scintillation and ionization mechanisms in xenon leads to the understanding of how 'S1' and 'S2' signals are generated in XENON1T, and how to distinguish them based on their pulse characteristics.

XENON1T is the first dual-phase liquid xenon direct detection experiment at the tonne scale, and it requires an ultra-low background for achieving its projected sensitivity. The experiment operates continuously purifying and cooling a total of 3.2 t of liquid xenon. All TPC components, such as the PMTs, high voltage grids and PTFE walls were chosen for high light yield and low radioactivity. Apart from the material screening and selection, the background is further suppressed by (active) shielding and distillation. In the next two chapters we will discuss if these goals of high light yield and low background levels have been achieved.

Chapter 3

Detector Performance

To measure is to know.
— Attributed to William Thomson, Lord Kelvin.

In the last chapter we discussed how light and charge signals are created in XENON1T. The goal of this chapter is to show how in XENON1T we start with the recorded light and charge signals, find the interaction position, reconstruct the interaction energy and finally discriminate between signal and background interactions. Particles interacting in the xenon target will deposit energy in the form of light (photons) and charge (electrons). The primary scintillation signal (due to light) and the proportional scintillation signal (due to charge) are called 'S1' and 'S2' signals, respectively. The ratio between S1 and S2, for a single particle interaction, will be used to discriminate between Nuclear Recoil (NR, signal-like) and Electronic Recoil (ER, background-like) interactions. The S1 and S2 signals first have to be corrected for any time- and space-dependent reconstruction efficiencies in the TPC. After those corrections are applied, we use known gamma lines from calibration sources to determine the relation between detected photoelectrons and deposited energy. Finally, the data from a NR and ER calibration source are presented to show how we can discriminate between WIMP and background events in XENON1T[1].

[1] Just like building a detector is done with a huge group of people, so is building all the corrections and cuts for a dark matter search analysis. Here we will try to give a complete overview of all the analysis components. Therefore, we will describe the efforts of a lot of colleagues and reference to their corresponding internal XENON1T notes.

3.1 Event reconstruction

Any particle interaction in the liquid xenon of sufficient energy will produce one S1 and at least one S2 signal as described in the previous chapter. The goal of event reconstruction is to characterize and match these individual signals to form *events*.

3.1.1 Event building

Every *pulse* from a single PMT is digitized and saved into a time-ordered database. From this *signals* are made ('S1', 'S2' or 'unknown') by looking at the time coincidence of PMT signals. To decide what one single event is, a process called an *event builder* loops over the database and tries to group signals into distinct *events*. This process is schematically shown in figure 3.1.

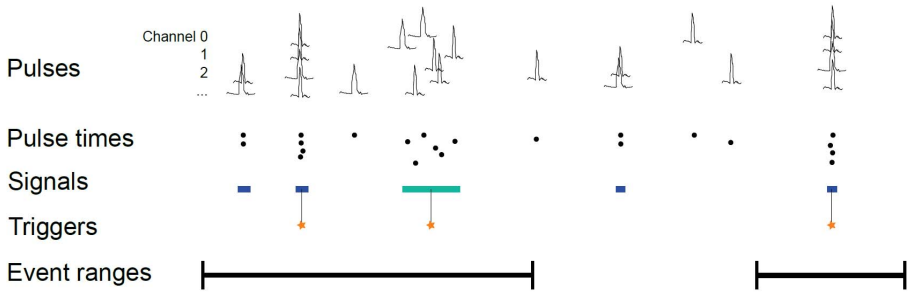

Figure 3.1: Process of how the event builder starts from individual PMT pulses (top) and ends up with grouping signals into events (bottom). For speed performance reasons, only the timing of pulses is taken into account when deciding if pulses should be grouped into signal. A coincidence of two PMT pulses is required for signals. These are tagged 'S1' (blue), 'S2' (green) or 'other'. Because XENON1T utilizes a software trigger, the trigger thresholds can be set and changed per run. A time period of 1 ms is added before and after a trigger to form events. From [99].

The times of pulses are grouped by the event builder into signals. The spread of the individual signals is used to distinguish between narrow S1 (about 100 ns) and broader S2 signals (about 1 μs). To distinguish between a particle interaction and electronic noise or PMT dark rate, a minimum of three coincidental signals is required to call it a *trigger*. From these triggers, the event is then built by adding a 1 ms period before and after any trigger. If two of these overlap, they are stitched together into one event. As the maximum drift time of electrons in the TPC is about 700 μs,

this ensures that all single interactions within the active xenon target are stitched together into one event. If, due to e.g. pileup, two interactions are stitched together, they will be cut out in the dark matter analysis. These cuts will be presented in section 3.4.

3.1.2 Signal matching

Once an event is formed, the correct signals need to be matched, ideally one single S1 with one single S2. Figure 3.2 shows an example waveform of a single event. The main panel displays the sum of the 248 PMT channel waveforms in amplitude versus time. The event is composed of one S1 (blue shaded region) signal of 77.4 PE, with 43 PMTs coincidence, and one S2 (green shaded region) of over 5000 PE, with 208 PMTs in coincidence. The two small black wiggles at around 5 and 7 μs after the S1 signal only occur on one PMT channel and are thus rejected as noise.

S1 and S2 signals are expected to be different in both width and shape. The S1 is characterized by a very short rise-time and an exponential tail, while the S2 is an approximately Gaussian shape. The S1 signal time-profile is determined by the decay of the excimers, while the S2 time profile is determined by the electron amplification in the gas region. The measured S1 and S2 shapes have been matched by dedicated simulation both by XENON1T and others [96].

The four panels of figure 3.2 show the PMT hit-patterns in the top and bottom PMT array for the S1 and S2 signals. The colors represent the amount of charge in photoelectrons (PE) that is measured per PMT. The individual PMT waveforms are shown in black for the time period of the respective S1 or S2. PMTs that are not used for analysis due to PMT problems are marked with a grey cross.

Because of the total light reflection at the liquid-gas layer, most of the S1 light is measured by the bottom array[2]. For a small number of emitted photons the S1 hit-pattern does not show any (x,y) correlation. For the S2 signal, which is created in the amplification region close to the top array, an (x,y) correlation is visible (here top right corner). The S2 hit-pattern in the top array is thus used for the (x,y) position reconstruction. The other variable needed to determine the point of interaction is the depth. This can be reconstructed from the time difference between the S1 and S2 signals, called *drift time*. As the drift speed of electrons is known, the drift time is used to establish the distance the electrons drifted from their interaction point to the gate mesh. The S1 and S2 values given in this figure will still need to be corrected for position and time-dependent

[2]Over the full depth range about 65-90% of the S1 light is measured by the top array, see figure 4.6b.

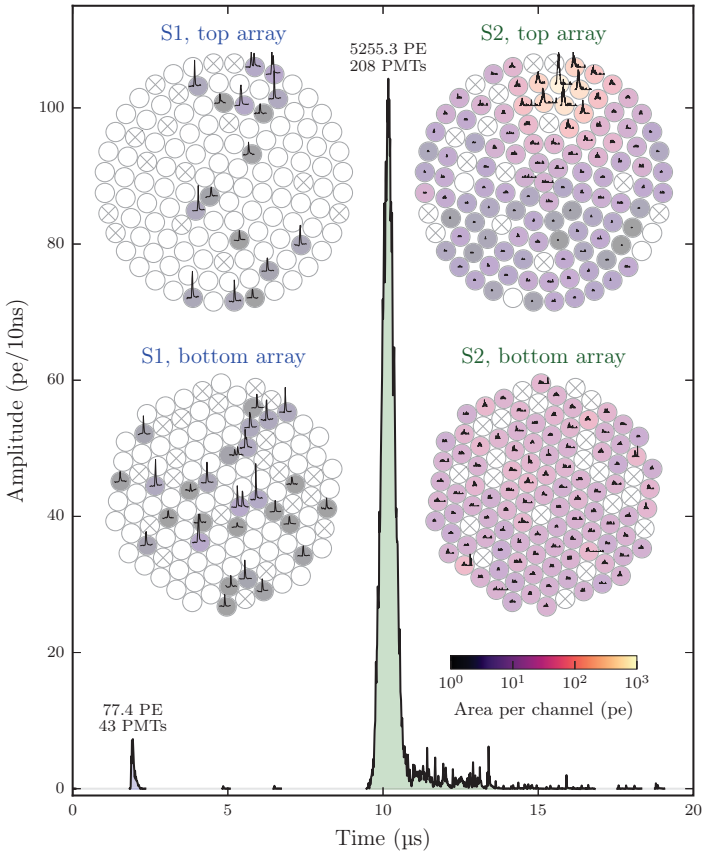

Figure 3.2: Example waveform of a low energy background event in XENON1T. The main panel shows the amplitude of the sum of the 248 PMT channel waveforms over time. The 77.4 PE S1 signal (blue shaded area) is matched with the 5255.3 PE S2 signal (green shaded). For both the S1 and S2 signals, the PMT hit-patterns in the top and bottom array are shown. In every PMT, the individual waveform part is shown together with the area per channel in color. The (x,y) position is taken from the S2 top hit-pattern, while the depth of the interaction can be calculated from the time between the S1 and S2 ($z \approx 1$ cm for this event).

efficiencies and will be discussed in section 3.3. First we will reconstruct the actual point of interaction in the TPC.

3.2 Interaction reconstruction

From the hit-pattern in the top PMT array, we reconstruct the (x,y) position of the S2 peak, which corresponds to the position where the electron

cloud passes through the liquid-gas interface. Under the assumption of a uniform E-field, this relates to the (x,y) position of the interaction within the TPC. The drift time between the main S1 and S2 is a measure of the depth (z). For every event we reconstruct the interaction position in (x,y,z).

3.2.1 Position reconstruction

Light Collection Efficiency Two different position reconstruction algorithms are used in XENON1T: *Top Pattern Fit* (TPF) and *NeuralNet* (NN). Both algorithms rely on Monte Carlo simulation of the light collection efficiency (LCE) for the PMTs. This simulated LCE map is shown in figure 3.3a for a single PMT. Such a map shows the probability distribution of the fraction of the total number of photons a PMT will receive from a position (x,y). The probability is highest right below the PMT location and falls off quickly within 10 cm of the lateral position from the PMT. The LCE maps are simulated on a grid with a grid spacing of 2.4 mm. This, combined with the interpolation method, results in a maximum achievable position reconstruction resolution depending on the algorithm.

Top Pattern Fit reconstruction (x,y) The *Top Pattern Fit* algorithm compares the measured hit-pattern to the expected pattern from the LCE maps. By minimizing a test statistic (a modified χ^2 for low counts), a reconstructed position in (x,y) is found together with a goodness-of-fit parameter. It works by comparing the number of PE measured in a PMT from a position (x,y) to the expected number of PE according to the LCE map, and doing this for all PMTs in the top array. An advantage of this method is that it not only gives the position, but also a measure of the uncertainty on the position.

Neural Network reconstruction (x,y) The *Neural Net* (NN) determines the position of the S2 using a neural network trained on GEANT4 [100] MC events. The NN works with a layer of 127 input nodes (number of PMTs in the top array), which take the measured hit-pattern as input. It has two hidden layers of nodes and a final output layer that returns the (x,y) position. Using known positions from the GEANT MC simulation the NN is trained. A benefit of the NN is that, once trained, it performs similarly to TPF in less time. Its drawback is that it is fully dependent on the correct implementation in the MC.

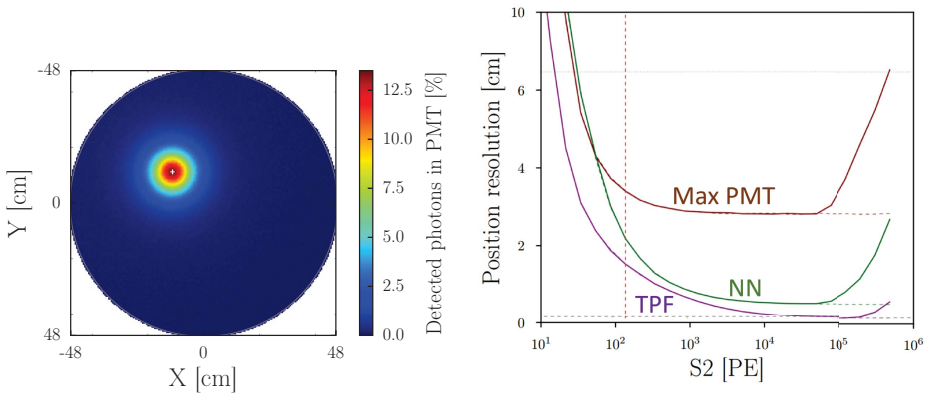

Figure 3.3: **(a)** Simulated light collection efficiency map of PMT 119 in the top array. The white marker ('+') shows the center of the PMT. The color scale shows the fraction of photons that would be detected by this PMT for an interaction in the gas-gap at a specific (x,y) position. From [101]. **(b)** Simulated position reconstruction resolution for Top Pattern Fit (purple) and NeuralNet (green) algorithms. For comparison a test algorithm Max PMT (brown) is shown. At the S2 trigger treshold (red dashed) the position resolution is below 2 cm for TPF and NN. At very high S2 area, non-linearity effects (i.e. ADC saturation) decrease the resolution. From [101].

Position resolution (x,y) Both algorithms were tested on MC data to determine their resolution as a function of S2 signal. In general, a higher energy deposition means more photons are measured by the top array and the algorithm's uncertainty on the reconstructed position decreases. In figure 3.3b, the resolution for both algorithms is shown versus the S2 area.

To contrast against TPF and NN, a test algorithm called *Max PMT* is shown. This algorithm just returns the position of the PMT that saw the most light. The vertical dashed red line represent the minimum S2 area used for dark matter searches. At this threshold of 200 PE, the reconstruction uncertainties are about 2 cm and 3 cm for positions determined by TPF and NN, respectively. For higher energies, the resolution improves until it reaches its maximum position reconstruction resolution. For even higher S2 areas (above 10^5 PE), the resolution worsens because of saturation effects, this is where the energy response is not linear any more. For every S1 and S2 peak, the reconstructed (x,y) of all different algorithms are saved.

Reconstruction of depth (z) The depth (z) of the interaction is calculated by the time difference between the main S1 and S2 signal[3]. The time of a signal is defined as the time where the area has its center of gravity. The depth is thus found by $z = t_{\text{drift}}/v_{\text{electron}}$. For a voltage of -12 kV on the cathode, a maximum drift time was measured of about 673 μs. This maximum drift time corresponds to events originating at the cathode, which is 96.9 cm away from the cathode. The corresponding drift velocity is found to be $v_{\text{electron}} = (1.440 \pm 0.003)\,\text{mm}/\mu\text{s}$. For every matched S1-S2 pair the (z) value is stored.

3.2.2 Field distortion correction

The XENON1T TPC was designed to operate at a 100 kV potential difference between the cathode and the gate, to ensure among others that multiple and single scatters can be distinguished and good ER discrimination from NR interactions. The field shaping rings, as shown in figure 2.7, ensure a homogeneousness drift field, so that electrons drift straight upwards. Unfortunately, due to problems with unexpected light and charge emission from the cathode, a decreased cathode voltage of $-12\,\text{kV}$ was chosen. With this configuration in XENON1T, a deviation in the electric field lines is found. The MC electric-field simulation shown in figure 3.4a demonstrates this effect. In the middle of the detector the field lines are straight, but at the outer edges the field lines show an inward deviation. Electrons that follow these field lines, are now reconstructed by the position reconstruction at a radius that is smaller than the true radius of their interaction point. A radial Field distortion Correction (FDC) rectifies the (x,y) position for all events.

The FDC is constructed by matching simulations of the electric field to calibration data from $^{83\text{m}}$Kr. This process has led to the 2D FDC map shown in figure 3.4b. For every position in z vs r, a radial correction is applied to the S2 signal. This ranges from zero correction at the center of the TPC to about +30 mm at the edges. Here we assume the field is rotationally symmetric, so no ϕ-dependent correction is applied.

[3] And a small correction is applied to account for the different electron drift speed in the liquid layer between gate and liquid-gas interface.

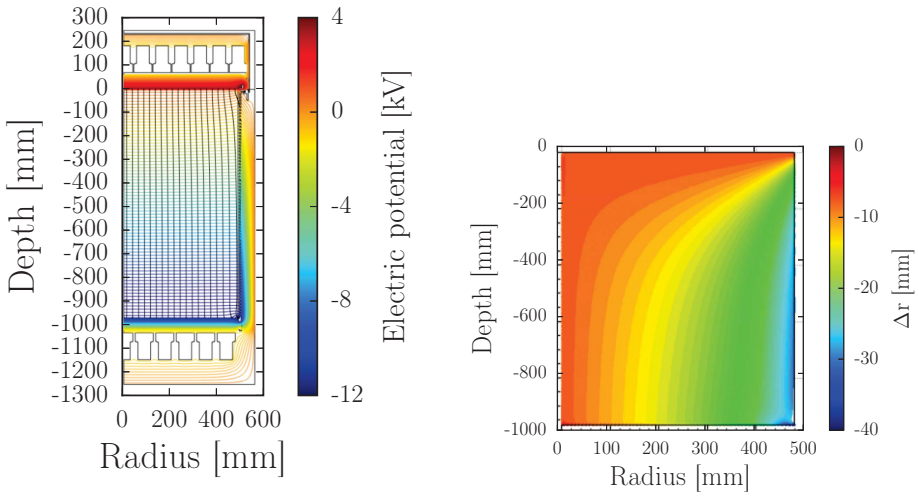

(a) **(b)**

Figure 3.4: **(a)** Simulation of the electric field in XENON1T. On the cathode, gate and anode, -12 kV, 0 and +4 kV is applied, respectively. The colors show the equipotentials, while the streamlines show the electric field. In the top right corner of the TPC the field lines are bended inwards due to the lower field configuration. From [102]. **(b)** Field Distortion Correction map. In color the applied radial correction is shown for the real interaction position of the event. This radial correction is applied to rectify the effect on the (x,y) position reconstruction due to the inward bending field lines. From [102].

3.3 S1 and S2 signal corrections

The next step is to correct S1 and S2 signals for position- and time-dependent signal losses. For S1 signals, a correction needs to be applied to account for the change in total Light Collection Efficiency (LCE) for different (x,y,z) interaction positions in the TPC. For the S2 signals, two different corrections are needed. Firstly, an (x,y)-dependent correction is applied to account for LCE changes in the top array, due to a non-uniform amplification field and dead PMTs[4]. Secondly, a time-dependent correction is applied to correct for an evolving purity of the liquid xenon over time. Electrons that generate an S2 can be lost during drift and this effect is corrected for. To determine these three corrections, ^{83m}Kr, a calibration source with mono-energetic lines, is used.

3.3.1 ^{83m}Kr calibration

Metastable ^{83m}Kr is soluble in liquid xenon, and is a very useful internal calibration source in a variety of liquid noble-gas detectors [91]. The decay scheme is shown in figure 3.5.

XENON1T utilizes a solution of ^{83}Rb (half-life of 86.2d) evaporated onto zeolite beads to generate ^{83m}Kr. From there, ^{83m}Kr, with a half-life of 1.83 h, generates a 32.1 keV conversion electron or gamma with an internal conversion coefficient of $\alpha = 2035$ ($\alpha \equiv N_{e^- \text{emission}}/N_{\gamma-ray\ \text{emission}}$). This is followed by a 9.4 keV conversion electron or gamma ($\alpha = 17.09$). These decays occur with a delay of (154.4 ± 1.1) ns (half-life) [103]. This characteristic delay makes selecting this event topology almost background free. Liquid xenon is flushed through the ^{83}Rb source to mix with the gaseous ^{83m}Kr, that then flows into the TPC. Due to the half-life of 1.83 h the krypton mixes almost homogeneous within the TPC after about 1 hr. These interactions can then be used for testing the position reconstruction algorithms, non-uniformities in drift field, relative Quantum Efficiencies (QE) of PMTs, light Collection Efficiency (LCE), and absolute light yield. ^{83m}Kr calibrations are taken biweekly to monitor any time-dependent effects. In the next sections the results of these calibrations are presented.

3.3.2 S1 Light Collection Efficiency map (x,y,z)

For the S1 LCE correction, the mono energetic peak of 32 keV from ^{83m}Kr is selected. The TPC is binned into r, ϕ and z. The total number of bins (about 1250) is chosen to maximize granularity, while still keeping

[4] To give an idea of the size of these corrections: the maximum relative S1 LCE (x,y,z) correction is about three times larger than that of the S2 LCE (x,y) correction.

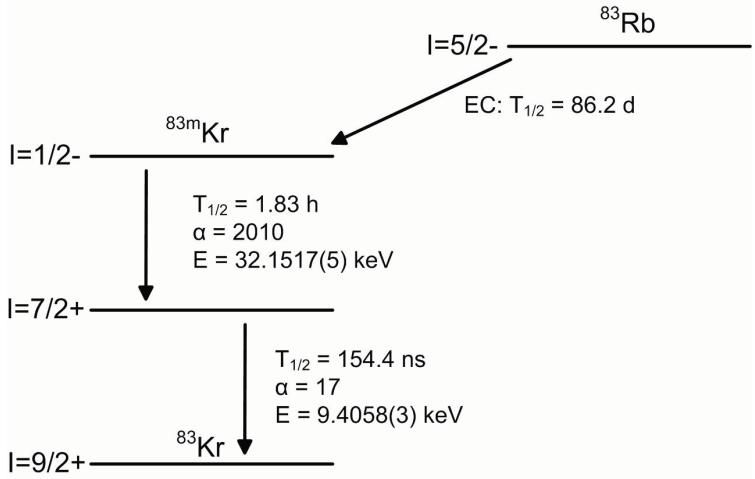

Figure 3.5: Decay scheme of ^{83}Rb by ^{83m}Kr to stable ^{83}Kr. The profile of this decay, a 41.5 keV conversion electron or gamma together with a 9.4 keV conversion electron or gamma within several hundreds of ns, means it is easily distinguishable from any background signal. As it decays quickly to stable ^{83}Kr, this calibration can be done within a day, after which dark matter search data taking is resumed. From [104].

3

sufficient data in each bin so that the statistical uncertainties of the fits are small. The relative number of bins in each dimension where optimized from the relative light yield (LY) changes in each dimension. A few example bins of the S1 LCE map are shown in figure 3.6. The map starts at bin -3.5 cm$> z > 0$ cm and ends at bin -96.9cm$> z > -93.4$ cm. In color the relative light yield is shown ranging from 4.8 to 10.4. The biggest light yield change is observed in the z-direction. At the gas-liquid interface a lot of light is reflected due to the small critical angle of reflection (about 36°). Thus the further away from the bottom array the interaction occurs, the more light is reflected at least once before reaching a PMT. The longer the path of the photon, the higher the probability is that it will be absorbed on a surfaces of the TPC or by internal impurities in the LXe.

For every S1 peak, the S1 LCE correction is applied after which it is named *corrected S1* (cS1). As the map itself is binned, the S1 LCE correction uses linear interpolation of the 6 nearest bins to achieve a higher precision.

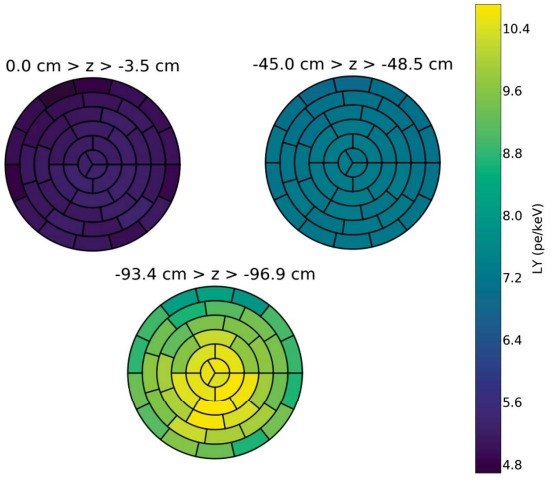

Figure 3.6: Three example z-slices of the S1 LCE map. The full S1 LCE map is divided into about 1250 bins in r, ϕ and z. It has 28 3.5 cm-thick slices in z, six 8 cm slices in r and a number of r-dependent slices in ϕ. In color the relative light yield (LY) is shown ranging from 4.8 to 10.4 PE/keV. This correction is made to account for the position-dependent light loss due to absorption on surfaces and internal impurities. Adapted from [105].

3.3.3 S2 Light Collection Efficiency map (x,y)

An S2 LCE (x,y) correction is needed due to a non-uniform amplification region and dead PMTs. ^{83m}Kr calibration data is also used to determine the S2 LCE correction. Figure 3.7a shows the S2 LCE correction map for the bottom (a) and top (b) PMT array. The amplification region has a large-scale charge yield variation, which can be observed in the bottom array. This is due to a combination of anode mesh warping and a residual tilt of the TPC. A more irregular variation is observed in the S2 (x,y) map of the top array. Here, because of the small distance between the PMTs and the gas-liquid interface, the effect of dead PMTs on the total collected light is clearly observable. The position of the dead PMTs, 15 in total, correspond to areas with lowest charge yield.

The (x,y)-dependent LCE correction is applied to every S2 signal. Depending on the specific analysis, either the total corrected S2 area (cS2) is used or only the corrected S2 area measured in the bottom array ($cS2_b$). The reason to select $cS2_b$ is that big S2 signals can saturate PMTs in the top array, which lead to non-linearities in the energy reconstruction.

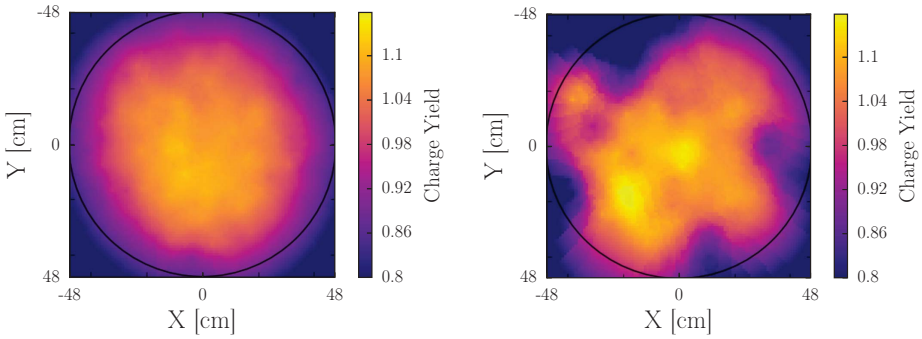

Figure 3.7: **(a)** S2 Light Collection Efficiency map of the bottom PMT array from krypton calibration data. The smooth variation of the charge yield is caused by a combination of anode mesh warping and the residual tilt of the TPC. From [106]. **(b)** S2 Light Collection Efficiency map of the top PMT array from krypton calibration data. The irregular variation of the light collection efficiency is caused by a total of 15 dead PMTs, with positions corresponding to the dark areas. From [106].

3

3.3.4 S2 electron lifetime correction

Electron lifetime fit The second S2 signal correction is to account for the charge losses during the drift of the electron cloud through the liquid xenon. The electron lifetime is defined as the mean lifetime of an electron drifting in the LXe, before it attaches to electronegative impurities:

$$S2(E) = S2_0(E)e^{\left(-\frac{\Delta t}{\tau}\right)}, \tag{3.1}$$

with $S2(E)$ the measured charge signal at a given energy, $S2_0(E)$ the charge signal corresponding to the same energy that would been measured if no impurities are present in the liquid xenon, Δt the drift time and τ the electron lifetime. Several different sources can be used for determining this correction, but for consistency we normally use events from ^{83m}Kr (32 keV). Figure 3.8 shows the fit of the electron lifetime for a krypton calibration dataset. As expected, the mean S2 area decreases for longer drift times (depth). The median of the distribution, in slices of drift time, are fitted with an exponential decay function[5]. This electron lifetime is then used to correct the S2 as if no electrons were lost during their drift. Together, the S2 (x,y) LCE and the S2 (z) electron lifetime correction lead to the final *corrected S2* (cS2) signal.

[5]The horizontal error bars here should be a maximum of one bin wide to account for the binning uncertainty in the drift time, but are wider due to a coding bug.

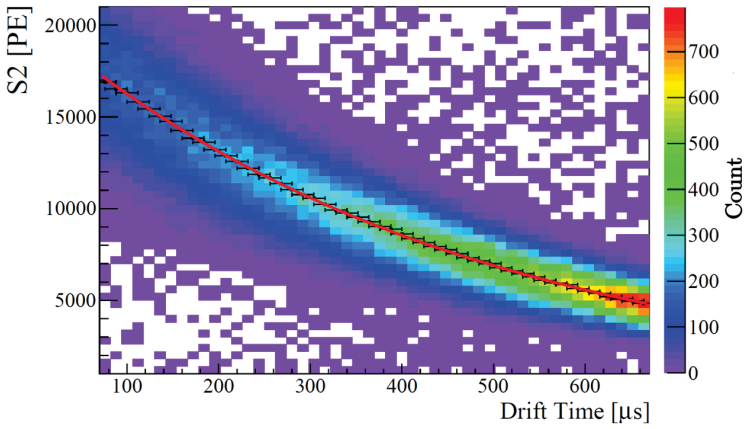

Figure 3.8: Electron lifetime fit of ^{83m}Kr calibration data shown in a density histogram. The decrease in S2 is caused by charge loss due to the attachment to electronegative impurities during the drift of the electron cloud. This example corresponds to an electron lifetime $\tau_e = (467 \pm 5)\,\mu$s, derived from the exponential fit (red line) to the median S2 values (black markers) of the drift time slices. From [84].

Trend over time The electron lifetime is a time-dependent variable, as the impurity level changes over time due to outgassing and constant purification. Even though in science run 1 (SR1) the electron lifetime is calculated from krypton calibration data (bi-weekly), for science run 0 (SR0) it was calculated from a daily fit to radon decays in the background data[6]. The advantage of using radon decays is that their activity is high enough to do daily electron lifetime measurements without losing time doing calibrations. The disadvantage is that due to the high energy (about 6 MeV) and interaction type (alpha interactions) of radon decays they are differently influenced by detector parameters than low energy ER backgrounds. Independent of the source, the electron lifetime measurements are used to fit the trend over time, and from this trend the day-by-day electron lifetime is used for the correction of search data[7].

3.4 Data quality cuts

Now that the S1 and S2 signals have been corrected for spatial- and time-dependent effects, one can start to select those events that can be used for analysis. Data quality cuts have the goal to select a specific set of

[6] Radon decays will be presented in chapter 4.
[7] The electron lifetime changed from about 400 to 500 μs during SR0.

events (e.g., an energy range or a region in the TPC), while at the same time rejecting events that don't fall into a specific quality standard (e.g., incomplete energy reconstruction, overlapping waveforms or position reconstruction problems). As the list of cuts is specific for each analysis goal, we will focus here on the set of cuts that are used for understanding the low energy background of XENON1T. These cuts will be used in the analysis of the first dark matter search results for XENON1T [3], which will be presented in the chapter 5.

3.4.1 List of SR0 cuts

Set	Cut name	Main goal	Acceptance
I	S1 Low Energy Range	S1 energy range	-
	S2 Threshold	S2 energy range	1.0
	Interaction Peak Biggest	Get main event	0.997
II	S1 Single Scatter	Reject double scatters	0.999*
	S2 Single Scatter		0.959
III	S1 Area Fraction Top	Select events in TPC	0.999
	S2 Area Fraction Top		0.998
	S2 Width		0.991*
IV	S1 Pattern Likelihood	Reject wrong S1-S2 pairs	0.999*
	S2 Pattern Likelihood		0.954
	S1 Max PMT	Reject afterpulses	0.999*
V	DAQ Veto	Reject partial waveforms	1.0
	S2 Tails	Reject single electrons	0.96
	Single Electron S2s		0.999
	Pre S2 Junk		0.999
VI	Fiducial Cylinder 1T	Reject external backgrounds	0.52

Table 3.1: List of the 16 cuts used for the SR0 WIMP search of XENON1T. The main goal of each cut is stated next to the cut name. The cuts are grouped into five sets, for each set a more detailed explanation of the cut is given in the text. For every cut the acceptance is given, this represents the percentage of signal-like events that will remain after this cut is applied. All the cut definitions can be found in appendix A. *These acceptances are given for a WIMP spectrum with a WIMP mass of 50 GeV.

I. Energy range and interaction cuts The *S1 Low Energy Range* ('$0 <$ cS1 < 200 [PE]') cut selects the energy region in which dark matter signals are expected. The *S2 threshold* ('$200 < S2$ [PE]') cut ensures a 100% trigger efficiency to detect the S2 signal. It does not use an upper

limit on the S2 area, as that is given by the upper limit of the S1 range. The *Interaction Peak Biggest* cut ensures we select the main interaction; i.e., match of the biggest S1 and S2 peak together[8].

II. Single scatter cuts For WIMP interactions in LXe, with cross sections below about $10^{-46}\,\mathrm{cm}^2$, one expects to see only single scatter interactions. Background signals, such as from neutrons, are able to double scatter (two distinct S2 signals for one S1 signal) in the detector. The S1 and S2 *Single Scatter* cuts use the area of the second largest S1 and S2, respectively, to reject double scatter events. The *S2 single scatter* cut is energy-dependent as the number of single electrons from photoionization, which mimic an S2 if they are piled up on top of each other, is depended on the amount of light from the S2.

III. Area Fraction Top and width cuts These cuts are designed to remove a whole set of different backgrounds: Accidental Coincidences of S1 and S2 signals, double-scatters, events below the cathode, mis-matched S1s and S2s, events with unphysical hit-patterns and gas events[9]. The Area Fraction Top (AFT) of a signal is defined as the relative amount of light measured in the top array compared to the total amount of light measured in the top plus bottom array. For S2s, that are produced at the gas-liquid interface, this is a well-defined and narrow distribution. The basis for the S1 AFT cut is that the number of photons observed in the top array is in principle a binomial distribution[10]. We compare if the measured S1 AFT value agrees with the expected one from the depth of the interaction. Using the LCE maps, one tests if the chance of the distribution of photons falls within a p-value of 1×10^{-4}. Finally, the *S2 Width* cut compares the width of the S2 signal, to the expected width for an S2 signal of the given depth and energy. The model is based on the diffusion model of the electron cloud drifting in LXe.

IV. Position reconstruction cuts These cuts are designed to reject double scatters or mismatched S1-S2 pairs. The *S1 Pattern Likelihood* cut compares the S1 hit-pattern with the expected hit-pattern from simulation. The simulated hit-pattern is built on the S1 LCE map by using the reconstructed (x,y) position from the S2. It can reject accidental coincidences, such as mismatched S1-S2 pairs from lone S1 and S2 signals being accidentally paired into one event. The *S2 Pattern Likelihood* cut is

[8] As causality is expected in the data processor, it is possible that it selects an S2 after the biggest S1 that is not the biggest S2 in the waveform.

[9] Gas events interact in the gas region of the TPC.

[10] Which we approximate with a Poisson.

designed to reject double scatters on the basis of their hit-pattern. Specifically rejecting double scatters that are not separated in time, but only in space. Hit-patterns, for which the position reconstruction algorithm finds two local minima, are rejected by this cut. The *S1 Max PMT* cut rejects accidental coincidences by comparing the area measured in the PMT that saw the most light, to the total area of the S1 signal. PMT problems, such as spontaneous light emission or afterpulses combined with a single electron S2s could otherwise be counted as real signals.

V. DAQ and single electron cuts These cuts are defined to reduce known background sources. The *DAQ Veto* cut rejects events where parts of the data in the waveform are lost due to e.g., a busy signal of the digitizers or due to an high-energy veto signal during the event. The *S2 Tail* cut is designed to reject events in the tail of a very big S2. The production of single electrons, due to photoionization on LXe impurities or metal surfaces by big S2 (or S1) signals, can lead to misidentification of S1-S2 pairs. For S2s signals above 1×10^6 PE (from, e.g., MeV γ-rays), these single electron tails last $\mathcal{O}$(ms). Another cut designed to handle the single electrons is the *Single Electron S2* cut. It is designed to remove events where the S1 signal actually is (or is part of) a misidentified single electron S2 signal. It combines the information of the rise time and the AFT of the signal to reject S1 signals that should have been identified as single electron S2 signals. Finally, the *Pre S2 Junk* cut rejects events where too many single electron S2 signals are found within a single waveform before the main S2 signal.

VI. Fiducial Cylinder 1T The last cut is the *Fiducial Cylinder 1T* selection. This is the selection of events by requiring $r < 36.94\,\text{cm}$ and $-92.9 < z < -9\,\text{cm}$. The two main goals of this selection are: firstly, select the center region where only the low internal backgrounds are present and thus discard the edges in which most background events interact[11]. Secondly, to discard events that interact close to the edges and thus lack full light or charge collection. The shape and size determination of the fiducial volume will be presented in chapter 5.

3.4.2 Total selection efficiency

For every cut that is applied on dark matter search data to reduce backgrounds, some percentage of signal events will also be removed. This cut acceptance has to be estimated to determine the sensitivity of XENON1T

[11] As the chance of a WIMP interaction is uniform over the whole target volume, this improves the signal/background event ratio.

to WIMP signals. To calculate the acceptance of a cut, one ideally uses a set of signal-like events, either from simulation or calibration data. The advantage of simulation data is that we know *a priori* if the cut should or should not remove the event. The disadvantage is that we cannot incorporate all possible (known) detector effects and backgrounds in the simulation. For this reason we also use calibration data. We will not discuss every cut in detail here, but limit ourselves to three examples of the methods used to calculate the acceptance. The three different ways we calculate the acceptance of a cut are:

- testing it on calibration data from either ^{220}Rn or ^{241}AmBe [12];
- using a data-driven model; and
- testing it on MC simulations.

Acceptance from calibration data The *S2 Area Fraction Top* cut acceptance is calculated with an 'N-1 method' using ^{220}Rn calibration data. This method assumes that a good set of cuts should result in a clean data sample of (physical) signal-like events. One then calculates the cut acceptance by applying the *S2 Area Fraction Top* cut last and count how many events failed and passed. Figure 3.9 shows the *S2 Area Fraction Top* cut boundaries on ^{220}Rn data with all other cuts applied first.

As the S2 is created in the gas-liquid interface, the S2 AFT values should have a distribution centered around the mean S2 AFT value. The spread of the S2 AFT value is influenced by statistical fluctuations, which in turn depends on the size of the S2. This behaviour is observed as the S2 AFT band becomes narrower for larger S2 signals. A source of events that this cut removes are gas interactions, which are expected to have S2 AFT values of about 0.7 and higher. The boundaries of the *S2 Area Fraction Top* cut removes three events (red markers). The acceptance is the ratio of the number of events that fail divided by the number of events that pass, resulting here in a cut acceptance of 0.998 for the *S2 Area Fraction Top* cut. The downside of the N-1 method is that one has to assume no cuts are correlated, and that the final sample holds only signal-like events.

Data-driven acceptance An example of the second method is the acceptance calculation of the *S2 Tails* cut. Large S2 signals can produce long trains of single electrons (SE) by photoionization on metal surfaces in the TPC. Such S2 tails can extend from microseconds (for small S2s)

[12] When possible, all cuts are tested both on ^{220}Rn and ^{241}AmBe data as a cross check.

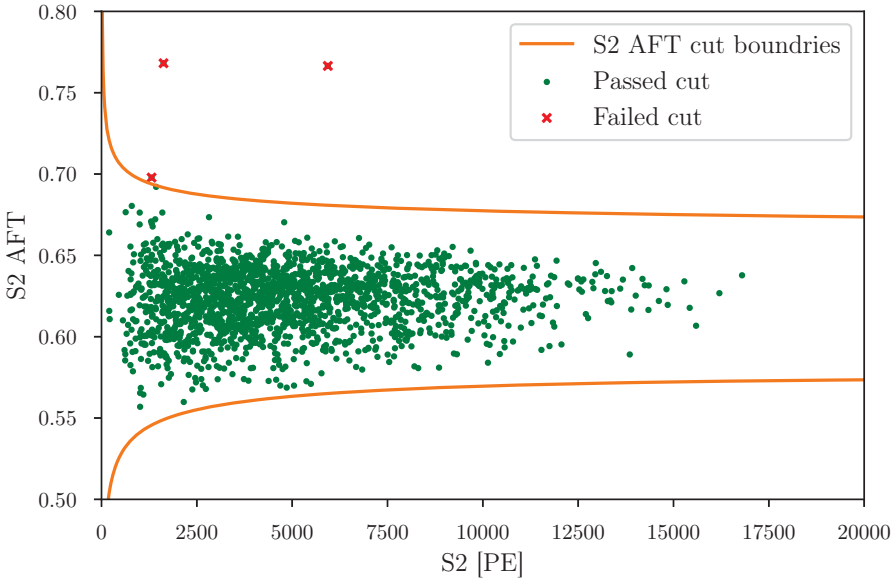

Figure 3.9: Events from ^{220}Rn calibration data that pass (green markers) and fail (red markers) the S2 Area Fraction Top (AFT) cut. All other SR0 cuts have been applied first. The acceptance is determined by the number of events that failed divided by the number of events passed, which here results in an acceptance of 0.998 for the S2 AFT cut.

up to a few seconds (for S2 signals from muons tracks). The most common SE tails are from S2s above 100,000 PE and last $\mathcal{O}$(ms). To minimize the risk of accepting events where either the S1 or S2 signal are created from pileup of SEs, we cut events within an S2-dependent time period after all S2 signals. The S2-dependent time period being cut is defined by: $S2\,[PE]/t_{\text{diff}}\,[ns] = 0.4$, with t_{diff} the time period after the S2 signal being vetoed. To calculate the acceptance we scan all S2s of the search data and calculate the total vetoed time period. This results in a live-time reduction of 4%. The cut acceptance of the *S2 Tails* cut is thus 96%.

Acceptance from MC simulation The acceptance of the *S1 Low Energy Range* cut is calculated using MC data. This cut includes the S1 detection efficiency, which cannot be calculated on real data, as one does not know *a priori* how many real S1 signals were not detected. A waveform simulator is used to produce S1 signals with low counts of photons (0-20 PE) and feed these into the data processor, which has the 3 PMT coincidence requirement. For three photons the detection efficiency is around

0.4 and reaches 1 at around 10 photons. As we define the acceptance after detection, we do not quote an acceptance for this cut, but show the found detection curve (blue) in figure 3.11. This figure is further discussed at the end of this section, after we present the total cut acceptance.

Energy dependent acceptances For all but four cuts we assume a flat acceptance in the WIMP search energy region. The *S1 Max PMT*, *S1 Single Scatter*, *S1 Pattern Likelihood* and *S2 width* have energy dependent acceptances. As the WIMP spectrum is mass dependent, so is the total cut acceptance value. Therefore the total cut acceptance is calculated as a function of cS1, and used by the limit code to calculate the WIMP sensitivity for every mass. Figure 3.10 shows the WIMP spectrum for a WIMP mass of 50 GeV/c^2 in cS1 vs cS2. On the right y-axis the acceptances are shown for the *S1 Max PMT*, *S1 Single Scatter* and *S1 Pattern Likelihood* cuts. The acceptances for these four cuts in table 3.1 are calculated on this specific WIMP mass.

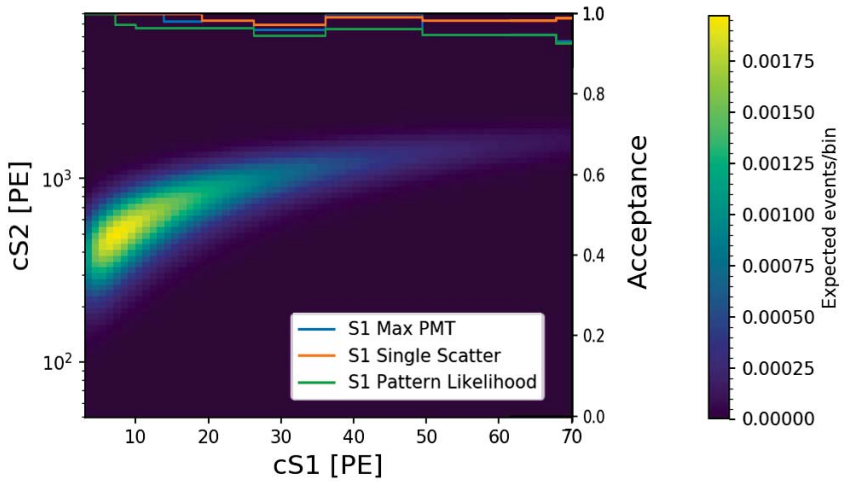

Figure 3.10: Simulated WIMP spectrum for a WIMP mass of 50 GeV with energy dependent cut acceptances for the *S1 Max PMT* (blue), *S1 Single Scatter* (orange) and *S1 Pattern Likelihood* (green cuts). The (normalized) WIMP probability density is represented by the color scale.

Total detection efficiency Figure 3.11 shows the total efficiency for SR0 of XENON1T. The total efficiency is a combination of the detection efficiency, cut acceptance ('Selection') and energy range selection ('Search region'). The detection efficiency is mainly dominated by the coincidence requirement of 3 PMT signals. When including the cut acceptance this leads to a total efficiency of about 89% for energy depositions above a few keV. Finally, the energy range selection (3 - 70 PE in cS1), used for the dark matter search analysis, is applied leading to the solid black line with the total uncertainty in grey. Thus below a few keV the loss mostly comes from the detection threshold, while at 20 keV the loss (about 11%) is fully due to the cuts.

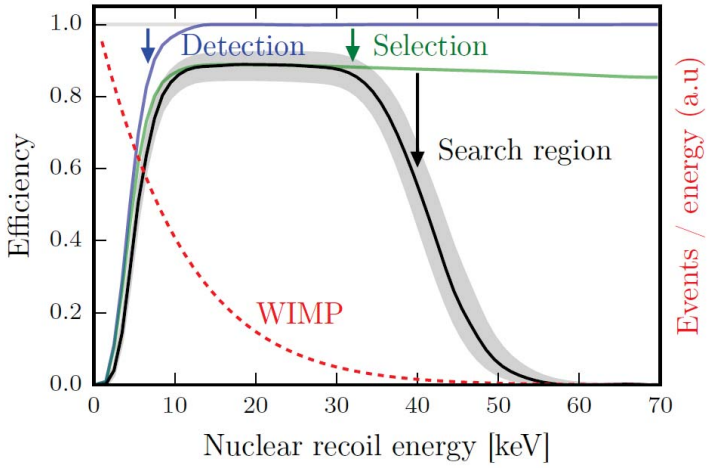

Figure 3.11: Total efficiency (black curve) for SR0 including detection efficiency (blue curve), cut acceptance ('Selection', green curve) and energy range ('Search region') selection. The uncertainty on the total NR detection efficiency is shown in grey. The search region shown here is for a dark matter search with an applied energy range of $3 < \text{cS1} < 70$ PE. For comparison the NR energy spectrum of a 50 GeV WIMP is shown (red dashed). From [99].

3.5 Energy reconstruction

Once we have the signal corrections in place and apply the cuts, we are able to make an energy spectrum of calibration data peaks. As the energy of these peaks is known, one can calculate the (energy dependent) light and charge yields. The *light yield* (LY) (given in in PE/keV) is the amount of light measured in cS1 for a given energy deposition. The *charge yield* (CY) (also given in PE/keV) is the amount of light measured in cS2 for a given energy deposition. From these values we can reconstruct the *primary scintillation yield* g_1[13] and *secondary scintillation gain* g_2[14]. The g_1 and g_2 are then used to convert cS1 and cS2 values (in PE) to a deposited energy (in keV)[15]. The width of the calibration data peaks is a measure of the energy-dependent energy resolution of XENON1T. Several different mono-energetic calibration peaks are used from internal beta and external gamma calibration sources, radioactive decays in the materials of the TPC and activated xenon lines due to neutron calibration.

3.5.1 Light and charge yield

Figure 3.12 shows the combined energy spectrum for background data in XENON1T. It shows several distinct peaks, which are used for energy calibration. As not all cuts were designed to work up to all energies, only a subset of cuts (*Fiducial Volume*, *S1 Single Scatter*, *S2 Single Scatter* and *S2 Area Fraction Top*) is used here. The x-axis shows deposited energy, where the cS1, cS2 signals are converted into a Combined Energy Scale, which will be presented in the next section.

The following peaks are identified (sorted from low to high energy):

- The 41.5 keV peak is the combined signal from the 9.4 keV and 32.1 keV decays from ^{83m}Kr [16]. This population is not from calibration data, but from a ^{83}Rb contamination in our piping system. As it does not affect our dark matter search region, it is now used as a permanent calibration source.

- The 163.9 keV peak is from the ^{131m}Xe activation line. The short-lived ^{131m}Xe isotope is produced during neutron calibration by thermal neutron activation and has a half-life of 11.8 d.

[13] Also known as the photon detection efficiency, even though it is only appropriate for the S1 signal.

[14] This is the photon multiplication value per electron for the S2 signal.

[15] Also known as the combined energy scale.

[16] As double scatters are rejected by cuts, only the events where both the two S1 and the two S2 signals overlap are kept.

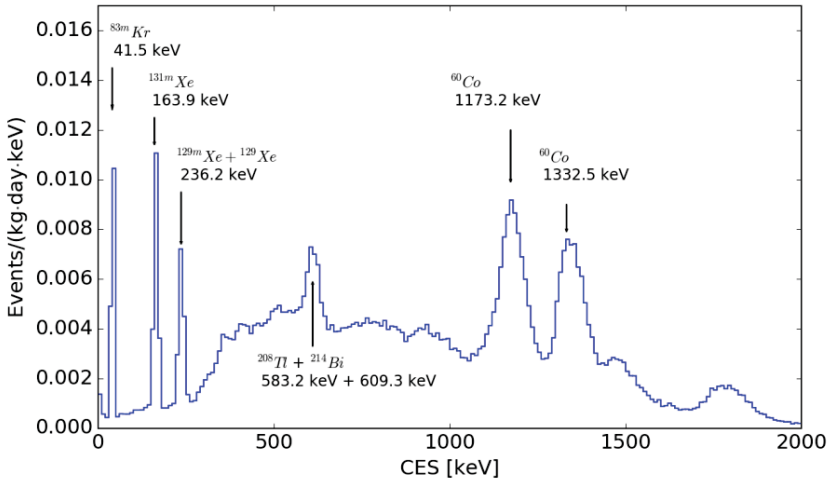

Figure 3.12: Combined Energy Spectrum (CES) from background data. The six named peaks originate from calibration sources, activated xenon lines and TPC materials. With the exception of the $^{214}\mathrm{Bi} + ^{208}\mathrm{Tl}$ peak, these peaks are used to determine the light and charge yield, and the energy resolution. From [107].

- The 263.2 keV peak is also an activated xenon peak, this time from $^{129\mathrm{m}}$Xe, which has a half life of 8.9 d [17].

- At around 600 keV a combined peak is visible originating from the primordial uranium (^{214}Bi at 609 keV) and thorium (^{208}Tl at 583 keV) decay chains, which originate from the materials of the TPC and cryostat. As they are not clearly separated, they are not used for the combined energy spectrum.

- At 1173.2 keV and 1332.5 keV the two peaks from ^{60}Co emerge. These also originate from materials, such as from the cryostat shells, the PMTs with bases, the cryostat flanges and the PTFE walls.

Starting with equation 2.9, we can now define a combined energy scale[18], which translates the measured cS1 and cS2 signals into deposited energy, as:

$$E_0 = W(n_\gamma + n_{e^-}) = W\left(\frac{cS1}{g_1} + \frac{cS2}{g_2}\right), \tag{3.2}$$

[17] This is actually a combined signal from the 196.6 keV gamma from $^{129\mathrm{m}}$Xe $\rightarrow$ ^{129}Xe* and the 39.6 keV gamma from ^{129}Xe$^* \rightarrow$ ^{129}Xe.

[18] As these are electronic recoil signals, we can ignore the NR quenching factor L.

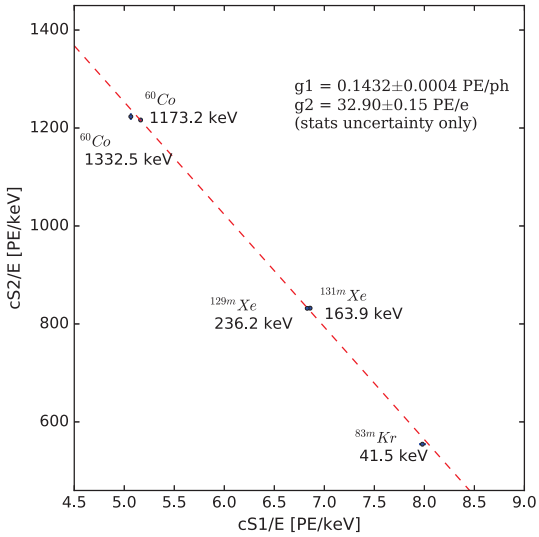

Figure 3.13: 'Doke plot' with measured light vs charge yield of the peaks identified in figure 3.12. The primary scintillation gain (g_1) and secondary scintillation gain (g_2) are found by a linear fit (red dashed line). This show excellent linearity for keV - MeV sources in XENON1T. The found g_1 and g_2 values, used in the combined energy scale equation 3.2, are used to translate the measured cS1 and cS2 signals into deposited energy. From [107].

with g_1 the primary scintillation gain and g_2 the secondary scintillation gain. The LY is defined as the number of photo electrons measured in the cS1 signal per keV of deposited energy. The CY is defined as the number of photo electrons measured in the cS2 signal per keV of deposited energy. The LY and CY are energy-dependent as the ratio between the number of photons and electrons is energy-dependent. The g_1 and g_2 values are calculated by a linear fit of the LY (cS1/E) and CY (cS2/E) values for the different peaks from figure 3.12, as shown in figure 3.13.

The found $g_1 = (0.1432 \pm 0.0068)$ PE/ph shows that in XENON1T for every 100 deposited photons we detect on average about 14 photoelectrons[19]. The found $g_2 = 32.90 \pm 2.26$ PE/e shows that for a single electron reaching the amplification region about 33 photoelectrons are detected. The stated uncertainty in figure 3.13 only includes the statistical uncertainties of the fit, while the numbers given in the text include the systematic uncertainties. To estimate the systematic uncertainty of $g1$ and $g2$ the influence of different detector volumes, different cuts and dif-

[19]This includes double photo-electron emission on the PMT cathode of xenon VUV photons, which is about 15% [108].

ferent energy regions was investigated[20]. XENON1T thus has a linear energy scale from keV to MeV signals.

3.5.2 Energy resolution

With the fitted peaks in figure 3.12, one can now also calculate the energy-dependent energy resolution. The energy resolution is defined as σ_E/μ_E, where σ_E is the standard deviation of a 2D Gaussian fit to the peak in the cS1-cS2 space and μ_E is the mean deposited energy, see figure 3.14. The energy resolution of XENON1T is shown in figure 3.15.

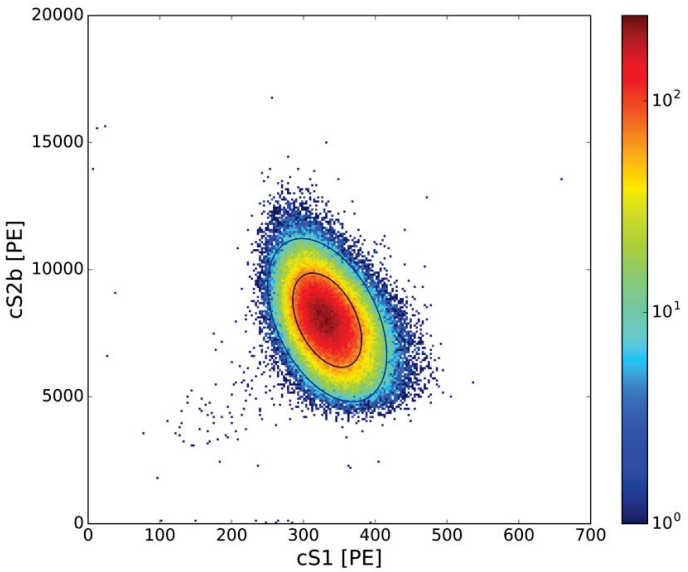

Figure 3.14: Primary scintillation signal (cS1) versus secondary scintillation signal in the bottom array (cS2b) for the 41.5 keV combined peak of ^{83m}Kr. The distribution is fit by a 2D Gaussian with found means of (333 ± 33) PE and (8010 ± 216) PE for cS1 and cS2, respectively. The number of events/bin is shown in color. From [109].

The energy resolution improves for higher energy depositions being due to more quanta being made in the liquid xenon and thus the statistical fluctuations become less prominent. A phenomenological fit function, $\frac{\sigma_E}{\mu_E} = \frac{a}{\sqrt{E(MeV)}} + b$, is chosen, which follows the behaviour of the energy-dependent energy resolution[21]. One reason for the ^{214}Bi + ^{208}Tl peak (at

[20] The systematic uncertainties are dominated by a depth dependence.
[21] The found values are $a = 26.3\text{MeV}^{1/2}$ and $b = 1.68$.

approximately 1.2 MeV) to be far off the empirical fit is that one expects a wider peak for a combined signal of different energies.

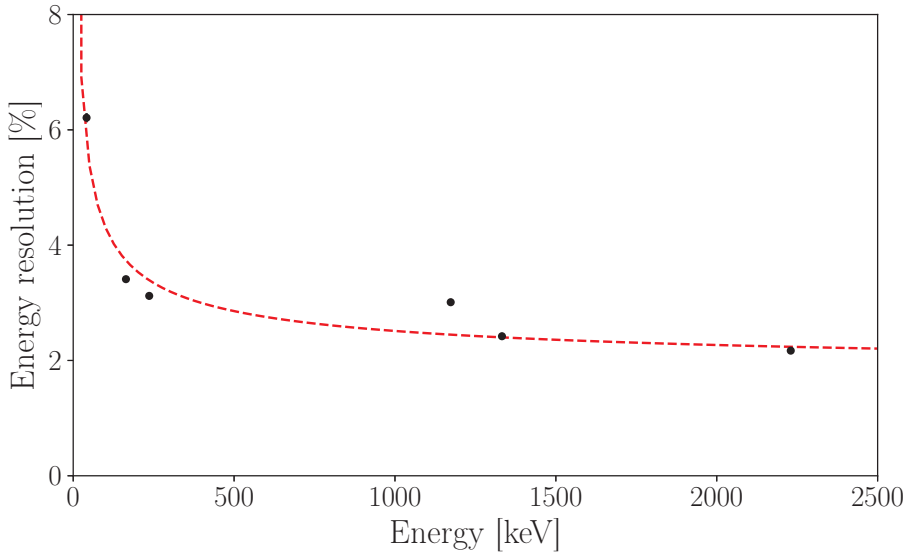

Figure 3.15: Energy resolution of the peaks found in figure 3.12 versus deposited energy. One extra high energy peak was added, the 2204.1 keV peak from ^{214}Bi. An empirical formula is fit to the data and follows the improving energy resolution for higher energies depositions. This is due to the increased number of quanta deposited in the liquid xenon, which decreases the relative statistical fluctuations, as shown in equation 3.2. The statistical uncertainties stay within the marker size. No sytematic uncertainties are shown, but are found to be $\mathcal{O}(0.1)\%$ in the SR1 analaysis. From [107]

3.6 Signal versus background discrimination

Finally everything is in place to discriminate between signal and background events in XENON1T. The discrimination space used is cS1 versus cS2, where nuclear recoils will have on average a lower cS2 value for the same cS1 value as electronic recoils[22]. To determine the discrimination efficiency from data, two different calibration sources are used. For the electronic recoil calibration the ^{220}Rn source is used, which is mixed into the liquid xenon[23]. The decay daughter of ^{220}Rn, ^{212}Pb is used as a low energy beta calibration source [89]. For the nuclear recoil calibration, the ^{241}AmBe source is deployed on the outside of the cryostat. The low energy neutrons interact with xenon nuclei to produce nuclear recoils, similar to the signals one expects from a WIMP interaction [88].

3.6.1 ER and NR band calibration

Figure 3.16a shows the events from the ^{220}Rn calibration data in the dark-matter search region of 3-70 PE in cS1 vs cS2. All cuts, as described in section 3.4, have been applied. Most events follow the expected correlation between cS1 and cS2 and thus form a narrow Electronic Recoil band (ER band), the deviations from the band come from statistical fluctuations and uncertainties in the signal corrections. The blue solid line shows the median of the ER band, while the blue dashed lines show the $\pm 2\sigma$ region, assuming a Gaussian distribution. The electronic recoil band has a flat spectrum and the events are therefore mostly homogeneously distributed in the ER band. Most events from background sources in the dark matter search data should cause electronic recoils and are thus expected to be distributed in a similar way.

Figure 3.16b shows the events from ^{241}AmBe calibration data in the same cS1-cS2 space. Again all SR0 cuts have been applied. This shows the nuclear recoil bands, which has on average a lower cS2 value for the same cS1 value. The solid red line is the fit of the median of the NR band distribution, while the red dashed lines are the $\pm 2\sigma$ regions. The higher density of events at lower cS1 values is due to the energy spectrum of the neutrons. A reason for seeing more events further away from the band than expected from a Gaussian distribution is caused by a small pollution of double scatter events after applying the single scatter cuts[24].

[22] See section 2.2.

[23] See section 2.3.3.

[24] Due to the low drift field and low e-life XENON1T is worse at rejecting double scatter events than expected.

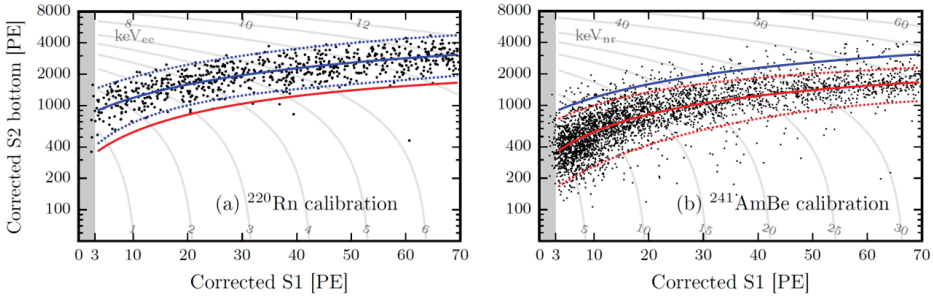

Figure 3.16: Observed event distribution in $cS2_b$ vs. cS1 for (a) ^{220}Rn ER calibration and (b) ^{241}AmBe NR calibration data. The mean (solid) and $\pm 2\sigma$ quantiles (dashed) are shown for both the ER band (blue) and NR band (red). To guide the eye the means of the ER and NR bands are shown in both figures. The shift in median cS2 value for the same cS1 value is used to distinguish between signal-like (NR) and background-like (ER) events. From [3].

ER discrimination For comparison, in both plots of figure 3.16 the median of the ER band (blue) and the median of the NR band (red) are shown. While there is a small neutron background, which is mostly indiscriminable from WIMPs (this will be presented in section 5.3), most of the background comes from ERs. From the position of the mean of the NR band it is clear that events above it in cS2 are also in the ER band and cannot easily be distinguished from ER background events. Events below the NR mean though, would be clearly distinguishable. From the calibration data it is now possible to calculate the ER discrimination. This we define as the percentage of ER (background like) events that are found above the NR mean in cS1-cS2 space. Using the NR mean gives per definition an NR (signal like) acceptance of 50%. The ER discrimination is calculated from calibration data after all the corrections and cuts have been applied. Table 3.2 shows for both SR0 and SR1 the calculated ER discrimination values, and for comparison the MC expectation value from [93].

Influence of the drift field strength The found SR0 ER discrimination of $(99.71 \pm 0.21)\%$ agrees with the expectation of the MC expectation. The uncertainty comes from low calibration statistics in SR0. For SR1 the calibration statistics were improved and the SR1 ER discrimination of $(99.82 \pm 0.05)\%$ shows we exceeded the MC expectation, even at a much lower drift field. This was an unexpected result, as the general consensus in the field is that the ER discrimination should improve with field strength.

	SR0	SR1	MC expectation
Cathode voltage [kV]	-12	-8	-100
E-field [V/cm]	116.7 ± 7.5	80.5 ± 2.2	~ 1000
ER discrimination [%]	99.71 ± 0.21	99.82 ± 0.05	99.5

Table 3.2: Measured ER discrimination at 50% NR acceptance for SR0 and SR1 [110] compared to the MC expectation [93]. For every science run the ER discrimination is calculated with the fraction of ^{220}Rn calibration events left in the range 3-70 PE in cS1, after cuts and being below the NR median in cS1-cS2 space. The quoted drift field strengths for SR0 and SR1 are derived from simulation for a 1 t and 1.3 t fiducial mass, respectively. Even at $\mathcal{O}(10)$ time lower field strength than designed for, the ER discrimination in XENON1T exceeds the expectation.

In table 3.2 the cathode voltages and drift field (in the FV from simulation) are shown for both science runs and the MC expetation. For lower drift fields many uncertainties in detector parameters get worse, which would lead to a broadening of the ER and NR bands. On the emission-physics side, broadening of the bands is also due to the photon yield and the recombination fluctuation being field dependent [111] [73].

One counter example of an actual one-to-one relation between field strength and ER discrimination comes from PandaX-II. They report for Run 10 a (99.47 ± 0.08)% ER discrimination (at 50% NR acceptance) with a drift field of 400 V/cm [112]. Dedicated ER discrimination measurements for different field strength are needed to give a final answer on this open question. But, looking back at the XENON1T, we can conclude that it exceeded the needed signal versus background discrimination, even though the achieved drift field strength fell a factor 10 short of its design value.

3.6.2 Light and charge depositions from electronic recoils

One other thing that we can now do is to compare the light and charge depositions from electronic recoils in XENON1T to simulation. Using equation 3.2 and the found g_1 and g_2 values we can convert the cS1 and cS2 values for known calibration peaks into deposited electrons and photons. For this purpose, we use the peaks found in section 3.5.1, and add two extra peaks at higher energy: 2204.1 keV from ^{214}Bi and 2614.5 keV from ^{208}Tl [25]. Figure 3.17 shows the measured light and charge yield in XENON1T versus deposited energy.

The photon yield and electron yield from data are compared to the expectation values from two different versions of NEST. The Noble El-

[25] Both are from materials.

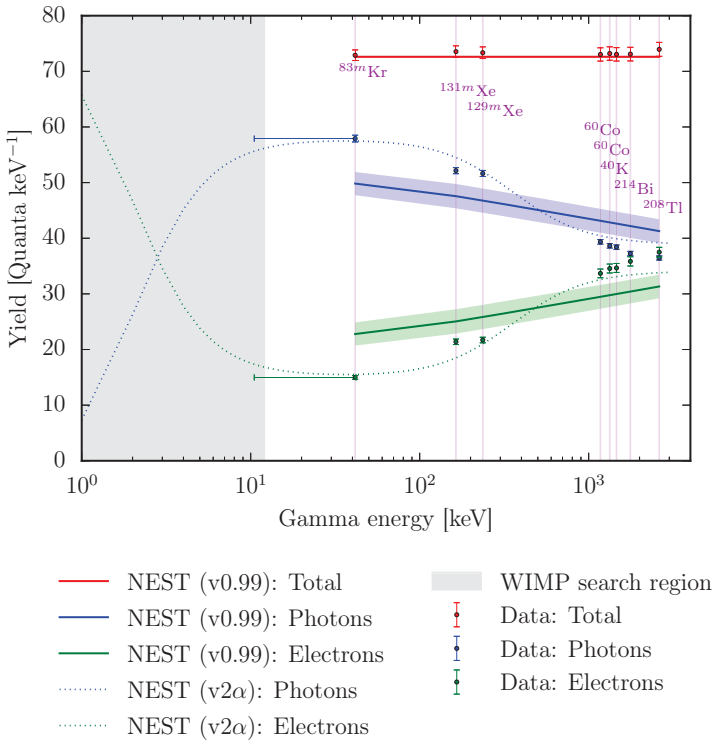

Figure 3.17: Light (blue) and charge (green) yield comparison between XENON1T data and NEST. The errorbars on the datapoints are from the systematic uncertainty of g_1 and g_2, which are an order of magnitude higher than the statistical uncertainty. The total yield for data (red markers) and NEST (red horizontal line) are shown, which agree within the errors. The older NEST (version 0.99) [96] does not agree with data, even within uncertainty (blue and green bands). The newer NEST v2α [113] (blue and green dotted lines) shows better agreement with data below 1.5 MeV. The grey band represents the energy region in which we expect WIMP signals. Other data points at lower energies are avalable from other experiments, but for clarity reasons not shown.

ement Simulation Technique (NEST) package is a comprehensive model for explaining scintillation yield in liquid xenon. It tries to unify various definitions of work functions found in literature and incorporate all available data from various liquid xenon experiments on the scintillation yield. The solid lines are from NEST version 0.99 with a xenon density of 2.863 g/cm^3 and a drift field of 80 V/cm. The bands show the total uncertainty on the NEST expectations by combining a 4% model uncertainty with a 10% uncertainty from an expected field strength variation. The first three

peaks (^{83m}Kr, ^{131m}Xe and ^{129m}Xe) are from internal sources and mostly measured in a homogeneous field in the center of the TPC. The last four peaks (^{60}Co, ^{214}Bi and ^{208}Tl) are from material sources and mostly measured close to the walls where field in-homogeneity could play a role (see figure 3.4a). The ^{83m}Kr value has a large energy uncertainty due to it being from a combined signal, as described in 3.3.1, and cannot as such be used as a mono-energetic peak.

In red the total number of quanta is shown for data and NEST. This agrees, within errors, with the expected value of (73 ± 1) quanta per keV, using a W value of (13.7 ± 0.2) eV/quanta. This shows all quanta in XENON1T can be reconstructed, even though the photon/electron ratio does not agree with NEST v0.99. Similar discrepancies in photon and charge yields between NEST and ER calibration data have already been shown in [94] and are thus not unexpected. NEST v2α shows a much better agreement with data. This version uses more and updated results from several ongoing experiments and is an improvement to NEST that is currently under construction [113]. The new NEST version shows great improvements at energies below about 1.5 MeV, but does not follow the trend at higher energies.

3.7 Summary and outlook

Krypton calibration data is used to identify and correct for the position- and time-dependent effects in the TPC. From the triggered events the main S1 and S2 signals are identified. The signals are corrected with an S1 light collection efficiency (LCE) correction map in (x,y,z), a time dependent S2 electron lifetime correction in (z) and an S2 LCE correction in (x,y). A field distortion, due to the low electric field configuration, was not expected, but a dedicated correction was found and is applied. After a total of 16 data quality and selection cuts, over 80% of events in our low energy region remain.

The energy calibration shows a high total photon detection efficiency of about 14%, which is in accordance with the designed high reflectivity of the walls, high transparency of the meshes and high QE of the PMTs. With all the parts in place, the shape and position of electronic-recoil and nuclear-recoil bands give a better-than-expected ER discrimination. Thus, at a 50% NR acceptance we can detect WIMP-like events in the TPC, while at the same time rejecting $(99.82 \pm 0.05)\%$ of all ER background events. The excellent performance of the XENON1T experiment enables us to discriminate between electronic (background) and nuclear (signal) recoils in the relevant energy region for WIMPs.

The next step, for a dark matter search, is to analyse the background levels. This will lead to a prediction of the expected number of background events for a given exposure. The determination of the electronic recoil background will be presented in the next chapter, followed by the XENON1T dark matter search results in the last chapter.

Chapter 4

Electronic Recoil Backgrounds in XENON1T

Nothing in life is to be feared. It is only to be understood.

— Marie Curie

Before we can make any statement on the WIMP-interaction sensitivity of XENON1T, we need to determine the background levels. Background interactions in XENON1T lead to either an electronic recoil (ER) or a nuclear recoil (NR). As the latter cannot be distinguished from a WIMP NR, even a few NR background events can greatly reduce the sensitivity of the experiment in detecting WIMPs. Backgrounds that induce NRs are neutrons and solar neutrinos undergoing Coherent Elastic Neutrino Nucleus Scattering (CEνNS). Together these backgrounds contribute to $\mathcal{O}(1)$ events in the relevant energy region of a dark matter search for a 1 tonne-year exposure. Background particles that induce ERs are: electrons, gammas and solar neutrinos. Due to their abundance, both from intrinsic and extrinsic sources, combined these sources contribute to $\mathcal{O}(1000)$ events. Fortunately, after 99.75% ER discrimination (as shown in section 3.6) this number is reduced to $\mathcal{O}(1)$ events in the relevant parameter space for WIMP NRs. In this chapter, we compare the background expectation from Monte Carlo simulation to the measured background rates in XENON1T data. We focus on the ER backgrounds as these are measured in background data before unblinding the signal region. The total low-energy ER background expectation is dominated by the radon daughter ^{214}Pb, we thus spend most time analysing the different isotopes of the radon decay chain.

4.1 Background expectations

4.1.1 Electronic recoil background expectation

Figure 4.1 shows the Monte Carlo (MC) energy spectrum of the total ER background rate (black) in a 1 t inner volume of LXe. The spectra were created with a full MC simulation of the XENON1T detector as described in [93]. An inner volume of 1 t LXe is chosen, to maximize the exposure and minimize the influence of the material background. Only single scatter events are selected, although a misidentified multiple scatter is not rejected if the interactions occur within 3 mm in the vertical direction. The resulting sum spectrum is dominated by radon below a few hundred keV (i.e., keV_{ee}[1]), while at higher energies it is mostly dominated by contributions from materials. No energy resolution smearing was applied. The individual contributions of the ER background components are shown in color. Before XENON1T started, we expected internal background concentrations in LXe of: 10 μBq/kg of ^{222}Rn, 0.2 ppt of ^{nat}Kr and from $2\nu2\beta$ of ^{136}Xe, which has 8.9% natural abundance. The other ER background contributions are from the TPC materials and solar neutrinos. We will now describe the five expected ER background sources.

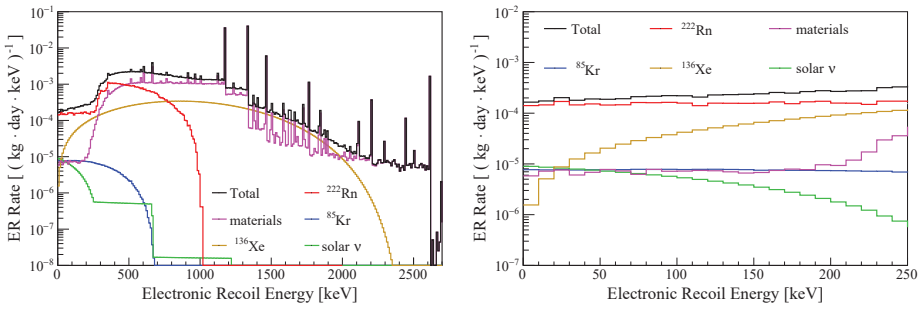

Figure 4.1: Simulated energy spectrum (black) of the total ER background rate in a 1 t fiducial volume for XENON1T, and the separate contributions from: detector components (purple), 10 μBq/kg of ^{222}Rn (red), 0.2 ppt of $^{\mathrm{nat}}$Kr (blue), solar neutrinos (green) and ^{136}Xe double-beta decay (yellow). The right plot details the spectrum at low energies. The background in the energy region for dark matter searches (1-12 keV) is dominated by the ^{222}Rn background. From [93].

^{222}Rn. The background from ^{222}Rn is due to its daughter isotope ^{214}Pb. ^{222}Rn emanates from all materials that are in contact with xenon, such as the TPC components and the purification and distillation sys-

[1]When writing 'keV' we mean electronic recoil equivalent energy keV_{ee}, only when 'kev_{nr}' is explicitly written we signify nuclear recoil equivalent energy.

tems. Due to its relative long half-life (3.8 days), ^{222}Rn distributes homogeneously throughout the LXe before decaying. The beta decay of ^{214}Pb will be discussed in much more detail in sections 4.1.3 and 4.5.1.

Materials. The material background is a combination of gamma rays from primordial and long-lived man-made radioactive isotopes such as: ^{238}U, ^{235}U, ^{226}Ra, ^{232}Th, ^{60}Co, ^{40}K, and ^{137}Cs. In order of total rate, the biggest contributions come from: the cryostat shells, the cryostat flanges, the PMTs and bases, and the PTFE and Cu in TPC. Due to the self-shielding of LXe, the rate of the material contribution in the central fiducial volume decreases by two orders of magnitude at energies below a few hundred keV.

^{136}Xe. Even though xenon itself has almost no long-lived radioactive isotopes, natural xenon contains 8.9% of ^{136}Xe, a two-neutrino double-beta emitter with a Q-value of 2458 keV. It is the only natural long-lived radioactive isotope of xenon and has a half-life of 2×10^{21} years [114].

^{85}Kr. Radioactive ^{85}Kr is released into the air by nuclear fuel plants and nuclear weapon tests. The xenon extracted from the atmosphere has a typical $^{\text{nat}}$Kr/Xe concentration at the parts per million (ppm) level. Natural krypton contains traces of ^{85}Kr, which is a beta-emitter with a half-life of 10.76 years and an endpoint energy of 687 keV. As described in section 2.4.2, the $^{\text{nat}}$Kr/Xe is reduced to the ppt level by cryogenic distillation.

Solar neutrinos. Neutrinos, originating from the sun, scatter elastically off the electrons in the LXe, producing low energy depositions. The distinct stepwise spectrum is due to the energy spectrum of solar neutrinos [9]. Most (92%) of the solar neutrino scatters are from *pp* fusion in the Sun, 7% are from ^{7}Be, while the other sources contribute less than 1%. This background cannot be reduced and scales linearly with exposure.

To make a prediction of the backgrounds for a dark matter search, table 4.1 shows the ER background rates calculated for a 1 t fiducial volume and (1,12) keV energy range. A total background rate of $(1.80 \pm 0.15) \times 10^{-4}$ events$(\text{kg} \cdot \text{day} \cdot \text{keV})^{-1}$ is predicted, which would be the lowest background ever achieved in a direct dark matter detection experiment. For one year of background data, this results in a total of 720 ± 60 expected ER background events. With radon contributing to 85% of the total background, it is clear why we will focus on this specific background source. The next step is to find out how big the predicted influence of the ER background is on a dark matter search in XENON1T.

Source	Background $[(\mathrm{kg}\cdot\mathrm{day}\cdot\mathrm{keV})^{-1}]$	Background $[\mathrm{y}^{-1}]$	Fraction [%]
Materials	$(7.3 \pm 0.7) \times 10^{-6}$	30 ± 3	4.1
^{222}Rn	$(1.54 \pm 0.15) \times 10^{-4}$	620 ± 60	85.4
^{85}Kr	$(7.7 \pm 1.5) \times 10^{-6}$	31 ± 6	4.3
^{136}Xe	$(2.3 \pm 0.3) \times 10^{-6}$	9 ± 1	1.4
Solar neutrinos	$(8.9 \pm 0.2) \times 10^{-6}$	36 ± 1	4.9
Total	$\mathbf{(1.80 \pm 0.15) \cdot 10^{-4}}$	$\mathbf{720 \pm 60}$	**100**

Table 4.1: Predicted ER background rates in a 1 t fiducial volume and (1,12) keV energy range. Concentrations of 10 μBq/kg of ^{222}Rn, 0.2 ppt of ^{nat}Kr and the natural abundance of ^{136}Xe are assumed. This leads to a total of 720 background events for a 1 tonne-year of dark matter exposure, but after ER discrimination only 1.6 events are left in the signal region. The ^{222}Rn background clearly dominates over all other backgrounds. From [93].

4.1.2 Expected impact on dark matter searches

After determining the full energy spectrum, we can now calculate how many events from background sources are expected in the dark matter search region for a given exposure of 2 t·y. This is shown in table 4.2.

Expectation values of events in XENON1T, in 2 t·y exposure		
	No discrimination	99.75% ER discrimination
Signal		
10 GeV/c^2 WIMP ($\sigma = 2 \cdot 10^{-46}$ cm^2)	4.65	1.86
Background		
Total ER	1300	3.25
NR from neutrons	1.10	0.44
NR from CEvNS	1.18	0.47
Total NR	2.28	0.91

Table 4.2: Number of expected signal and background events in XENON1T before and after 99.75% ER discrimination (at 40% NR acceptance) in 1 t fiducial volume and 2 years of measurement. The energy range is (1,12) keV, corresponding to an expected cS1 range of (3,70) PE. From [93].

Assuming an ER rejection power of 99.75% at 40% WIMP acceptance, this results in 3.25 expected ER background events. For NR backgrounds from neutrons and Coherent Elastic Neutrino Nucleus Scattering (CEνNS)

of solar neutrinos a total of 0.91 NR background events are expected in the same energy range and fiducial volume [93]. Assuming instead one year of dark matter data with 1 t of LXe, this leads to a total expected background rate of about 2 events, comparable to the expectation of about 1 WIMP scatter, assuming a WIMP mass of 10 GeV/c^2 and cross section of 2 $\times 10^{-46}$ cm^2. To achieve the design sensitivity, it is thus vital to stay below the above-mentioned background levels and reach the quoted ER discrimination.

4.1.3 The origin of the radon background

Radon belongs to the group of noble gasses and is the only one that does not have any stable isotopes [2]. It is chemically inert and in room conditions gaseous. Radon (^{222}Rn) and 'thoron' (^{220}Rn) originate from the alpha decay of the long-lived ^{226}Ra and ^{228}Th isotopes, respectively. ^{226}Ra is part of the primordial ^{238}U chain, while ^{228}Th comes from the primordial ^{232}Th chain. Trace amounts of ^{238}U and ^{228}Th are present in all materials, making radon a persistent background in all low-background counting experiments.

When ^{226}Ra undergoes alpha decay on the surface of any detector construction material, the recoil due to the alpha emission can repel the ^{222}Rn nucleus into the (liquid or gaseous) xenon. Due to the relatively long half-life of ^{222}Rn (3.8 d), it mixes homogeneously throughout the whole LXe volume of the TPC before decaying. In contrast to radon, its daughters belong to the group of metals, and adhere more easily to surfaces. One of the ^{222}Rn daughters, ^{214}Pb, undergoes beta decay and is the dominant background for low energy dark matter searches. The other present radon isotope, ^{220}Rn, has a relatively short half-life (55.6 s). Since it disintegrates shortly after being produced, the probability of thoron daughters sticking on the surface of the materials is higher. For ^{220}Rn it is the decay daughter ^{212}Pb, which gives low energy beta decays. Both the decay chains of ^{222}Rn and ^{220}Rn are shown in figure 4.2.

The radon decay chain starts with two alpha decays (^{222}Rn and ^{218}Po) close together in both time and energy. This is followed by the beta decay of ^{214}Pb with a maximum beta energy of 1019 keV. In 9.2% of the cases, ^{214}Pb decays to the ground state without emitting any additional gamma rays. This so-called *naked beta decay* is the problematic low energy single scatter. Even though its endpoint energy is far above the few-keV range of a dark matter search, the continuity of the spectrum down to zero kinetic energy does overlap with the dark matter search region. This will described in section 4.5.1. The following two daughter isotopes in the

[2] Apart from the artificially produced noble element Oganesson ($^{294}_{118}$Og).

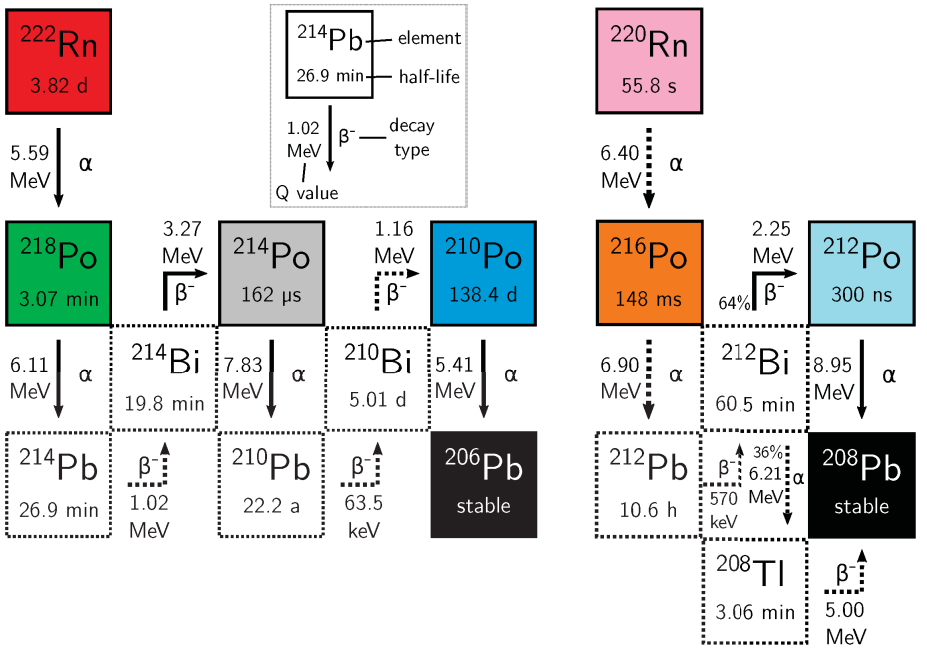

Figure 4.2: Illustration of the ^{222}Rn (radon) and ^{220}Rn (thoron) decay chains (ignoring isotopes with a branching ratio $< 0.1\%$). The solid boxes indicate the isotopes that are quantified in this chapter, the colors are used throughout this chapter to identify the specific isotopes. All half-lifes, branching ratios and Q values are taken from [115]. Adapted from [116].

chain (^{214}Bi and ^{214}Po) decay so quickly after each other that the beta decay of ^{214}Bi can always be tagged by the alpha decay of ^{214}Po within the same event time window. Therefore it is no background source in the WIMP search energy region as it is cut by the single scatter cuts. Up to ^{210}Pb all isotopes in this chain are in secular equilibrium within the LXe[3]. Due to the relatively long half-life of ^{210}Pb (22.2 years), this equilibrium is broken at this point. We still will find ^{210}Po in XENON1T, but not due to the release of ^{222}Rn during the running of the experiment, but from the deposition of radon progeny during the manufacturing of the materials. The isotopes depicted with a solid box in figure 4.2 are quantified in this chapter, while the rate of others will be inferred from these. The colors given here to the isotopes will be used consequently in most figures to help identify the specific isotope.

The thoron (^{220}Rn) decay chain starts again with two alpha decays, both close in time and energy. This is followed by the beta decay of ^{212}Pb.

[3]In secular equilibrium, the quantity of the radioactive isotope stays constant due to the production rate being equal to the decay rate.

^{212}Pb decays to the ground state without emitting additional gammas with a branching ratio of 13% and an endpoint energy of 570 keV. This isotope is used in XENON1T as a calibration source to determine the low energy response because it is so similar to the main background of ^{214}Pb beta decays. Next comes ^{212}Bi which can decay into ^{212}Po and has a similar topology as the ^{214}Bi-^{214}Po decays in the ^{222}Rn chain. 36% of ^{212}Bi decays with an alpha decay energy of 6.21 MeV to ^{208}Tl. This decay will unfortunately not be distinguishable in energy from the ^{218}Po decay. With the knowledge of both decay chains we can identify the different alpha decays, with the end goal of determining the influence of ^{214}Pb and ^{212}Pb as low energy backgrounds.

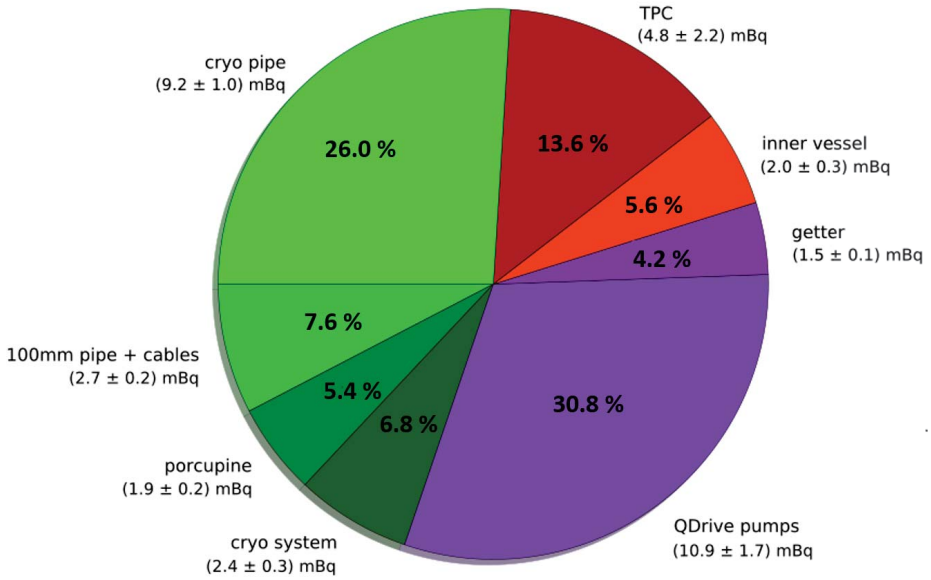

Figure 4.3: Radon emanation measurements for the different detector components in XENON1T. The biggest contribution (44%) comes from the cryogenic system which includes the piping towards the TPC and all PMT cabling. The second largest contribution is from the purification system (39%) due to the QDrive pumps. The TPC itself is only responsible for 17% of the radon emanation. The total adds up to about 37 mBq, which leads to a total expected ^{222}Rn concentration of about 11±2 μBq per kg of LXe. Adapted from [117].

To estimate the ^{222}Rn emanation from material surfaces in XENON1T, dedicated ^{222}Rn emanation measurements were done after construction, but before commissioning. Depending on the size of the detector component, different techniques were used to extract a sample emanation gas into a canister filled with a radon-free carrier gas. The radon concentration was determined using miniaturized proportional counters [118]. The

results of these emanation measurements for XENON1T are shown in figure 4.3. Of the total activity measurement of (35.4 ± 6.0) mBq of ^{222}Rn, about 44% comes from the cryogenics (green), about 39% comes from the purification (purple) and only about 17% comes from the TPC and cryostat (red). On the total LXe amount of 3200 kg in the system, this leads to an expectation of $(11 \pm 2)\,\mu$Bq/kg of ^{222}Rn in XENON1T[4]. This first ^{222}Rn measurement is in agreement with the required ^{222}Rn background level of about $10\,\mu$Bq/kg stated in section 4.1.1.

[4] Assuming there is no radon originating from the LXe itself.

4.2 Alpha spectroscopy

4.2.1 Data selection and method

Only background data is selected for this radon analysis as it is not contaminated with high-energy events from calibration sources. The two available periods of data used are:

- Science run 0 (SR0), consisting of 37.4 live days of data taken between November 22, 2016 and January 18, 2017; and
- Science run 1 (SR1), consisting of 273.3 live days of data taken between February 2, 2017 and February 8, 2018.

The main difference in operation conditions between SR0 and SR1 is the electric field in the drift region, $(116.7 \pm 7.5)\,\mathrm{V/cm}$ and $(80.5 \pm 2.2)\,\mathrm{V/cm}$ [119], respectively. SR0 is used to define the analysis methods, they are then applied to SR1 for comparison.

To estimate the number of low energy electronic recoil events from ^{214}Pb, two different methods are available. The first method is to count the number of alpha decays from the isotopes in the decay chain that directly precede (^{222}Rn and ^{218}Po) and follow (^{214}BiPo) the decay of ^{214}Pb. The concentrations of ^{218}Po and ^{214}BiPo thus give the upper and lower limit, respectively, on the concentration of ^{214}Pb. An advantage of this first method is that all three, above-mentioned, isotopes decay by means of emitting an alpha particle. Due to their high energy deposition of $\mathcal{O}$(MeV) they can be identified with an almost background-free analysis. The disadvantage of this method is that the upper and lower limits will leave a big uncertainty on the concentration of ^{214}Pb. The second method directly fits the concentration of ^{214}Pb to the full low-energy electronic-recoil background spectrum. This method will be presented in section 4.5.2. Matching the spectrum can give a smaller uncertainty, but requires a lot more knowledge of the other contributions.

First alpha selection To start with a sample of alpha events we apply two selections: a fiducial volume and an energy range (no other cuts are applied). The fiducial volume is bound by $-58.45 > z > -38.45$ cm and $r < 30\,\mathrm{cm}$, this insures no light- or charge-loss from regions such as the wall, the cathode and the gate are included. The energy range we select is $3 \times 10^5 < cS1 < 8 \times 10^5\,\mathrm{PE}$ and $0 < cS2 < 2 \times 10^5\,\mathrm{PE}$, which is the relevant energy range for alpha signals in S1 and S2. The last requirement is that every event must include at least one S1 and one S2 peak. The result of this primary selection is shown in figure 4.4.

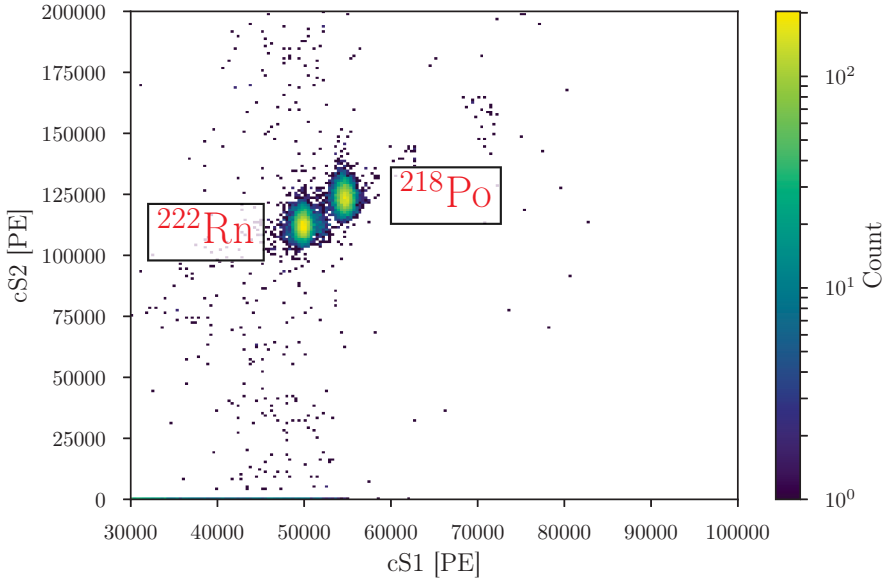

Figure 4.4: Combined distribution of corrected secondary (cS2) vs. primary (cS1) scintillation light for alpha signals. No data quality cuts have been applied, but only a fiducial volume selection of an inner 162 kg of LXe (-58.45 > z > -38.45 cm and r < 30 cm). Two clear event populations from ^{222}Rn and ^{218}Po are visible. The expected event distribution from ^{214}BiPo is missing. The vertical band of events is due to alpha S1 peaks that are incorrectly matched to uncorrelated S2 peaks.

The two clearly identifiable distributions in figure 4.4 are from ^{222}Rn and ^{218}Po, with energies of 5.6 and 6.1 MeV respectively. Apart from these two, no other clear distributions are visible, even though one expects to also see a contribution from ^{214}Po, which has an energy of 7.8 MeV. Even though this simple data selection can be used to calculate the concentration of ^{222}Rn and ^{218}Po, it fails to do so for any others. To understand why this is, we look at how cS1 changes versus depth in figure 4.5. Here no fiducial volume selection or energy selection in cS2 is applied.

A problem with matching In figure 4.5 the upper and lower selection bounds in z, used in figure 4.4, are depicted by red dashed lines. One now distinguishes four different isotopes in this figure. The ^{222}Rn and ^{218}Po are the two narrow bands ($cS1 \approx 5 \times 10^4$ and $cS1 \approx 5.5 \times 10^4$, respectively). At higher energies ($6 \times 10^4 < cS1 < 1 \times 10^5$ PE) the events from ^{214}Po are now visible, showing up as a smeared-out triangular distribution. The reason for this is that the S1 and S2 peaks in these events are incorrectly

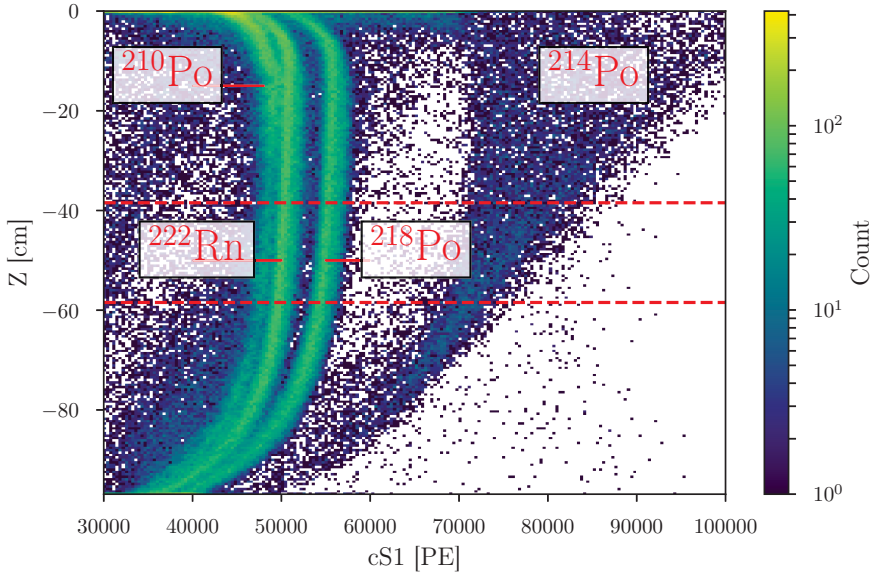

Figure 4.5: Depth dependence of the primary (cS1) scintillation light of the alpha event distributions within in the TPC. No cuts or fiducial volume selections have been applied. The red dashed lines show upper and lower bounds of the selection in z applied to create figure 4.4. In order of energy, event distributions from the following four isotopes can be observed: ^{210}Po, ^{222}Rn, ^{218}Po and (^{214}Bi-)^{214}Po. The slanting of these alpha lines, towards lower cS1 values, at the top and bottom part of the detector is caused by saturation effects. It is clear that the applied corrections (from chapter 3) are not sufficient to correct these high-energy alpha events over the full TPC volume.

matched. Due to the very short half-life of ^{214}Po (162.3 μs), which comes after ^{214}Bi, one expects that all these events have two S1 and two S2 peaks. The XENON1T peak classifier is designed to match the biggest S1 signal to the first big S2. Due to the difference in the ratio of deposited photons to electrons being much higher for alpha than for gamma interactions, the alpha S1 is matched to the beta S2. This incorrect matching causes both the cS1 and the z values to also be incorrectly calculated.

The last missing isotope from the radon chain is ^{210}Po, with an energy of 5.4 MeV. It is shown as an extra line to the left of the ^{212}Rn line, portraying near the top of figure 4.5. This isotope, which comes almost at the end of the decay chain after ^{210}Pb ($T_{1/2}$ = 22.3 y), originates from the PTFE walls or metal grids. The spatial distribution of all four alpha isotopes will be discussed in section 4.3.

All four lines show slanting in the top ($z > -10$ cm) and bottom ($z < -60$ cm) parts of the detector, towards lower cS1 values. This is

dominantly caused by saturation of PMT pulses, which will be presented in section 4.3.1. Additional corrections, specifically tailored for alpha decays, are needed to calculate the concentration of ^{214}BiPo.

4.2.2 S1-only analysis

Area fraction top versus depth Assuming that in the events from ^{210}Po and ^{214}BiPo decays, the S1-S2 have been incorrectly matched, we build an *S1-only analysis* to work around it. This means we calculate the concentrations without using any of the matching information. By estimating the interaction depth with the *S1 area fraction top* (S1 AFT) we can do a full analysis without using the S2 peaks. The S1 AFT value is defined as the ratio of light measured in the top PMT array divided by the amount of light measured in the top and bottom arrays combined. As the normal S1 LCE map is built on z (see section 3.3.2), we need to build a new depth-dependent correction map on S1 AFT.

We select only ^{222}Rn and ^{218}Po events for the relationship between S1 AFT and z, under the assumptions that these isotopes are homogeneously distributed throughout the TPC and have correct S1-S2 matching. The rough selection of these events is done on SR0 data, without a fiducial volume cut, and in cS1 vs. cS2 space, as shown in figure 4.6a. This selection is good enough to examine the relation between S1 AFT and Z with high statistics, as shown in figure 4.6b.

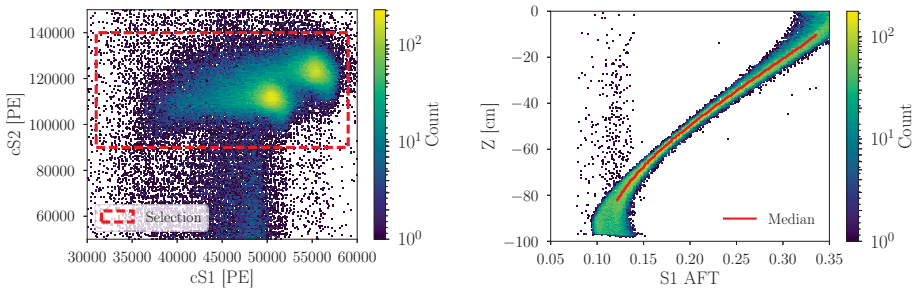

(a) **(b)**

Figure 4.6: **(a)** Selection box in cS2 vs. cS1 of ^{222}Rn, ^{218}Po events used to determine the mapping of S1 area fraction top (AFT) to z, as shown in figure 4.6b. No cuts or fiducial volume selections are used. The event distribution below the selection box are mainly ^{210}Po decays from the walls. **(b)** Correlation between S1 area fraction top (S1 AFT) and interaction depth (z) inside the TPC for events in the selection box in figure 4.6a. The median of the distribution (red line), taken in slices in z, is used for the mapping between S1 AFT and z.

In figure 4.6b we see that S1 AFT, at these energies, has to first order a smooth linear relationship with the interaction depth. The median of the distribution (red line), calculated in slices in z, is used for the mapping between S1 AFT and z. The other population, with constant S1 AFT (between 0.1 and 0.15), but far-ranging z positions, is most likely caused by alpha decays in the charge-insensitive region below the cathode. These are then picked up in time correlation with a random S2 from another event. The difference between these two populations shows the clear difference between correct and incorrect S1-S2 matched events.

Calculating the S1 AFT LCE correction Figure 4.7a shows S1 AFT versus the uncorrected primary (S1) scintillation signal. As expected, event interactions deeper in the TPC (lower S1 AFT) have a higher overall LCE (total S1).

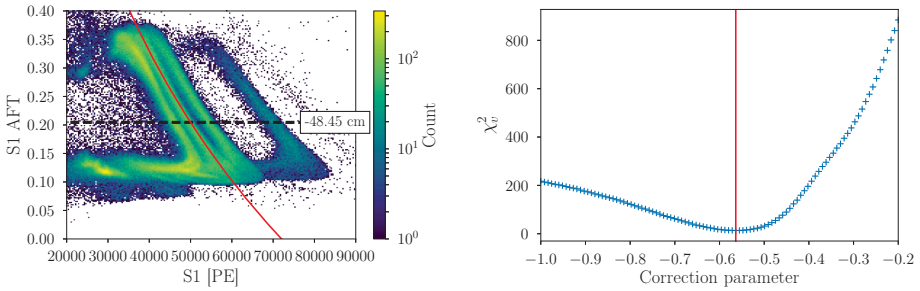

Figure 4.7: (a) Uncorrected primary (S1) scintillation signal versus S1 area fraction top (AFT). Because no S2 information is used, all four radon isotopes have distinct event distributions. The middle of the TPC in S1 AFT ($z = -48.45\,\text{cm}$) is used as reference value $S1AFT_0$ (black dashed line). The red line depicts $cS1_{aft} = 5 \times 10^4$ PE in S1 for the best found slope of 0.56, using equation 4.1. **(b)** Evaluated reduced chi-square distribution versus slope parameter of the spectral alignment method based on the data of figure 4.7a. For every correction parameter (*slope*) of equation 4.1 the difference with the mean spectrum is computed. The best slope is found to be -0.56 (red line).

The idea of a new depth-dependent S1 LCE correction [120] is based on trying out different correction parameters (*slope*) in S1 AFT and comparing the individual $cS1_{aft}$ spectra of the S1 AFT-slices with the mean spectrum of the S1 AFT-slices. The best correction parameter should give the least difference between the individual slices and the mean. Our ansatz is to correct the S1 values with an empirical multiplicative area

correction for the depth dependence (measured by S1 AFT) of the LCE:

$$cS1_{aft} = S1 \times \exp\left(\frac{S1AFT - S1AFT_0}{slope}\right), \tag{4.1}$$

where $S1$ is the uncorrected S1 value, $S1AFT$ is the S1 area fraction top value, $S1AFT_0$ is the reference point in AFT corresponding to the midpoint in z of the TPC and *slope* is (minus) the slope of the spectral lines shown in figure 4.7a.

We start by calculating $cS1_{aft}$ of the data in figure 4.7a, using equation 4.1, with a slope between -1 and -0.2. The data within the center AFT region ($S1AFT_0 \pm 0.05$) is sliced in 20 bins in S1 AFT. For every S1 AFT-slice, the agreement between the (normalized) spectrum and the mean spectrum of all the slices is computed, giving a reduced chi-square (χ^2_v) value for a tested slope. This is repeated for all slope values and the resulting χ^2_v values are shown in figure 4.7b. The slope that minimizes χ^2_v is chosen, which is found to be -0.56. This new S1 correction method uses the same methodology of the S1 LCE correction in the sense that the depth dependence of the LCE is corrected to the midpoint value in z [5]. Figure 4.8 shows the result of the corrected $cS1_{aft}$ values versus S1 AFT, using this best slope value.

[5] For this reason the units of $cS1_{aft}$ are still photoelectrons (PE).

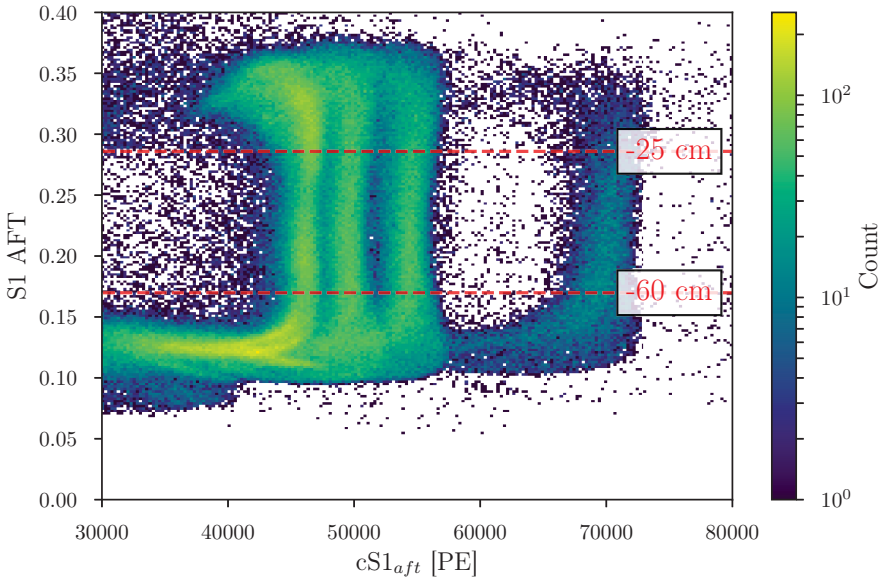

Figure 4.8: S1 area fraction top (AFT) vs corrected primary scintillation light (cS1) of the four alpha lines after applying the empirical LCE correction. The S1 AFT is a measure of depth. These alpha lines correspond, in order of energy, to: ^{210}Po, ^{222}Rn, ^{218}Po and ^{214}Bi-^{214}Po. Since no S2 information is used, no events with a valid S1 in the alpha energy range are removed due to incorrect S1-S2 matching. The two red dashed lines show the depth in z corresponding to S1 AFT, as estimated in figure 4.6b. This corrected data can now be used to calculate the concentration of the four different isotopes.

4.2.3 Radon spectrum

Finally, in figure 4.8 four distinct event distributions are visible. These are in order of energy: ^{210}Po, ^{222}Rn, ^{218}Po and ^{214}BiPo. The big difference between this result and that in figure 4.4, is that now no events are removed due to an incomplete or incorrectly matched S2 peak. For ^{210}Po events, which originate close to the PTFE wall, incomplete charge collection leads to events without an S2 peak. For ^{214}BiPo events, where two S1 and two S2 signals are present, incorrect S1-S2 matching leads to an incorrect depth calculation and thus an incorrect S1 (x,y,z) LCE correction. Building the S1 LCE correction only on S1 information, solves both these problems. Now we can compute the concentrations of all four isotopes at the same time.

Unfortunately, the top and bottom part of the TPC still show light-loss effects due to saturation. For this reason, the S1-only method can only determine the concentrations of the four isotopes between $-60 < z < -25\,\mathrm{cm}$ [6] (red dashed lines). Figure 4.9 shows the resulting alpha spectrum for this depth slice. Not only the four peaks of the radon decay chain are visible, but also three from the thoron decay chain.

All seven peaks are fitted simultaneously and their individual fit results are shown in color. For the ^{210}Po peak (blue) a Crystal Ball (CB) function is used, while skewed Gaussians are used for to the other six peaks[7]. The Crystal Ball function, developed by the Crystal Ball collaboration [121], consist of a power law tail stitched to a Gaussian core. It is mostly used to describe energy loss processes, such as the ^{210}Po decays originating from the PTFE on the TPC wall. The skewed Gaussian, first introduced by [122], is defined as the convolution of the pdf and the cdf of a normal distribution:

$$f(x) = 2\phi(x) \cdot \Phi(ax), \tag{4.2}$$

with $\phi(x)$ the standard normal probability density function:

$$\phi(x) = \frac{1}{\sqrt{2\pi}} e^{-\frac{x^2}{2}}, \tag{4.3}$$

and $\Phi(y)$ the cumulative distribution function:

$$\Phi(y) = \int_{-\infty}^{y} \phi(t)\, dt = \frac{1}{2}\left[1 + \mathrm{erf}\left(\frac{y}{\sqrt{2}}\right)\right], \tag{4.4}$$

with a the skewness[8] and 'erf' the error function[9]. The use of a skewed Gaussian is motivated by the data and hints at a non-linear depth-dependent

[6] Using the relation between S1 AFT and z, as shown in figure 4.6b.

[7] Leading to a 30 parameter fit.

[8] For $a = 0$ there is zero skewness and the normal distribution is restored.

[9] $\mathrm{erf}(x) = \frac{1}{\sqrt{\pi}} \int_{-x}^{x} e^{-t^2}\, dt$.

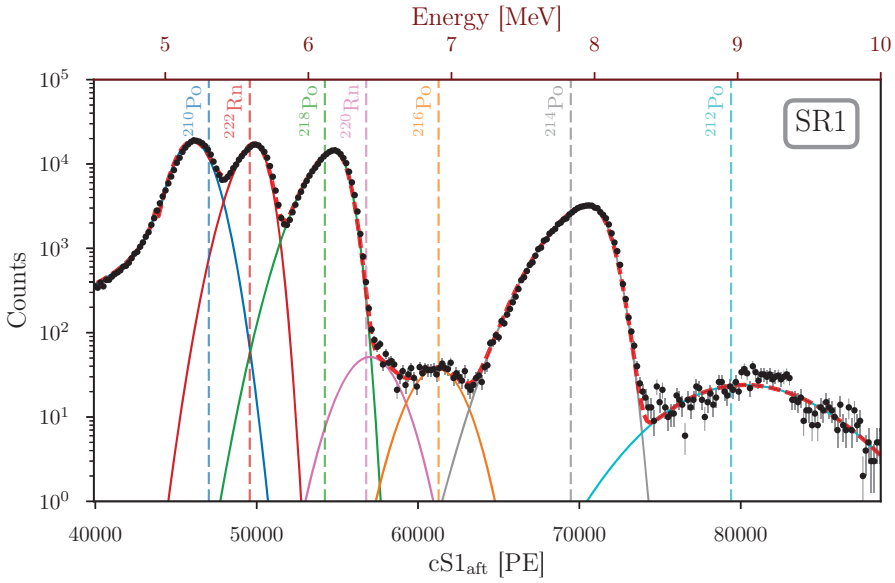

Figure 4.9: Alpha spectrum of ^{210}Po (blue), ^{222}Rn (red), ^{218}Po (green), ^{220}Rn (pink), ^{216}Po (orange), ^{214}Po (grey) and ^{212}Po (light blue) in SR1, with the S1 area fraction top (AFT) LCE correction applied. The spectrum is fitted with a Crystal Ball function (for ^{210}Po) and with six skewed Gaussians. The top axis shows scaling to energy, assuming a linear scaling relationship with photoelectrons (PE), using the ^{222}Rn peak as anchor. The dashed lines show the respective alpha energies. Based on the χ^2/ndf this model is a poor fit to the data, but this model fits the data best.

S1-AFT correction. For the fit, skewness parameters are found of -2.1, -3.0 and -3.1 for ^{222}Rn, ^{218}Po and ^{214}Po respectively[10].

The spectrum of S1 pulses is scaled (top axis) from pulse size in photoelectrons (PE) to energy (MeV) with a single scaling parameter using the position of the ^{222}Rn peak as an anchor. The known energies are shown as vertical dashed lines, representing not the kinetic energy of the alpha decay, but the Q-value. The Q-value is used because for each decay both the deposited energy of the alpha and the recoiling daughter nucleus are measured in the TPC.

From the fit, the found energy and light yield of the seven isotopes are shown in tables 4.3 and 4.4. The presented measured energies are the μ and σ values from the Gaussian part (the pdf) of the fit skewed

[10]The fact the skewness increases for higher energies hints also at an energy-dependent S1 AFT correction (slope).

Gaussians[11]. The measured energies of all the alpha peaks except for ^{210}Po agree with the known energies (total Q-value) within the uncertainty. The errors on the measured energies are the statistical errors of the means from the fit. The reason for the mismatch in the measured energy of ^{210}Po will be discussed in section 4.4, where we look at the spatial distribution of this specific isotope. The measured light yield of (8.9 ± 0.2) PE/keV for ^{222}Rn is more than twice as high as the 3.7 PE/keV reported by XENON100 [123]. This validates the expected average light yield increase of a factor two for XENON1T compared to XENON100 [93]. The full width at half maximum (FWHM) of 4.4 % for the ^{222}Rn peak is broader than the 3 % reported for XENON100. This could be caused by correcting the S1 only in depth-slices in S1 AFT, without taking any radial effects into account. The very broad FWHM of ^{212}Po hints at some additional unknown background.

Decay isotope	**Q-value** [MeV]	**Energy** [MeV]	**Mean cS1$_{aft}$** [PE]	**FWHM** [%]	**Light Yield** [PE/keV]
^{210}Po	5.30*	5.19 ± 0.12	46035 ± 1050	5.4	8.7 ± 0.2
^{222}Rn	5.59	5.59 ± 0.10	49570 ± 927	4.4	8.9 ± 0.2
^{218}Po	6.12	6.12 ± 0.13	54231 ± 1155	5.0	8.9 ± 0.2
^{220}Rn	6.40	6.43 ± 0.16	57012 ± 1413	5.8	8.9 ± 0.2
^{216}Po	6.91	6.89 ± 0.15	61131 ± 1372	5.3	8.8 ± 0.2
^{214}Po	7.83	7.87 ± 0.18	69758 ± 1623	5.5	8.9 ± 0.2
^{212}Po	8.95	9.08 ± 0.47	80541 ± 4126	12.1	9.0 ± 0.5

Table 4.3: Energy and light yield measurements of the seven alpha peaks fitted in figure 4.9. Apart from the ^{210}Po peak the measured energies in XENON1T agree with the known energies (total decay Q-values). An average S1 scintillation light yield is found of (8.9 ± 0.2) PE/keV for radon alpha decays. The presented uncertainties are statistical only. *for ^{210}Po the reported energy is the kinetic energy for the alpha only, as the nuclear recoil is lost in the wall.

For comparison, the SR0 alpha spectrum is shown in figure 4.10. The SR0 fit parameters for the isotopes of the radon decay chain isotopes all agree (within errors) with those of SR1. For the fit parameters of the thoron decay chain isotopes small differences are observed. This can be expected due to the lower statistics of these isotopes in the smaller SR0 exposure.

[11] We are interested in the underlaying distribution, not in the artificially skewed one due to the applied correction method.

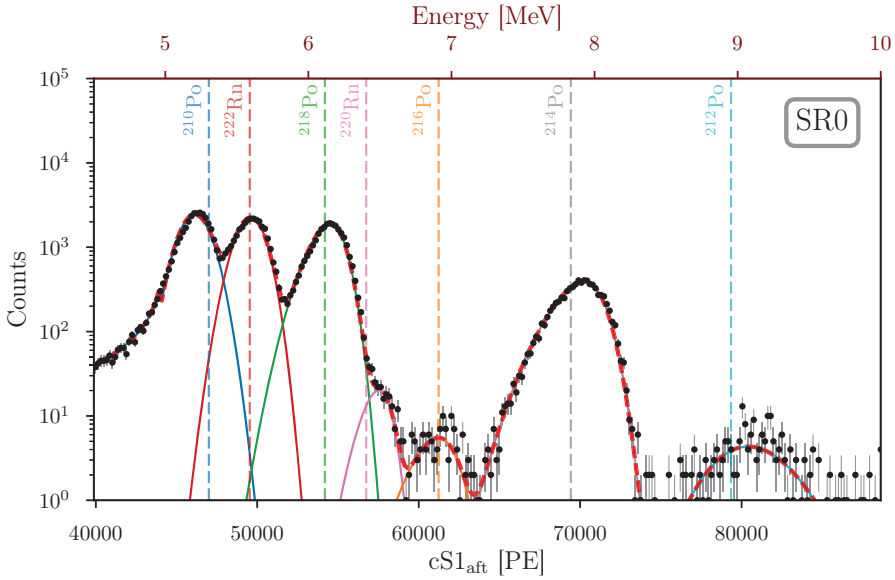

Figure 4.10: Alpha spectrum of ^{210}Po (blue), ^{222}Rn (red), ^{218}Po (green), ^{220}Rn (pink), ^{216}Po (orange), ^{214}Po (grey) and ^{212}Po (light blue) in SR0, with the S1 area fraction top (AFT) LCE correction applied. Due to the low exposure of SR0, the thoron daughters can only be fitted by constraining the means and widths. Based on the χ^2/ndf this model is a poor fit to the data, but this model fits the data best.

4.2.4 Radon concentrations

Figure 4.11 shows the time evolution of the concentration of ^{222}Rn (red), ^{218}Po (green) and ^{214}Po (orange) in the LXe during the first and second science run (SR0 and SR1). The concentration is calculated using the presented S1-only analysis, but instead of fitting the whole time period at once, the fit is done per day. To exclude possible contamination from calibration sources (coloured bands), only background data are selected. The data can be split into three periods, each having different detector conditions: SR0 before radon distillation, SR0 during radon distillation and SR1. Radon distillation started during the ^{220}Rn calibration in December 2017 (purple band) and ended together with SR0 when an earthquake occurred on January 18, 2017 (red dashed line). SR1 started after the voltage test (grey band), and ended on February 8, 2018. The average concentration per time period is given in table 4.4.

Decay isotope	**SR0 no distil.** [μBq/kg]	**SR0 distil.** [μBq/kg]	**SR0 average** [μBq/kg]	**SR1** [μBq/kg]
^{222}Rn	14.7 ± 1.5	12.5 ± 1.7	13.7 ± 1.6	13.4 ± 0.9
^{218}Po	14.3 ± 0.9	11.8 ± 0.8	13.2 ± 0.8	13.7 ± 0.7
^{214}Po	4.2 ± 0.3	3.3 ± 0.3	3.8 ± 0.2	4.4 ± 0.2

Table 4.4: Average concentrations of ^{222}Rn, ^{218}Po and ^{214}Po for the different time periods with stable detector conditions as shown in figure 4.11. These concentrations are determined using the S1-only method in a central 724 kg LXe volume. The difference in the concentrations during SR0 with and without radon distillation show the effect of using the cryogenic distillation column in reverse on the background level of radon. The decreasing concentration of the three isotopes for any single period is caused by charged isotopes plating out on the negative cathode wires. To determine the concentration of ^{214}Pb we can use the concentrations of ^{218}Po and ^{214}Po as upper and lower limits, respectively. The stated uncertainties include statistical (about 1%), and systematic from the fiducial volume (about 4%), fit uncertainty (about 4-10%) and time period (about 2%), added in quadrature.

Cathode cleaning effect The first observation is that the average concentration of all three isotopes for a single period shows a decreasing trend following the decay chain of radon. One would *a priori* expect the concentrations to be in equilibrium, as the experiment's run time exceeds the longest half-life in this part of the decay chain of ^{222}Rn ($t_{1/2}$ = 3.8 d). The fact that the concentrations for ^{222}Rn, ^{218}Po and ^{214}Po decrease, the further they are in the decay chain, can be explained by a *cathode cleaning effect*: charged radon daughters are removed from the active TPC region

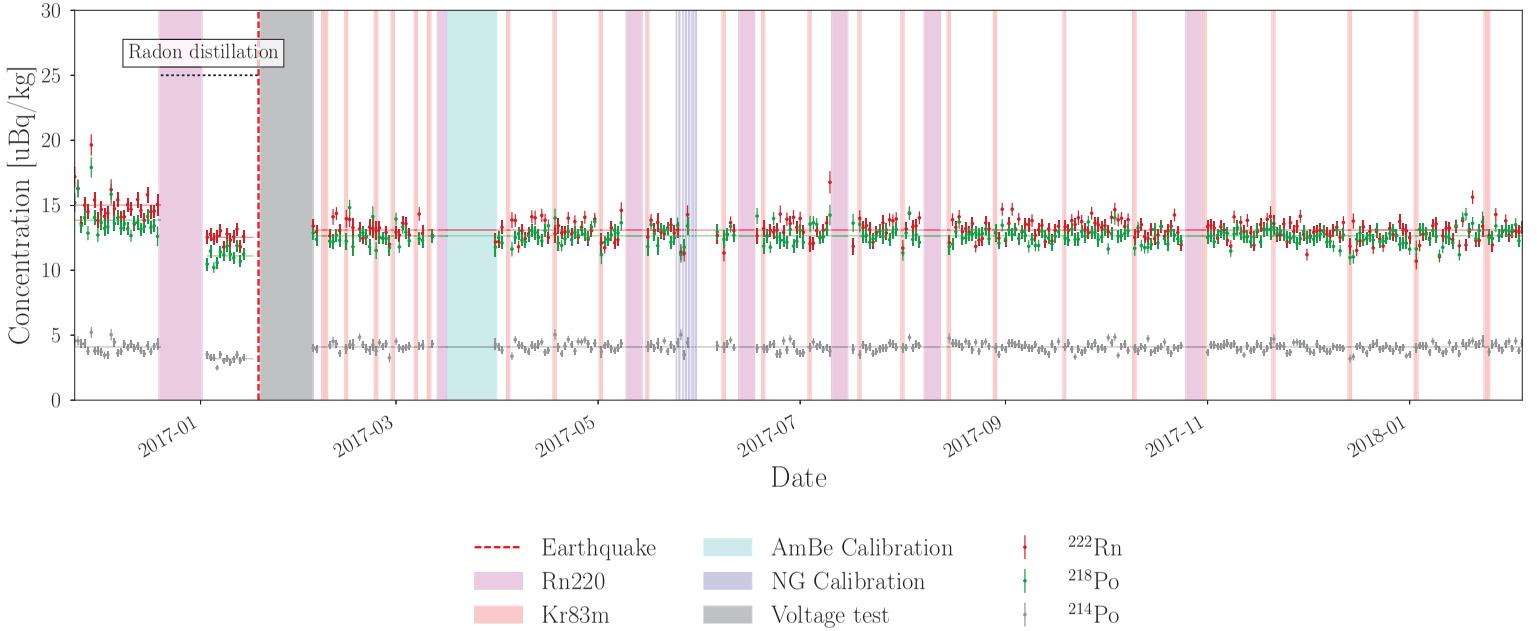

Figure 4.11: Radon evolution over time for ^{222}Rn (red), ^{218}Po (green) and ^{214}Po (orange) in the LXe during the first (SR0)and second (SR1) science runs. To exclude possible contamination from calibration sources (coloured bands), only background data is selected for daily concentration measurement points. All data before the earthquake on January 18, 2017 (red dashed line) belongs to SR0, while SR1 started after the voltage test (grey band) and ended on February 8, 2018. A decrease in the concentration of all three isotopes is visible during SR0 with on-line radon distillation using the krypton column in reverse.

by plating out on the negative cathode[12]. Convection measurements show that the LXe flow in the TPC can be represented to first order by a single-cell convection pattern [124] . In one half of the TPC the LXe is moving upwards, while in the other half it is moving downwards. The LXe flows with an average velocity of $\mathcal{O}(1)$ mm/s up or down, while the ions drift towards the cathode with $\mathcal{O}(0.1)$ mm/s. On average, a ^{218}Po atom thus travels about 18 cm in the TPC before decaying ($t_{1/2} = 3.05$ min), while a ^{214}Pb travels on average over 1.5 m. Measurements from EXO in LXe [125] show that after ^{222}Rn decay (50.3 ± 3.0)% of the ^{218}Po atoms are positively charged and (76.4 ± 5.7)% of the ^{214}Bi are positively charged after ^{214}Pb decay. As the cathode is set to negative high-voltage, every time an ionized atom passes there is a probability it is attracted to the cathode wires themselves, where it stays. This *cathode cleaning effect* can thus explain the observed decreasing concentration of isotopes in the radon decay chain.

Radon distillation The second observation is that the average concentration per isotope shows a significant difference between the period of SR0 with and without distillation. This shows the effect of removing radon from the TPC by cryogenic distillation using the krypton distillation column in reverse. The vapour pressure of radon is lower than xenon ($P_{Rn}/P_{Xe} = 0.1$ at T = 178 K) [126], which means that in a single distillation stage the radon will be enriched in the liquid phase. This is the opposite effect compared to the krypton distillation process presented in section 2.4.2. For radon distillation, out of a total flow of 51.4 slpm of Xe in the purification loop, 3.6 slpm of GXe from the TPC is siphoned off and redirected into the distillation column. Instead of taking LXe we now take -radon depleted- GXe out of the column, liquefy it and bring it back into the TPC.

This technique was already shown to work with a calibration source of ^{222}Rn in XENON100 [127], but was never before shown to work on reducing the low ^{222}Rn background during normal operation of a TPC. During distillation, a decrease of (17 ± 5)%, (17 ± 5)% and (19 ± 9)% is found for ^{222}Rn, ^{218}Po and ^{214}Po, respectively[13]. This demonstrates that cryogenic radon distillation is already possible with the current equipment to reduce the radon induced background by about 20%. To further decrease this background by cryogenic distillation several technical improvements have to be made to increase the maximum Xe throughput. Research and

[12] Plating is the deposition of a metal on a conductive surface.
[13] These uncertainties are statistical only.

development is ongoing to build a radon distillation column that can handle the full recirculation speed of XENONnT, the upgrade of XENON1T.

Detailed studies [126] show no correlation between radon concentration in air and within the TPC, as was the case in XENON100. There, it was caused by a tiny air leak into the gas system [123]. The absolute concentration of $(13.4 \pm 0.9)\,\mu$Bq/kg of ^{222}Rn found in SR1 is comparable to the expected concentration of about $10\,\mu$Bq/kg from emanation measurements. The concentration of ^{214}Pb is lower than this expectation value and will be discussed in the last section of this chapter.

For ^{220}Rn and ^{216}Po a concentration of (0.05 ± 0.05) μBq/kg is found in SR1, showing that the thoron decay chain is at least a 100 times lower in concentration than the radon decay chain[14]. We use the concentration of ^{216}Po as an upper limit on the concentration of ^{212}Pb. The expected rate of ^{212}Pb is thus about a factor 100 lower than ^{214}Pb, therefore we will neglect the influence of thoron on the low-energy background.

4.3 Spatial distribution of ^{222}Rn and ^{218}Po

The radon concentration measurement using the S1-only analysis, relies on the assumption that the radon isotopes are homogeneously distributed throughout the whole TPC. The four peaks in figure 4.8 could only be distinguished between $-60\,\text{cm} < z < -25\,\text{cm}$, due to the different populations overlapping in S1 AFT outside of this range. To select events in the whole TPC region, we use the depth information (z) from the time difference between the S1 and S2 signal. The disadvantage of doing a *combined S1-S2 analysis* is that we discard events from populations that have incorrect S1-S2 matching, such as most of the the ^{210}Po events, thus we will here first focus on the ^{222}Rn and ^{218}Po events.

4.3.1 Saturation of S1 signals

Before finding a solution to the saturation problem in the top and bottom parts of the detector, we first have to better understand the problem of signal saturation. A sample in a waveform is *ADC saturated* when it reaches the maximum input voltage of the analog-to-digital converter (ADC) (section 2.3.4). The more samples of a peak are ADC-saturated in the individual PMT channels, the more information is lost about the actual deposited energy of the event. In general, the closer to a PMT a high energy alpha event occurs, the higher the chance of that PMT being saturated. This is shown in figure 4.12, where the number of saturated

[14] A lower thoron concentration was indeed expected, partly due to its short half-life reducing the probability of mixing into the LXe.

PMT channels is shown as a function of where in the TPC the alpha decay occurred.

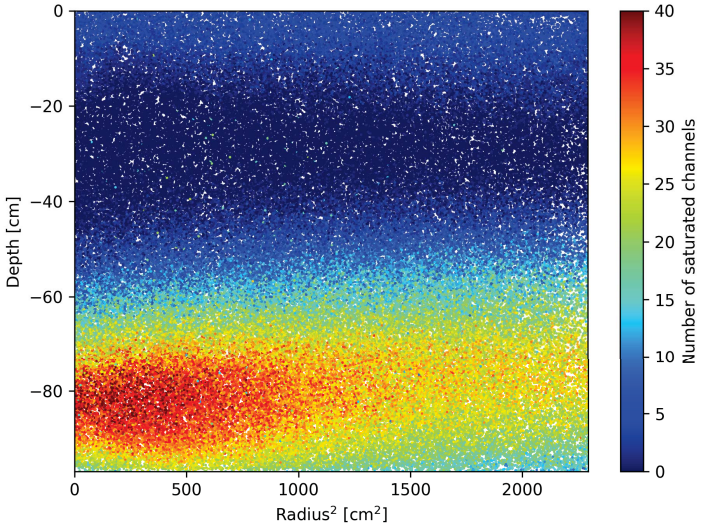

Figure 4.12: Number of ADC-saturated PMT channels in the S1 peaks of ^{222}Rn and ^{218}Po events (using the selection in figure 4.6a) with their interaction position in the TPC. Events in regions with a higher average LCE have a higher number of saturated channels. The more channels are saturated, the lower the total reconstructed cS1 value is for these events, as shown in figure 4.5. In the top 10 cm, only up to 10 channels are saturated (lighter blue), due to the fact that most of the light at the liquid-gas interface is reflected downwards.

Due to the higher average LCE at the bottom of the TPC, more events are saturated and have on average more ADC saturated PMT channels. Only between approximately $-40\,\text{cm} < z < -20\,\text{cm}$ no ADC-saturation occurs. The relation between the number of saturated channels and measured cS1 values for the four radon isotopes can be observed by comparing this figure with figure 4.5. Events with more ADC-saturated PMT channels are reconstructed with a lower total cS1 value. This leads to overlapping event distributions observed in the top and bottom part of figure 4.5. To separate ^{222}Rn and ^{218}Po events in the whole TPC region, a method needs to be implemented that deals with the ADC saturation problem in S1 signals.

One solution is to only use either the top or bottom PMT array depending on the TPC region that is being analysed. Figures 4.13a and 4.13b show the relationship between the interaction depth z and the direct scintillation light measured only in the top and bottom array, respectively. As expected from geometry, the two populations only overlap in $S1_{top}$ in the

upper TPC region ($z > -60\,\mathrm{cm}$) due to saturation in the top PMT array. A similar observation is visible in figure 4.13b, where the two populations only overlap in $S1_{bottom}$ in the lower TPC region ($z < -60\,\mathrm{cm}$) due to saturation in the bottom PMT array.

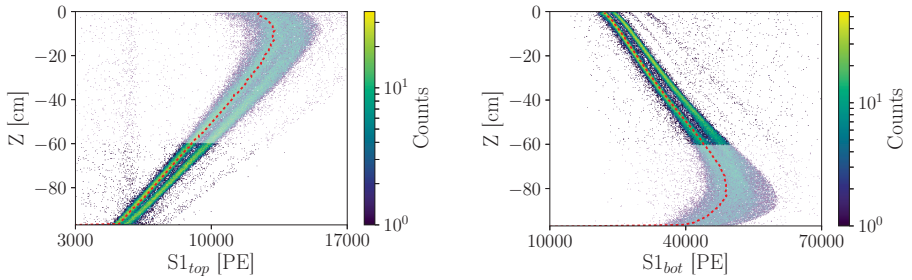

Figure 4.13: Uncorrected primary scintillation light of ^{222}Rn and ^{218}Po measured only in the top (a) or bottom (b) PMT array. Only the information of the non-shaded region is used to distinguish between the two isotopes, as ADC saturation effects are only visible above (a) or below (b) z = -60 cm. The 30th percentile in z slices, used to correct for the depth dependence, is depicted by the red dotted line.

4.3.2 Correcting for saturation

We will now correct the depth-dependent light yield of $S1_{top}$ and $S1_{bot}$ individually. We first compute the 30th percentile in 100 z-slices (red dotted lines in figures 4.13a and 4.13b), because it corresponds to the median of the ^{222}Rn population. The correction value is calculated by comparing the 30th percentile value at every slice with the value of the 30th percentile found at the half way point in depth ($z = -48.45\,\mathrm{cm}$). This method is similar to the one used for figure 4.8, but is not using any *a priori* knowledge of the form of the correction function. The result again corrects against any depth dependence of the cS1 value of a single mono-energetic alpha line. After correcting the $S1_{top}$ and $S1_{bot}$ independently, we take the $cS1_{top}$ values for $z < -60\,\mathrm{cm}$ and $cS1_{bot}$ values for $z > -60\,\mathrm{cm}$ and stitch these together as shown in figure 4.14a.

As the average total amount of light measured in the bottom and top array differs, both distributions are shifted to 5×10^4 PE, the mean cS1 value of ^{222}Rn found from the distribution shown in figure 4.4 [15]. For almost all depths, a clear separation between the two bands is visible,

[15] As this method will only be used for determining the spatial distributions, any possible bias in the average cS1 value will not affect the results.

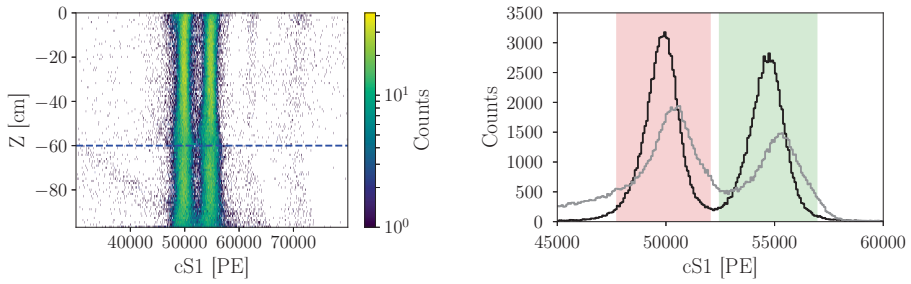

(a) **(b)**

Figure 4.14: (a) Corrected primary scintillation light of ^{222}Rn and ^{218}Po using the bottom PMT array for everything above z = -60 cm (blue dashed line) and the top PMT array for everything below. Both distributions are now clearly distinguishable. **(b)** Spectrum of ^{222}Rn and ^{218}Po decays using the top and bottom array individually (figure 4.14a) (black line) and using the S1 LCE correction (figure 4.5) (grey line). ^{222}Rn (red shaded) and ^{218}Po (green shaded) events are selected assuming a Gaussian distribution with $\pm\, 2\,\sigma$ bounds. This selection is used to determine their spatial distributions.

which means the individual isotopes can be selected over the full TPC region. With this isotope selection, we will determine in the next section if the spatial distributions are homogeneously distributed, as was assumed for the concentration calculation.

4.3.3 Spatial distributions

The spatial distribution of ^{222}Rn in depth vs. radius^2 is shown in figure 4.15 for the full TPC region. The top and right panel show the 1D histograms for 50 slices in r^2 and z, respectively. A slight overpopulation is visible in the top right corner, where, due to the selection in cS2, ^{210}Po events leak in. A small under-fluctuation is visible in the lowest z-bin, where due to the field-distortion correction events are reconstructed below the cathode.

The spatial distribution of ^{218}Po in depth vs. radius^2 is shown in figure 4.16 for the full TPC region. The top and right panel show again the 1D histograms for 50 slices in r^2 and z, respectively. No clear over-densities in the event distribution are visible, hinting at the fact that if some ^{218}Po events leaked into (or out of) the selection, they too are homogeneously distributed.

The homogeneity of ^{222}Rn and ^{218}Po over the whole z-range and within $r < 45\,\text{cm}$ is at the $(6 \pm 1)\%$ and $(7 \pm 1)\%$ $(1\ \sigma)$ level, respectively. When also removing the top and bottom z-bin, both distributions agree

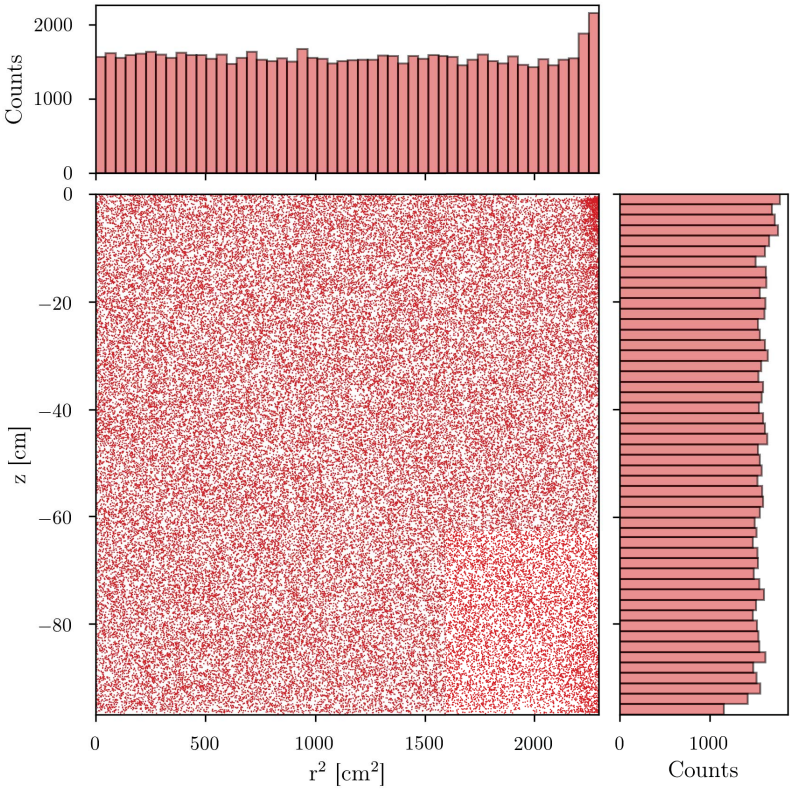

Figure 4.15: Spatial distribution in depth vs radius^2 (main panel) for the selection of ^{222}Rn events (red points) shown in figure 4.14b. The 1D histograms show the distribution in r^2 (right panel) and z (top panel). An over density of events is visible in the top right corner, probably caused by ^{210}Po events leaking into the selection. The lower rate in the lowest z-bin is due to events being reconstructed below the cathode. For a maximum radius of r = 45 cm (r^2 = 2025 cm^2), ^{222}Rn is homogeneously distributed at the (6 ± 1) % (1 σ) level.

with being drawn from a normal distribution following the Shapiro-Wilk test for normality. This shows that the assumption of homogeneity, as expected from how ^{222}Rn dissolves and distributes throughout the LXe before decaying, is correct up to the 7% level within a radius of 45 cm. For ^{218}Po the homogeneity level does not change significantly when increasing the radius to the full TPC radius of r =47.9 cm. The same cannot be said for ^{222}Rn due to ^{210}Po events leaking into the selection box at high radii. The last step is to check these event distributions in x-y space. This is shown in figure 4.17a and 4.17b for ^{222}Rn and ^{218}Po, respectively.

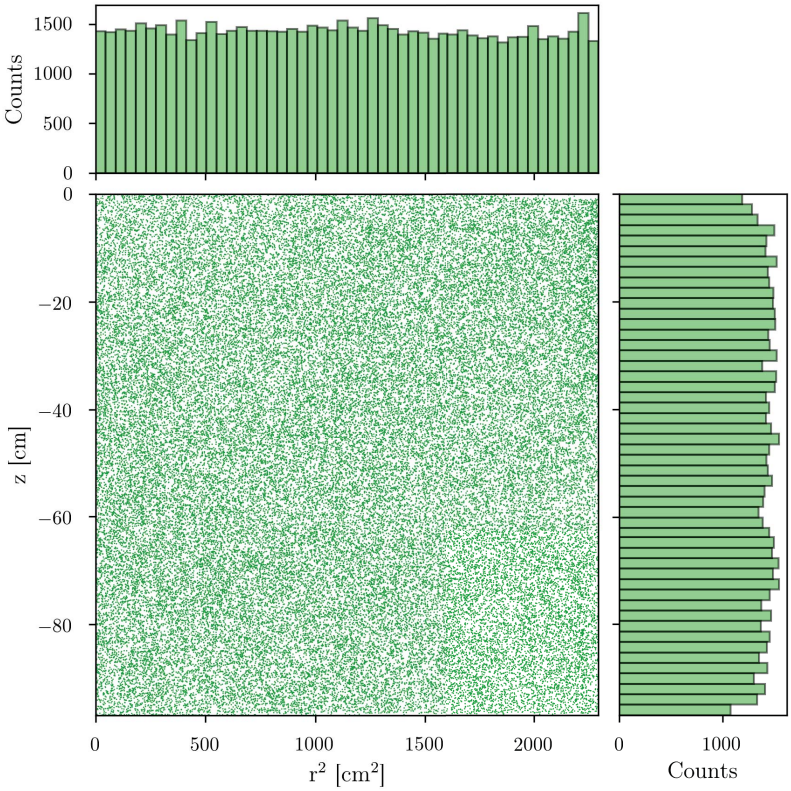

Figure 4.16: Spatial distribution in depth vs radius^2 (main panel) for the selection of ^{218}Po events (green points) shown in figure 4.14b. The 1D histograms shows the distribution in z (right panel) and r^2 (top panel). The lower rate in the lowest z bin is caused due to events being reconstructed below the cathode. For a maximum radius of r = 47.9 cm (r^2 = 2294 cm^2), ^{218}Po is homogeneously distributed at the (7.5 ± 1) % (1 σ) level.

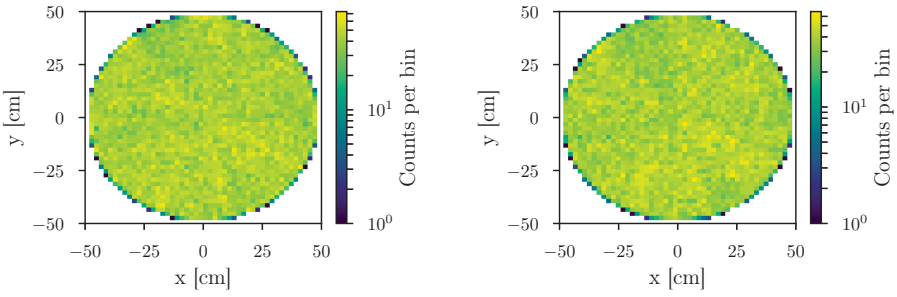

Figure 4.17: Position distribution in (x,y) for ^{222}Rn **(a)** and ^{218}Po **(b)**.

4.4 The ^{210}Po surface background

4.4.1 Selection of ^{210}Po events

After determining the spatial distribution of ^{222}Rn and ^{218}Po, we now look at the spatial distribution of ^{210}Po and its origin. The ^{210}Po background is *a priori* not expected to be at equilibrium with the radon isotopes down to ^{210}Pb in the radon chain. Due to the long half-life of ^{210}Pb ($T_{1/2} \approx 22\,y$), compared to the short running time of XENON1T (about 1 y), a high count rate of ^{210}Po must come from another source within the TPC.

To select ^{210}Po decays (in SR0) we start with the distributions of cS1 vs. cS2 for the full TPC region, as shown in figure 4.18a. The only selection cut applied here is $-90 < z < -10\,cm$, this to exclude any cathode or gate effects. The radial cut, which was applied in section 4.2, is not applied here. The ^{222}Po and ^{218}Po distributions are clearly visible (as already identified in figure 4.4), although now a third population is visible at cS2 < 90k PE and centred around cS1 ≈ 48k PE. The cS1 value of this population agrees with coming from ^{210}Po, as it was measured in the alpha spectrum (figure 4.9), yet there is some mechanism of charge (S2) loss apparent. To determine where in the TPC this charge-loss is happening, the ratio of cS2/cS1 vs. the radius^2 is shown in figure 4.18b.

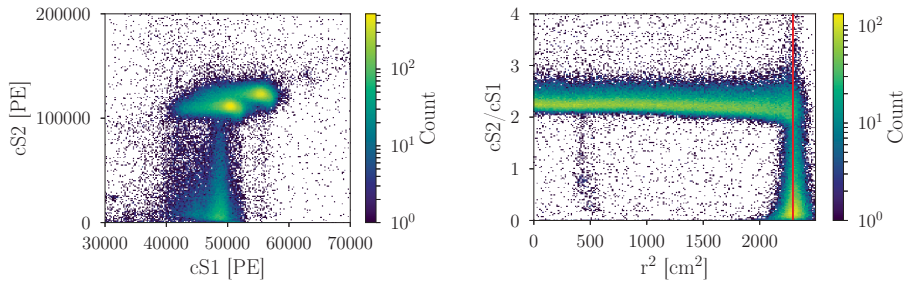

(a) **(b)**

Figure 4.18: **(a)** Combined distribution of corrected secondary (cS2) vs. primary (cS1) scintillation light for alpha signals. Data is shown for SR0 with a depth selection of -90 < z < -10 cm. The ^{222}Rn and ^{218}Po distributions are more spread out than in figure 4.4, mostly due to S1 saturation. The third distribution, with cS2 < 9×10^4 PE, is from ^{210}Po. **(b)** Ratio of cS2/cS1 vs r^2 distribution of all the events from figure 4.18a. The horizontal band is from ^{222}Rn and ^{218}Po, while the vertical distribution at the maximum TPC radius (red line) are the events affected by charge loss. This observation agrees with the hypothesis that ^{210}Po decays originate at the PTFE walls.

Figure 4.18b shows that the events from ^{222}Rn and ^{218}Pb form a flat horizontal band at all radii. The event distribution with cS2 below 90k PE

in figure 4.18a comes from the edge of the TPC. The physical location of the PTFE wall at $r = 47.9$ cm ($r^2 = 2294$ cm^2) is depicted by the red solid line. Events can be reconstructed outside of the physical boundary of the TPC due to position mis-reconstruction. If the events originate fully at the PTFE wall one would expect them to be reconstructed symmetrically around the TPC wall in r^2, with the spread correlated with the position reconstruction uncertainty. The fact that the distribution widens for lower cS2/cS1 values relates to the increase in position reconstruction uncertainty for events with lower S2 values. It is now clear that these ^{210}Po events originate from the PTFE walls, which also explains why they can experience charge loss. Close to the wall there is a higher probability that freed electrons in LXe are attracted to the electronegative wall and will thus not arrive at the liquid-gas interface to form the S2 signal.

4.4.2 ^{210}Po events with a valid S1-S2 pair

Selection and cuts To select a clean sample of ^{210}Po events, we first require cS2 $< 9 \times 10^4$ PE, which removes most of the ^{222}Rn and ^{218}Po events. This selection assumes that ^{210}Po events are affected by charge (S2) loss. Dedicated studies show that in the 1 t fiducial volume no clear ^{210}Po population is found [128]. Next we select ^{210}Po events that have correct S1-S2 matching, that is, events where the S2 is causally connected to the S1. This procedure is shown in figure 4.19, where we show the correlation between S1 AFT and depth.

The three different regions (marked 'A', 'B' and 'C') correspond to three different event topologies. In region 'A', the measured drift time between the S1 and S2 peak agrees with the expected S1 AFT at that depth (as shown in figure 4.6b). In region 'B', the S1 from ^{210}Po decay at the cathode (S1 AFT ≈ 0.1) are matched to an S2 from other real events (accidental coincidence). These will be cut by the S1 and S2 single scatter cuts. The third region 'C', is filled with events where the S1 from ^{210}Po is matched to an S2-type peak that is created by the S1 itself. These events are cut by requiring $z < -0.5$ cm and will be studied in more detail later on in the last paragraph. Events in region 'B' and 'C' have for some reason lost most of their deposited electrons and don't create a correct S2. No z cuts other than $z < -0.5$ cm are applied. The sample of ^{210}Po events, which have a causally connected S1-S2, thus require them to be in region 'A'. We furthermore require $cS2 > 3000$ PE to remove any events with an unphysically small S2. To remove accidental coincidences we require S1s[1] < 100 PE and S2s[1] < 4000 PE [16].

[16] S1 and S2 peaks are ordered in size in descending order.

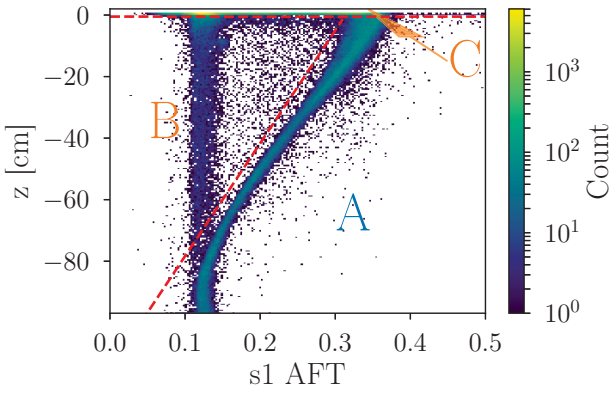

Figure 4.19: ^{210}Po events divided into three regions depending on the origin of the matched S2. Region 'A' are events with correctly matched S1-S2 peaks, as they agree with the expected correlation found in figure 4.6b. In region 'B' the S1 originating from the cathode is matched to an S2 peak from a different interaction within the TPC. Region 'C'($z > -0.5\,\mathrm{cm}$) contains events where the S2 is created by the S1 itself. Only events in region 'A' are selected for a selection of clean ^{210}Po events.

Finally, we apply a depth-dependent S1 correction, fit the distribution with a Gaussian and select the events within ± 2 sigma of the mean ^{210}Po energy[17]. This empirical depth-dependent S1 correction is done by slicing the S1 values in 100 depth slices, fitting the median, calculating the correction by comparing to the half way point in depth and applying the found correction to the S1 values. The result of this procedure is shown in figure 4.20. The events that pass all the above-mentioned selection criteria we call correctly S1-S2 matched ^{210}Po events (blue), incorrectly S1-S2 matched ^{210}Po events (orange) only pass cS2 $< 9\times10^4$ PE, but none of the other cuts[18].

Spatial distribution There is a clear difference between the spectrum of the correctly S1-S2 matched and incorrectly S1-S2 matched ^{210}Po. Assuming all these events are from ^{210}Po, the difference can be explained by the incorrect S1 depth (LCE) correction that is applied. Only for the correctly S1-S2 matched events the real interaction depth is known. Before we investigate what these incorrectly S1-S2 matched events are, we first

[17] Contrary to the fit used in the S1-only analysis, the shape here does not warrant a Crystal Ball function. We fit a mean of (46061 ± 1462) PE, in agreement with the results in table 4.3.

[18] With incorrectly matched S1-S2 pairs we mean events that have no S2 because they lost their charge to a surface.

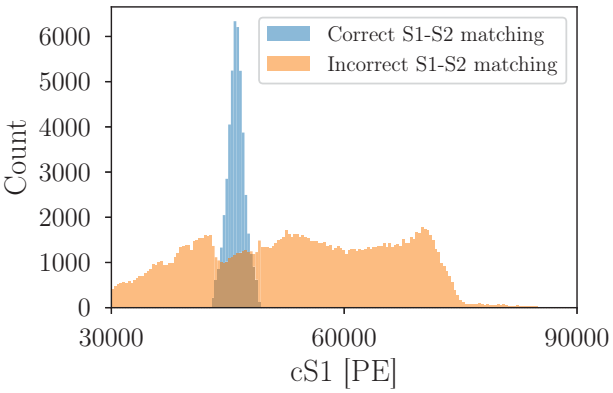

Figure 4.20: Spectral comparison of correctly S1-S2 matched ^{210}Po events (blue) that pass all cuts, and incorrectly S1-S2 matched ^{210}Po events (orange) that did not. Several extra quality cuts have been applied to the events in the region 'A' of figure 4.19. The blue distribution can be described by a Gaussian with mean and sigma in agreement with ^{210}Po values found in table 4.3.

investigate the spatial distribution of the clean sample of ^{210}Po events. The spatial distribution of the correctly S1-S2 matched ^{210}Po events is shown in figure 4.21.

As expected, from the hypothesis that ^{210}Po events originate from the PTFE, almost all events have a reconstructed position close to the maximum TPC radius (black vertical line). The symmetric spread of the events around the TPC edge is likely due to position mis-reconstruction at this radius. Looking at the depth histogram, we see that more events are found in the top region of the TPC ($-30 < z < 0\,\mathrm{cm}$). The reason for this remains unclear, but could indicate that the influence of charge-loss at the PTFE wall is depth-dependent. A horizontal line of events, at all radii, is clearly observed at the cathode ($z = -96.9\,\mathrm{cm}$). Most importantly, only a handful of ^{210}Po events are found in the center of the TPC. This means that any isotope after ^{210}Po in the decay chain (such as ^{210}Pb) cannot have a big background influence on the dark matter search. The spatial distributions of correctly S1-S2 matched ^{210}Po events are also shown as 2D histograms in depth vs radius^2 and y vs x position in figures 4.22a and 4.22b, respectively. The distributions agree with what we concluded from the scatter information of figure 4.21.

4.4.3 ^{210}Po events without a valid S1-S2 pair

Identifying the origin of the incorrectly matched events After determining the spatial distribution of correctly S1-S2 matched ^{210}Po events

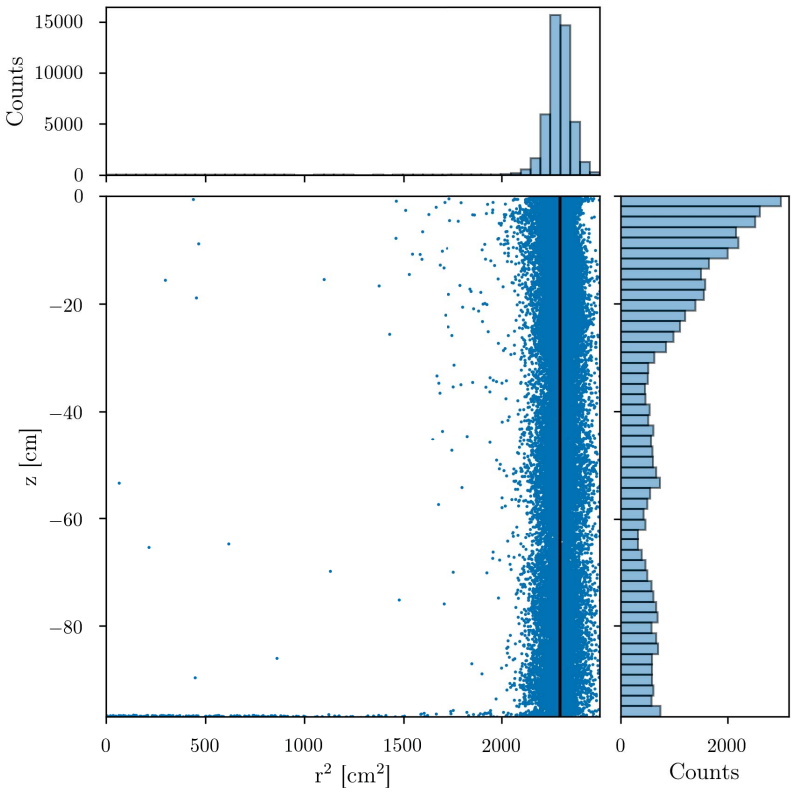

Figure 4.21: Spatial distribution (scatter plot) of correctly S1-S2 matched ^{210}Po events (blue points) in depth vs radius^2 (main panel). The 1D histograms show the distributions in r^2 (top panel) and z (right panel). The ^{210}Po events clearly originate from the PTFE walls at the maximum TPC radius (black line) and at the cathode ($z = -96.9\,\text{cm}$). Any radon isotope after ^{210}Po in the decay chain is not expected to be a big background within the center region of the TPC.

we want to check if the incorrectly S1-S2 matched events are also from ^{210}Po, and if they follow the same depth distribution. Figure 4.23a shows the events with correctly matched S1-S2 peaks now in S1 vs S1 AFT. Figure 4.23b shows the ^{210}Po events with incorrectly matched S1-S2 peaks in the same parameter space. The distribution of incorrectly matched events corresponds to the main distribution of correctly matched events. This shows almost all events in figure 4.23b are also from ^{210}Po, and not from one of the other radon isotopes[19]. One clear difference is visible in the region of S1 $< 40000\,\text{PE}$ and S1 AFT < 0.15. These are events from deep within the TPC that have a distinctly lower S1 value. The only other

[19] For a visual comparison see figure 4.7a for all four distributions in the same space.

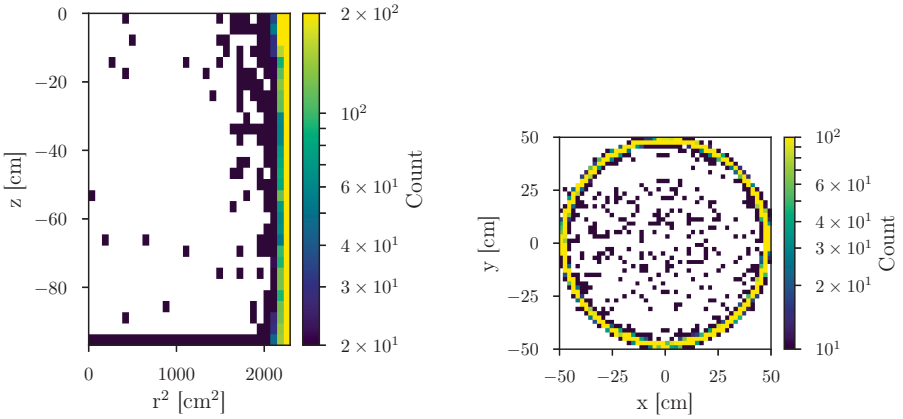

(a) **(b)**

Figure 4.22: Spatial distribution of correctly S1-S2 matched ^{210}Po events in depth vs radius^2 **(a)** and y vs x position **(b)**.

surface at this depth within the active region of the TPC is the cathode. Thus we assume these events are coming from the cathode, which will be shown in figure 4.25.

Assigning a depth value per event from S1 attributes Without a valid S2, the real (z) and (x,y) interaction position of the events in figure 4.23b are unknown. Using again the S1 area fraction top to estimate the depth, as done for figure 4.6b, will not work in the bottom region of the TPC (S1 AFT < 0.15). There is no one-to-one relation between S1 and S1 AFT in this region due to the ADC saturation. As a consequence, no relation of how S1 behaves versus depth over the full TPC range can be acquired. To estimate the depth, using only knowledge of the S1, we will try to use the behaviour of $S1_{top}$ and $S1_{bottom}$ individually in different depth regions. This method, which we developed for reconstructing the spatial distribution of ^{222}Rn and ^{218}Po, showed in figures 4.13a and 4.13b that for a given energy deposition $S1_{top}$ and $S1_{bottom}$ we can estimate z.

The bottom panel of figure 4.24a shows the $S1_{bottom}$ distribution for the correctly (blue) and incorrectly (orange) S1-S2 matched ^{210}Po events. The top panel shows, for the correctly S1-S2 matched events, how $S1_{bottom}$ relates to depth. The median of the $S1_{bottom}$ distribution, in 400 z slices, is represented by the black dotted line. Figure 4.24b shows the same parameter spaces, but now for the top array. We will assume that for both the correctly and incorrectly matched S1-S2 ^{210}Po events, the relationship between $S1_{bottom}$ and z is the same. For $2 \times 10^4 < S1_{bottom} < 3.4 \times 10^4$ PE

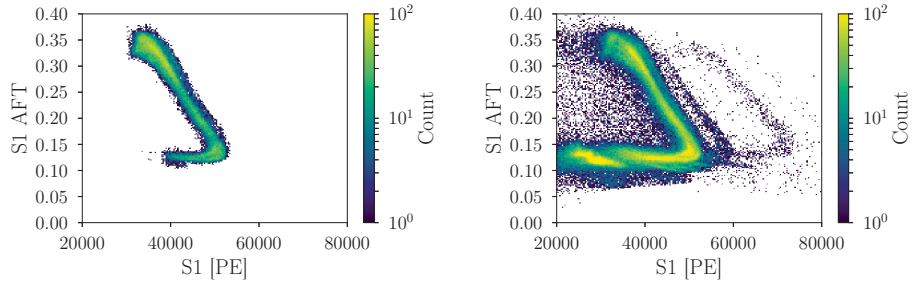

Figure 4.23: **(a)** S1 area fraction top (AFT) vs uncorrected primary (S1) scintillation signal for correctly S1-S2 matched ^{210}Po events (blue histogram in figure 4.20). Due to the applied cuts no other backgrounds are present. **(b)** Same parameter space as figure 4.23a, but for incorrectly S1-S2 matched ^{210}Po events (red histogram in figure 4.20). The shape matches that of the correctly S1-S2 matched ^{210}Po events. In the region of S1 < 40000 PE and S1 AFT <0.15 an extra population is visible, originating from the cathode. Events at higher S1 energies (S1 > 55k PE) are from the other radon isotopes (see figure 4.7a).

(red shaded region, corresponding to $-40\,\text{cm} < z < 0\,\text{cm}$) we define a one-to-one relationship between $S1_{bottom}$ and the corresponding z-value through the median. For every incorrectly matched S1-S2 ^{210}Po event in the region $2 \times 10^4 < S1_{bottom} < 3.4 \times 10^4$ PE we now assign the z value depending on the $S1_{bottom}$ value. With figure 4.24b we conduct the same procedure, but now for $S1_{top}$ in the region $4.2 \times 10^3 < S1_{top} < 1 \times 10^4$ PE (red shaded region, corresponding to -96.7 cm < z < -40 cm).

^{210}Po events from the cathode After assigning the z-values for these two regions, two populations have not been assigned a z-value in the incorrectly matched S1-S2 ^{210}Po event population. The first, and biggest population, are events with $S1_{top} < 4.2{\times}10^4$ PE, visible left of the red dashed line in the bottom panel of figure 4.24b. This population is shown in figure 4.25 in S1 AFT vs S1.

Their S1 AFT values correspond to the region of maximum depth of the TPC. If these events come indeed from the cathode, that means that the cathode is not only a charge-insensitive region, but that it is also a light-insensitive region. This could be caused by the extremely high electric fields at the cathode wires (which suppresses recombination) or by a shadowing effect from the cathode wires themselves. For now, we assume these events are from the cathode and assign them all a z-value of -96.7 cm. The second population, about 1% of all events, do not fall within both correction regions (the red shaded regions). Due to the spread on

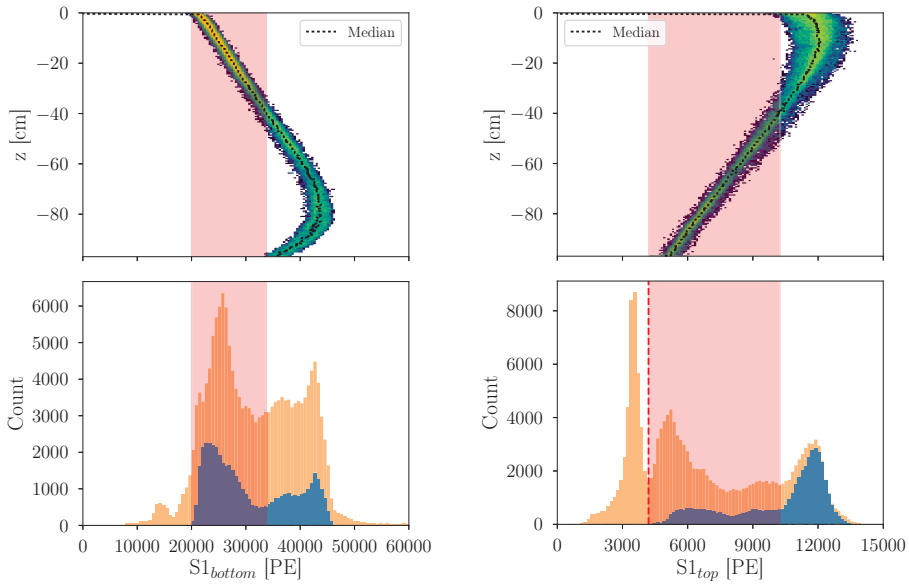

(a) **(b)**

Figure 4.24: **(a)** *Top panel:* Depth vs S1$_{bottom}$ for correctly matched S1-S2 ^{210}Po events in the bottom PMT array. The median (black dotted line) is calculated for 400 slices of z. Within the red shaded region ($2 \times 10^4 <$ S1$_{bottom}$ $< 3.4 \times 10^4$ PE) the value of the median is used to assign an S1$_{bottom}$-dependent z-value to the incorrectly matched S1-S2 ^{210}Po events. *Bottom panel:* Distribution of uncorrected primary scintillation light of correctly (blue) and incorrectly (orange) matched S1-S2 ^{210}Po events measured only in the bottom PMT array. **(b)** *Top panel:* Depth vs S1$_{top}$ for correctly matched S1-S2 ^{210}Po in the top PMT array. The median (black dotted line) is calculated for 400 slices of z. Within the red shaded region ($4.2 \times 10^3 <$ S1$_{top}$ $< 1 \times 10^4$ PE) the value of the median is used to assign a S1$_{top}$-dependent z-value to the incorrectly matched S1-S2 ^{210}Po events. *Bottom panel:* Distribution of uncorrected primary scintillation light of correctly (blue) and incorrectly (orange) matched S1-S2 ^{210}Po events measured only in the top PMT array. The event population left of the red dashed line originates from the cathode and is given the corresponding depth value.

the S1$_{top}$ (and S1$_{bottom}$) vs z of several centimetres, this is not unexpected. These last few events are given a z-value conform their S1$_{bottom}$ value. It is not clear that all events found here are from ^{210}Po, because, due to the extreme fields close to the cathode wires, we cannot distinguish them in S1 energy from other alpha decays.

We will assume the following uncertainties for the total depth profile: the incorrectly matched S1-S2 ^{210}Po event histogram includes events from the other radon isotopes ($\mathcal{O}(1\%)$ out of a total of 166k events), and the

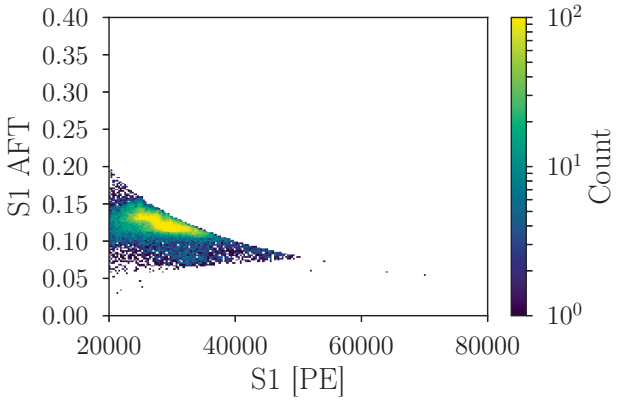

Figure 4.25: S1 area fraction top (AFT) vs. uncorrected primary scintillation (S1) signal for incorrectly S1-S2 matched ^{210}Po events that originate from the cathode. These are selected by requiring $S1_{top} < 4.2{\times}10^4$ PE, as shown in figure 4.24b (left of the red dashed line). This suggests that events on the cathode wires do not only lose all their deposited electrons, but also lose part of their primary scintillation light.

uncertainty on the inferred z from the $S1_{top}$ and $S1_{bottom}$ values is about 2.5 cm (68% CL).

4.4.4 Depth profile of all ^{210}Po events

Now that all the incorrectly matched S1-S2 ^{210}Po events are assigned a z-value, we compare this depth profile with the one from the correctly matched S1-S2 ^{210}Po events. Figure 4.26 shows the z-distributions for the correctly (blue) and incorrectly (red) matched S1-S2 ^{210}Po events, together with the sum (green).

Out of the total of 200k ^{210}Po events found in SR0, 40k have an S2 that causally corresponds to the S1 and 160k did not. This clearly demonstrates that to estimate the concentration and depth profile of ^{210}Po we cannot solely rely on the information extracted from the S2 (x,y and drift time). As ^{210}Po events originate from the surface of the materials within the TPC they are thus created in a charge-insensitive region. Of the 160k events found without a correct S2, 40k are assumed to originate from the cathode wires[20]. The depth profile of the correctly matched S1-S2 ^{210}Po events does not follow that of all ^{210}Po events. Where the blue line shows a higher concentration of events in the top 30 cm, the green line shows both

[20] We assume all these alphas are from ^{210}Po, but they should also include other isotopes from the radon decay chain.

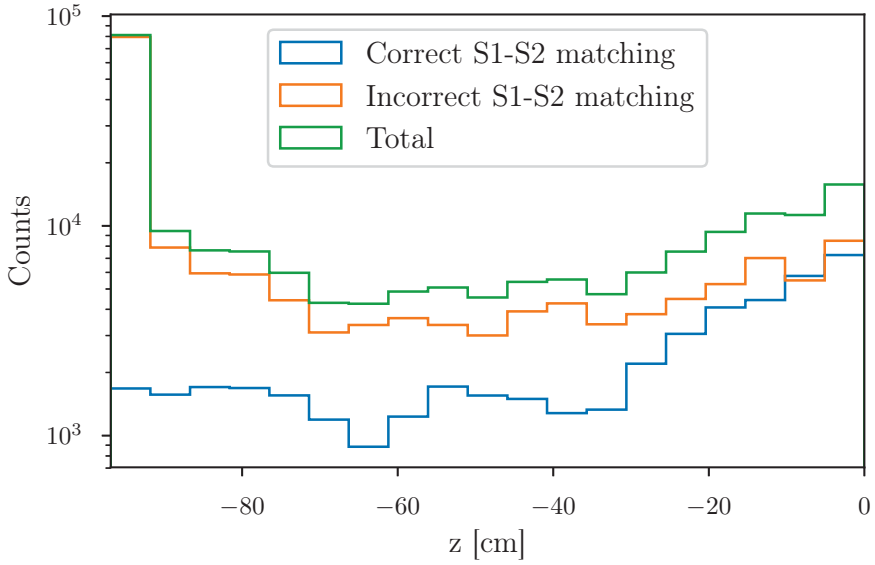

Figure 4.26: Depth distribution distributions of correctly (blue) and incorrectly (red) matched S1-S2 ^{210}Po events, together with the sum of both (green). Of the total of 200k ^{210}Po events, 20% are correctly matched, 20% are incorrectly matched and originate at the cathode, and 60% are incorrectly matched and come from the walls.

an increase in the top and bottom of the TPC. Furthermore, it shows that one fifth of all the ^{210}Po events are found at the cathode. Several questions remain open for now: *Why does the probability of losing electrons seem depth-dependent? Why do we measure less ^{210}Po events in the middle region (-70 cm < z < -40 cm) of the TPC?* Such questions ask for further research[21], not only for a better understanding of the XENON1T TPC, but also for the development of cleaner material surfaces for the next generation of dark matter detectors.

4.4.5 Identifying afterpulses with ^{210}Po events

The last thing to do in this section is to come back to the question: What produces the measured S2 for those ^{210}Po events that lose all their electrons on material surfaces? Figure 4.19 did not investigate the origin of the events in region 'C', which we will do now. In the region of

[21] One possible explanation is that there is a depth-dependent selection effect. We only select events with a valid S1 and S2, but the creation probability of the S2 (by the size of the measured S1 in the PMT array) could be depth dependent.

$-0.5\,\text{cm} < z < 0.25\,\text{cm}$, the event populations have discrete z-values. Figure 4.27 shows the events from region 'C', now as a function of drift time between S1 and S2, instead of reconstructed depth. Both the unusually short drift times [22] and the fact that they are discrete, hint at a detector artefact.

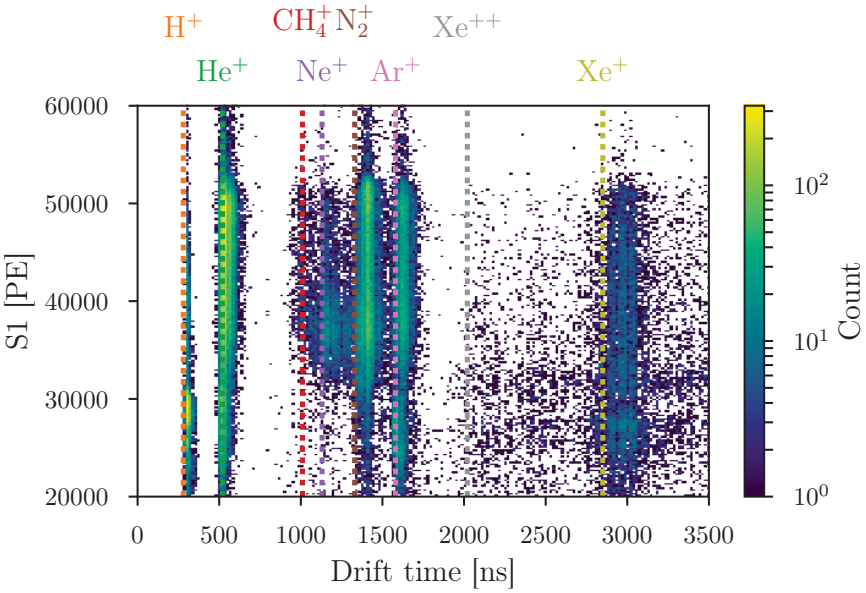

Figure 4.27: Uncorrected primary scintillation signal (S1) vs drift time of the incorrectly S1-S2 matched ^{210}Po events with $z > -0.5\,\text{cm}$ (events in region 'C' of figure 4.19). The discrete drift times can be explained by afterpulses from ionized residual gas within the PMTs. The color dashed lines correspond to the measured delay times for specific ion afterpulses in XENON1T PMTs [85].

One such known artefact are afterpulses within the PMTs. During PMT testing, these were observed together with their characteristic delay times [85]. Afterpulses are created by ionization of residual gas molecules in the PMT by accelerated photoelectrons. These positive ions drift to the photo cathode, where they release electrons and create an afterpulse. As the delay time is both mass and charge dependent, it can be written as [85]:

$$t = \left(1.134\,\frac{\text{V}^{1/2}\mu\text{s}}{\text{cm}}\right)\sqrt{\frac{L^2}{V_0}\frac{M}{Q}}, \tag{4.5}$$

[22] The maximum drift time in the TPC is about 700 μs.

with L in cm, V_0 in volts and t in μs. M/Q is the mass-to-charge ratio of the specific resiudual gas ion. It is set in number-of-nucleons/units-of-charge and is thus dimensionless. In the case of XENON1T PMT (R11410-21) the distance is $L = 4.1\,\text{cm}$. When operated at 1500 V, using the XENON1T voltage divider, the potential difference between the cathode and the first dynode corresponds to $V_0 = 323.4\,\text{V}$ [85]. These delay times are shown in figure 4.27 as coloured dashed lines, corresponding to the ions. Figure 4.27 shows that the event populations coincides with the delay times for eight different ions. The fact that the created signals are identified as S2 signals by the data processor can be explained by the fact that a big S1 signal triggers also a train of single electrons (SE). The SE combined with the afterpulses could lead to an S2-like signal. Only if the afterpulse is leading in determining the reconstructed S2 peak time, can these discrete drift times be matched to the characteristic delay times. To check for Xe leaking into the PMTs, weekly LED measurements are used. A leaking PMT will show an increasing afterpulse rate over time. This analysis shows that afterpulses in XENON1T can also be investigated by high energy ^{210}Po alpha events in background data.

4.5 Matching the ER background spectrum

Up to now, we focused on alpha decays to determine the upper and lower bounds on the concentration of ^{214}Pb. This set for SR1 an upper bound of $(13.7 \pm 0.7)\,\mu$Bq/kg from ^{218}Po and a lower bound of $(4.4 \pm 0.2)\,\mu$Bq/kg from ^{214}Po. There is no known model of how the cathode cleaning effect is dependent on the decay time, the LXe flow, the electric fields or the cathode design. For this reason, we cannot get a better estimate of the concentration of ^{214}Pb with this method. The other method, which we will present now, is based on fitting the ^{214}Pb spectrum together with all the other components to the total ER background spectrum. This requires detailed knowledge of the spectral shapes of all components, the cut efficiencies over the full energy range (up to about 3 MeV), the energy dependent energy resolution and the depth dependence of *g1* and *g2*. This analysis is work in progress and we only present preliminary results. These we compare with the Monte Carlo expectations (section 4.1.1) and the alpha analysis (section 4.2.2). After comparing the measured and expected background levels, we determinate if XENON1T achieved its ultra-low background goals.

4.5.1 The ^{214}Pb spectrum

As described in section 4.1.3, ^{214}Pb and ^{212}Pb are the only two isotopes in the radon and thoron decay chains that contribute to the low energy ER background. Since the rate of ^{220}Rn is about a factor of 100 lower than that of ^{222}Rn, and the spectral shapes of ^{212}Pb and ^{214}Pb behave similarly, we only focus on ^{214}Pb. Figure 4.28 shows the decay scheme of ^{214}Pb. It decays by e^- emission to either one of the excited states, or immediately to the ground state of ^{214}Bi. It has six β^- and about 20 internal γ transitions. With a branching ratio of (9.2 ± 0.7)% and endpoint energy of $E_{\beta,max}$ = 1019 keV, it decays directly to the ground state without emitting additional gammas. Due to the complexity of the decay, we calculate the energy overlap of the spectrum with the dark matter search region (1 - 12 keV) with dedicated Monte Carlo simulations.

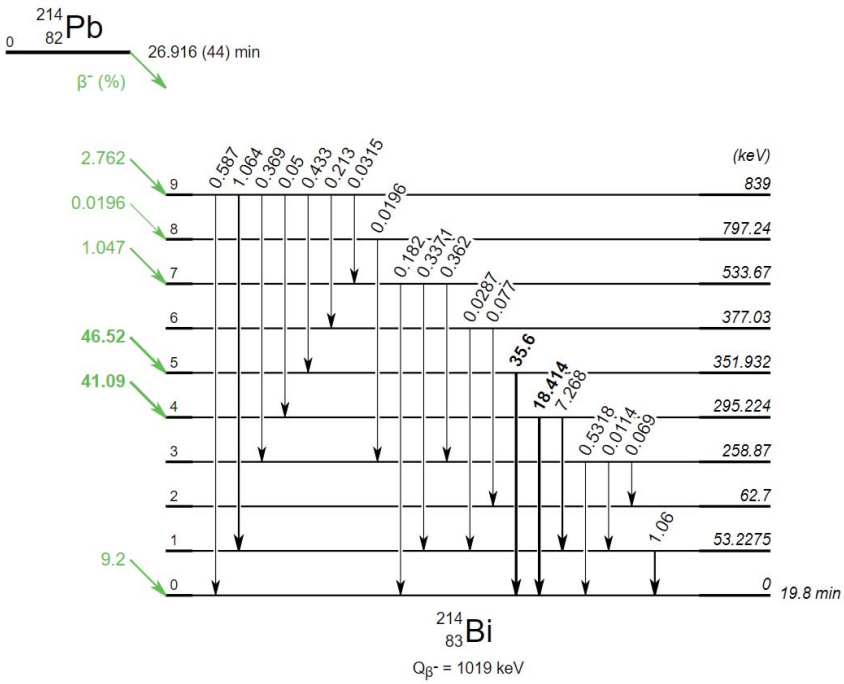

Figure 4.28: Decay scheme of ^{214}Pb. From [129].

A total of 5×10^8 ^{214}Pb events are simulated using the particle simulation framework GEANT4 [130], using a full description of the XENON1T detector geometry [84] and physics list [93]. For every particle interaction inside the LXe, the position, time, deposited energy, particle type and responsible energy-loss process are recorded. The ^{214}Pb decays are assumed

to be homogeneously distributed throughout the active xenon volume[23]. We select events within the 1 ton SR0 fiducial volume, select single scatters only and apply energy smearing. The energy smearing is to account for the finite (energy-dependent) energy-resolution found in XENON1T [131]. The energy smearing function is:

$$\frac{\sigma_E}{E} = \frac{a}{\sqrt{E(\mathrm{MeV})}} + b, \tag{4.6}$$

with $(a = 31.17 \pm 0.26)\,\mathrm{MeV}^{1/2}$ and $b = 0.39 \pm 0.02$, as found by fitting the peaks of the ER background spectrum, see figure 3.14.

In 90.8% of the time ^{214}Pb decays by emitting a gamma ray. The question is if the emitted photon will create a second scatter that is resolvable in XENON1T by the vertex reconstruction of the interaction. The actual interaction distance depends on the Compton and photo absorption scattering lengths in LXe, which are both dependent on the gamma ray energy. The difference between a measured single and multiple scatter is determined by the S2 peak separation resolution. Depending on both the interaction depth and the S2 sizes, between 2 and 20 mm separation in the z-direction is needed to identify a multiple scatter in XENON1T [132]. Only events which effectively appear as a single scatter are selected. The result of this procedure for the ^{214}Pb spectrum is shown in figure 4.29.

Figure 4.29 compares the ^{214}Pb spectrum with two different S2 separation resolutions. The blue spectrum assumes a constant S2 peak separation resolution of 3 mm along the z-axis over the full depth range. This assumption was based on knowledge from XENON100 [133]. The red curve incorporates the knowledge gained from XENON1T, which assumes a new depth-dependent S2 peak separation resolution. Below 250 keV no real difference is visible between the two curves[24], this is because the naked decay of ^{214}Pb (without an additional gamma ray) is not influenced by the ability to distinguish between single and multiple scatters. Only above about 300 keV are rate differences clearly visible. Due to the decrease of the S2 peak separation resolution for lower z-values, XENON1T does not achieve the expected power in separating single scatters from multiple scatters. The vertical gray dashed lines depict the energies of gammas, with the highest branching ratios, originating from the excited ^{214}Bi states. The rate is normalized to $(\mathrm{kg} \cdot \mathrm{day} \cdot \mathrm{keV})^{-1}$, given a ^{214}Pb concentration of 10 μBq/kg. With this knowledge of the shape of the ^{214}Pb spectrum we can now fit it to the whole ER background spectrum.

[23] This assumption was confirmed in section 4.3.

[24] The small wiggles in the Monte Carlo paper spectrum (blue) are due to low statistics.

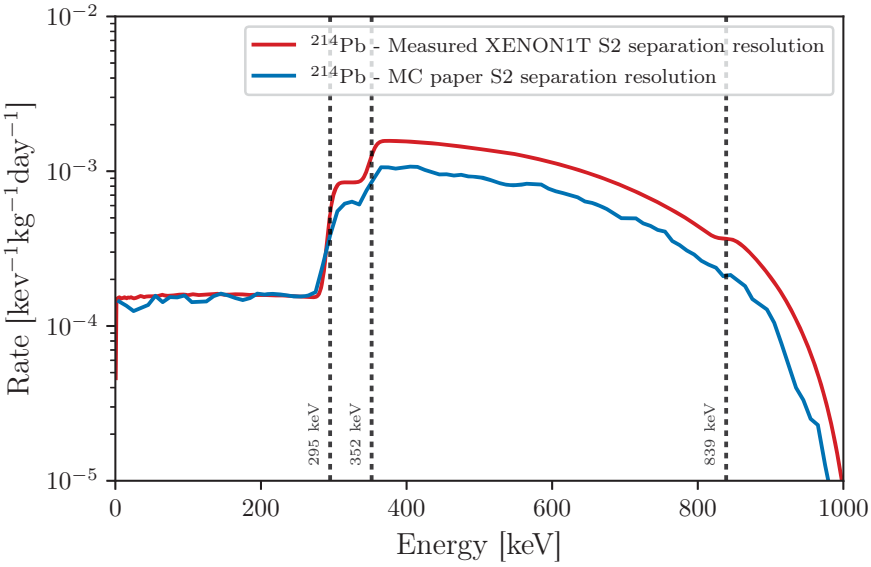

Figure 4.29: Spectral shapes of ^{214}Pb for different S2 peak separation resolutions. The assumed resolution (blue curve) of 3 mm in z was used in [93], and is constant over the whole depth of the TPC. The actual resolution in XENON1T of 2-20 mm is energy- and depth-dependent (red curve). At low energies (<250 keV) they predict the same rate, but for higher energies the decrease in resolution predicts more multiple scatters to be counted as single scatters. The vertical gray dashed lines depict the energies of gammas originating directly from the excited ^{214}Bi states.

4.5.2 Fitting the ER background spectrum

Full spectrum The following cuts are applied to the SR1 background data used for the ER spectrum: *DAQ veto*, *S2 Threshold*, *S2 Width*, *S1 Single Scatter*, *S2 Single Scatter* and *S2 Area Fraction Top*. The other cuts described in section 3.4 cannot be applied over the full energy range (0 - 3 MeV), as they are mostly optimized to work below 100 keV. The acceptance of this subset of cuts is flat up to about 200 keV, but decreases for higher energies. Therefore we will use the full-energy-range fit of the ER background spectrum only to identify the peaks. For determining the concentrations of the individual components a smaller energy range will be used. To convert cS1 and cS2 into energy we use the *g1* and *g2* values from section 3.5.1 in:

$$E_{\text{dep}} = 0.0137 \text{ keV} \times \left(\frac{cs1}{g_1} + \frac{cs2_b}{g_2} \right). \tag{4.7}$$

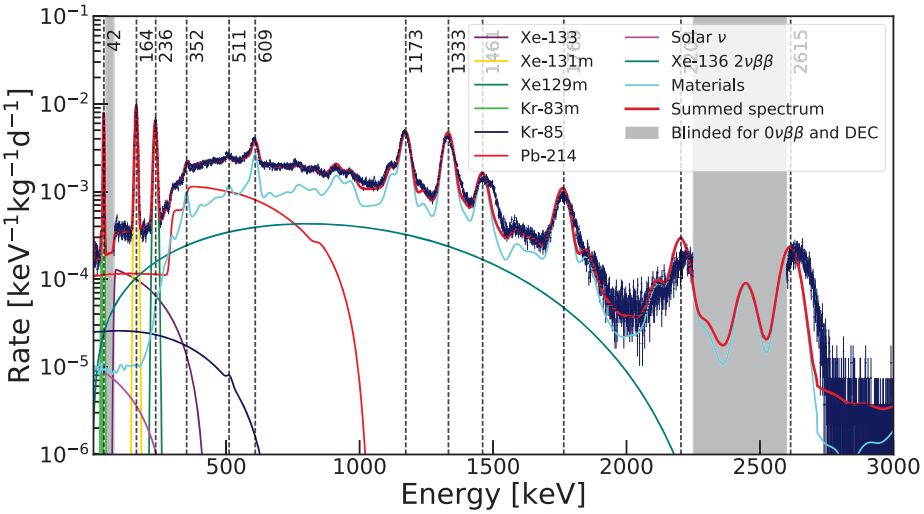

Figure 4.30: Full ER background spectrum of XENON1T (SR1) in 1 t fiducial volume with matched background sources [134]. The data is depicted by the blue points, while the MC spectra are depicted by the solid coloured lines. Up to about 2 MeV the sum spectrum (red) has good agreement with the peak positions in the data. The two grey energy regions are blinded for double electron capture and $0\nu\beta\beta$ searches. The fit to the full energy range of the ER background spectrum is used to identify the peaks, but due to not fully knowing the acceptance at high energies of the cuts, it is not used to determine the actual background rates.

The full-energy-range fit of the ER background spectrum (blue markers) for XENON1T is shown in figure 4.30. The individual components are shown for ^{222}Rn (red), materials (light blue), ^{136}Xe (dark green), ^{85}Kr (blue) and solar neutrinos (pink). Apart from these expected backgrounds, which were included in the MC ER background spectrum (see figure 4.1), several other components show up in the detector. These mostly originate from xenon isotopes [135] being activated during neutron calibrations. The following new sources are found:

- **^{133}Xe** (purple). This short-lived xenon isotope is activated by neutron calibration. It has a half-life of 5.2 d and decays by β^- emission ($E_{\beta,max}$ = 346.4 keV), followed by an immediate gamma of 81 keV. Due to the shape being more complex than the following three sources, the ^{133}Xe spectrum is constructed by Monte Carlo simulation.

- **^{131m}Xe** (yellow). This short-lived xenon isotope is also activated by neutron calibration. It has a half-life of 11.84 d and decays by

emitting a single gamma of 163.9 keV. Thus it is fitted with a single Gaussian.

- ^{129m}**Xe** (green). This short-lived metastable xenon isotope ($T_{1/2}$ = 8.9 d) is also activated by neutron calibration. It decays with a single gamma emission of 236.1 keV and is fitted by a single Gaussian.

- ^{83m}**Kr** (light green). The also metastable ^{83}Kr is used as a calibration source (as described in section 3.3.1) and originates from a small contamination of ^{83}Rb ($T_{1/2}$ = 86.2 d)[25] during commissioning. With internal conversion electron energies of 41.5 keV and 32.1 keV it is not a background for the dark matter search and can be used as a continuous calibration source in background data by fitting it as a double Gaussian.

Two energy regions (grey bands) in the data are still blinded: 50 - 80 keV to search for the double electron capture signal at 64 keV from ^{124}Xe and ^{126}Xe, and 2250 - 2600 keV to search for the signal of 2458 keV from neutrinoless double-beta decay from ^{136}Xe. The most stringent limits on these searches have been set by [136] and [137], respectively. Up to approximately 2000 keV, the peaks in the MC sum spectrum coincide with the location of the peaks in the data, but at higher energies a slight shift is visible, hinting at a non-linear energy response. This is not unexpected, as the experiment and the data processing is optimized for low energy response and this non-linearity could be caused by, e.g., ADC saturation and single electron tails.

Low-energy spectrum To determine the concentrations of the different ER components, the low-energy region of the ER background spectrum is fitted, shown in figure 4.31.

In this spectrum we fit only up to 300 keV, but use a 1.3 ton fiducial volume for the SR1 data [138]. The data shows good agreement with the combined fit, as shown by the residuals in the lower panel of the figure. The SR1 cuts are optimized for lower energy, but have an approximately flat acceptance of 0.93 up to 200 keV [139]. For higher energies, this decreases down to 0.8 at 300 keV. Therefore, we apply the cut acceptance to the individual spectra of the components and only fit up to 300 keV. At the lowest energies (< 10 keV), a new background is found of surface events[26] contaminating the ER band. Thus, the bins up to 10 keV are excluded from fitting [140]. Compared to figure 4.30, one extra component is added:

[25] No gammas from rubidium itself are found within the detector.
[26] These wall leakage events will be presented in section 5.2.

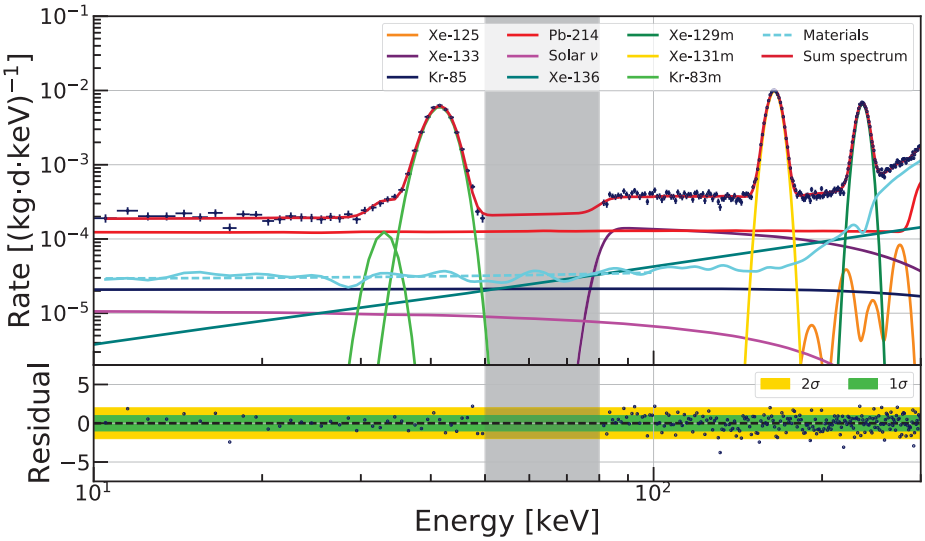

Figure 4.31: Fit of ER background spectrum in 10 - 300 keV in a 1.3 ton fiducial volume using SR1 data (χ^2/ndf = 1.17). The data (blue markers) shows good agreement with the sum spectrum (red) of the individual background components (in color). The double electron capture region (grey band) is blinded and not taken into account for the fitting. The residuals are shown below with the 1- and 2 σ bands. This fit is used to determine the background rates in table 4.6.

- ^{125}**Xe** (orange) This short-lived xenon isotope is created from ^{124}Xe, has a relatively low natural abundance (0.1%). But, due to its high thermal neutron capture cross section, it is produced during neutron calibration. With a half-life of 16.8 h it decays by β^+ or electron capture with energies of 188 keV and 243.4 keV, respectively. Its daughter is an excited state of ^{125}I, which immediately de-excites with the emission of an X-ray of 5.2 keV (L shell) or 33.2 keV (K shell) [141].

4.5.3 ER background levels

Total background Table 4.5 compares the expected background rates from MC [93] with the measured background rates found ER background spectrum fit of figure 4.31.

Source	Expected background (1 t) $[(\text{kg}\cdot\text{day}\cdot\text{keV})^{-1}]$	Measured background (1.3 t) $[(\text{kg}\cdot\text{day}\cdot\text{keV})^{-1}]$
Materials	$(7.3 \pm 0.7)\cdot 10^{-6}$	$(3.1 \pm 1.0)\cdot 10^{-5}$
^{222}Rn	$(1.54 \pm 0.15)\cdot 10^{-4}$	$(1.29 \pm 0.22)\cdot 10^{-4}$
^{85}Kr	$(7.7 \pm 1.5)\cdot 10^{-6}$	$(2.1 \pm 0.5)\cdot 10^{-5}$
^{136}Xe	$(2.3 \pm 0.3)\cdot 10^{-6}$	$(2.3 \pm 0.4)\cdot 10^{-6}$
Solar neutrinos	$(8.9 \pm 0.2)\cdot 10^{-6}$	$(6.8 \pm 0.9)\cdot 10^{-6}$
Total	$\mathbf{(1.80 \pm 0.15)\cdot 10^{-4}}$	$\mathbf{(1.90 \pm 0.24)\cdot 10^{-4}}$

Table 4.5: Expected [93] and measured ER background rates in the (1,12) keV energy range. The measured material and ^{222}Rn background rates are from the fit in figure 4.31 and are corrected for the cut acceptance. The other measured background rates are from RGMS measurements (^{85}Kr) or MC (^{136}Xe and ν), and are constraint in the fit.

While the material and radon concentrations are unconstrained in the fit of the background spectrum, the others are not. Due to the possible degeneracy of featureless (flat) spectra at low energy, the krypton, solar neutrino and ^{136}Xe spectra are fit using a prior of the expected value with Gaussian uncertainty. The value for the ^{85}Kr concentration is determined by Rare Gas Mass Spectrometry (RGMS), which is measured every few weeks. A value of $^{\text{nat}}\text{Kr/Xe} = (0.66 \pm 0.11)$ ppt is found, assuming the $^{85}\text{Kr}/^{\text{nat}}\text{Kr}$ ratio $= 1.65 \times 10^{-11}$ mol/mol from measurement [142]. We assume the same rate for ^{136}Xe as in [93], while the rate for solar neutrinos is lowered by 24% from [93], due to the suppression of the neutrino-electron scattering cross-section at low energy by the atomic binding effect [143]. The stated uncertainties in table 4.5 include the fit uncertainty and an systematic uncertainty on the acceptance of about 12% [27].

The measured material background is about four times higher due to an increase in the fiducial volume from 1 to 1.3 ton. This increase in fiducial mass is motivated by an increase in overall WIMP sensitivity[28]. The uncertainty of all the different material components are Gaussian-propagated in the sum. The radon background is about 15% lower due to the cathode cleaning effect, which was not taken into account in the

[27] The uncertainty on the cut acceptance is estimated by including the acceptance curve with a scaling and offset parameter in the background fit.

[28] These fiducial volumes will be presented in section 5.5.2.

MC. The krypton rate is about 2.7 times higher. This krypton concentration could have been reduced even further by the distillation column, but did not seem necessary before SR0, as it is a sub-dominant background. Overall, this shows that XENON1T has successfully reached its predicted background level.

Radon background Finally, the concentration of ^{214}Pb is constraint by the ER background fit and can be compared to the previous presented measurements. Table 4.6 shows the concentration of ^{222}Rn and ^{214}Pb from MC [93], emanation measurements (section 4.1.3), the S1-only α analysis (section 4.2.2)) and the ER background fit results. The α analysis sets a lower and upper limit from the concentration of ^{214}Po and ^{218}Po, respectively. The MC expectation assumes the same concentration of ^{222}Rn as of ^{214}Pb, because no cathode cleaning effect was taken into account. The found concentration of (8.4 ± 1.2) μBq/kg[29] for ^{214}Pb is in agreement with the limits from the S1-only analysis, and is below the MC expectation.

Method	^{222}**Rn**	^{214}**Pb**	**Units**
MC expectation	10	10	μBq/kg
Emanation measurements	11 ± 2		μBq/kg
S1-only α analysis	13.4 ± 0.9	4.4 - 13.7	μBq/kg
ER BG fit		8.4 ± 1.2	μBq/kg

Table 4.6: Comparison of expected and measured ^{222}Rn and its progeny, ^{214}Pb, concentrations in XENON1T.

The relationship between the internal radon concentration (A_{Rn}) and the differential background rate (R_{Rn}) in the energy region of interest (1 - 12 keV) is:

$$R_{Rn} = A_{Rn} \times 1.54 \cdot 10^{-5} \text{events/(kg day keV)}, \tag{4.8}$$

where the scale factor is derived from MC [93]. This relation has a 10% uncertainty due to different branching ratios in literature and the shape of the spectrum itself. The radon induced background rate is about 68% of the total background rate found from the ER background fit. The total ER background rate of XENON1T in the (1 - 12 keV) energy region is the lowest ever achieved in a dark matter detector. Figure 4.32 shows a comparison of the background rate for different experiments.

[29] This includes an additional 8% overal systematic fit uncertainty, estimated by changing the end point of the fit range to 250 keV and 350 keV.

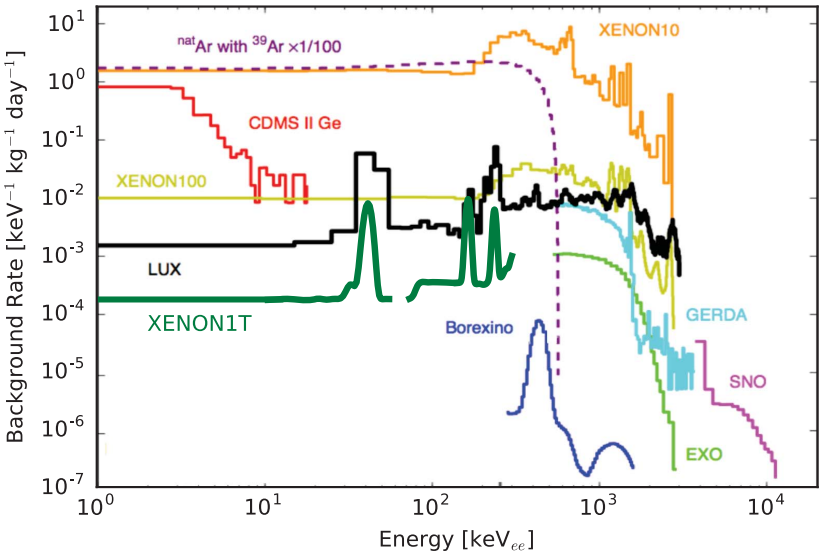

Figure 4.32: Background rate comparison between different experiments. The XENON1T spectrum (green) has the lowest ER background at low energy. XENON100 (orange), CDMS (red), XENON100 (yellow) and LUX (black) search for dark matter. Borexino (blue) and SNO (pink) are neutrino observatories, while EXO (light green) and GERDA (turquoise) are looking for $0\nu\beta\beta$ decay. A reference line (purple) for the rate of depleted argon is also shown.

4.6 Conclusion and outlook

To have a chance of measuring WIMPs scattering off xenon nuclei, XENON1T was designed and built as an ultra-low background experiment. Even with the discrimination power of 99.8% between nuclear and electronic recoils, the total electronic recoil background cannot exceed $\mathcal{O}(1000)$ events. From Monte Carlo we know the main background component in the low energy region (1-12 keV) is from radon.

To constrain the concentration of ^{214}Pb, the concentration of ^{218}Po and ^{214}Po were determined by means of an S1-only alpha analysis. Seven alpha lines were identified, all originating from the radon and thoron decay chains. The found concentrations of ^{218}Po (13.7 ± 1.1) μBq/kg and ^{214}Po (4.4 ± 0.2) μBq/kg give and upper and lower limit on the concentration of ^{214}Pb, respectively. Both isotopes showed stable decay rates over time and a homogeneous distribution throughout the TPC. From the alpha spectrum it is clear that ^{212}Pb, coming from the thoron decay chain, will not contribute to the total ER background above the 1% level.

The one isotope in the alpha spectrum, ^{210}Po, that could not originate from radon decaying within the liquid xenon, was found to originate from the PTFE walls and the cathode. Showing that its decay daughter, ^{210}Pb, can not decay into the inner fiducial volume to influence the WIMP search.

To get a better estimate of the precise ^{214}Pb concentration, its spectrum was determined and fitted against the full ER background spectrum. A ^{214}Pb concentration of (8.4 ± 1.2) μBq/kg was found, about 16% lower than the Monte Carlo expectations. By fitting all the individual ER background components together, a total ER BG rate was found of $(1.90 \pm 0.24) \times 10^{-4}$ $(\mathrm{kg \cdot day \cdot keV})^{-1}$, which is in agreement with the expected $(1.80 \pm 0.15) \times 10^{-4}$ $(\mathrm{kg \cdot day \cdot keV})^{-1}$. This does not only show that XENON1T has achieved its ultra-low background goals, but also that XENON1T has the lowest low-energy ER background rate of all dark matter experiments (as shown in figure 4.32). After determining the ER backgrounds, we are now ready to present the WIMP search results, which will be done in the next chapter.

Chapter 5

Fiducial volumes for WIMP analyses

I can proudly say that we are world leading in finding nothing.
— P.A. Breur

This chapter presents the construction of the fiducial volume (FV) used for the WIMP search of Science Run 0 (SR0). With the fiducial volume set, science data are unblinded and the result is interpreted to be consistent with a background-only hypothesis. For Science Run 1 (SR1) the spatial reconstruction was improved, leading to an increased fiducial mass and the final XENON1T result on the spin independent WIMP-nucleon cross section.

5.1 Determining the fiducial volume of SR0

The fiducial volume is the the LXe volume within the TPC that maximizes the sensitivity for detecting wimps. The sensitivity is influenced by both the total exposure (ton $\times$ year) and the ratio of expected signal over background events. Under the assumption of a flat signal acceptance within the whole TPC, the goal is thus to find the largest LXe volume in which the background is only dominated by the internal (i.e., radon) and not the external (i.e., material) backgrounds. Before optimizing the fiducial volume, we investigate the spatial distribution of low-energy background events within the TPC.

5.1.1 The background distribution

Figure 5.1 shows the low-energy[1] (cS1 < 200 PE) background distribution for the full SR0 exposure. All SR0 cuts (table 3.1) have been applied, except for the fiducial volume cut.

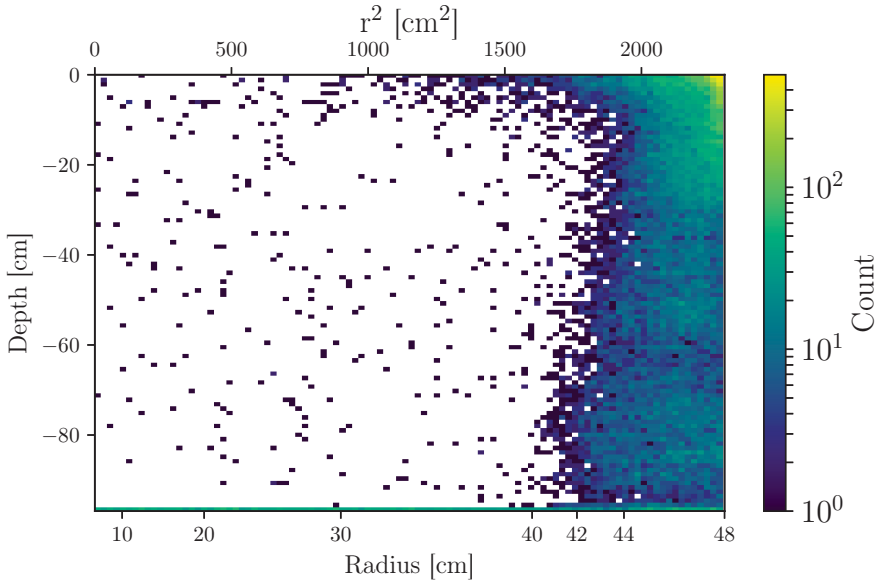

Figure 5.1: Spatial distribution of low-energy (cS1 < 200 PE) SR0 background events in depth versus radius. All SR0 cuts, except the fiducial volume cut, have been applied. The center region with only a few events is dominated by internal backgrounds, while the region at high radius ($r > 42$ cm) is dominated by material backgrounds. The horizontal line of events at the bottom of the figure correspond to events originating from the cathode ($z = -96.9$ cm).

As expected, most events interact at large radii, due to the self shielding property of LXe. Within the event distribution at the edge of the TPC ($r > 42$ cm), most events are in the top region ($z > -20$ cm). The region above the anode is filled with GXe, while the region below to cathode is filled with LXe. As the mean free path of a gamma ray is dependent on the density, the GXe provides less shielding than the LXe[2]. The horizontal line of events at $z \approx -96.9$ cm correspond to events originating from the cathode. The following two observations in the data were not expected:

[1] The WIMP search energy region ends at cS1 = 70 PE, but to increase statistics we enlarge the energy range.

[2] Due to the difference in vapour pressure more krypton is also found in the gas phase.

- In the top region of the TPC ($0\,\text{cm} > r > 30\,\text{cm}$ and $-10\,\text{cm} > z > 0\,\text{cm}$), one expects more events from the MC [93] than are observed in data. In the top few cm of LXe low-energy gamma rays, originating from within the gas, should interact. After the SR0 analysis, it was discovered that the lack of events in this region is caused by the merging of S1 and S2 signals by the processor for short drift times.

- The event distribution at the TPC wall ($40 < r < 48\,\text{cm}$) is too broadly distributed in r. The event selection of $\text{cS1} < 200\,\text{PE}$, corresponds to $\text{cS2} < 1 \times 10^4\,\text{PE}$. Using equation 3.2 to convert cS1 and cS2 into deposited energy, this gives gamma energies of up to about 20 keV. Gamma rays up to such energies have a mean free path (see figure 2.13) smaller than $10^{-2}\,\text{cm}$. Thus, the interaction is expected to occur within the first cm of LXe. The position reconstruction resolution of TPF (figure 3.3b) is better than 2 cm at the S2 threshold[3] of 200 PE. Together these two effects should not result in such a broad event distribution in r. We will discuss this problem further in this section.

Figures 5.2 and 5.3 show the spatial distributions off the same low energy background, but now in (x,y) and (ϕ, r^2,), respectively.

A ϕ-dependent TPC radius Figures 5.2 and 5.3 show that the broad event distribution at the edge is ϕ-dependent. To get a better understanding of where these events originate from, a study was done on the ϕ-dependence of ^{210}Po alpha decays. Because these originate from the PTFE wall, the lower 99% quantile of the ^{210}Po distribution in each ϕ-slice represents where the TPC wall is reconstructed [144]. This ϕ-dependent TPC radius, shown in figure 5.3, represents how much radial bias an event that originates at the PTFE wall can have. The fact that this ϕ-dependent TPC radius from ^{210}Po follows the same structure as observed in the low energy background distribution, tells us that the probable origin of these events is also the PTFE wall. The reason that this radial effect did not show up in the ^{210}Po analysis of section 4.4, is that for that study a 3D time-dependent Field Distortion Correction (FDC) was applied. For SR0, only a simpler 2D FDC was applied (section 3.2.2). We will present the 3D FDC in section 5.5.

Charge-up of the PTFE wall The working hypothesis for the observed ϕ-dependent radial bias [145] is that the individual PTFE panels

[3] It improves for bigger S2 signals.

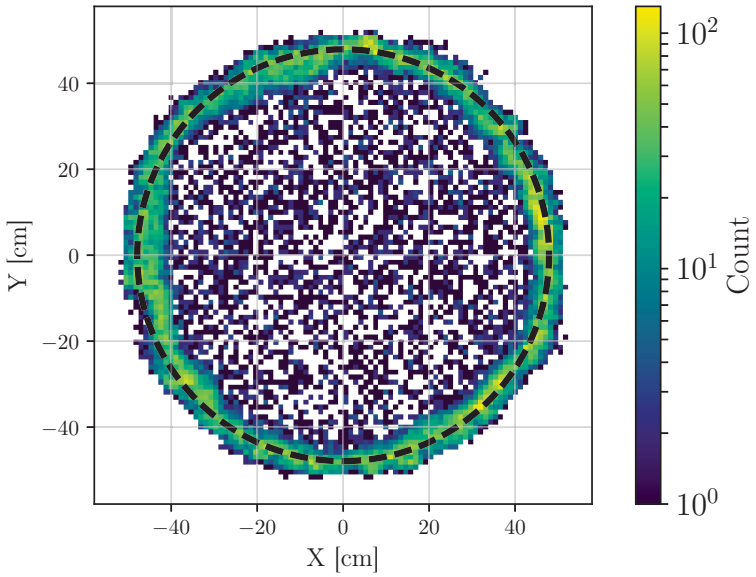

Figure 5.2: Spatial distribution of the low energy background in y versus x. The event distribution at high radius shows signs of a ϕ-dependent radial bias.

become more (negatively) charged over time, and such an effect has already been reported by LUX [146]. The negative charge of the PTFE panels will push the upward drifting electrons inwards, depending on the amount of charge buildup and the distance to the wall. The PTFE wall of XENON1T consists of 48 individual full-height PTFE panels and it is unclear why some regions show more charge-up than others. Two regions with a large inward bias correspond to regions with more turned off PMTs [101] in the outer ring of the top PMT array. Specifically, the regions around $x = -20,\ y = 40\,\text{cm}$ ($\phi \approx 110\,\text{degree}$) and $x = -40,\ y = -20\,\text{cm}$ ($\phi \approx -150\,\text{degree}$) both show a large inward bias of events and have two dead PMTs each in the top ring of the top PMT array. Regions with more dead PMTs have on average a larger position reconstruction uncertainty [147], which would increase the inward radial reconstruction bias. The large inward bias at $\phi \approx 40\,\text{degree}$ ($x = 38,\ y = 26\,\text{cm}$) does not correspond with any dead PMTs.

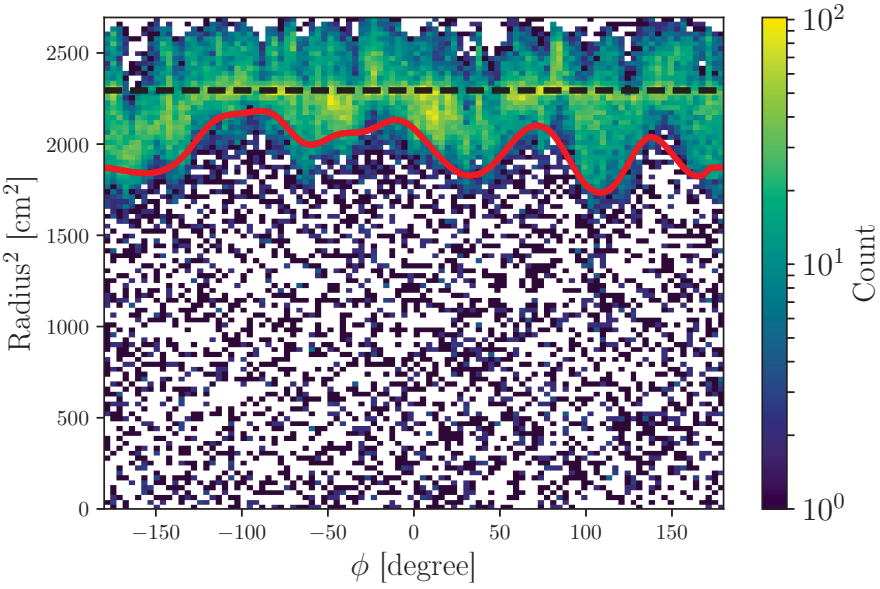

Figure 5.3: Spatial distribution of the low energy background in radius^2 versus ϕ. The event distribution at large radii follows the same ϕ-dependent radial bias found for the ^{210}Po distribution (red line) originating from the PTFE wall. Low-energy background events originating at the PTFE wall can thus be reconstructed inwards with a ϕ-dependent radial bias. The maximum TPC radius is represented by the dashed black line.

5.1.2 The fiducial volume shape

Figure 5.4 shows the low-energy background distribution with two different fiducial volume shapes. The cylindrical volume is the official SR0 FV (see section 3.4), it is bound by $-92.9\,\mathrm{cm} < z < -9\,\mathrm{cm}$ and $r < 36.94\,\mathrm{cm}$. For comparison, a superellipse is shown, defined in $z - r^2$ space by

$$\left(\frac{|z - z_0|}{v_z}\right)^p + \left(\frac{r^2}{v_r}\right)^p < 1, \tag{5.1}$$

with z_0 the center of the ellipsoid along the z-axis, v_z the maximum elongation along the Z-axis, v_r the maximum elongation along the r^2-axis and p the curvature factor. The superellipse shown in figure 5.4 has the same lower and upper z-bound as the SR0 FV, and has $v_r = 40.12\,\mathrm{cm}$ and $p = 2.5$.

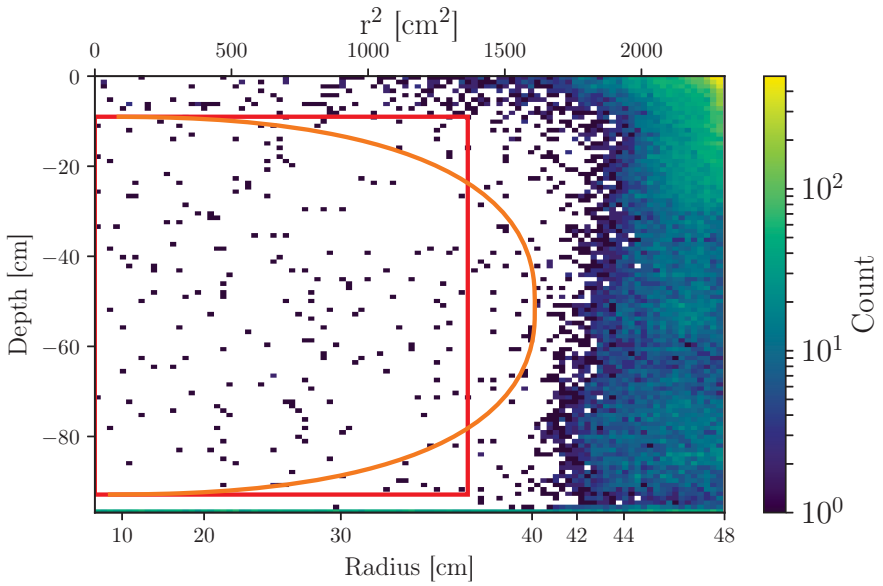

Figure 5.4: The low-energy background event distribution together with a cylindrical (red) and super-elliptical (orange) fiducial volume. The cylinder is the official SR0 fiducial volume, while the superellipse is shown for comparison. Both volumes contain equal xenon mass ($\approx 1\,\mathrm{t}$).

The cyindrical and super-ellipse fiducial volumes contain equal liquid xenon mass. For XENON100, the superellipse shape maximised the WIMP sensitivity [5]. We will now investigate if the observed spatial distribution of the low energy background in XENON1T advocates for one shape over another.

Lower z-bound Figure 5.5 shows the low-energy background event distribution in the bottom region (-98 cm $< z < -90$ cm) of the TPC for different r-slices. The r-slices are chosen such as to ensure equal volumes in each slice. The event distributions for the different r-slices mostly overlap and the mean of the distributions of cathode events is not r-dependent (up to 40 cm). Therefore, the combined data of all slices is fit with a Gaussian of $\mu = (-96.32 \pm 0.11)$ cm ($1\,\sigma$). No other structure is observed between -95 cm $< z < -90$ cm in the event distribution. The lower z-bound (z_{min}) for the FV is (conservatively) set to -92.9 cm, which is 4 cm away from the cathode[4], and about $28\,\sigma$ away from the observed cathode event distribution[5].

Upper z-bound Figure 5.6 shows the low-energy background event distribution in the top region ($z > 10$ cm) of the TPC for different r-slices. An r-dependence of the event distribution is visible: for higher radii, more events interact within the first 10 cm in z. There is also an over-density of events in all four r-slices in the region $-7 < z < -6$ cm.

Figure 5.7 shows again the low-energy background distribution in depth versus radius, but now with extended radius and in color the value of S2 Area Fraction Top (AFT). A horizontal line of events within -7 cm $< z < -6$ cm all have an S2 AFT of around 0.7. These events interacted in the first cm of gas around the PMTs, from where their electrons drifted towards the anode and created an S2 [6]. With a drift distance of about 6 cm and a maximum electron drift velocity in gas[7] of $1.4\,\mu$m/μs, these events get an associated depth of around -7 cm.

To exclude these gas events, the upper z-bound (z_{max}) is set to -9 cm, as shown in figure 5.6. This has the added benefit of also excluding the top few centimetres of LXe, where there is an unknown detection efficiency loss. Including a region with a lower signal acceptance would lead to an overestimation of the WIMP sensitivity. Figure 5.7 also reveals another problem for events reconstructed with radii outside the TPC. The position reconstruction algorithm, Top Pattern Fit (TPF), mis-reconstructs events in a sort of 'elephant-trunk' pattern up to $r^2 = 3000\,\text{cm}^2$. These events should be reconstructed at the TPC wall. This effect is found in both the TPF and Neural Net (NN) reconstructed positions and is understood to

[4] The 2D FDC correction changes the observed cathode position to the 'reconstructed' cathode position, leading to about a 1% shift of the depth reconstruction.

[5] Assuming the cathode event distribution is Gaussian in nature.

[6] This is caused by the high fields close to the anode mesh, and not by the amplification region between the gate and anode, as is the case for events from the LXe.

[7] The electron drift velocity in gas is calculated at -95 C and 1.94 bar with Garfield++ for a drift field of 1 kV/cm.

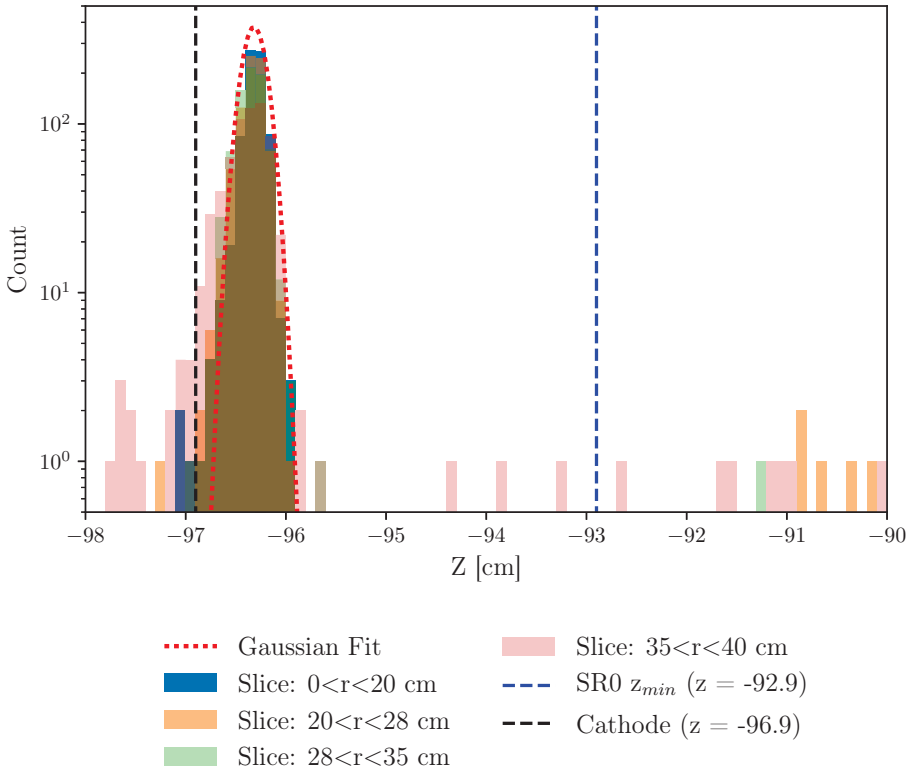

Figure 5.5: Depth distribution of the low-energy background events in the bottom region of the TPC for different r-slices (coloured histograms). The lower z-bound (z_{min}) for the fiducial volumes in figure 5.4 is set to -92.9 cm. The combined slices are fitted with a Gaussian (red dotted) and the z_{min} bound is about 28 σ away from the reconstructed cathode event distribution.

be a problem with the simulated LCE maps for the outer two top PMT rings [101].

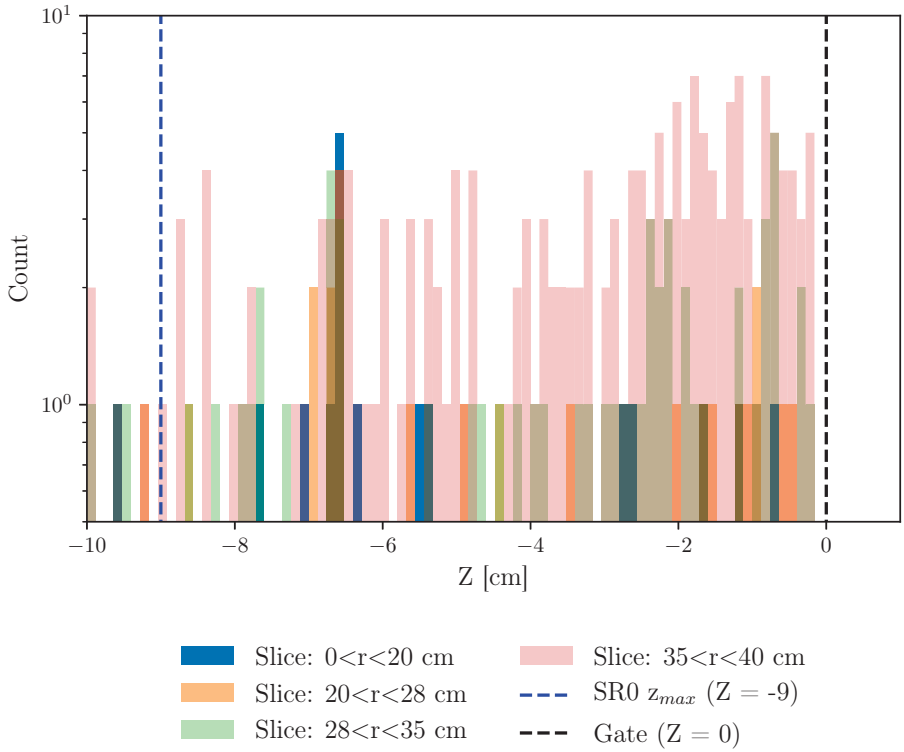

Figure 5.6: Depth distribution of the low-energy background in the top region of the TPC for different r-slices (coloured histograms). For r-slices with higher radii, more events interact in the top 10 cm of the TPC. An over-density of events is observed in the region -7 cm $< z < -6$ cm, which are gas events passing the cuts. The $z_{max} = -9$ cm bound is about 2 cm away from the gas event distribution, and 9 cm away from location of the gate (black dashed).

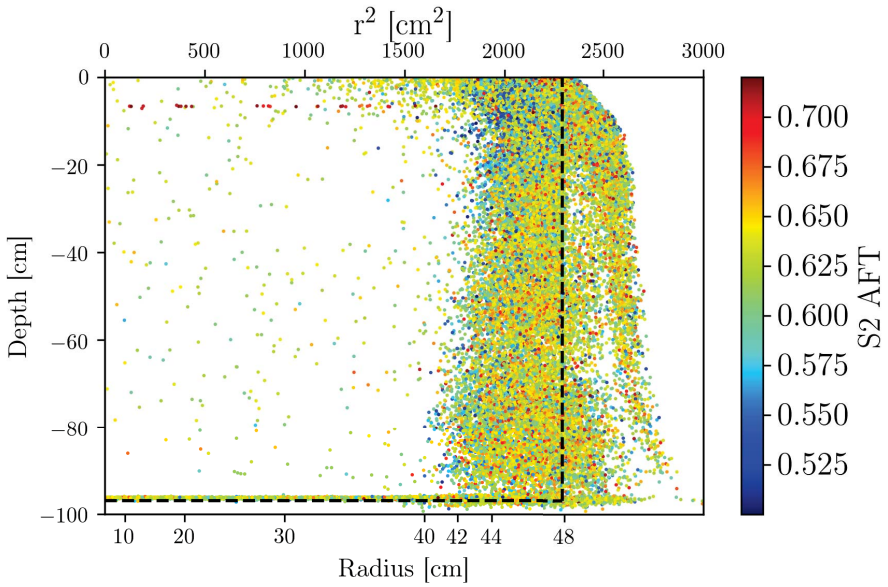

Figure 5.7: Scatter-plot of low-energy backgrounds events in depth versus radius with the associated S2 area fraction top (AFT) value in color. A (horizontal) distribution of gas events with high S2 AFT is observed around z = −7 cm. The position of the cathode and TPC wall are shown by the horizontal and vertical black dashed lines, respectively. Due to a problem with the MC LCE maps, TPF mis-reconstructs a population of events into an 'elephant-trunk' shape around $r^2 > 2500$ cm^2.

5.2 The surface background

With the lower and upper z-bounds fixed, only the maximum radius and the shape of the fiducial volume have to be determined. The z-bounds are set to exclude specific backgrounds such as events from the cathode and from the gas. Both the shape and maximum radius of the SR0 FV were chosen to exclude a new background: surface events originating from the wall that could leak into the fiducial volume. Any electronic recoil background can be discriminated from nuclear recoils (signal like) with $(99.71 \pm 0.21)\%$ efficiency, as calculated from the ER and NR calibration (section 3.6). The problem with events originating at the PTFE wall is that they loose part of their charge signal, as shown by the ^{210}Po events (see figure 4.18b of section 4.4). If an electronic recoil originating at the TPC wall lost part of its charge signal, it could not be distinguishable from a nuclear recoil by its position in cS1-cS2 space relative to the ER and NR band.

This problem could have been solved by incorporating the spatial information (r,z) into the likelihood. This was not done for SR0, because, due to the problems with the position reconstruction of wall events, it was unclear how to build a correct model. The surface background does not show a z-dependence, but only an r-dependence [148]. This lead to the decision of a cylindrical FV for SR0 with an maximum radius that ensures an expectation value of about zero wall leakage events.

Figure 5.8 shows for three cylindrical volumes the leakage events in $\log_{10}$(cS2/cS1) versus cS1 space. This analysis was done by unblinding the region of interest ROI outside the SR0 FV, while keeping the ROI within that volume blinded. Even though these events are below the NR median, and would thus be counted as WIMP-like events, it is clear that the bulk of these events cannot be WIMP signals. For a WIMP signal we expect $\mathcal{O}(1)$ events (section 4.1.2), and they would be homogeneously distributed throughout the LXe volume.

Figure 5.8 also shows a sideband region of $100 < cS1 < 200$ PE. This sideband was unblinded at an earlier stage to test if a fiducial volume larger than 1100 kg was possible without having $\mathcal{O}(1)$ surface background events in the ROI, which was not the case. For the SR0 cylindrical volume ($r_{max} = 36.94$ cm) the expected backgrounds from surface events can now be calculated.

Figure 5.9 shows how the number of events leaking into the region of interest increases for larger cylindrical volumes[8]. The upper and lower z-bounds are set and only the radius is increased. The ROI is defined here

[8] This an approximate fiducial mass due to a slight underestimation of the LXe density.

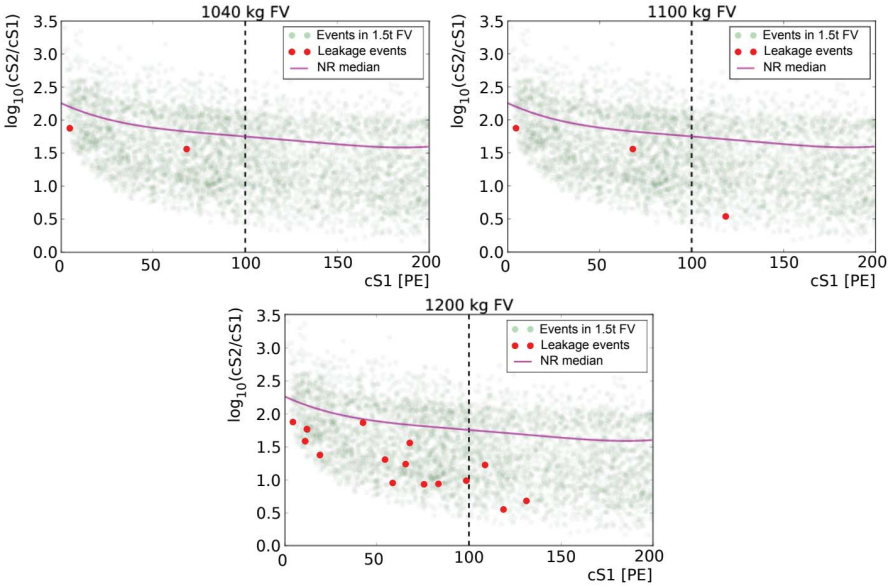

Figure 5.8: Leakage events in three representative fiducial volumes used in figure 5.9 in $\log_{10}$(cS2/cS1) versus cS1. The NR median (purple) is taken from calibration data. Cylindrical fiducial volumes with larger radii show more leakage events that could be counted as nuclear recoils (signal like). Only data outside the SR0 FV was unblinded for this analysis.

as cS1 < 100 PE, cS2 > 200 PE and $\log_{10}$(cS2/cS1) below the NR median. This surface background shows a clear r-dependence, and is fit with both an exponential and a power law (of the form $1/m_{xenon}^{p}$).

The exponential fit to the data in figure 5.9 results in an expectation value of (0.5 ± 0.3) wall leakage events in the SR0 FV for the full exposure. The uncertainty is calculated from the difference in fit results between the exponential and the power law fit. The fit range could not be increased up to the maximum volume (maximum TPC radius). Figure 5.7 shows that part of the event distribution close to the TPC wall is mis-reconstructed far outside the TPC. Therefore, modelling the wall leakage backgrounds up to the TPC wall seems not feasible without first improving the position reconstruction.

5.2.1 Mass of the SR0 fiducial volume

The LXe density is calculated using the average temperature of $(-96 \pm 0.8)\,^{\circ}$C and pressure of (1.936 ± 0.017) bar during SR0 operation [149]. Using the NIST webbook for LXe density [150], this gives a (conservative)

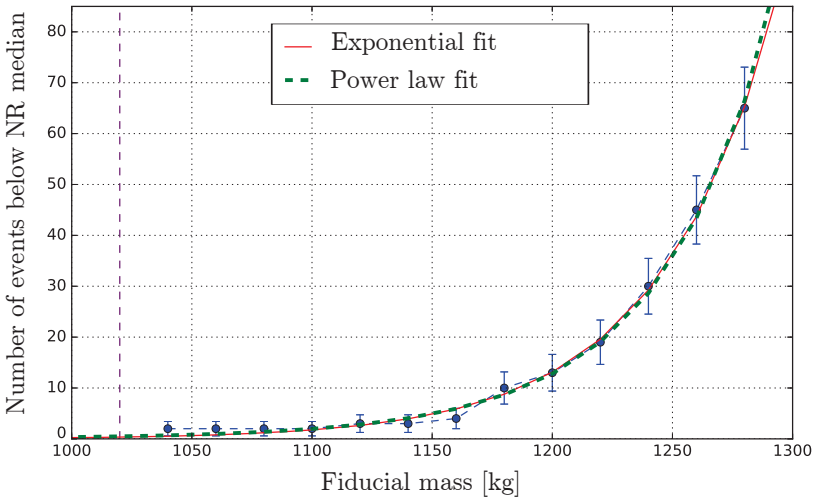

Figure 5.9: Number of events (blue markers) leaking below the NR median in the region of interest versus approximate fiducial mass of the cylindrical fiducial volume. The cylindrical fiducial volumes only differ in radius. The data is fit by an exponential (red) and power-law (green dashed) fit to estimate the expected number of wall leakage events in the SR0 FV (purple dashed). The uncertainties on the data points are overestimated and come only from statistics (Poisson distributed).

estimate for the LXe density of $(2.862 \pm 0.004)\,\mathrm{g/cm^3}$. The total active TPC volume (confined between the cathode and gate) is $(700.2 \pm 1.5)\,\mathrm{l}$, resulting in an active target mass of $(2003.8 \pm 5.2)\,\mathrm{kg}$. The SR0 fiducial volume, defined by $-92.9\ \mathrm{cm} < z < -9\,\mathrm{cm}$ and $r < 36.94\,\mathrm{cm}$, thus has a geometric mass of $(1029.4 \pm 2.8)\,\mathrm{kg}$. This is cross checked with the percentage (52.61%) of all krypton calibration events (assumed to be homogeneously distributed) in the SR0 FV, resulting in a data-driven mass of 1054.2 kg. The official mass of the SR0 FV is $(1041.8 \pm 12.4)\,\mathrm{kg}$. This is the average of the geometric and data-driven mass, using the difference as the uncertainty [151].

5.3 Total background expectation

The total background expectation for SR0 is composed of six background components: Electronic recoils from primarily radon (see section 4.5.2), nuclear recoils from radiogenic neutrons and CEvNS, accidental coincidences from random pairing of uncorrelated lone S1 and S2 peaks, wall

leakage as described in section 5.2 and an anomalous background observed in ER calibration data. For each background the spectral shape (in $cS2_b$ vs cS1) and expected rate are determined before unblinding.

5.3.1 Background sources and spectral shapes

Figure 5.10 shows the dominant backgrounds in $cS2_b$ vs cS1 for SR0.

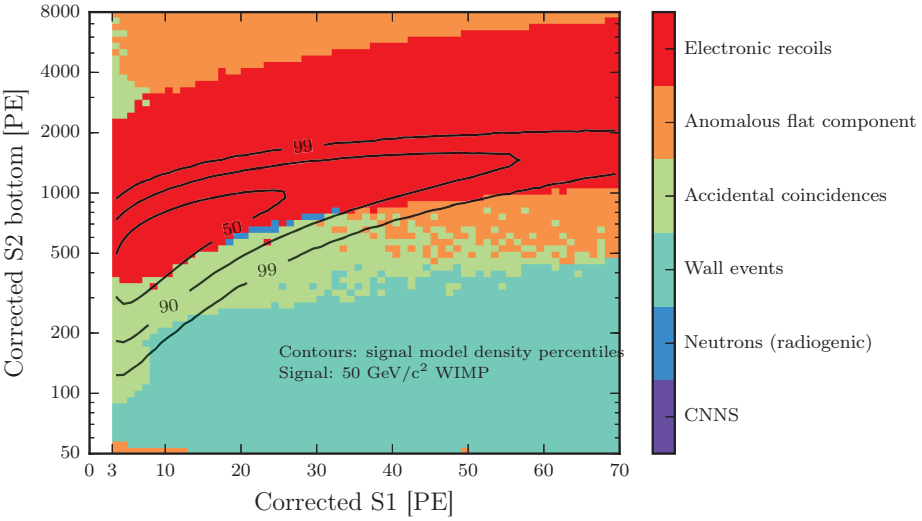

Figure 5.10: Expectation of dominant backgrounds in $cS2_b$ vs. cS1 for SR0. The expected signal for a 50 GeV WIMP is given by the contours in density percentiles. The expected rate for each background component is given in table 5.1.

The **ER background** mainly consists of beta decays of ^{214}Pb and ^{85}Kr which cause a flat energy spectrum in this energy range (see section 4.5.2). An ER model is build using the simulated XENON1T detector response. The energy deposition is converted into electrons and photons using a model similarly to [152]. The most important model parameters defining the shape of the ER band are the energy dependent light yield[9] and recombination fluctuation[10] [153]. The ER model is fit to the ER calibration data (section 3.6) [154]. The best fit values of both are comparable to those found in [152].

[9] Interchangeable with the charge yield, as they together add up to the same total number of deposited quanta, see equation 3.2.

[10] The recombination fluctuation manifests itself, among others, into the width of the ER band (in $\log_{10}(cS2/cS1)$).

The ER rate is left unconstrained in the fit, as the most stringent constraint comes from the data itself. The model incorporates uncertainties from the primary and secondary scintillation gains (g_1 and g_2), the processor and cut efficiencies, the electron extraction efficiency, the S1 and S2 spatial corrections and the electron lifetimes correction. Due to its high rate, the ER background is dominant over the full ER band region.

Nuclear recoils are expected from **radiogenic neutrons**, cosmogenic neutrons[11] and **CEvNS** (in figure 5.10 labelled as 'CNNS'). The spectra from MC simulation are converted into S1 and S2 signals using a NR response model, fit to the NR calibration data (section 3.6). The spectral shapes are very similar to those of WIMPs, but, due to their low rates, they are only the dominant background in a small part of the total parameter space.

Accidental coincidence (AC) events are created by pairing in time of uncorrelated lone S1 and S2 signals within one event window. Lone S1 signals can be created in charge insensitive regions (such as below to cathode), while lone S2 signals can be induced by photoionization at the electrodes. The AC model is created by selecting S1 signals appearing before the main S1 and randomly pairing them to S2 signals from events that have no valid S1. The model only incorporates events that pass all SR0 cuts.

An **anomalous background** is added to the background model due to non-Gaussian leakage found in the ER calibration data. It is a featureless (flat in $\log_{10}(\mathrm{cS2/cS1})$) background that mostly dominates in the regions where no other backgrounds are found.

The **wall background**, as discussed in the last section, is mostly dominant in the region $\mathrm{cS2}_b < 200\,\mathrm{PE}$. The measured S2 signal is reduced by charge-loss effects at the PTFE wall. The spectral shape of the wall background was determined in [155]. On top of the background model, the expected signal model of a 50 GeV WIMP is shown in density percentiles.

5.3.2 Background rate expectation

Table 5.1 shows the expected number of background events for SR0 (34.2 life days) in the $(1042 \pm 12)\,\mathrm{kg}$ fiducial volume.

The number of expected events is calculated in two different regions. The full region is defined by $\mathrm{cS1} \in [3, 70]$ PE, $\mathrm{cS2}_b \in [50, 8000]$ PE, which are also the ranges used for the ER and NR bands in figure 5.10. The reference region is constrained by the mean and the $-2\,\sigma$ line of the NR band. In the full region a total background of (63 ± 8) events is expected.

[11] As the expected rate of cosmogenic neutrons is one order lower than the rate of the other two contributions, it is neglected here.

	Full	**Reference**
Electronic recoils (*ER*)	(62 ± 8)	$(0.26^{+0.11}_{-0.07})$
Radiogenic neutrons	0.05 ± 0.01	0.02
CEvNS	0.02	0.01
Accidental coincidences	0.22 ± 0.01	0.06
Wall leakage	0.52 ± 0.3	0.01
Anomalous	$0.09^{+0.12}_{-0.06}$	0.01 ± 0.01
Total background	63 ± 8	$0.36^{+0.11}_{-0.07}$
50 GeV, 10^{-46}cm^2 WIMP	1.66 ± 0.01	0.82 ± 0.06

Table 5.1: Expected number of events in SR0 for each background component in the cylindrical (1042 ± 12) kg fiducial volume. The numbers are calculated for two diferent regions: the full cS1 $\in [3, 70]$ PE, cS2$_b$ $\in [50, 8000]$ PE search region and in a reference region between the NR median and its -2σ quantile in cS2$_b$ (see figure 5.11). Uncertainties on background components < 0.005 events are omitted. The ER rate is unconstrained in the likelihood, the best-fit values to the data are shown in parentheses. For comparison, the number of expected events from a 50 GeV, 10^{-46}cm^2 WIMP signal are shown for both regions for comparison. From [3].

If we would do a 'box counting' analysis in the full region[12], it is clear that a signal from a 50 GeV/c^{2}WIMP, with a cross section of 10^{-46} cm^2, is hard to distinguish from the expected statistical fluctuation of the total number of background events. In the reference region, on the other hand, the expected signal far exceeds the uncertainty on the total background expectation. Still, these numbers are not used to derive the dark-matter result, but only to guide the eye when the data is presented after unblinding. To derive the actual limit a profile likelihoods analysis is done[13]. This means that for every event found after unblinding, the probability is calculated of it being signal- or background-like, using the knowledge of the expected rate and spectral shape. For SR1 this is expanded to also include the event position (spatial distribution).

[12] Which we do not!
[13] Assuming no WIMP signal is found.

5.4 SR0 dark matter search result

5.4.1 Blinding

Up until now, the science data within the signal region was blinded to avoid introducing a human bias. This blinding criterion is defined as all events below the lower 1% Gaussian quantile of the ER band in cS2 vs. cS1 space[14]. It is dominated by the systematic uncertainty for a possible deviation of the fit model. Events with an S2 smaller than 150 PE are excluded from blinding, and used, e.g., for constructing the AC background model. The blinding criterion is applied to events with an cS1 up to 200 PE. Even though the WIMP search region is constrained to $\mathrm{cS1} \in [3, 70]$ PE, the region $\mathrm{cS1} \in [100, 200]$ PE can be used as a sideband. This sideband region was unblinded before the final unblinding to determine the influence of the wall background on the choice of FV in figure 5.8. Four days of science data were unblinded before the final unblinding as a cross check. This data was evenly distribution throughout the SR0 data taking period and no changes to the event selection were made afterwards.

5.4.2 Observed event distribution

Table 5.2 shows how the SR0 cuts, that were established pre-unblinding, select the data after unblinding.

First, the energy selection of $\mathrm{cS1} \in [3, 70]$ PE[15] was applied to reduce data[16]. In this energy range, about 10% of the events interacted within the fiducial volume. After selecting events with a valid S1 and S2 (S2 Threshold and Interaction Peak Biggest), about 900 events are left. This number reduces to 63 events after all cuts are done. This final event selection can now be compared to the expected spectrum (section 5.3.1) and rate (section 5.3.2) of the backgrounds.

Figure 5.11 shows the final 63 events in cS1 vs. $\mathrm{cS2}_b$. It is dominated by the systematic uncertainty for a possible deviation of the fit model. A total of 62 events are observed around the ER median and above the NR median. The spectrum and rate of these 62 events are compatible with coming from ER backgrounds. The 62 events in SR0 give a rate[17] of $(1.93 \pm 0.25) \times 10^{-4}\ (\mathrm{kg \cdot day \cdot keV})^{-1}$, which is compatible with the prediction of $(1.8 \pm 0.2) \times 10^{-4}\ (\mathrm{kg \cdot day \cdot keV})^{-1}$ from section 4.5.2.

[14] This is just above the NR median.

[15] The low energy background selection shown before was $\mathrm{cS1} \in [0, 200]$ PE

[16] The total number of digitized events in SR0 is about 16 Million.

[17] Calculated with: 62 events $\times$ 1041 $\mathrm{kg}^{-1}\times$ 34.2 $\mathrm{days}^{-1}\times$ 7.22 keV^{-1}. The last value is the integral over the detection efficiency of figure 3.11.

Cut name	N_{before}	N_{after}	$N_{removed}$	Fraction passed
S1 Low Energy Range	6071	6071	0	1.0
Fiducial Cylinder 1T	56831	6071	50760	0.10683
S2 Threshold	6071	1670	4401	0.27508
Interaction Peak Biggest	1670	932	738	0.55808
S1 Single Scatter	932	925	7	0.99249
S2 Single Scatter	925	504	421	0.54486
S1 Area Fraction Top	504	251	253	0.49802
S2 Area Fraction Top	251	139	112	0.55378
S2 Width	139	76	63	0.54676
S1 Pattern Likelihood	76	74	2	0.97368
S2 Pattern Likelihood	74	73	1	0.98649
S1 Max PMT	73	71	2	0.9726
DAQ Veto	71	68	3	0.95775
S2 Tails	68	64	4	0.94118
Single Electron S2s	64	63	1	0.98438
Pre S2 Junk	63	63	0	1.0

Table 5.2: Cuts applied to XENON1T SR0 data after unblinding. The description of these cuts are found in section 3.4.

Only one event (cS1 ≈ 68 PE) is found within the blinded region. This (outlier) event was already observed in the staged unblinding of four days. Due to its high energy (> 35 keV nuclear recoil energy) and its low cS2 value (being below the $-2\,\sigma$ of the NR band), it has a low probability of being a WIMP ($P \lessapprox 10^{-3}$ for all WIMP masses [99]). It is unclear what the origin is of this event. The spectrum of a $50\,\mathrm{GeV/c^2}$ WIMP is shown for comparison in purple.

5.4.3 Statistical interpretation

For the statistical interpretation an extended unbinned profile likelihood test statistic in (cS1, $cS2_b$) is used. The uncertainties of the most significant shape parameters, acquired from the posteriors of the ER and NR calibration fits, are propagated into the likelihood. The same was done for the uncertainties on the rate of the backgrounds in section 5.3. The likelihood ratio distribution is approximated by an asymptotic distribution [156]. A safeguard parameter is included to account for possible

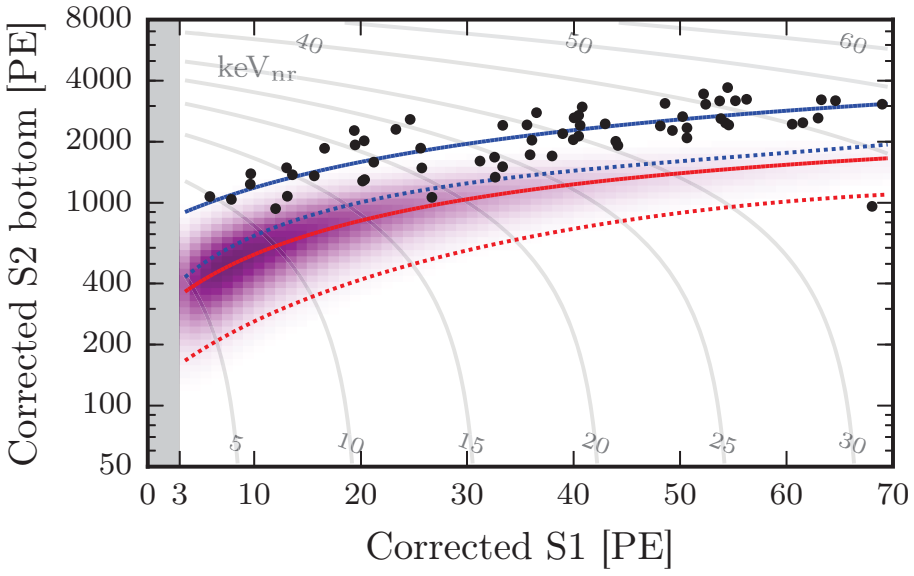

Figure 5.11: Event distribution of SR0 in $cS2_b$ It is dominated by the systematic uncertainty for a possible deviation of the fit model. cS1 after unblinding. Most events are between the median (blue line) and $-2\,\sigma$ (blue dotted) of the ER band. No events are observed in the reference region between the NR median (red line) and $-2\,\sigma$ (red dotted). One event ($cS1 \approx 68\,\mathrm{PE}$) is found in the blinded region, but is far away from e.g., a 50 GeV WIMP spectrum (purple density). From [3].

mis-modeling of the ER background, using the procedure from [157]. The data is consistent with the background-only hypothesis. Figure 5.12 shows the corresponding 90% confidence upper limit on the spin-independent WIMP-nucleon cross section.

The upper limit is power constrained to -1σ of the sensitivity bound and is within 10% of the unconstrained limit for all WIMP masses. For the WIMP spectrum, the standard halo model (SHM) parameters (section 2.1.2) are assumed, together with the standard xenon Helm form factor (section 2.1.3). For WIMP interactions below 1 keV nuclear recoil energy, no light and charge emission is assumed. None of the best-fit values of the nuisance parameters deviates significantly from their nominal values for any WIMP mass. The strongest exclusion limit is for 35 GeV WIMPs at $7.7 \times 10^{-47}\mathrm{cm}^2$ [3].

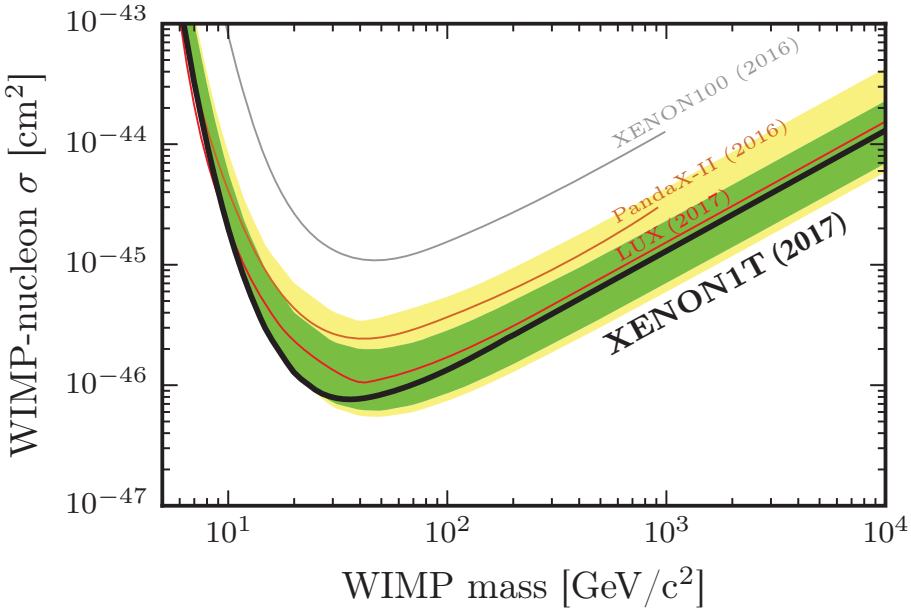

Figure 5.12: The limit on the spin-independent WIMP-nucleon cross section versus WIMP mass for SR0 at 90% confidence (black line). The 1- and 2 σ sensitivity band are given by the green and yellow bands, respectively. For comparison, results from XENON100 [5], LUX [6] and PandaX-II [7] are shown. From [3].

5.5 Improvements and the SR1 result

Science run 1 (SR1) improves on SR0 with an exposure of 273.3 live days instead of 34.2 live days. The data of SR1 was taken between February 2, 2017 and February 8, 2018. To maximise sensitivity a combined analysis was done on SR0 and SR1, resulting in a combined exposure of about 1 tonne-year. All correction maps and cuts (from chapter 3) were remade and improved upon. Here we limit ourselves to discuss the improvements made on the construction of the fiducial volume and present the final limit of the XENON1T experiment on the SI WIMP-nucleon cross section.

5.5.1 A 3D time-dependent Field Distortion Correction

One such improvement for SR1, especially important for the fiducial volume, is the 3D time-dependent field distortion correction (3D FDC) [158]. Because the radial bias in figure 5.2 is ϕ-dependent, the 2D FDC used in SR0 is not sufficient. The SR1 krypton calibration data shows a time-dependent inward position reconstruction bias, assumed to be due to on-

going charge accumulation on the wall. To correct for both effects, a data-driven correction map is constructed using krypton calibration data. This can be done under the assumption that the field distortion is only a radial effect, and that krypton is uniformly distributed in the radial direction.

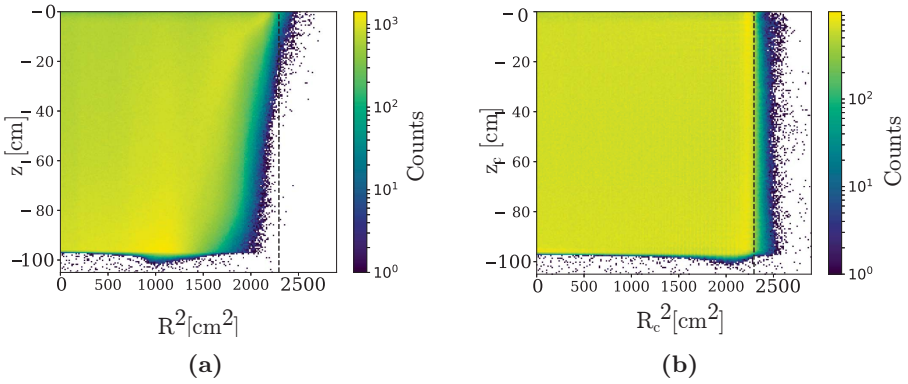

Figure 5.13: **(a)** Distribution of observed (NN) interaction positions of krypton events from calibration data. Due to charge up accumulation on the wall, events reaching the gate have a depth-dependent radius. **(b)** Distribution of corrected (NN) interaction positions of krypton events from calibration data after applying the 3D FDC. The result is a homogeneous distribution of krypton events in radial slices. The TPC boundary (black dashed) is located at the 98% percentile of the krypton distribution. From [158].

Figure 5.13a shows the observed Neural Net (NN) reconstructed positions of krypton calibration data without an FDC applied. To construct the 3D FDC map, this data is divided into 40 slices in the z-direction and 180 slices in the ϕ-direction. Within one slice, events are shifted from uncorrected positions to corrected positions, under the constraint (from MC [159]) that the TPC boundary is at the 98% percentile. Figure 5.13b shows the result of this map, where krypton is now by definition homogeneously distributed[18]. This procedure was tested on ^{210}Po events and ^{241}AmBe calibration data, for which the interaction position distribution is known from Monte Carlo. An interpolation is performed on the discrete mapping, thus making the correction more smooth and such that it also can be applied to events outside of the TPC boundary. After getting the corrected position r_c from the FDC, the corrected position z_c is found by the geometry relation:

$$r_c = f(r_{nn}, \phi_{nn}, z), \qquad z_c = -\sqrt{z^2 - (r_c - r_{nn})^2}, \tag{5.2}$$

[18] It has to be said that a disadvantage of this procedure is that it washes out any other reconstruction artefacts.

with r_{nn} and z the uncorrected positions.

5.5.2 Increasing the FV of SR1

Figure 5.14 shows the low-energy background of SR0 (same data as in figure 5.4), but now with the 3D FDC (and other improvements[19]) applied. Events originating from the TPC walls are now reconstructed at larger radii (less inward bias). Due to the improvements of the reconstructed positions, it is now possible to increase the fiducial volume from about 1 to 1.3 tonne[20] of LXe.

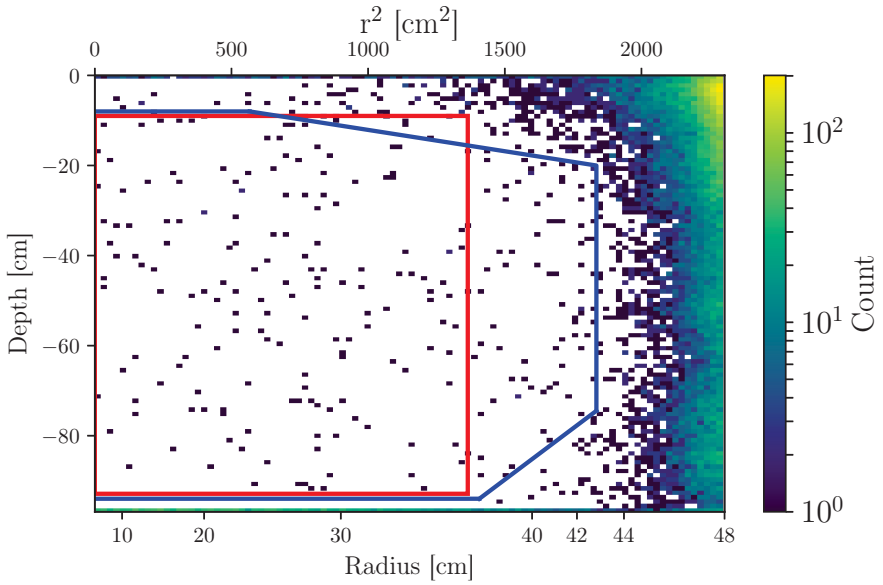

Figure 5.14: The low-energy background event distribution of SR0 after applying the 3D FDC (compare to figure 5.4). The fiducial volume is increased from the cylindrical 1 tonne (red) to an optimized 1.3 tonne (blue). This new FV for SR0 and SR1 is optimized on the spatial background model by requiring that the rate increase does not exceed 10%.

To construct the new FV for SR1, several improvements are made to the SR0 method [160]. Firstly, the z- and r-bounds are determined on simulation data instead of on background data. This increases the statistics and thus decreases the risk of optimizing on statistical fluctuation.

[19] Due to improvements of the LCE MC maps the 'elephant trunk' is gone, as shown in figure 5.13a.

[20] This volume has bounds of: z_{min} = -94 cm, z_{max} = -8 cm and r_{max} = -42.8 cm.

Secondly, for different WIMP masses the signal over background ratio is used as a tests statistic to determine the sensitivity of the volumes[21]. The z- and r-bounds are determined using the spatial templates of ER, AC and wall leakage backgrounds models. The maximum radius is chosen to be 42.8 cm, based on the wall leakage model validity and keeping $\mathcal{O}(100)$ events in a sideband to constrain the expected wall-leakage rate in the FV itself. The z-bounds are chosen by requiring that for a given z-bin the rate increase from the total background does not exceed 10% when moving the bin further towards the cathode or gate[22]. The result is a 1.3 t cylinder-shaped fiducial volume with slanted corners that incorporates more mass at higher radius.

To better account for the wall leakage, the radial information (of all background components) is added to the profile likelihood, together with the rates and spectral shapes (in cS1, $cS2_b$) (section 5.3.1.). The total ER background rate of SR0 and SR1 together, as measured from the data in the WIMP search energy region, is $(2.2^{+0.1}_{-0.1}(\text{syst}) \pm 0.1(\text{stat})) \times 10^{-4}$ $(\text{kg} \cdot \text{day} \cdot \text{keV})^{-1}$ [3]. This is in agreement with the $(1.9 \pm 0.24) \times 10^{-4}$ $(\text{kg} \cdot \text{day} \cdot \text{keV})^{-1}$ from the ER background fit (section 4.5.2).

5.5.3 SR0 + SR1 dark matter search result

The profile likelihood analysis of SR0 and SR1, resulting in a 1 tonne-year (278.8 days $\times$ 1.30 t) exposure, is again consistent with a background-only hypothesis [161]. XENON1T thus excludes new parameter space for the WIMP-nucleon spin-independent cross section for WIMP masses above 6 GeV, with a minimum of $4.1 \times 10^{-47}\text{cm}^2$ at 30 GeV and 90% confidence level. Figure 5.15 shows the 90% confidence upper limit of this result, together with the previous results from XENON10 [4], XENON100 [5], LUX [6] and PandaX-II [7]. XENON1T is presently the world's most sensitive dark matter detector. The sensitivity projection of XENONnT [162], the upgrade of XENON1T, shows the next step in the evolution of liquid-xenon dual phase TPCs.

Changes with respect to SR0 Due to the low number of events in SR0, where most are far away from the region of interest, the asymptotic distribution assumption of the likelihood was found to be biased and led to an overestimation of the confidence of the limit [99]. This caused a $\sim$ 38% (44%) decrease in the upper limit (median sensitivity) at a WIMP mass of 50 GeV/c^2 in the SR0 limit of figure 5.12. In the reanalysis of SR0 + SR1 this was solved and it now avoids undercoverage that can

[21] For the corners the 50 GeV WIMP model is used.

[22] The value of 10% is slightly arbitrary, but protects against overfitting.

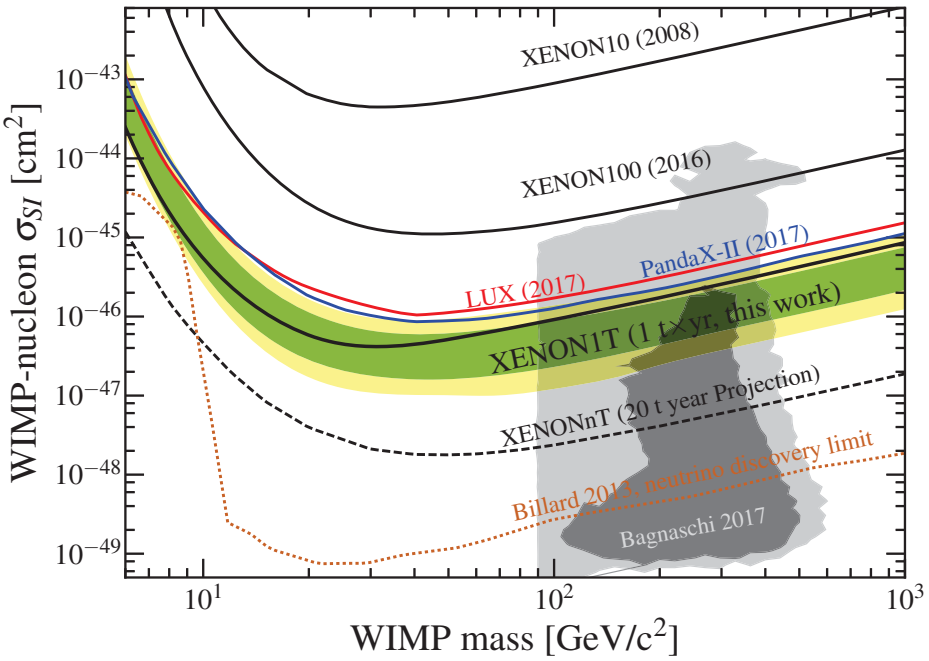

Figure 5.15: Limit on the spin-independent WIMP-nucleon cross section versus WIMP mass for SR0 + SR1 at 90% confidence (black line). The 1- and 2 σ sensitivity band are given by the green and yellow bands, respectively. For comparison, previous results are shown from XENON10 [4], XENON100 [5], LUX [6] and PandaX-II [7]. The projected sensitivity of XENONnT [8], the upgrade of XENON1T, shows the next step from the XENON collaboration in the search for WIMPs. Not all current theoretical WIMP space [8] can be probed before experiments start measuring more nuclear recoils from CEvNS (orange dotted) [9] than from WIMPs.

result from applying asymptotic assumptions. The (outlier) event at cS1 $\approx$ 68 PE, found in SR0 data, did not pass the event selection criteria in the reanalysis due to improvements to the MC simulation used for the S2 hit-pattern likelihood. It is now removed by the S2 Pattern Likelihood cut[23]. This single event caused a 22% worsening of the SR0 limit [99] in figure 5.12.

[23]It was already close to the boundary of the cut in SR0.

5.6 Summary and outlook

The determination of the fiducial volume for SR0 was influenced by unexpected backgrounds such as gas events and the wall leakage backgrounds. Unfortunately, XENON1T was not successful in achieving the designed high-voltage goal of -100 kV on the cathode[24]. The lower field configuration, together with the charge up over time of the PTFE wall, resulted in a ϕ-dependent radial bias of the reconstructed positions. This was discovered by cross checking the low energy background distribution with the ^{210}Po decay distribution originating from the PTFE wall. The SR0 cylindrical fiducial volume of (1042 ± 12) kg is designed to exclude both backgrounds.

By unblinding the region of interest outside the SR0 FV, the expected rate of wall events leaking into it was calculated to be 0.5 ± 0.3. For the six expected backgrounds, both spectral shape and the rates were fixed before unblinding. The total background expectation in the cS1 $\in [3, 70]$ PE, cS2$_b$ $\in [50, 8000]$ PE search region was (63 ± 8) events. From the about 16 M events digitized during SR0, only 63 survived the selection criteria after unblinding. Only one of these events was found below the NR median. The data of SR0 is consistent with a background-only hypothesis.

For the analysis of SR0 + SR1, resulting in a 1 tonne-year exposure, the spatial reconstruction was improved by including a 3D field distortion correction. The fiducial volume was increased to (1.30 ± 0.01) t and the spatial distribution of the background models were included into the likelihood. XENON1T reached the lowest ER background level of $(2.2^{+0.1}_{-0.1}(\text{syst}) \pm 0.1(\text{stat})) \times 10^{-4}$ (kg·day·keV)$^{-1}$ in this energy range of all dark matter detectors. Again, the data is consistent with the background-only hypothesis. This (final) result of XENON1T on the spin independent WIMP-nucleon cross section is the most stringent (as of the time of writing). It is now up to the next generation of detectors to discover a dark matter particle, and hopefully explain an observation that is now almost a century old.

[24] A 10 times higher drift field would decrease the effect of charge accumulation on the PTFE walls on the position reconstruction.

Bibliography

[1] G. Bertone, J. Silk, *et al.*, *Particle Dark Matter: Observations, Models and Searches*. Cambridge Univ. Press, Cambridge, 2010. https://books.google.nl/books?id=szrTSWO7D-8C.

[2] L. Althuser, *Light collection efficiency simulations of the XENON1T experiment and comparison to data*. Master's thesis, University of Münster, 2017.

[3] **XENON** Collaboration, E. Aprile *et al.*, "First Dark Matter Search Results from the XENON1T Experiment," arXiv:1705.06655 [astro-ph.CO]. https://arxiv.org/abs/1705.06655.

[4] J. Angle *et al.*, "Limits on spin-dependent WIMP-nucleon cross-sections from the XENON10 experiment," *Phys. Rev. Lett.* **101** (2008) 091301, arXiv:0805.2939 [astro-ph].

[5] **XENON100** Collaboration, E. Aprile *et al.*, "XENON100 Dark Matter Results from a Combination of 477 Live Days," *Phys. Rev.* **D94** no. 12, (2016) 122001, arXiv:1609.06154 [astro-ph.CO].

[6] **LUX** Collaboration, D. S. Akerib *et al.*, "Results from a search for dark matter in the complete LUX exposure," *Phys. Rev. Lett.* **118** no. 2, (2017) 021303, arXiv:1608.07648 [astro-ph.CO].

[7] **PandaX-II** Collaboration, A. Tan *et al.*, "Dark Matter Results from First 98.7 Days of Data from the PandaX-II Experiment," *Phys. Rev. Lett.* **117** no. 12, (2016) 121303, arXiv:1607.07400 [hep-ex].

[8] E. Bagnaschi *et al.*, "Likelihood Analysis of Supersymmetric SU(5) GUTs," *Eur. Phys. J.* **C77** no. 2, (2017) 104, arXiv:1610.10084 [hep-ph].

[9] J. Billard, L. Strigari, and E. Figueroa-Feliciano, "Implication of neutrino backgrounds on the reach of next generation dark matter direct detection experiments," *Phys. Rev.* **D89** no. 2, (2014) 023524, arXiv:1307.5458 [hep-ph].

[10] E. S. Morrison, T. Frels, E. H. Miller, R. W. Schnee, and J. Street, "Radon Daughter Plate-out onto Teflon," *AIP Conf. Proc.* **1921** no. 1, (2018) 090002, arXiv:1708.08534 [physics.ins-det].

[11] A. Bradley *et al.*, "Radon-related Backgrounds in the LUX Dark Matter Search," *Phys. Procedia* **61** (2015) 658–665.

[12] N. Rupp, "Neutron background estimation from (alpha,n) reactions created by Po210 on the Teflon walls." Internal XENON1T note.

[13] G. Bertone and D. Hooper, "A History of Dark Matter," *Submitted to: Rev. Mod. Phys.* (2016) , arXiv:1605.04909 [astro-ph.CO]. https://arxiv.org/abs/1605.04909v2.

[14] J. Kapteyn, "First Attempt at a Theory of the Arrangement and Motion of the Sidereal System," *Astrophysical Journal* **55** (May, 1922) 302. http://articles.adsabs.harvard.edu//full/1922ApJ....55..302K/0000302.000.html.

[15] F. Zwicky, "Die Rotverschiebung von extragalaktischen Nebeln," *Helvetica Physica Acta* **6** (1933) 110–127.

[16] F. Zwicky, "On the Masses of Nebulae and of Clusters of Nebulae," *Astrophysical Journal* **86** (Oct., 1937) 217.

[17] S. Dodelson, *Modern cosmology*. 2003. http://adsabs.harvard.edu/abs/2003moco.book.....D.

[18] E. W. Kolb and M. S. Turner, *The early universe*. 1990. http://adsabs.harvard.edu/abs/1990eaun.book.....K.

[19] A. Einstein, "Approximative Integration of the Field Equations of Gravitation," *Sitzungsber. Preuss. Akad. Wiss. Berlin (Math. Phys.)* **1916** (1916) 688–696.

[20] G. Bertone, D. Hooper, and J. Silk, "Particle dark matter: Evidence, candidates and constraints," *Phys. Rept.* **405** (2005) 279–390, arXiv:hep-ph/0404175 [hep-ph].

[21] S. Walters, "How Einstein Got His Field Equations," *arXiv:1608.05752 [gr-qc, physics:physics]* (Aug., 2016) . http://arxiv.org/abs/1608.05752. arXiv: 1608.05752.

[22] A. Friedmann, "Über die Krümmung des Raumes," *Zeitschrift fur Physik* **10** (1922) 377–386. http://adsabs.harvard.edu/abs/1922ZPhy...10..377F.

[23] W. Hu and M. White, "The Cosmic Symphony," *Scientific American* (2004) . http://background.uchicago.edu/%7Ewhu/SciAm/sym1.html.

[24] R. H. Cyburt, B. D. Fields, K. A. Olive, and T.-H. Yeh, "Big Bang Nucleosynthesis: 2015," *Rev. Mod. Phys.* **88** (2016) 015004, arXiv:1505.01076 [astro-ph.CO]. https://arxiv.org/abs/1505.01076.

[25] **Planck** Collaboration, P. A. R. Ade *et al.*, "Planck 2015 results. XIII. Cosmological parameters," *Astron. Astrophys.* **594** (2016) A13, arXiv:1502.01589 [astro-ph.CO]. https://arxiv.org/abs/1502.01589.

[26] C. L. Bennett, A. Banday, K. M. Gorski, *et al.*, "4-Year COBE DMR Cosmic Microwave Background Observations: Maps and Basic Results," *The Astrophysical Journal* **464** no. 1, (June, 1996) L1–L4. http://arxiv.org/abs/astro-ph/9601067. arXiv: astro-ph/9601067.

[27] C. L. Bennett, D. Larson, J. L. Weiland, *et al.*, "Nine-Year Wilkinson Microwave Anisotropy Probe (WMAP) Observations: Final Maps and Results," *The Astrophysical Journal Supplement Series* **208** no. 2, (Sept., 2013) 20. http://arxiv.org/abs/1212.5225. arXiv: 1212.5225.

[28] Planck Collaboration, R. Adam, P. A. R. Ade, *et al.*, "Planck 2015 results. I. Overview of products and scientific results," *Astronomy & Astrophysics* **594** (Oct., 2016) A1. http://arxiv.org/abs/1502.01582. arXiv: 1502.01582.

[29] H. J. de Vega, "The Effective Theory of Inflation and the Dark Matter Status in the Standard Model of the Universe," in *In *Diakonov, D. (ed.): Subtleties in quantum field theory* 17-66*, pp. 17–66. 2010. arXiv:1006.0486 [astro-ph.CO]. https://arxiv.org/pdf/1006.0486.pdf.

[30] Planck Collaboration, N. Aghanim, M. Arnaud, *et al.*, "Planck 2015 results. XI. CMB power spectra, likelihoods, and robustness of parameters," *Astronomy & Astrophysics* **594** (Oct., 2016) A11. http://arxiv.org/abs/1507.02704. arXiv: 1507.02704.

[31] **Planck** Collaboration, R. Adam *et al.*, "Planck 2015 results. I. Overview of products and scientific results," *Astron. Astrophys.* **594** (2016) A1, arXiv:1502.01582 [astro-ph.CO]. https://arxiv.org/pdf/1502.01582.pdf.

[32] L. Husdal, "On Effective Degrees of Freedom in the Early Universe," *Galaxies* **4** (2016) 78, arXiv:1609.04979 [astro-ph.CO]. https://arxiv.org/abs/1609.04979.

[33] P. Bras, *Finding a needle in a haystack: Background studies and WIMP detection effciency in LUX*. PhD thesis, Universidade de Coimbra, 2015.

[34] G. D'Amico, M. Kamionkowski, and K. Sigurdson, "Dark Matter Astrophysics," *arXiv:0907.1912 [astro-ph]* (July, 2009) . http://arxiv.org/abs/0907.1912. arXiv: 0907.1912.

[35] M. Roos, "Dark Matter: The evidence from astronomy, astrophysics and cosmology," *arXiv:1001.0316 [astro-ph]* (Jan., 2010) . http://arxiv.org/abs/1001.0316. arXiv: 1001.0316.

[36] V. C. Rubin, W. K. Ford, Jr., and N. Thonnard, "Rotational properties of 21 SC galaxies with a large range of luminosities and radii, from NGC 4605 /R = 4kpc/ to UGC 2885 /R = 122 kpc/," *Astrophysical Journal* **238** (June, 1980) 471–487.

[37] K. Freese, "Review of Observational Evidence for Dark Matter in the Universe and in upcoming searches for Dark Stars," *EAS Publ. Ser.* **36** (2009) 113–126, arXiv:0812.4005 [astro-ph]. https://arxiv.org/abs/0812.4005.

[38] R. Amanullah, C. Lidman, D. Rubin, *et al.*, "Spectra and Light Curves of Six Type Ia Supernovae at 0.511 < z < 1.12 and the Union2 Compilation," *The Astrophysical Journal* **716** no. 1, (Apr., 2010) 712–738, arXiv:1004.1711. http://dx.doi.org/10.1088/0004-637x/716/1/712.

[39] N. Suzuki, D. Rubin, and C. Lidman, "The Hubble Space Telescope Cluster Supernova Survey. V. Improving the Dark-energy Constraints above z = 1 and Building an Early-type-hosted Supernova Sample," *Astrophysical Journal* **746** (Feb., 2012) 85, arXiv:1105.3470 [astro-ph.CO].

[40] C. S. Kochanek, M. White, J. Huchra, *et al.*, "Clusters of galaxies in the local universe," *The Astrophysical Journal* **585** no. 1, (2003) 161. http://stacks.iop.org/0004-637X/585/i=1/a=161.

[41] S. W. Allen, R. W. Schmidt, and A. C. Fabian, "Cosmological constraints from the x-ray gas mass fraction in relaxed lensing clusters observed with Chandra," *Mon. Not. Roy. Astron. Soc.* **334** (2002) L11, arXiv:astro-ph/0205007 [astro-ph].

[42] D. Clowe, M. Bradac, A. H. Gonzalez, *et al.*, "A direct empirical proof of the existence of dark matter," *Astrophys. J.* **648** (2006) L109–L113, arXiv:astro-ph/0608407 [astro-ph].

[43] D. Harvey, R. Massey, T. Kitching, A. Taylor, and E. Tittley, "The non-gravitational interactions of dark matter in colliding galaxy clusters," *Science* **347** (2015) 1462–1465, arXiv:1503.07675 [astro-ph.CO].

[44] B. D. Wandelt, R. Dave, G. R. Farrar, *et al.*, "Selfinteracting dark matter," in *Sources and detection of dark matter and dark energy in the universe. Proceedings, 4th International Symposium, DM 2000, Marina del Rey, USA, February 23-25, 2000*, pp. 263–274. 2000. arXiv:astro-ph/0006344 [astro-ph]. https://arxiv.org/abs/astro-ph/0006344.

[45] T. Bringmann, F. Kahlhoefer, K. Schmidt-Hoberg, and P. Walia, "Strong constraints on self-interacting dark matter with light mediators," *Phys. Rev. Lett.* **118** no. 14, (2017) 141802, arXiv:1612.00845 [hep-ph]. https://arxiv.org/abs/1612.00845.

[46] L. Roszkowski, "Particle Dark Matter - A Theorist's Perspective," *Pramana* **62** no. 2, (Feb., 2004) 389–401. http://arxiv.org/abs/hep-ph/0404052. arXiv: hep-ph/0404052.

[47] G. G. Raffelt, "Dark Matter: Motivation, Candidates and Searches," *arXiv:hep-ph/9712538* (Dec., 1997) . http://arxiv.org/abs/hep-ph/9712538. arXiv: hep-ph/9712538.

[48] J. L. Feng, "Dark Matter Candidates from Particle Physics and Methods of Detection," *Annual Review of Astronomy and Astrophysics* **48** no. 1, (Aug., 2010) 495–545. http://arxiv.org/abs/1003.0904. arXiv: 1003.0904.

[49] M. Drewes *et al.*, "A White Paper on keV Sterile Neutrino Dark Matter," *JCAP* **1701** no. 01, (2017) 025, arXiv:1602.04816 [hep-ph]. https://arxiv.org/abs/1602.04816.

[50] S. Dodelson and L. M. Widrow, "Sterile-neutrinos as dark matter," *Phys. Rev. Lett.* **72** (1994) 17–20, arXiv:hep-ph/9303287 [hep-ph]. https://arxiv.org/abs/hep-ph/9303287.

[51] R. D. Peccei and H. R. Quinn, "CP conservation in the presence of pseudoparticles," *Physical Review Letters* **38** (June, 1977) 1440–1443.

[52] D. J. E. Marsh, "Axion Cosmology," *Phys. Rept.* **643** (2016) 1–79, arXiv:1510.07633 [astro-ph.CO]. https://arxiv.org/abs/1510.07633.

[53] M. S. Turner, "Windows on the Axion," *Phys. Rept.* **197** (1990) 67–97.

[54] J. E. Kim and G. Carosi, "Axions and the Strong CP Problem," *Rev. Mod. Phys.* **82** (2010) 557–602, arXiv:0807.3125 [hep-ph].

[55] M. Srednicki, "Relic abundances and the Boltzmann equation," in *Proceedings, 3rd International Heidelberg Conference on Dark matter in astro- and particle physics (DARK 2000): Heidelberg, Germany, July 10-14, 2000*, pp. 244–247. 2000. arXiv:hep-ph/0005174 [hep-ph]. https://arxiv.org/abs/hep-ph/0005174.

[56] S. P. Martin, "A Supersymmetry primer," arXiv:hep-ph/9709356 [hep-ph]. https://arxiv.org/abs/hep-ph/9709356. [Adv. Ser. Direct. High Energy Phys.18,1(1998)].

[57] J. Ellis and K. A. Olive, "Supersymmetric Dark Matter Candidates," arXiv:1001.3651 [astro-ph.CO]. https://arxiv.org/abs/1001.3651.

[58] **MSSM Working Group** Collaboration, A. Djouadi *et al.*, "The Minimal supersymmetric standard model: Group summary report," in *GDR (Groupement De Recherche) - Supersymetrie Montpellier, France, April 15-17, 1998*. 1998. arXiv:hep-ph/9901246 [hep-ph]. https://arxiv.org/abs/hep-ph/9901246.

[59] E. Witten, "Dynamical Breaking of Supersymmetry," *Nucl. Phys.* **B188** (1981) 513.

[60] H. Baer, V. Barger, and H. Serce, "SUSY under siege from direct and indirect WIMP detection experiments," *Physical Review D* **94** no. 11, (Dec., 2016) . http://arxiv.org/abs/1609.06735. arXiv: 1609.06735.

[61] J. D. Lewin and P. F. Smith, "Review of mathematics, numerical factors, and corrections for dark matter experiments based on elastic nuclear recoil," *Astropart. Phys.* **6** (1996) 87–112. http://pa.brown.edu/articles/Lewin_Smith_DM_Review.pdf.

[62] R. W. Schnee, "Introduction to dark matter experiments," in *In Physics of the Large and Small: Proceedings of the 2009 Theoretical Advanced Study Institute in Elementary Particle Physics, 629-681 (World Scientific, Singapore) Ed. Csaba Csaki and Scott Dodelson (2010)*. 2011. arXiv:1101.5205 [astro-ph.CO]. https://arxiv.org/abs/1101.5205.

[63] T. Piffl *et al.*, "The RAVE survey: the Galactic escape speed and the mass of the Milky Way," *Astron. Astrophys.* **562** (2014) A91, arXiv:1309.4293 [astro-ph.GA]. https://arxiv.org/abs/1309.4293.

[64] E. Hogenbirk, "Erikhogenbirk/dmplots: First release," Aug., 2018. https://doi.org/10.5281/zenodo.1400310.

[65] R. Catena and P. Ullio, "A novel determination of the local dark matter density," *JCAP* **1008** (2010) 004, arXiv:0907.0018 [astro-ph.CO]. https://arxiv.org/abs/0907.0018.

[66] J. I. Read, "The Local Dark Matter Density," *J. Phys.* **G41** (2014) 063101, arXiv:1404.1938 [astro-ph.GA]. https://arxiv.org/abs/1404.1938.

[67] A. M. Green, "Astrophysical uncertainties on the local dark matter distribution and direct detection experiments," *J. Phys.* **G44** no. 8, (2017) 084001, arXiv:1703.10102 [astro-ph.CO].

[68] G. Duda, A. Kemper, and P. Gondolo, "Model Independent Form Factors for Spin Independent Neutralino-Nucleon Scattering from Elastic Electron Scattering Data," *JCAP* **0704** (2007) 012, arXiv:hep-ph/0608035 [hep-ph]. https://arxiv.org/abs/hep-ph/0608035.

[69] Y.-Z. Chen, Y.-A. Luo, L. Li, H. Shen, and X.-Q. Li, "Determining the nuclear form factor for detection of dark matter in the relativistic mean field theory," *Commun. Theor. Phys.* **55** (2011) 1059–1064, arXiv:1101.3049 [hep-ph]. https://arxiv.org/abs/1101.3049.

[70] M. T. Ressell and D. J. Dean, "Spin dependent neutralino - nucleus scattering for A approximately 127 nuclei," *Phys. Rev.* **C56** (1997) 535–546, arXiv:hep-ph/9702290 [hep-ph]. https://arxiv.org/abs/hep-ph/9702290.

[71] P. Toivanen, M. Kortelainen, J. Suhonen, and J. Toivanen, "Large-scale shell-model calculations of elastic and inelastic scattering rates of lightest supersymmetric particles (LSP) on I-127, Xe-129, Xe-131, and Cs-133 nuclei," *Phys. Rev.* **C79** (2009) 044302.

[72] T. Marrodán Undagoitia and L. Rauch, "Dark matter direct-detection experiments," *J. Phys.* **G43** no. 1, (2016) 013001, arXiv:1509.08767 [physics.ins-det]. https://arxiv.org/abs/1509.08767.

[73] E. Aprile and T. Doke, "Liquid Xenon Detectors for Particle Physics and Astrophysics," *Reviews of Modern Physics* **82** no. 3, (July, 2010) 2053–2097. http://arxiv.org/abs/0910.4956. arXiv: 0910.4956.

[74] V. Chepel and H. Araújo, "Liquid noble gas detectors for low energy particle physics," *Journal of Instrumentation* **8** no. 04, (Apr., 2013) R04001–R04001. http://arxiv.org/abs/1207.2292. arXiv: 1207.2292.

[75] B. Lenardo, K. Kazkaz, A. Manalaysay, *et al.*, "A Global Analysis of Light and Charge Yields in Liquid Xenon," *IEEE Trans. Nucl. Sci.* **62** no. 6, (2015) 3387–3396, arXiv:1412.4417 [astro-ph.IM]. https://arxiv.org/abs/1412.4417.

[76] R. Platzman, "Total ionization in gases by high-energy particles: An appraisal of our understanding," *The International Journal of Applied Radiation and Isotopes* **10** no. 2, (1961) 116 – 127. http://www.sciencedirect.com/science/article/pii/0020708X61901089.

[77] E. Hogenbirk, J. Aalbers, P. A. Breur, *et al.*, "Precision measurements of the scintillation pulse shape for low-energy recoils in liquid xenon," *JINST* **13** no. 05, (2018) P05016, arXiv:1803.07935 [physics.ins-det].

[78] J. Lindhard and M. Scharff, "E., schott h.: Range concepts and heavy ion ranges (notes on atomic collisions, ii)," *Kong. Danske Vid. Selsk* **33** 1.

[79] D. M. Mei, Z. B. Yin, L. C. Stonehill, and A. Hime, "A Model of Nuclear Recoil Scintillation Efficiency in Noble Liquids," *Astropart. Phys.* **30** (2008) 12–17, arXiv:0712.2470 [nucl-ex]. https://arxiv.org/abs/0712.2470.

[80] A. Hitachi, "Properties of liquid xenon scintillation for dark matter searches," *Astroparticle Physics* **24** no. 3, (2005) 247 – 256. http://www.sciencedirect.com/science/article/pii/S0927650505000964.

[81] S. Kubota, M. Hishida, M. Suzuki, and J. zhi Ruan, "Liquid and solid argon, krypton and xenon scintillators," *Nuclear Instruments and Methods in Physics Research* **196** no. 1, (1982) 101 – 105. http://www.sciencedirect.com/science/article/pii/0029554X82906231.

[82] A. Hitachi, T. Takahashi, N. Funayama, *et al.*, "Effect of ionization density on the time dependence of luminescence from liquid argon and xenon," *Phys. Rev. B* **27** (May, 1983) 5279–5285. https://link.aps.org/doi/10.1103/PhysRevB.27.5279.

[83] K. Miller, "Preliminary update of the single electron pulse shape model in SR1." Internal XENON1T note.

[84] **XENON** Collaboration, E. Aprile *et al.*, "The XENON1T Dark Matter Experiment," arXiv:1708.07051 [astro-ph.IM].

[85] P. Barrow *et al.*, "Qualification Tests of the R11410-21 Photomultiplier Tubes for the XENON1T Detector," *JINST* **12** no. 01, (2017) P01024, arXiv:1609.01654 [astro-ph.IM].

[86] J. Wolf, "Linearity Estimation and Measurement of the Final XENON1T 3'PMT Base." Internal XENON1T note.

[87] D. Masson, *Novel Ideas and Techniques for Large Dark Matter Detectors*. Phd thesis, Purdue University, 2018.

[88] **XENON100** Collaboration, E. Aprile *et al.*, "Response of the XENON100 Dark Matter Detector to Nuclear Recoils," *Phys. Rev.* **D88** (2013) 012006, arXiv:1304.1427 [astro-ph.IM].

[89] R. F. Lang, A. Brown, E. Brown, *et al.*, "A ^{220}Rn source for the calibration of low-background experiments," *JINST* **11** no. 04, (2016) P04004, arXiv:1602.01138 [physics.ins-det].

[90] **XENON** Collaboration, E. Aprile *et al.*, "Results from a Calibration of XENON100 Using a Source of Dissolved Radon-220," *Phys. Rev.* **D95** no. 7, (2017) 072008, arXiv:1611.03585 [physics.ins-det].

[91] S. Rosendahl *et al.*, "A novel ^{83m}Kr tracer method for characterizing xenon gas and cryogenic distillation systems," *JINST* **9** no. 10, (2014) P10010, arXiv:1407.3981 [astro-ph.IM]. https://arxiv.org/abs/1407.3981.

[92] **XENON** Collaboration, E. Aprile *et al.*, "Material radioassay and selection for the XENON1T dark matter experiment," arXiv:1705.01828 [physics.ins-det].

[93] **XENON** Collaboration, E. Aprile *et al.*, "Physics reach of the XENON1T dark matter experiment," *JCAP* **1604** no. 04, (2016) 027, arXiv:1512.07501 [physics.ins-det].

[94] M. Szydagis, N. Barry, K. Kazkaz, *et al.*, "NEST: A Comprehensive Model for Scintillation Yield in Liquid Xenon," *Journal of Instrumentation* **6** no. 10, (Oct., 2011) P10002–P10002. http://arxiv.org/abs/1106.1613. arXiv: 1106.1613.

[95] M. Szydagis, A. Fyhrie, D. Thorngren, and M. Tripathi, "Enhancement of NEST Capabilities for Simulating Low-Energy Recoils in Liquid Xenon," *Journal of Instrumentation* **8** no. 10, (Oct., 2013) C10003–C10003. http://arxiv.org/abs/1307.6601. arXiv: 1307.6601.

[96] J. Mock, N. Barry, K. Kazkaz, *et al.*, "Modeling Pulse Characteristics in Xenon with NEST," *JINST* **9** (2014) T04002, arXiv:1310.1117 [physics.ins-det]. https://arxiv.org/abs/1310.1117.

[97] C. Suplee, "XCOM: Photon Cross Sections Database," Sept., 2009. https://www.nist.gov/pml/xcom-photon-cross-sections-database.

[98] **XENON** Collaboration, E. Aprile *et al.*, "Removing krypton from xenon by cryogenic distillation to the ppq level," *Eur. Phys. J.* **C77** no. 5, (2017) 275, arXiv:1612.04284 [physics.ins-det].

[99] J. Aalbers, *Dark Matter Search with XENON1T*. Phd thesis, University of Amsterdam, 2018.

[100] J. Allison, K. Amako, J. Apostolakis, *et al.*, "Recent developments in geant4," *Nuclear Instruments and Methods in Physics Research Section A: Accelerators, Spectrometers, Detectors and Associated Equipment* **835** no. Supplement C, (2016) 186 – 225. http://www.sciencedirect.com/science/article/pii/S0168900216306957.

[101] B. Pelssers, "Position Reconstruction Summary." Internal XENON1T note.

[102] J. Naganoma, "Position correction of field distortion summary." Internal XENON1T note.

[103] E. McCutchan, "Nuclear data sheets for a = 83," *Nuclear Data Sheets* **125** (2015) 201 – 394. http://www.sciencedirect.com/science/article/pii/S0090375215000034.

[104] **NEXT** Collaboration, G. Martínez-Lema *et al.*, "Calibration of the NEXT-White detector using ^{83m}Kr decays," arXiv:1804.01780 [physics.ins-det].

[105] T. Berget, "Summery Note on S1 LCE Correction for XENON1T sciencerun 0." Internal XENON1T note.

[106] A. Brown, "S2 xy correction summary." Internal XENON1T note.

[107] J. Ye, A. Fieguth, and S. D. Chiara Capelli, "Summary of the g1,g2 investigation from mono-energetic lines." Internal XENON1T note.

[108] J. Aalbers, "Double photoelectron emission in XENON1T." Internal XENON1T note.

[109] J. Ye, "cS1 and cS2b 2D gaussian fitting for g1 g2 calibration in SR0." Internal XENON1T note.

[110] J. Howlett, "Moving towards a simultaneous fit to ER/NR Calibration Data from SR0 and SR1." Internal XENON1T note.

[111] E. Hogenbirk, M. P. Decowski, K. McEwan, and A. P. Colijn, "Field dependence of electronic recoil signals in a dual-phase liquid xenon time projection chamber," `arXiv:1807.07121 [physics.ins-det]`.

[112] **PandaX-II** Collaboration, X. Cui *et al.*, "Dark Matter Results From 54-Ton-Day Exposure of PandaX-II Experiment," *Phys. Rev. Lett.* **119** no. 18, (2017) 181302, `arXiv:1708.06917 [astro-ph.CO]`.

[113] M. Szydagis. 2017-10-21, private communication.

[114] **EXO-200** Collaboration, J. B. Albert *et al.*, "Improved measurement of the $2\nu\beta\beta$ half-life of ^{136}Xe with the EXO-200 detector," *Phys. Rev.* **C89** no. 1, (2014) 015502, `arXiv:1306.6106 [nucl-ex]`.

[115] M.-M. B. *et al.*, "Table of Radionuclides vol. 1/2/4/7,". `http://www.nucleide.org/DDEP_WG/DDEPdata.htm`.

[116] **XENON** Collaboration, E. Aprile *et al.*, "Intrinsic backgrounds from Rn and Kr in the XENON100 experiment," *Eur. Phys. J.* **C78** no. 2, (2018) 132, `arXiv:1708.03617 [astro-ph.IM]`.

[117] H. Simgen, "The 222Rn pie: Distribution of 222Rn sources in XENON1T." Internal XENON1T note.

[118] H. Simgen, G. Heusser, and G. Zuzel, "Highly sensitive measurements of radioactive noble gas nuclides in the borexino solar neutrino experiment," *Applied Radiation and Isotopes* **61** no. 2, (2004) 213 – 217. `http://www.sciencedirect.com/science/article/pii/S0969804304001083`. Low Level Radionuclide Measurement Techniques - ICRM.

[119] J. Wolf, "Xenon1T 3D Field simulation." Internal XENON1T note.

[120] J. Aalbers and P. Breur, "Revealing XENON1T's unshielded gamma-ray background with an empirical LCE correctiony." Internal XENON1T note.

[121] M. Oreglia, *A Study of the Reactions $\psi' \to \gamma\gamma\psi$*. PhD thesis, SLAC, 1980. `http://www-public.slac.stanford.edu/sciDoc/docMeta.aspx?slacPubNumber=slac-r-236.html`.

[122] A. Azzalini, "A class of distributions which includes the normal ones," *Scandinavian Journal of Statistics* **12** no. 2, (1985) 171–178. `http://www.jstor.org/stable/4615982`.

[123] M. Weber, *Gentle Neutron Signals and Noble Background in the XENON100 Dark Matter Search Experiment*. PhD thesis, Heidelberg U., 2013. `http://www.ub.uni-heidelberg.de/archiv/15155`.

[124] D. Masson, "Convection in XENON1T in SR0 and SR1." Internal XENON1T note.

[125] **EXO-200** Collaboration, J. B. Albert *et al.*, "Measurements of the ion fraction and mobility of α- and β-decay products in liquid xenon using the EXO-200 detector," *Phys. Rev.* **C92** no. 4, (2015) 045504, `arXiv:1506.00317 [nucl-ex]`.

[126] M. Murra and P. Breur, "Radon removal by cryogenic distillation at XENON1T." Internal XENON1T note.

[127] **XENON100** Collaboration, E. Aprile *et al.*, "Online ^{222}Rn removal by cryogenic distillation in the XENON100 experiment," *Eur. Phys. J.* **C77** no. 6, (2017) 358, arXiv:1702.06942 [physics.ins-det].

[128] N. Rupp, "Rn222 and Po218 rate in SR1." Internal XENON1T note.

[129] L. N. H. Becquerel, "Nucléide-lara," 2018. http://www.lnhb.fr/nuclear-data/module-lara/.

[130] S. Agostinelli, J. Allison, K. Amako, *et al.*, "Geant4—a simulation toolkit," *Nuclear Instruments and Methods in Physics Research Section A: Accelerators, Spectrometers, Detectors and Associated Equipment* **506** no. 3, (2003) 250 – 303. http://www.sciencedirect.com/science/article/pii/S0168900203013688.

[131] C. Wittweg, "Energy calibration and resolution for Double Electron Capture." Internal XENON1T note.

[132] E. Hogenbirk, "Revisit of S2 separation resolution." Internal XENON1T note.

[133] E. Aprile, K. Arisaka, F. Arneodo, *et al.*, "Study of the electromagnetic background in the XENON100 experiment," *Phys. Rev. D* **83** no. 8, (Apr., 2011) 082001, arXiv:1101.3866 [astro-ph.IM].

[134] C. W. et al., "BG/MC data comparison for SR1." Internal XENON1T note.

[135] K. Ni, R. Hasty, T. M. Wongjirad, *et al.*, "Preparation of Neutron-activated Xenon for Liquid Xenon Detector Calibration," *Nucl. Instrum. Meth.* **A582** (2007) 569–574, arXiv:0708.1976 [physics.ins-det].

[136] **XMASS** Collaboration, K. Abe *et al.*, "Improved search for two-neutrino double electron capture on ^{124}Xe and ^{126}Xe using particle identification in XMASS-I," arXiv:1801.03251 [nucl-ex].

[137] **EXO** Collaboration, J. B. Albert *et al.*, "Search for Neutrinoless Double-Beta Decay with the Upgraded EXO-200 Detector," *Phys. Rev. Lett.* **120** no. 7, (2018) 072701, arXiv:1707.08707 [hep-ex].

[138] C. Wittweg, "Material background in the 1.3 ton fiducial volume." Internal XENON1T note.

[139] A. Fieguth and C. Wittweg, "Cut summary for DEC." Internal XENON1T note.

[140] C. Wittweg and A. Fieguth, "A background model for double electron capture search." Internal XENON1T note.

[141] C. Wittweg, "Search for long-lived neutron activations from the neutron generator." Internal XENON1T note.

[142] M. A. V. Jara and Z. Greene, "Summary note on Kr-85 concentration for SR1." Internal XENON1T note.

[143] J.-W. Chen, H.-C. Chi, C. P. Liu, and C.-P. Wu, "Low-energy electronic recoil in xenon detectors by solar neutrinos," *Phys. Lett.* **B774** (2017) 656–661, arXiv:1610.04177 [hep-ex].

[144] C. Hasterok, "Study of Events at the Detector Wall." Internal XENON1T note.

[145] M. A. V. Jara and N. Rupp, "Summary note on Wall Charge up for SR1." Internal XENON1T note.

[146] **LUX** Collaboration, D. S. Akerib *et al.*, "3D Modeling of Electric Fields in the LUX Detector," *JINST* **12** no. 11, (2017) P11022, arXiv:1709.00095 [physics.ins-det].

[147] Y. Wei, "Field Distortion Correction: Towards SR1." Internal XENON1T note.

[148] P. A. Breur, C. Hasteroke, and P. Di Gangi, "Wall leakage expectation." Internal XENON1T note.

[149] M. Galloway, "Estimate of XENON1T Target Mass." Internal XENON1T note.

[150] "Nist chemistry webbook, srd 69." `https://webbook.nist.gov/chemistry/fluid/`. Accessed: 2017-02-01.

[151] P. A. Breur and et al., "Summery note on the Fiducial volume for sciencerun 0." Internal XENON1T note.

[152] **LUX** Collaboration, D. S. Akerib *et al.*, "Tritium calibration of the LUX dark matter experiment," *Phys. Rev.* **D93** no. 7, (2016) 072009, `arXiv:1512.03133 [physics.ins-det]`.

[153] J. Thomas and D. A. Imel, "Recombination of electron-ion pairs in liquid argon and liquid xenon," *Phys. Rev. A* **36** (Jul, 1987) 614–616. `https://link.aps.org/doi/10.1103/PhysRevA.36.614`.

[154] Q. Lin, "Details of the ER low-energy signal response model and fit to Rn220 data." Internal XENON1T note.

[155] C. Hasterok, *Gas Purity Analytics, Calibration Studies, and Background Predictions towards the First Results of XENON1T*. Phd thesis, University of Heidelberg, 2018. `http://www.ub.uni-heidelberg.de/archiv/23693`.

[156] G. Cowan, K. Cranmer, E. Gross, and O. Vitells, "Asymptotic formulae for likelihood-based tests of new physics," *Eur. Phys. J.* **C71** (2011) 1554, `arXiv:1007.1727 [physics.data-an]`. [Erratum: Eur. Phys. J.C73,2501(2013)].

[157] N. Priel, L. Rauch, H. Landsman, A. Manfredini, and R. Budnik, "A model independent safeguard against background mismodeling for statistical inference," *JCAP* **1705** no. 05, (2017) 013, `arXiv:1610.02643 [physics.data-an]`.

[158] J. Ye, "Summary note for data-driven 3D FDC in SR1 in XENON1T." Internal XENON1T note.

[159] J. Ye, "Data-Driven 3D position correction in SR1." Internal XENON1T note.

[160] M. A. V. Jara, C. Hasteroke, N. Rupp, *et al.*, "Summary note on the Fiducial volume for SR1." Internal XENON1T note.

[161] **XENON** Collaboration, E. Aprile *et al.*, "Dark Matter Search Results from a One Tonne×Year Exposure of XENON1T," `arXiv:1805.12562 [astro-ph.CO]`.

[162] **DARWIN** Collaboration, J. Aalbers *et al.*, "DARWIN: towards the ultimate dark matter detector," *JCAP* **1611** (2016) 017, `arXiv:1606.07001 [astro-ph.IM]`.

Samenvatting: De zoektocht naar donkere materie met XENON1T

We missen 85% van alle materie in ons Universum. Deze eenvoudige uitspraak motiveert duizenden natuurkundigen over de hele wereld om naar donkere materie te zoeken. De eerste waarnemingen die suggereren dat er meer niet-zichtbare (bijv. donkere materie en neutrinos) dan zichtbare materie (bijv. sterren, planeten en gas) is, zijn nu ongeveer 100 jaar oud. In het laatste decennium is het gebied van de experimentele donkere materie fysica hard gegroeid. De reden hiervoor is dat steeds meer grond-, lucht- en ruimtetelescopen zeer precies hebben kunnen meten hoeveel massa we werkelijk missen. Figuur 7.16 toont dit het beste: slechts 1% van de massa van het heelal kan worden verklaard door sterren (en planeten) en slechts 14% door (diffuus) gas. Zonder de ontbrekende 85% van de massa kunnen we het begin van ons Universum, de structuurformatie van sterrenstelsels of zelfs het feit dat we planeten en sterren hebben, niet verklaren.

Het proberen te beantwoorden van de volgende vijf hoofdvragen heeft geleid tot de vijf hoofdstukken in dit proefschrift:

- Hoofdstuk 1: Waarom geloven we dat er donkere materie is?
- Hoofdstuk 2: Hoe gebruiken we de XENON1T-detector om donkere materie te vinden?
- Hoofdstuk 3: Hoe onderscheidt XENON1T tussen donkere materie en achtergrondsignalen?
- Hoofdstuk 4: Waar komen de achtergrondsignalen in XENON1T vandaan?
- Hoofdstuk 5: Hebben we donkere materie gevonden met XENON1T?

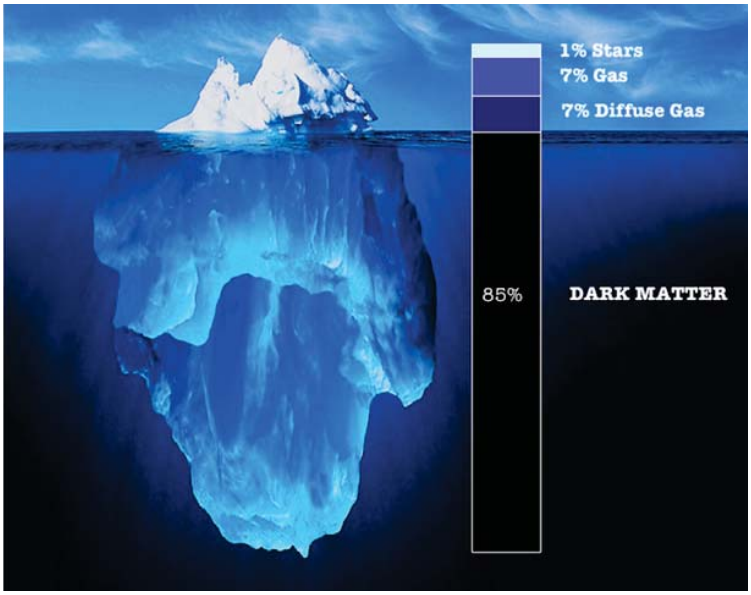

Figure 7.16: Een prachtige ijsberg die de omvang van onze kennis over de materie inhoud van het Universum illustreert. We hebben momenteel slechts ongeveer 15% van alle materie in het heelal waargenomen (inclusief sterren, planeten, gas, enz.). Het grootste deel van de ijsberg, nog steeds verborgen voor onze visie, komt overeen met de ontbrekende 85% donkere materie. Origineel van [1], credits: Ralph Clevenger.

De eerste vier antwoorden zijn te vinden in de hoofdstukken, maar de laatste vraag beantwoord ik meteen. Nee, helaas hebben we geen donkere materie gevonden. Maar ik kan met trots zeggen dat we wereldleider zijn in het vinden van niets.

De data van ons experiment was consistent met het vinden van alleen achtergrondsignalen. Dit resultaat van XENON1T, weergegeven in figuur 7.17, sluit daarmee meer mogelijke donkere materie modellen uit dan alle vorige experimenten. In de figuur zijn alle modellen uitgesloten boven de zwarte 'XENON1T' lijn. Voor elke mogelijke massa van een donker materie deeltje kunnen we bepalen bij welke interactiesterkte met gewone materie we hem kunnen uitsluiten. Het is nu aan de volgende generatie detectors om een donker materie deeltje te ontdekken en om hopelijk een observatie te verklaren die nu bijna een eeuw oud is.

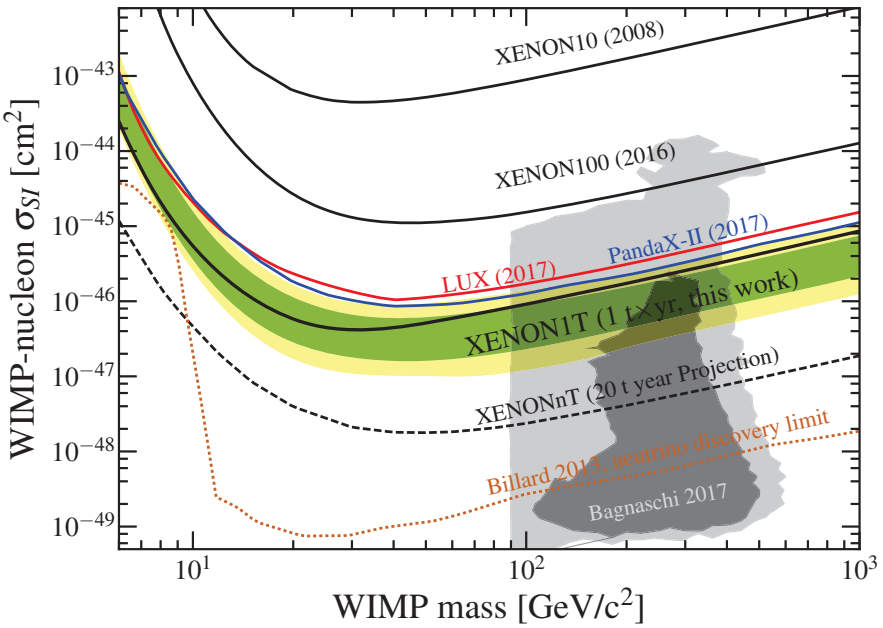

Figure 7.17: Limiet van de spin-onafhankelijke WIMP-nucleon dwarsdoorsnede versus WIMP-massa voor XENON1T bij 90% vertrouwen (zwarte lijn). De 1σ en 2σ gevoeligheidsbanden worden gegeven door respectievelijk de groene en gele banden. Ter vergelijking worden eerdere resultaten getoond van XENON10 [4], XENON100 [5], LUX [6] en PandaX-II [7]. De geprojecteerde gevoeligheid van XENONnT [8], de upgrade van XENON1T, toont de volgende stap van de XENON-samenwerking bij het zoeken naar de donkere materie deeltjes (WIMPs). Niet alle huidige theoretische WIMP-ruimte [8] kan worden onderzocht voordat de experimenten meer nucleaire terugslag van neutrinos (oranje gestippeld) gaan meten [9] dan van WIMPs.

Acknowledgements

Doing a PhD is easy, finishing it is hard, and without my great colleagues, friends and family it would have been so much harder. Even though it is impossible to thank everybody, here I'll try to do my best to acknowledge those that helped in so many ways.

My supervisors. Looking back, I really made a fantastic decision to join the dark matter group at Nikhef (actually, I was just very lucky they asked me). In the last four years I was given the freedom to define my own path in physics, and that is mostly credited to my supervisors Patrick and Auke-Pieter. And for that reason you deserved the joint first place award of 'best supervisor' we gave you.

Auke-Pieter, your never ending enthusiasm for physics is inspiring. You have taught us to always ask questions, to always investigate what we don't understand, and to never be shy about what we don't know. This has created a group that is both critical and appreciative at the same time, and has made all our results so much better. Keep building small experiments, keep feeling responsible for those who are not PIs in our collaboration, keep awarding champagne for papers, but most importantly, keep doing what you love. And if you ever want to trade jobs let me know ;)

Patrick, thanks for being my mentor. You gave me the room to grow by letting me choose my own path, and being patient if it didn't immediately succeed. You always had my back when it was needed, and you stood up for me even when I didn't ask for it. Thanks for helping me improve my writing, without the many hours you spend reddening my pages I would not be as proud, as I am today, with the end result.

Frank, thanks for being my promoter. It was an honour that you chose me to accompany you to the 70th anniversary (or more precise, the funeral) of FOM. It was always an eye opener when you helped me (with the RSI) by just being pragmatic in a world that can look filled with rules and regulations. I will never make a double captions again ;)

Mark and Rafael, thanks for being a role model within the collaboration on how to do physics. You've always taken time to really understand the analysis that is going on and give us useful feedback, something that is rare among PIs. During our first results analysis you two have been the first (and only one) to break me down into tears after my n-th presentation on the fiducial volume. It taught me two valuable lessons. Firstly, that professors can be wrong in what we can achieve ;) Secondly, that if this is the world I want to live in, I need to accept that these situations will happen. So I was very adamant in requesting that you two be part of

my thesis committee. Because, the best scientific results require the most critical (and nice!) physicists.

The last person to thank as part of my physics upbringing is Christian Weinheimer. Even though my path took me elsewhere, you believed in me as someone who can one day lead his own group, and that I'll never forget. You've always stayed true to your word on a personal level, and that is something sometimes rare to find. I hope our paths will keep crossing.

My colleagues. Jelle, let's be clear, no one made a bigger impact on my work then you did, and I cannot even imagine how my PhD would have turned out without you. I haven't met anyone smarter and humbler at the same time. Thank you for always being patient with me when we we're talking about programming or statistics. Randomly throwing physics over our monitors led to debugging DAQ problems, understanding how to run radon calibrations over Christmas and revealing the unshielded spectrum of our beautiful detector. Forever there will be a little Jelle sitting on my shoulder making sure I write functions, dict(zip())s and list comprehensions instead of copy pasting code. And the deal will always remain, if you ever want to share a professorship, and need your local experimentalist, let me know.

Eric, we started working in the same lab, but our relationship actually became stronger the further we were near the end of our PhD. I will always admire your ability to run an experiments, while at the same creating the Monte Carlo that actually fits the data. Thank you so much for incorporating me within XAMS, and for always taking the time to provide the feedback on the content of my papers. I will miss the idea of always being able to disturb you for a new plot I just made. And yes, you will always be remembered as the one who saved me during my first PhD presentation ;)

Peter and Joran, now it will be your honour to bring our group into the XNEONnT era. I fully believe you two will do a great job and keep the Nikhef torch burning in both analysis and hardware. And never worry if it feels a bit too much in the beginning, you guys are already doing better than I ever did when I started my PhD (just ask Chris ;).

And now I've put our two postdocs, Chris and Andrew, who spent most time supervising me, under the section of colleagues. And to be honest, that should be seen as a great complement. Because even when you two were way more experience than us, you've always treated us as equals. Chris, thank you very much for showing me how important it is to correctly setup the software part of an experiment. I will never be able to work again without python, jupyter hubs, github and gitter. And, I will do my best to keep the revolution going in my future experiments. Thank

you also for helping me understand how a collaboration works, during one of our many 'fresh air' brakes. Andrew, you've become a real friend. But maybe more importantly, you've shown me how to be ethical in the work we do. Even at the risk of personal costs, you've been an example of where to draw the line, and that you should never compromise when we know something is wrong. Thanks for all the games we played, we share a similar love for strategy games, and the diplomacy games (and many a catan game) were just epic.

Jasper, of the many master students I supervised, you've been the one I've worked most closely with. We've published one paper together, and are in the process of writing another. Thank you for all the work you've put into it. Without your ever lasting willingness, we would never have gotten the one paper that could get through a review process without a single comment. And as cherry on top, you made the most beautiful cover design for my thesis.

The XENON1T collaboration. Within the XENON1T collaboration there are so many people I've worked with that I can't name you all, without almost adding the full author's list. So thanks, Fei for a great teamwork in leading the background group, Constanze for the fun time with the wall leakage, Michael for discussing the detector during many a drink, Alex for the great physics discussions that we will continue in California, Christian for the amazing background fitting framework, Jacques for being the best neutron generator dismantling helpdesk in het Afrikaans, Joey for being such a great co-author during our writing of the SD paper, Dan for always putting our work in perspective with a little black humour, Junji for always keeping our detector running, Laura for letting me test our amplifiers in Zürich, Marco for all your amazing background knowledge, Pietro for creating so many fiducial volumes, Bart for accompanying me to see the best view of Chicago, Kaixuan for taking the hammer and screwdriver out of my hands at the best possible moment, and Elena for creating this amazing XENON collaboration.

Nikhef. Socially, I have grown up at Nikhef during the last six years. An amazing atmosphere with a collection of smart and ever helping people. So thanks Niels for making me part of RnD, Els for not giving up on me, Jan for showing that we can connect physics and industry, Ivo for showing that outreach is a great choice to inspire the next generation, Lydia for really understanding how to give a good presentation, Jacco for understanding the hard Mondays, Muzaffer for speed rushing my orders, Fred for paying for everything, Ahmed for being able to fix we broke, Trees for always smiling when I walk in, Nico for giving me the great pleasure of

training, Arjen en Pieter for allowing it, Frans and Guido for helping me design, test and build a real working amplifier, all the long gone PhD'rs I had so many drinks and coffees with, and finally Stan for keeping it all together.

My thesis. For actually finishing my thesis, I thank Gerhard Raven as my C-3 member, and the committee for reading my thesis. Special thanks to AP and Paul, who took the effort to still find missing characters after reading almost 200 pages of thesis. Thanks to Alvaro and Bouke for being my arms, when my own wouldn't go any further.

Evert en Rolien, thank you for always supporting me, both in believing in me and practically helping me with this thesis and promotion. Marlie, thanks for accepting me and the fact that I like to share physics figures at any time (especially when their is a fish in the data!). And finally, Gerben en Abe for being my para-nimfen, and Chris and Chandar for being my party-nimfen. Old friends are hard to find, and I really appreciate you stuck with me for all this time.